VERY LOW EARTH ORBIT PROPELLANT COLLECTION

FEASIBILITY ASSESSMENT

A Dissertation
Presented to
The Academic Faculty

by

Lake A. Singh

In Partial Fulfillment
of the Requirements for the Degree
Doctor of Philosophy in the
School of Aerospace Engineering

Georgia Institute of Technology
September 5, 2014

VERY LOW EARTH ORBIT PROPELLANT COLLECTION

FEASIBILITY ASSESSMENT

Approved by:

Dr. Mitchell Walker, Advisor
School of Aerospace Engineering
Georgia Institute of Technology

Dr. Brian Gunter
School of Aerospace Engineering
Georgia Institute of Technology

Dr. Jerry Seitzman
School of Aerospace Engineering
Georgia Institute of Technology

Dr. Ryan Russell
School of Aerospace Engineering
University of Texas at Austin

Dr. Alan Wilhite
School of Aerospace Engineering
Georgia Institute of Technology

Date Approved: September 5, 2014

From this distant vantage point, the Earth might not seem of any particular interest. But for us, it's different. Consider again that dot. That's here. That's home. That's us. On it everyone you love, everyone you know, everyone you ever heard of, every human being who ever was, lived out their lives. The aggregate of our joy and suffering, thousands of confident religions, ideologies, and economic doctrines, every hunter and forager, every hero and coward, every creator and destroyer of civilization, every king and peasant, every young couple in love, every mother and father, hopeful child, inventor and explorer, every teacher of morals, every corrupt politician, every "superstar," every "supreme leader," every saint and sinner in the history of our species lived there – on a mote of dust suspended in a sunbeam.

The Earth is a very small stage in a vast cosmic arena. Think of the rivers of blood spilled by all those generals and emperors so that in glory and triumph they could become the momentary masters of a fraction of a dot. Think of the endless cruelties visited by the inhabitants of one corner of this pixel on the scarcely distinguishable inhabitants of some other corner. How frequent their misunderstandings, how eager they are to kill one another, how fervent their hatreds. Our posturings, our imagined self-importance, the delusion that we have some privileged position in the universe, are challenged by this point of pale light. Our planet is a lonely speck in the great enveloping cosmic dark. In our obscurity – in all this vastness – there is no hint that help will come from elsewhere to save us from ourselves.

The Earth is the only world known, so far, to harbor life. There is nowhere else, at least in the near future, to which our species could migrate. Visit, yes. Settle, not yet. Like it or not, for the moment, the Earth is where we make our stand. It has been said that astronomy is a humbling and character-building experience. There is perhaps no better demonstration of the folly of human conceits than this distant image of our tiny world. To me, it underscores our responsibility to deal more kindly with one another and to preserve and cherish the pale blue dot, the only home we've ever known.

-Carl Sagan

ACKNOWLEDGEMENTS

First and foremost I would like to thank my mother, father, and brother for being supportive during my time in grad school, and for pushing me when I needed it. My father deserves extra thanks for inspiring me and for being my technical editor and proof reader during the creation of my dissertation. I would also like to extend my thanks to my extended family for never failing to be proud of my academic pursuits.

I could not have made it through this process without my second family here in Atlanta. My lab mates deserve my appreciation for their moral support and friendship over these years. In particular, I would like to thank Samuel Langendorf for checking my math and for attending more events with free and free-ish food than I can count. I would like to thank Aaron Schinder for his indirect help with this dissertation. He casually mentioned an idea one day, and it helped me figure this whole thing out. I doubt anyone else remembers it, but I do. Finally, I would like to thank my fellow lab mate Scott King for all of his contributions first as an experienced grad student, then as a fellow Ph.D. candidate. I have enjoyed sharing the Ph.D. experience with him these past few years, and I hope our weekly trips to Fellini's continue even after we are both hooded.

I would like to thank the committee as a whole for their efforts, patience, and presumably for passing me. In particular, I want to recognize Dr. Jerry Seitzman. As the professor for the class I was a teaching assistant for in my first semester, he began the process of teaching me how to work in a lab. His classes were the best, and got me through qualifying exams. Most importantly, he provided me with critical advice I needed towards the end of my time in grad school. I cannot thank him enough. I must

also single out Dr. Alan Wilhite. His ears probably burned a couple of times on my account during this process, but I can say with certainty that his guidance helped me produce a better thesis.

I would like to thank my friends outside of the lab, especially Joe, Kristen, and Jitesh. My years in grad school have been the best of my life so far, and I owe that to them. I also owe that to all of my other friends here for all the weekend fun we have had together, and to this city for being such an incredible place to live. These past five years have been transformative for me in every way I can think of.

Finally, I cannot end these acknowledgments without extending my thanks to all those creative minds who make science fiction. You inspire many in my field, including myself to rise to the occasion and make fantasy into reality. Keep challenging us.

TABLE OF CONTENTS

LIST OF TABLES

LIST OF FIGURES

NOMENCLATURE

A	=	A general function which varies with *x*
$A_{collector}$	=	Collector area
A_e	=	Thruster exit area
A_{PA}	=	Planform area
A_{rad}	=	Radiator area
A_{SP}	=	Solar panel area
$A_{s/c}$	=	Spacecraft frontal area
a	=	Speed of sound, Semi-major axis
a_g	=	Gravitational acceleration vector
B	=	Magnetic field vector
b	=	Orbit normal vector
$C_{D,cyl}$	=	Hyperthermal drag coefficient on a cylinder
$C_{D,FP}$	=	Hyperthermal drag coefficient on a flat plate
$C_{D,min}$	=	Minimum drag coefficient
$C_{D,PA}$	=	Planform area drag coefficient
$C_{D,s/c}$	=	Spacecraft body drag coefficient
$C_{D,s/c,max}$	=	Maximum spacecraft body drag coefficient
$C_{D,s/c,min}$	=	Minimum spacecraft body drag coefficient
c_p	=	Specific heat at constant pressure
D	=	Aerodynamic Drag, Aperture diameter, Spacecraft diameter
E	=	Electric field vector
$E_{x,A}$	=	Elasticity of A with respect to x
e	=	Orbit eccentricity
e_{comp}	=	Specific energy for isothermal compression
e_{liq}	=	Specific energy for liquefaction
F_e	=	Electrostatic force
F_g	=	Gravitational force vector
F_m	=	Magnetic force vector
f	=	Solar viewing factor
G	=	Gravitational constant
g_0	=	Gravitational acceleration at sea level
h	=	Orbital altitude, Planck's constant, Sensible enthalpy
h_e	=	Sensible enthalpy at the exit
h_0	=	Stagnation enthalpy
h_1	=	Initial sensible enthalpy
i	=	Orbit inclination
I_{sp}	=	Specific impulse
$I_{sp,req}$	=	Required specific impulse
I_0	=	Solar intensity
j	=	Current vector

Kn	=	Knudsen number
L	=	Characteristic length, Spacecraft length
MR	=	Mass ratio
m_i	=	Ion mass
m_{dry}	=	Non-propellant mass
m_{tot}	=	Total initial mass
m_1	=	Mass one
m_2	=	Mass two
$\dot{m}$	=	Mass flow rate
$\dot{m}_{avail}$	=	Available mass flow rate for collection
$\dot{m}_{in}$	=	Mass flow rate ingested by the collector
$\dot{m}_{out}$	=	Mass flow rate exhausted by the thruster
$\dot{m}_{store}$	=	Mass flow rate stored by the spacecraft
n	=	Number of gas molecules
$\mathcal{O}$	=	Un-eclipsed portion of the solar disk
P	=	Power
P_{comp}	=	Compression power
P_e	=	Net electrical power
P_{input}	=	Electrical power output
P_{jet}	=	Jet power output
P_{rad}	=	Radiated power
P_{req}	=	Required power
P_{SP}	=	Solar power
P_t	=	Net thermal power
P_{thrust}	=	Thrust power
p	=	Vector perpendicular to the solar array
p_a	=	Thruster ambient pressure
p_e	=	Thruster exit pressure
p_1	=	Initial pressure
p_2	=	Final pressure
q	=	Electric charge
R	=	Gas constant
r_{12}	=	Distance vector between mass one and mass two
S	=	Sun vector
s	=	Speed ratio
T	=	Temperature, Thrust
T_c	=	Core temperature
T_{gas}	=	Gas temperature
T_L	=	Liquid air temperature
T_{LR}	=	Liquefaction radiator temperature
T_R	=	Radiator temperature
$T_{s/c}$	=	Spacecraft temperature
TP	=	Orbital period
u	=	Flow velocity
u_e	=	Exit velocity

u_{eq}	=	Equivalent exhaust velocity
u_{in}	=	Incoming velocity
V_{NC}	=	Neutralizer coupling potential
v	=	Velocity vector
v_{bulk}	=	Bulk velocity of the flow
$v_{E\times B}$	=	E x B drift velocity
v_x, v_y, v_z	=	x, y, and z component of velocity
X'	=	Ground resolution
x	=	A variable present in the function *A*

γ	=	Ratio of specific heats, Beam divergence factor
γ_c	=	Drag coefficient for stopped component of flow
Δh_{vap}	=	Heat of vaporization
ΔV	=	Delta-v
$\mathcal{E}$	=	Specific orbital energy
ε	=	Emissivity
ε_i	=	Ion production cost
ϵ	=	Usage ratio
η_{comp}	=	Compressor efficiency
η_e	=	Power efficiency
η_c	=	Collector efficiency
η_{liq}	=	Efficiency of liquefaction
η_R	=	Reactor thermal efficiency
η_{SP}	=	Total solar panel efficiency
η_t	=	Thruster efficiency
η_u	=	Propellant utilization efficiency
θ	=	Angle between the sun and the perpendicular of the solar array
λ	=	Wavelength of light, mean free path
μ	=	Gravitational parameter
ν	=	True anomaly
ρ	=	Atmospheric density
σ	=	Collision cross-section, Stephan-Boltzmann constant
ϕ	=	Spacecraft roll angle
Ω	=	Right ascension of ascending node
ω	=	Argument of periapsis
ω_c	=	Cyclotron frequency

SUMMARY

This work focuses on the concept of sustainable propellant collection. The concept consists of gathering ambient gas while on-orbit and using it as propellant. Propellant collection could potentially enable operation in very-low Earth orbits without compromising spacecraft lifetime. Very-low Earth orbit presents distinct advantages for Earth observation and some science missions. Another application is as a collection mechanism to generate a surplus of propellant for use by other missions. A propellant depot is a reasonable analog of this mission type. This work conducts a detailed analysis of propellant collection from a physics perspective in order to test the assertions of previous researchers that propellant collection can dramatically reduce the cost of propellant on-orbit.

Major design factors for propellant collection are identified from the fundamental propellant collection equations, which are derived in this work from first principles. A sensitivity analysis on the parameters in these equations determines the relative importance of each parameter to the overall performance of a propellant-collecting vehicle. The propellant collection equations enable the study of where propellant collection is technically feasible as a function of orbit and vehicle performance parameters. This work conducts a detailed survey to identify where propellant collection is technically feasible. Two case studies conducted for a very-low Earth orbit science mission and a propellant depot-type mission serve to demonstrate the application of the propellant collection equations derived in this work. The results of the case studies provide insight into where propellant collection can be beneficial for space missions.

The results of this work show where propellant collection is technically feasible for a wide range of orbit and vehicle performance parameters. Propellant collection can support very-low Earth operation with presently available technology, and a number of research developments can further extend propellant-collecting concepts' ability to operate at low altitudes. However, propellant collection is not presently suitable for propellant depot applications due to limitations in power.

CHAPTER 1
INTRODUCTION

Rocket propulsion requires the expenditure of two fundamental quantities: energy and mass. A growing number of spacecraft collect the energy they need to execute propulsive maneuvers in-situ using solar panels. In contrast, every spacecraft using rocket propulsion has carried all of the propellant mass needed for their mission from the ground. No spacecraft has ever collected propellant in-situ. Spacecraft have limited range and mission capabilities as a result of having no on-orbit source of propellant. This dissertation examines the possibility of collecting the oncoming flow which causes aerodynamic drag and using it to produce thrust to counteract that drag, while potentially storing some of the collected flow for later use.

1.1 Motivation

Propellant collection from the atmosphere has the potential to be a game changing technology for the utilization and exploitation of space. Collecting propellant from the atmosphere enables access to very low Earth orbits (VLEO) that are presently inaccessible to spacecraft for average spacecraft lifetimes [1]. In this study, VLEO orbits are considered to be those orbits with periapsis altitude ranging between 100 and 300 km. These orbits are inaccessible today for long durations due to large aerodynamic drag forces associated with the low altitudes of such orbits. Spacecraft designers have to accept a short lifetime for designs which operate in VLEO because the propellant budget required to maintain such an orbit grows rapidly with design life.

Some spacecraft such as the European Space Agency's (ESA) Gravity Field and Steady-State Ocean Circulation Explorer (GOCE) have operated in the upper reaches of VLEO with the help of stabilizing fins and ion propulsion to continuously counteract

aerodynamic drag [2]. GOCE in particular operated in a 260 km near-circular orbit with an anticipated orbit lifetime of just over 4 years. In contrast, a geostationary orbit (GEO) satellite at an altitude of 35,876 km may remain operational for 15 years or longer [1].

Orbital operation at low altitudes presents advantages for the spacecraft designer [3]. For Earth observation, being close to the Earth reduces the mass and complexity of optics required for a desired resolution and/or increases the optical resolution for a given scale of spacecraft. This is demonstrated through Eq. (1.1) [4], which provides an estimate of ground resolution X' as a function of the orbit altitude h, observed wavelength λ, and aperture diameter D.

$$X' = \frac{2.44h\lambda}{D} \tag{1.1}$$

Figure 1 illustrates that, for the same aperture diameter, a spacecraft operating in VLEO can see dramatic improvement in ground resolution over one operating in low Earth orbit (LEO). A study of telescope cost scaling with respect to aperture diameter reveals that cost scales roughly with the square of the aperture diameter [5]. Thus, a smaller instrument can gather the same resolution imagery in VLEO as a larger instrument in LEO for dramatically reduced cost. However, this advantage comes at the notable cost of reduced total coverage area viewable by the vehicle.

Operation of a spacecraft in VLEO can improve the quality of geodesy and atmospheric measurements as well. Improved quality of gravity field mapping was a driving factor in deploying GOCE at its low orbit [6]. Atmospheric measurements in VLEO space have been limited because it is too high for a balloon to reach and yet too low for current satellites to inhabit without undergoing rapid orbit decay. As such, the region of Earth's atmosphere between 60 and 200 km has been modeled only from

localized data gathered from sounding rockets. Developing technologies to allow long duration missions in VLEO promises to create new opportunities for scientific research.

Atmospheric variations are more important in VLEO than at higher altitudes and can introduce orbit perturbations which are more difficult to predict. This effect is beneficial for defense assets because it increases the difficulty of targeting for adversaries. These benefits are desirable for a variety of Earth-observing missions because they reduce costs and improve data quality and survivability.

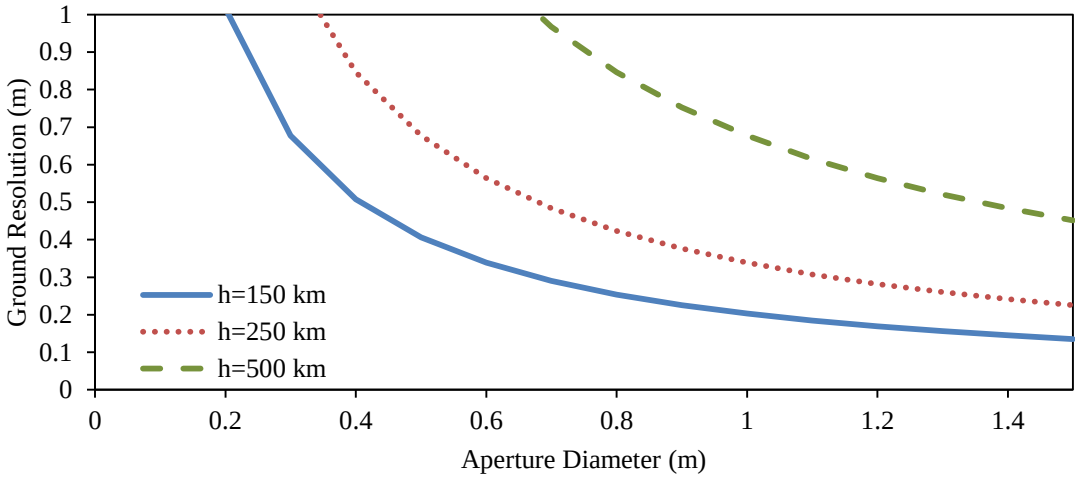

Figure 1. Ground resolution for 555 nm light for varying aperture diameter at selected altitudes.

In addition to the advantages of VLEO operation, collecting propellant directly on-orbit can potentially create an on-orbit source of propellant. This applies not only for the collector spacecraft, but potentially for other spacecraft as well. At current prices, a SpaceX Falcon 9 v1.1 can lift payload into LEO for a price of ~$4,300/kg. Current all-electric GEO spacecraft carry on the order of 25% of their total mass in propellant alone [7]. Carrying the full mission propellant requirement from launch is a major cost to the spacecraft designer.

On-orbit collection of propellant eliminates the cost of launching propellant and may lead to other financial benefits for spacecraft designers and operators. Reduction of

the spacecraft mass at launch may permit launch on a smaller launch vehicle or the launch of additional spacecraft on a single launch vehicle. Additional mass budget for payload permits spacecraft designers to include more and larger instruments. This can potentially lead to improved scientific returns and revenue.

Spacecraft may remain functional at their propellant budget dictated end-of-life. By introducing a source of propellant available on-orbit, spacecraft which continue to operate past their initial design life can be refueled and continue to operate. This allows the spacecraft to continue to generate revenue without having to launch an entirely new spacecraft.

There are obvious effects of propellant collection in mitigating space debris by reducing spacecraft launch rates. If economically and technically feasible, collecting propellant in VLEO may reduce the cost of active debris remediation in LEO and GEO which would have a dramatic and positive effect on the sustainability of our space infrastructure.

Many researchers, detailed later in this work, have looked at collecting propellant from the atmospheres of other planets. Launch costs to deliver payload to other planets are significantly higher than launch costs to deliver payload to Earth orbit. For example, a Boeing Delta II rocket can launch payload to a heliocentric orbit at a price of ~$51,000/kg [8] compared with the aforementioned $4,300/kg price for delivery to LEO on a Falcon 9 v1.1. Even if not economical for near-Earth spacecraft, propellant collection may be an attractive option for journeying around the rest of the solar system. While there are exciting potential applications around bodies like Mars, Titan, and the outer planets this work concentrates on the application of propellant collection around Earth only [9-12]. Much of the work performed here can however be applied to other bodies.

Despite these potential advantages, no mission has yet attempted to collect propellant on-orbit. A complete and well-documented analysis of the available design

space is presently lacking in the literature. Without an understanding of what is possible, mission designers cannot exploit this novel concept.

1.2 Research Contribution

Previous studies of propellant collection in VLEO are incomplete. Many studies consider specific orbits and specific vehicle designs in an attempt to prove their individual feasibility. Most publications neglect important design considerations such as eclipsing, collector performance, thermal loads, power requirements, or thruster performance. Some studies make use of unrealistic or inaccurate performance parameters such as specific impulse, thrust-to-power ratio, and collection efficiency in their analyses. Others make use of unrealistic properties in their analyses such as atmospheric composition, density, and drag coefficient. The result of these limitations is a body of literature which promises feasibility and high performance, but fails to deliver it in a quantifiable way.

This work shows where propellant collection technology can sustain a VLEO orbit and where it can store a surplus of atmospheric gases for other applications. This work utilizes a design-agnostic approach to:

- ***Identify major design factors for propellant collection from first principles.***

Prior studies of propellant collection in VLEO consider specific designs and applications for the technology, but no analysis of propellant collection as a broader concept is present in the literature. Identifying the major design factors for propellant collection allows us to understand what drives the system design in a broadly applicable way. In this work, we take a physics-based approach from first principles to arrive at general governing equations for propellant collection. Performing a sensitivity analysis on these governing equations determines the factors which the system is most sensitive to.

- ***Identify design points where propellant collection is technically feasible from a propulsion perspective.***

Identifying design points where propellant collection is technically feasible from a propulsion perspective constitutes the primary effort in this work. Using the governing equations developed in completion of the previous objective, this work identifies where propellant collection technology can sustain an orbit and where it can store a specified portion of the ingested flow as a function of relevant design factors. Bounds on the ranges of the design factors studied consist of presently available capability and theoretical limitations.

- ***Determine designs for two mission types using presently available technology.***

This final objective serves to highlight the potential benefits of propellant collection technology and demonstrate application of the contributions made in pursuit of the first two objectives. This work considers two mission types. The first mission type is a VLEO science mission similar to GOCE where the minimum achievable and sustainable altitude provides the highest scientific return. The second mission type is a propellant collection mission which seeks to acquire as much ambient propellant as possible while maintaining a stable orbit.

This approach identifies potential design spaces for propellant collection to counteract drag and to store surplus propellant for a mission in place of including the necessary propellant at launch. Identifying these design spaces allows future researchers to quickly determine the propulsive technical feasibility of their propellant collection approaches. This work reveals the areas of technical development which will best expand the feasibility of propellant collection on-orbit, and it reveals designs which are achievable with presently available technology.

1.3 Overview of the Study

The remainder of this document is divided into seven additional chapters, organized as follows. Chapter 2 details relevant background information required to understand the concepts presented in this work along with a review of previous air-breathing proposals in the literature. Chapter 3 presents the approach taken to accomplish the stated research goals. This includes the derivation of the fundamental equations of this work, presentation of the ranges of study for the design parameters, and a detailed description of the specific mission types examined. Chapters 4-7 present the results of this work. Chapter 4 presents the time-average parameters calculated to estimate quantities such as oncoming mass flow rate and ambient temperature. Chapter 5 discusses the results of the sensitivity analysis performed in support of the first research goal. Chapter 6 provides the results of the propulsive technical feasibility assessment component from the second research goal. Chapter 7 presents the results of the case studies mentioned in the final research goal. The final chapter, Chapter 8 summarizes the major conclusions and contributions of this work, and presents avenues for future work.

CHAPTER 2
BACKGROUND

This chapter covers some background concepts necessary for understanding the work to follow as well as an overview of previous efforts in propellant collection in VLEO. The first section provides background information on the composition and behavior of the upper atmosphere. The second section details some fundamental concepts of spacecraft propulsion. The third section provides the tools necessary to understand the orbital mechanics in this work. Finally, the fourth section details the previous work of researchers that is relevant to propellant collection in VLEO.

2.1 The Upper Atmosphere and Gas Dynamics

The upper atmosphere not only provides the material propellant-collecting spacecraft seek to collect, but is also responsible for the aerodynamic drag force propellant-collecting spacecraft must counteract. The upper atmosphere is composed of several different elements including nitrogen, oxygen, helium, hydrogen, and argon. These elements form a number of compounds ranging in complexity from atomic hydrogen to oxides of nitrogen. Additionally, the upper atmosphere contains a population of ionized species. This mixture of diverse species varies with altitude, solar activity, time, and position above the Earth. Altitude leads to particularly strong variations in composition as indicated in Figure 2 [13].

The most significant components making up the atmosphere in the VLEO region between 100 km and 300 km altitude by number density are molecular nitrogen (N_2), molecular oxygen (O_2), and atomic oxygen (O). Helium (He) is also significant in the upper altitudes of interest. Nitrogen and helium are both inert and tend to be non-reactive with materials used in spacecraft construction. In contrast, oxygen species are chemically

reactive with many spacecraft materials. Designers must take this reactivity into account when designing any component which interacts with the flow, especially at high temperatures.

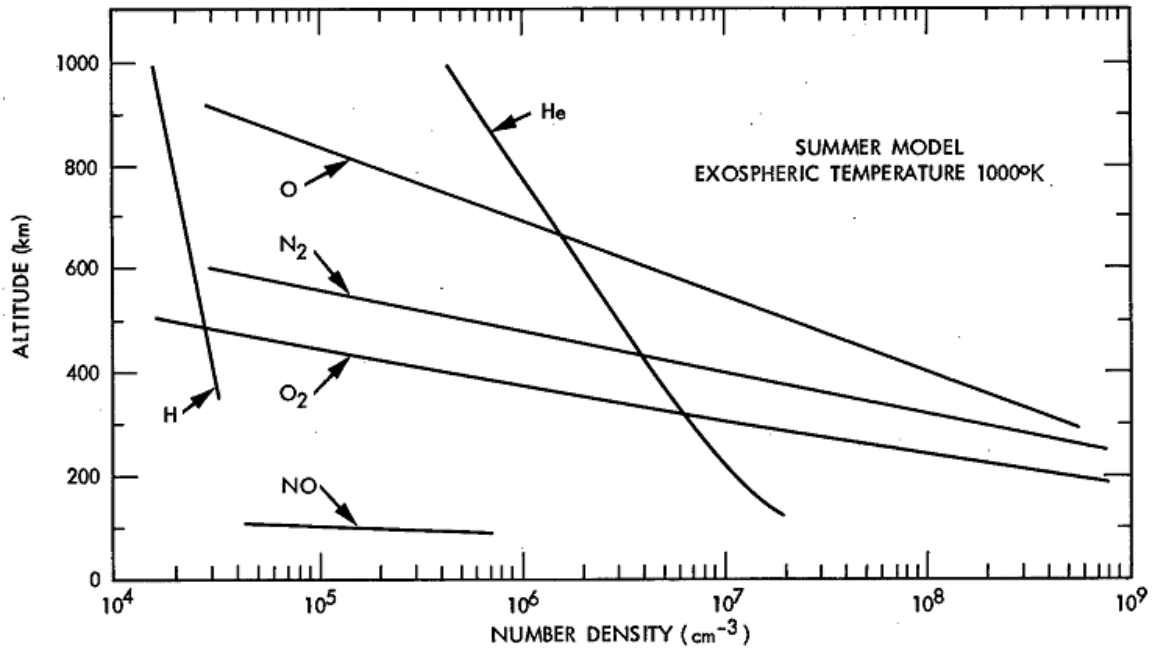

Figure 2. Approximate atmospheric composition with varying altitude [13].

As will be seen later in this work, the aerodynamic drag experienced by a vehicle is directly proportional to the density of the ambient environment around the spacecraft. As can be inferred from Figure 2, the ambient density is inversely proportional to altitude. Figure 3 is a general profile of atmospheric density as a function of altitude and supports this inference. Spacecraft at lower altitudes will thus experience higher drag, all other factors remaining equal.

As atmospheric density changes, so too does the mean free path of the gas. The mean free path, λ represents the statistical average distance a particle in a gas travels before colliding with another particle. The number density of the gas, n and the cross-section for collision σ determine λ as demonstrated in Eq. (2.1). Number density is an alternate formulation of classical density with units of number of particles per unit

volume rather than mass per unit volume. The cross-section for collision has units of area and represents the likelihood of a collision occurring. Figure 4 shows a representative curve of mean free path with respect to altitude and demonstrates its wide range over VLEO altitudes.

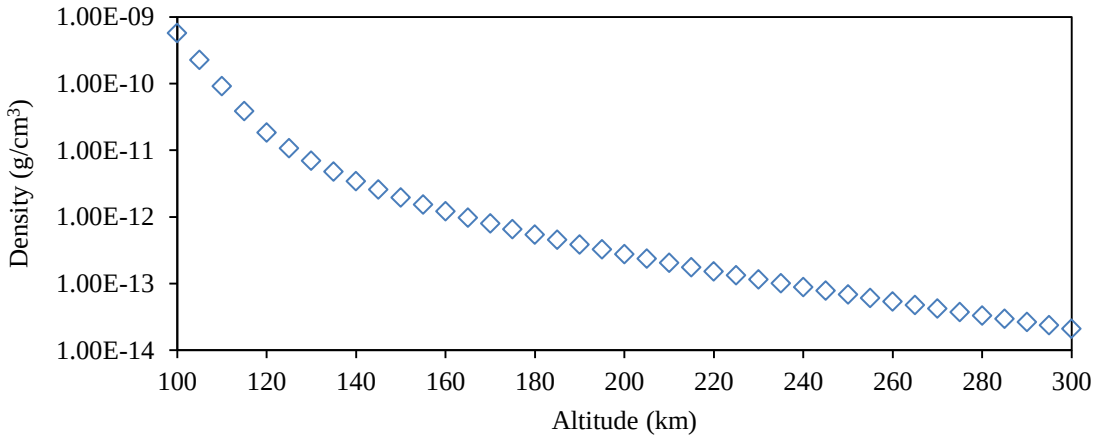

Figure 3. Representative curve of density with varying altitude.

$$\lambda = \frac{1}{n\sigma} \tag{2.1}$$

Mean free path determines how a gas responds to the motion of an object through it. The dimensionless parameter known as the Knudsen number provides a mechanism for understanding this response. Expressed in Eq. (2.2), *Kn* is a function both of the mean free path and a representative length scale of the object, *L* with which the gas is responding to. For $Kn << 1$, the flow is considered to act as a continuum with particles able to exchange information with one another through collisions, while for $Kn >> 1$ the flow is considered to act as a collection of non-interacting particles also known as free-molecular flow. Spacecraft typically operate in a free-molecular flow regime, but at the low altitudes considered in this work the Knudsen number may be sufficiently close to one that continuum-like behaviors arise.

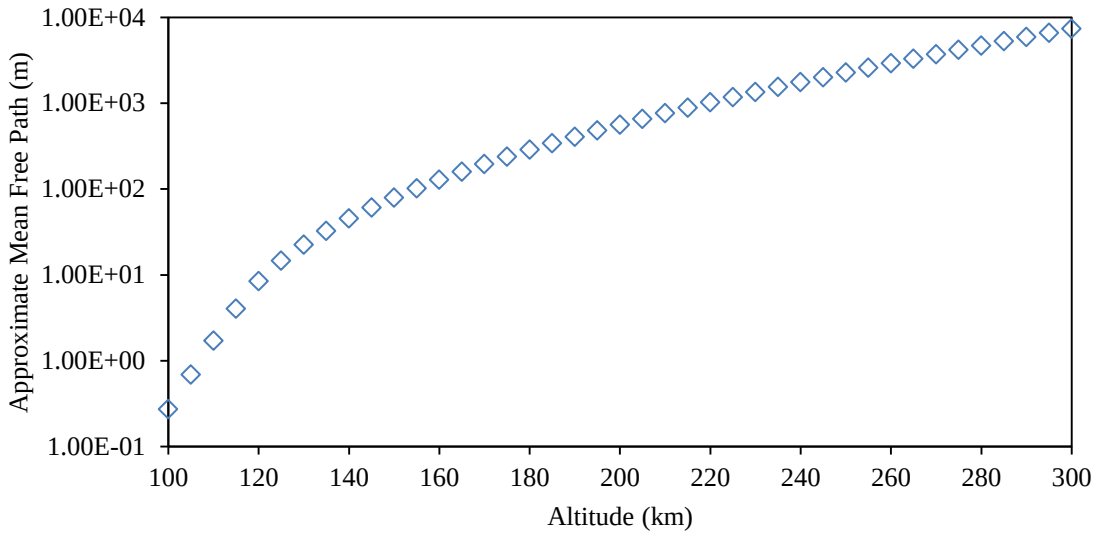

Figure 4. Approximate mean free path for nitrogen molecules with varying altitude (calculated assuming hard-sphere model).

$$Kn = \frac{\lambda}{L} \tag{2.2}$$

The ability to exchange information between particles in the gas dictates its response to an object. The mean free path provides a measure of how available collision partners are through considering the density of potential partners and their relative size, but the velocity of the particles also contributes to the ability of the flow to transport information. Information transport through collisions in a flow occurs at the local speed of sound. Eq. (2.3) expresses the speed of sound a as a function of the temperature T, the gas constant for the gas R, and the specific heat ratio γ. If the bulk flow of the gas is much larger than the speed of sound, then the ability of the flow to transmit information upstream becomes restricted. This is because the bulk flow of the gas effectively outpaces the upstream transmission of information, thus altering the behavior of the flow. In continuum flow, this condition is called supersonic or hypersonic flow. In free-molecular flow, it is called hyperthermal flow. A propellant-collecting spacecraft operates in these types of flows as a result of its orbital speed on the order of 8 km/s compared to the speed of sound on the order of 300 m/s.

$$a = \sqrt{\gamma RT} \tag{2.3}$$

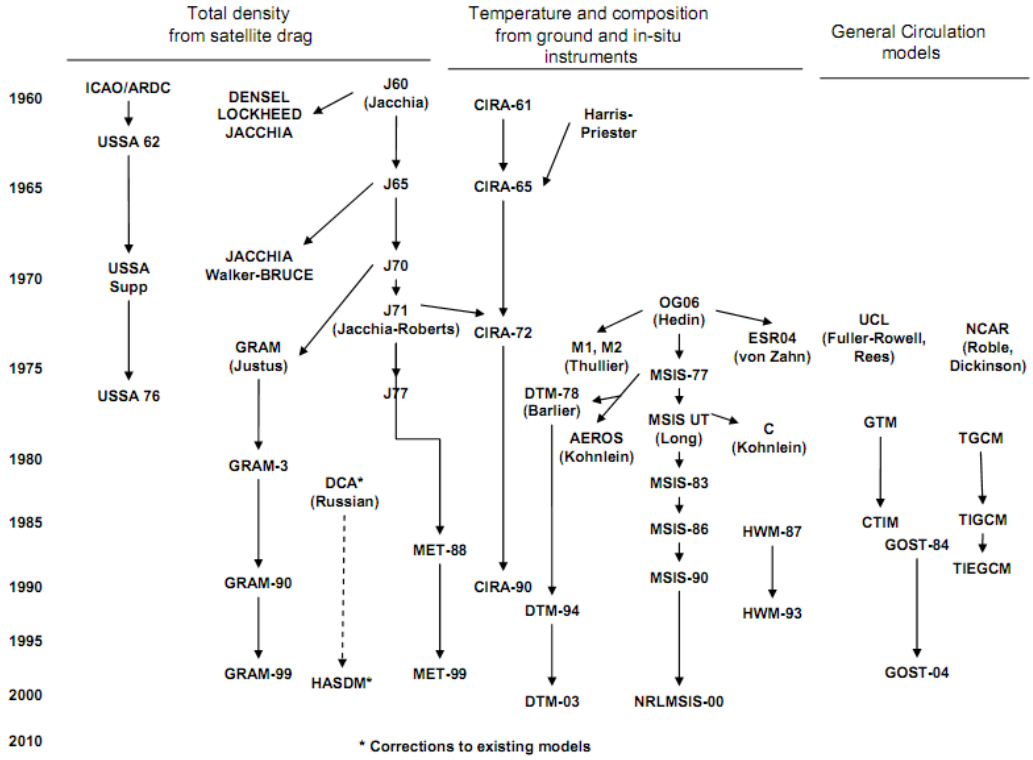

Figure 5. Evolution of atmospheric models circa 2007. Models vary in data source, fidelity, and national origin. Diagram adapted from [14].

Numerous atmosphere models estimate the atmospheric density as a function of time, location, and space weather conditions. Figure 5 demonstrates the diverse options available for atmospheric models. Models vary in their data sources, fidelity, and national origin. The Jacchia series of atmosphere models ascertain total density only through satellite drag measurements. The most recent JB2006 and JB2008 Jacchia models provide the highest fidelity for determining the drag on a satellite, but do not model composition. In contrast, the mass spectrometer incoherent scatter (MSIS) series of models provide high-fidelity predictions of composition but are considered less accurate for modeling total density than the Jacchia series. The presented data and models provide a good

census of what is available on-orbit to collect. However, the collected species must still be accelerated to produce thrust. This is accomplished through propulsion.

2.2 Spacecraft Propulsion

Rocket propulsion is the most common way spacecraft change their orbits and trajectories. A rocket propulsion system is characterized as a system which accelerates a vehicle through the acceleration and expulsion of stored propellant. The force applied on the spacecraft by a rocket propulsion system is called thrust, T. Thrust is a function of the mass flow rate of propellant out of the system $\dot{m}$, the exit velocity of the propellant u_e, the exit area of the propellant exhaust A_e, and the difference between the exit pressure and the ambient pressures, p_e and p_a respectively. As can be seen from Eq. (2.4), the thrust produced by a rocket propulsion system is a combination of a flow term and a pressure term. Typically, we combine these terms as an equivalent exhaust velocity, u_{eq}, given in Eq. (2.5):

$$T = \dot{m}u_e + A_e(p_e - p_a) \tag{2.4}$$

$$u_{eq} = u_e + \frac{A_e}{\dot{m}}(p_e - p_a) \tag{2.5}$$

Substituting into Eq. (2.4), the thrust from a rocket propulsion system can be expressed as Eq. (2.6):

$$T = \dot{m}u_{eq} \tag{2.6}$$

It can be seen from Eq. (2.6) that the equivalent exhaust velocity is an important parameter in determining the thrust. In order to avoid confusion with units, we typically express this parameter as specific impulse, I_{sp}. Eq. (2.7) defines the specific impulse for a rocket propulsion system:

$$I_{sp} \equiv \frac{u_{eq}}{g_0} \tag{2.7}$$

where g_0 is the standard acceleration of gravity at sea level on Earth (even if the rocket is on another planet, or in space). Specific impulse has units of seconds, and can be understood as the amount of time a rocket can produce one unit of force with one unit of mass. Rockets with higher specific impulse are characterized by higher exhaust velocities and lower mass flow rate for a given thrust level.

Specific impulse is important to the spacecraft designer because it constrains the payload mass available at the desired destination or end of mission. Eq. (2.8) defines the mass ratio *MR* as the ratio of the non-propellant mass, m_{dry}, to the total initial mass, m_{tot}.

$$MR \equiv \frac{m_{tot}}{m_{dry}} \tag{2.8}$$

Spacecraft designers use this non-dimensional parameter as a measure of the performance of the spacecraft, and to size propellant storage. A higher mass ratio means more dry mass is available for instruments and support components. By integrating Eq. (2.6) from m_{tot} to m_{dry} we arrive at Eq. (2.9): the Tsiolkovsky rocket equation which relates rocket performance to payload mass fraction and destination:

$$MR = e^{\frac{\Delta V}{g_0 Isp}} \tag{2.9}$$

where ΔV (pronounced "delta-vee") is the available change in velocity available to the spacecraft. ΔV is a measure of a spacecraft's ability to change its orbit or trajectory. A spacecraft with more available ΔV can change its orbit or trajectory more than a spacecraft with less available ΔV. This term accounts for all of the additional losses a spacecraft may encounter during propulsion such as gravity losses, drag, and steering losses. Tsiolkovsky's rocket equation shows that the specific impulse of a rocket system is directly related to how much propellant a spacecraft must accommodate in order to attain the required performance for a given mission.

In-space rocket propulsion systems can be roughly divided into the categories of chemical propulsion and electric propulsion (EP). Other, more exotic propulsion options exist, but they are either not flight-proven or do not rely on propellant stored within the vehicle. Some examples include nuclear thermal propulsion and electrodynamic tethers, but these options are not considered in this work. Chemical propulsion systems store the energy required to accelerate propellant in the propellant itself as chemical energy whereas electric propulsion systems use electrical energy provided by the spacecraft to energize the propellant.

As seen in Section 2.1, the upper atmosphere is primarily composed of a chemically inert mixture of nitrogen and oxygen. As will be seen later, the available chemical energy in the air at the altitudes of interest is insufficient to sustain orbit without supplement from the spacecraft in the form of energy or reactive species. Thus, this work examines EP in particular because it does not require propellants to have available chemical energy and is able to attain higher specific impulse than chemical propulsion. These advantages come at the cost of increased electrical power requirements for the spacecraft. EP systems have additional performance metrics regarding power consumption compared to chemical propulsion systems.

One such performance metric is the thruster efficiency, η_t. This parameter is defined as the ratio of the jet power produced by the EP device to the total electrical input

power, as expressed in Eq. (2.10). The thruster efficiency is a measure of how effectively the EP device translates electric power into mechanical acceleration.

$$\eta_t = \frac{TI_{sp}g_0}{2P} \tag{2.10}$$

Electric propulsion systems can be split into three classifications based on the mechanism by which they use electrical energy to accelerate propellant: electrothermal, electromagnetic, and electrostatic. Electrothermal propulsion adds electrical energy to the propellant as heat before accelerating it through a nozzle. An increase to the stagnation enthalpy h_0 of the propellant drives an increase in exit velocity. Eq. (2.11) demonstrates the relationship between stagnation enthalpy, sensible enthalpy h, and flow velocity u. Eq. (2.12) results from realizing the initial flow velocity is negligible and that initial and final stagnation enthalpies must be the same through the nozzle.

$$h_0 = h + \frac{u^2}{2} \tag{2.11}$$

$$h_1 = h_e + \frac{u_e^2}{2} \tag{2.12}$$

Devices that use this mechanism include resistojets and arcjets. These devices achieve specific impulse in the range of 300 to 1100 seconds [15]. Because they inject energy into the propellant as heat, electrothermal devices have surfaces which can exceed 3000 K. These temperatures make surfaces susceptible to oxidation from any oxygen present in the propellant as will be the case for ambient gas in VLEO. Without separating out the oxygen, present limitations in materials make electrothermal thrusters unsuitable for use with systems which consume ambient gas.

Electromagnetic thrusters operate by using an electromagnetic force to accelerate ionized propellant. This force is the product of the plasma current *j* and magnetic field *B* as expressed in Eq. (2.13).

$$\boldsymbol{F_m = j \times B} \tag{2.13}$$

Numerous types of electromagnetic thrusters exist. Each employs unique configurations of magnetic field and current flow to generate an accelerating force on the propellant. One such configuration is the pulsed plasma thruster (PPT) which has recently been proposed as a candidate for use with air [16]. Figure 6 shows a diagram of a solid propellant PPT device. The igniter triggers an arc in the top layer of the propellant between the cathode and anode that vaporizes and ionizes some of the propellant. The ionized propellant is accelerated out of the thruster due to the self-applied magnetic field to generate thrust. This relatively simple device has been flown for minor station-keeping and attitude control applications [17].

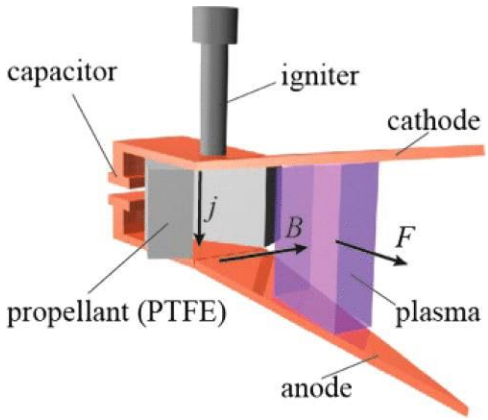

Figure 6. Diagram of a pulsed plasma thruster [18]. The igniter triggers an arc in the propellant between the cathode and anode that vaporizes and ionizes some of the propellant. The ionized propellant is accelerated out of the thruster due to the self-applied magnetic field.

Another type of electromagnetic thruster which has been suggested by previous efforts as an option for propellant collection vehicles is the magnetohydrodynamic

(MHD) ramjet [19, 20]. An MHD ramjet ingests oncoming flow without stopping it, ionizes it, and accelerates it via Eq. (2.13) out of the vehicle. In this manner, an ideal MHD ramjet needs only to accelerate the ingested flow from the vehicle velocity to the desired thrust velocity. By preserving the initial energy of the flow, a ramjet-type electric thruster can potentially realize dramatic power savings.

Electrostatic propulsion utilizes an electrostatic force to accelerate ionized propellant. This electrostatic force is the product of the charge state of the ions, q and the applied electric field, E as expressed in Eq. (2.14).

$$\boldsymbol{F_e = qE} \tag{2.14}$$

The primary electrostatic propulsion devices of interest in this work are the gridded ion thruster and Hall effect thruster (HET). These devices have flight heritage on numerous spacecraft and have operated on a range of propellants [2, 7, 21, 22]. Their technical maturity makes them attractive options for application to propellant collection.

An ion engine has three basic components: (1) a means to generate a plasma, (2) acceleration grids, and (3) a neutralizing cathode. Figure 7 shows a schematic of the relevant components of an ion engine [23]. Propellant feeds into the plasma generator portion of the device where it is ionized. The accelerator grids extract ions from the plasma and accelerate them to produce thrust. Electrons from the neutralizer cathode neutralize the accelerated ions to prevent them from back-streaming to the thruster and maintain spacecraft charge neutrality.

Three methods for ionization have been used on flight hardware: direct current (DC) discharge, radiofrequency (rf), and microwave-based electron cyclotron resonance (ECR). DC discharge plasma generation uses a thermionic cathode to inject an electron current into the discharge chamber. The electrons undergo collisions with neutral propellant which leads to the formation of ions and additional electrons. A confining

magnetic field extends the residence time of the electrons in the chamber by directing their natural flow away from the chamber wall. Ultimately, collisions will provide the electrons with sufficient energy to overcome the magnetic field and conduct to the wall.

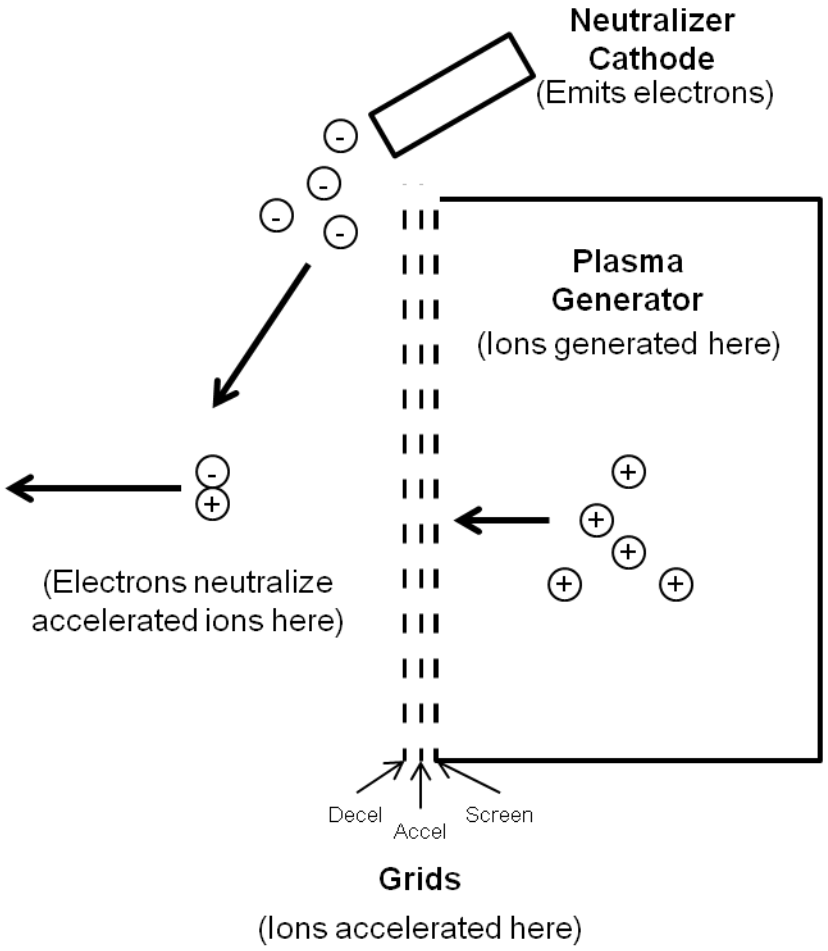

Figure 7. Ion thruster schematic showing grids, plasma generator, and neutralizer cathode A more detailed diagram is available from [23].

The thermionic cathode must reach high temperatures in order to emit electrons. Thus, while DC discharge is the most popular method for plasma generation in ion thrusters it is unsuitable for operation with air for the same reason as arcjets and resistojets. The oxygen in the air will rapidly oxidize the cathode emission material, reducing lifetime.

Radiofrequency sources replace the thermionic cathode with an antenna structure that delivers rf power into the discharge chamber. The rf energy couples to the electrons and heats them to sufficient energy to ionize the propellant injected into the chamber. The antenna structure is commonly mounted on the exterior of the discharge chamber to avoid any direct interaction with the plasma. Insulating materials make up the discharge chamber wall in rf devices to allow transmission of rf energy into the chamber from the external antenna. Previous researchers have documented three distinct coupling mechanisms between rf and plasma electrons. These are capacitive coupling, inductive coupling, and helicon wave coupling. Plasmas generated through these coupling mechanisms each exhibit unique density and distribution properties [24, 25]. A 0-D particle and energy balance model shows that the net energy cost to produce an ion using rf is somewhat higher than in a well-designed DC system [23]. This means that the total efficiency is lower for an rf system.

ECR heating is the least mature of the three plasma generation methods and the most technically challenging. These systems consist of a microwave source and an intense magnetic field on the order of 1000-2000 gauss [23]. Charged particles in a magnetic field rotate around the magnetic field lines at the gyro frequency or cyclotron frequency as expressed in Eq. (2.15) where ω_c is the cyclotron frequency, q is the electric charge, B is the magnetic field strength and m is the mass of the charged particle. Coupling to this frequency for the electrons with microwave power leads to resonant heating of the electrons to provide sufficient energy to ionize injected propellant through collisions. An ECR system shares many of the same advantages and disadvantages as rf does over DC discharge. However, ECR systems are limited in size because of the necessary magnetic field strength and present limitations in microwave power sources [23].

$$\omega_c \equiv \frac{q|B|}{m} \tag{2.15}$$

Once the plasma is generated, ions must be extracted and accelerated. Ion engines accomplish this with a series of grids typically referred to as the ion optics. Figure 8 adapted from Goebel shows a simplified diagram of an ion thruster operating with a three-grid configuration [23]. The screen grid is typically biased at the discharge cathode potential to attract ions and repel electrons. Once past the screen grid, the ions encounter the accel grid which is biased far below the screen voltage in order to generate the accelerating electric field. After accelerating through the accel grid, ions pass through a final decel grid which serves to protect the accel grid from back flowing charge exchange (CEX) ions which can otherwise erode the accel grid. Grid erosion is the primary life determining mechanism for ion thrusters. As such, much care is taken with the selection of materials and design geometry of the grids to minimize ion impingement to the grids and maximize resistance to erosion.

Once downstream of the ion optics, the ions must be neutralized to prevent charge buildup and backflow of the accelerated ions to the spacecraft. This is accomplished with a neutralizer cathode. The current state of the art is the thermionic cathode, but this has already been deemed unsuitable for use with air because of the presence of oxygen and its deleterious effect on lifetime. An alternative technology may be field emission cathodes, but they are still in the early stages of development for use with electric propulsion devices. Yet another possible alternative is the microwave cathode proposed by Diamant, which operates in a similar way to ECR plasma generation [26].

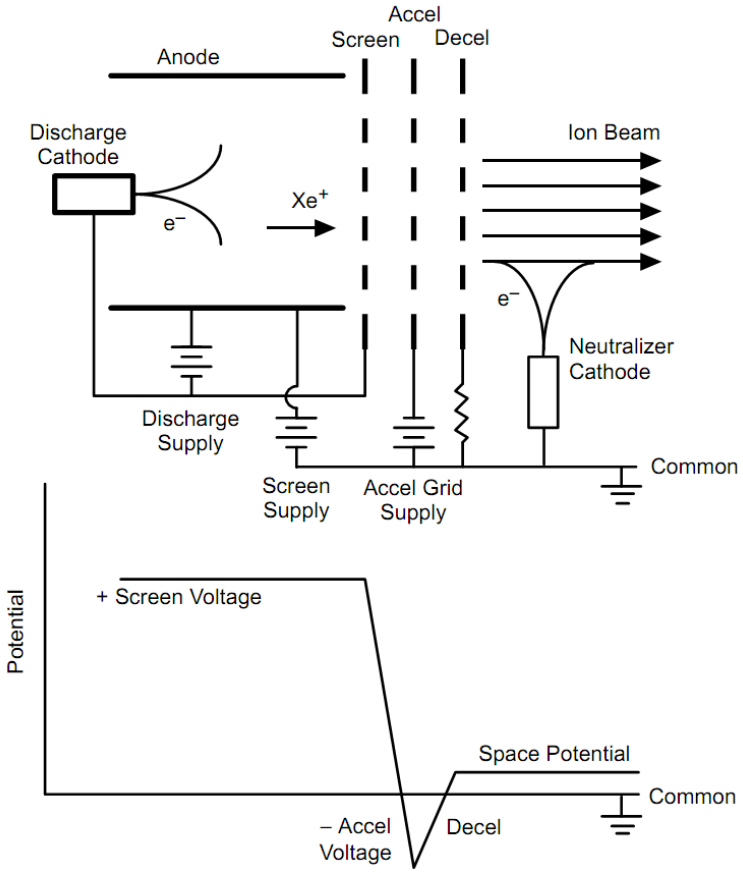

Figure 8. Simplified schematic and potential diagram of an ion thruster with a three-grid configuration [23].

Hall effect thrusters (HET) are simple devices when compared with an ion thruster. Whereas an ion thruster has a discharge chamber, multiple grids, and a neutralizer cathode, a basic HET has only a single cylindrical channel with an anode, a magnet which generates a radial magnetic field, and a neutralizer cathode. While simpler to construct, the HET relies on more complicated plasma interactions to generate thrust than an ion thruster [23]. Ion thrusters break up the process of accelerating the propellant into three steps which occur in three different regions of the device. In contrast, the HET performs ionization and acceleration in a single region [27, 28].

Figure 9 is a notional schematic of a HET. The anode serves to inject propellant into the thruster and produce the electrostatic field necessary for acceleration. Electrons from the external cathode flow into the thruster towards the anode where they become

trapped by the combined electric and magnetic fields. The trapped electrons flow azimuthally around the thruster at the E x B drift velocity, expressed in Eq. (2.16) for electric field $\boldsymbol{E}$ and magnetic field $\boldsymbol{B}$ [29]. The neutral propellant from the anode flows towards the channel exit as a result of the pressure gradient where it encounters the confined electron flow. Collisions between the electrons and neutral propellant ionize the propellant, making it susceptible to the electric field which accelerates it out of the thruster. Electron flow from the external cathode neutralizes the accelerated propellant.

$$\boldsymbol{v_{E\times B}} = \frac{\boldsymbol{E}\times\boldsymbol{B}}{B^2} \tag{2.16}$$

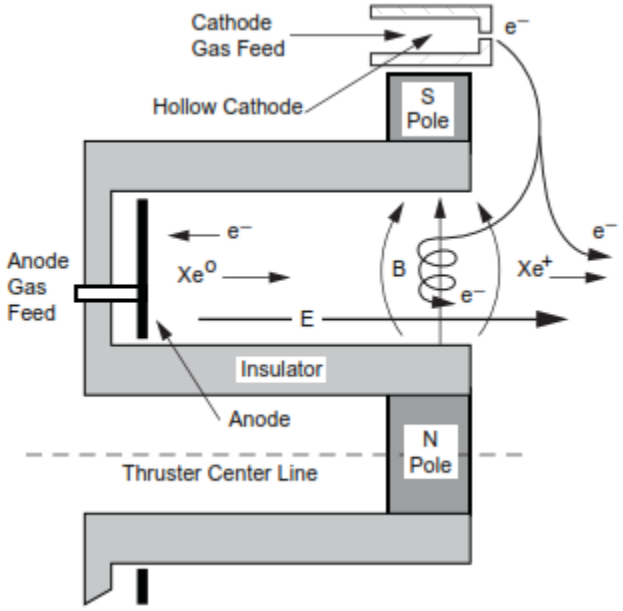

Figure 9. Notional HET schematic, showing the anode, magnet, and cathode [23].

The primary region of electric potential drop overlaps with the peak radial magnetic field region [23]. This means that the ionization and acceleration regions overlap in a HET. As a consequence, ions generated later in the ionization region see a smaller potential drop than those generated at the beginning of the ionization region. Thus, unlike an ion thruster, a HET does not generate a mono-energetic ion beam. While

this is a summary of HET operation, it should suffice for an understanding of the concepts discussed in this work.

2.3 Orbital Mechanics

The strongest natural force which influences the motion of a spacecraft in orbit is gravity. Eq. (2.17) is the fundamental equation governing gravitational force. G is the gravitational constant, specified as $6.674\times10^{-11}\text{m}^3\text{kg}^{-1}\text{s}^{-2}$. The terms m_1 and m_2 are the masses of the two bodies attracting one another, and r_{12} is the vector between them. In most spacecraft applications, one of the masses is that of a planet which is much larger than the spacecraft mass. Further simplification of Eq. (2.17) results by dividing both sides by the mass of the spacecraft and combining the gravitational constant and planetary mass together to arrive at Eq. (2.18). The new term μ is called the gravitational parameter and is a constant determined by the nearest planetary body.

$$\boldsymbol{F_g} = \frac{Gm_1m_2}{r_{12}^2}\hat{\boldsymbol{r}}_{\boldsymbol{12}} \tag{2.17}$$

$$\boldsymbol{a_g} = \frac{\mu}{r_{12}^2}\hat{\boldsymbol{r}}_{\boldsymbol{12}} \tag{2.18}$$

These equations describe the acceleration present on a spacecraft near a planet, but do not describe the position or pattern of motion. Classical orbital elements accomplish this with six unique parameters. Figure 10, adapted from Vallado's text [30], shows a visual representation of the orbital parameters. These include the semi-major axis a, eccentricity e, inclination i, argument of periapsis ω, right ascension of the ascending node (RAAN) Ω, and true anomaly ν. Together, these elements describe a position on a specific conic orbit in a specific plane.

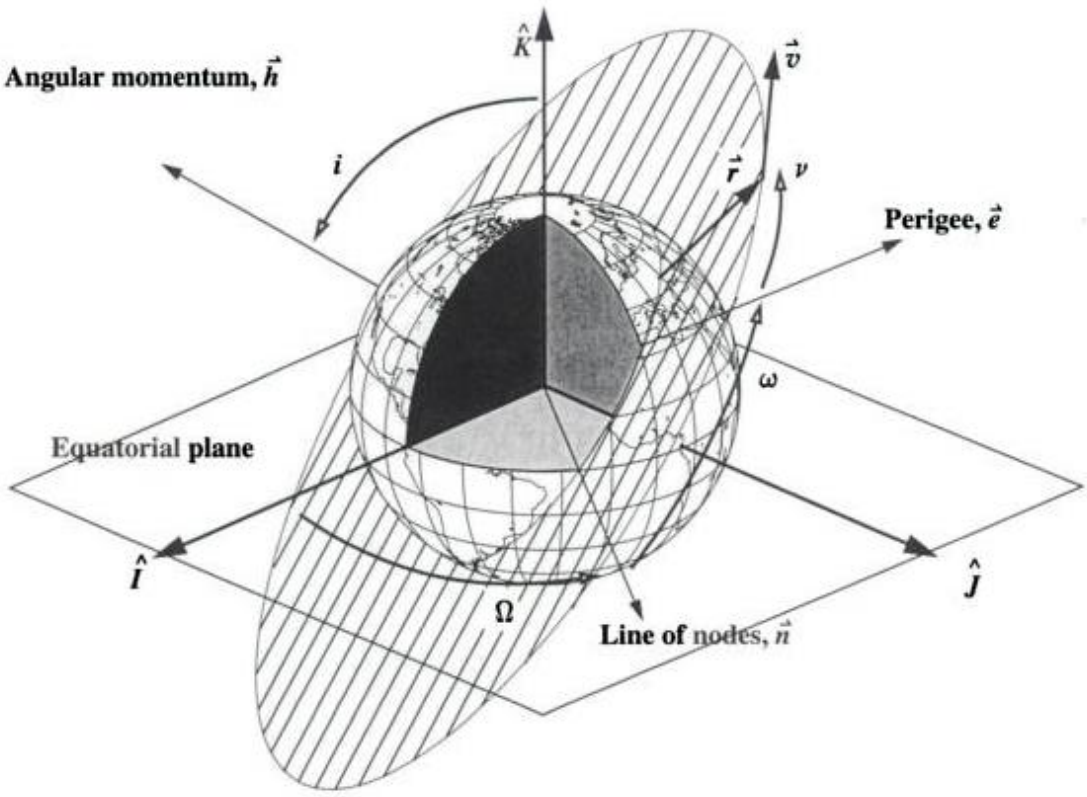

Figure 10. Diagram indicating classical orbital elements [30].

The semi-major axis defines the size of the orbit and is the average of the periapsis (closest) and apoapsis (farthest) radii for the orbit. Eccentricity is a measure of how elongated an orbit is. Circular orbits have eccentricity equal to zero while elliptical orbits have eccentricity between zero and one. Inclination is the angle between the normal vector of the equatorial plane (the plane in space defined by the equator) and the normal vector of the orbital plane. RAAN is the angle between the vernal equinox vector (the direction to the sun on the vernal equinox, denoted as $\hat{\boldsymbol{I}}$) and the point where the spacecraft crosses the equatorial plane. Argument of periapsis is the angle between the equatorial plane and the radius vector at periapsis. True anomaly is the angle between the radius vector at periapsis and the current radius vector of the spacecraft.

While these orbital elements can describe any conical orbit, those of interest in this work are circular and elliptical orbits. The orbital period *TP* for these orbits is a

function only of the semi-major axis and the gravitational parameter as expressed in Eq. (2.19).

$$TP = \frac{2\pi}{\sqrt{\mu}} a^{3/2} \tag{2.19}$$

In the absence of external energy inputs, the specific mechanical energy $\mathcal{E}$ is a function only of semi-major axis and is a constant as expressed in Eq. (2.20).

$$\mathcal{E} = -\frac{\mu}{2a} \tag{2.20}$$

In addition to central-body gravity, other forces and perturbations may impact the motion of a spacecraft. The most commonly considered second-order effects are aerodynamic drag, solar radiation pressure, third body effects, and anisotropic contributions to Earth's gravity. Aerodynamic drag is the primary second-order effect considered in this work, and results from friction between the spacecraft and the rarefied gases of the upper atmosphere. Solar radiation pressure is the momentum transfer to the spacecraft from incident solar radiation. Solar radiation can become important if left uncompensated for over a long period of time, but its effect is far less than aerodynamic drag in the orbital regions of interest in this work.

Third body effects are gravitational forces exerted upon spacecraft by celestial objects aside from Earth. The Sun, Moon, and other planets all exert measurable forces on orbiting vehicles. This work includes the third body effects from the Sun and Moon. Anisotropic contributions to Earth's gravity result from deviations in the Earth's mass distribution from a uniformly distributed sphere. The largest deviation occurs from the Earth's rotation about its polar axis, which serves to oblate the Earth such that its circumference around the Equator is larger than its circumference around lines of

longitude. Because the altitudes studied in this work are unusually low for spacecraft to inhabit, Earth oblateness is included in the calculations performed in this work.

2.4 Review of Air-Breathing Spacecraft Concepts

As discussed in Chapter 1, numerous researchers have explored the concept of collecting propellant while in space. These concepts have varied in scale and complexity from chemical ramjets to fusion-driven interstellar vessels. This section examines the efforts of previous researchers to develop concepts for air-breathing spacecraft, estimate their performance, and understand the physics involved.

Research into propellant-collecting concepts occurred in distinct eras. During the Cold War, concepts tended to be large, complex, and nuclear powered. After the Cold War, concepts transitioned to solar power sources and more effort has been devoted to detailed analysis of specific components of a propellant-collecting architecture.

2.4.1 Cold War Era Air-Breathing Spacecraft Concepts

Sterge Demetriades was the first researcher to propose collection of air by an orbiting spacecraft in his seminal 1959 paper [19]. He proposed a Propulsive Fluid Accumulator (PROFAC) device that would collect, liquefy, and store incident air for use as propellant. PROFAC would collect air on-orbit rather than carrying its required propellant from the ground. In this way, the PROFAC system would dramatically reduce launch mass needed for a mission. Demetriades envisioned this device as a direct competitor to the chemical and nuclear propulsion options which were being explored by others at the time for an eventual moon mission.

In PROFAC's original envisioning, an 11-ton vehicle would collect approximately 400 kg of air each day from a 10 m^2 collector at an orbital altitude of 100 km. To

counteract drag, Demetriades proposed a magnetohydrodynamic (MHD) thruster powered via a nuclear reactor with a total electrical output of 6 MW. His 1959 work briefly mentions solar power. It asserts, without proof, that solar power is viable at altitudes above 150 km while the PROFAC concept is only economically feasible below 135 km. Without any details, it is not possible to determine how Demetriades arrived at this conclusion.

Demetriades cites earlier work he presented with Kretschmer in 1958 as the origination for the PROFAC concept [31]. The 1958 work involved utilizing the energy stored in the form of dissociated oxygen in the upper atmosphere as a power source for propulsion of exospheric aircraft. As an aircraft, this work was intended to power vehicles operating at sub-orbital velocities.

A final paper by Demetriades in 1962 lays out some concepts of operations (CONOPS), but does not discuss them in detail [32]. Demetriades performs the first analysis of the thermodynamics of cryopumping in a modified Brayton cycle to collect propellant in this work. However, Demetriades does not suggest a mechanism to move cryopumped air from the cryopumping surface into storage. He also attempts to optimize the PROFAC concept for minimum energy expended per unit mass of stored air. He finds that the minimum rests at roughly the design point where half of the collected air is used for propulsion while the other half is stored. This finding is an important result which will be verified in this work.

In 1960, only a year after Demetriades' seminal work; Bussard proposed scooping hydrogen from the interstellar medium [33]. The vehicle would release energy from the collected hydrogen via fusion and accelerate the reaction products to generate thrust. This concept has been made famous in Science Fiction works as the Bussard Ramjet [34] (or similarly Bussard collectors located on the leading edges of warp nacelles on Federation starships in *Star Trek*) and remains the most extreme "air" breathing concept in scientific literature. While all documented air-breathing concepts developed in the Cold War era

considered nuclear power sources [9, 19, 32, 33, 35-39], no other concept proposed performing nuclear reactions directly with the collected matter.

Berner and Camac worked concurrently with Demetriades to develop a detailed analysis of an air-breathing concept for collecting propellant for other vehicles [35, 40]. Their work includes a basic analysis of all of the major components of a propellant-collecting spacecraft and makes a number of notable contributions. This is the first work to seriously consider and analyze solar power in addition to nuclear power. It is also the first work to propose and analyze a chemical absorption process for collecting incoming air as opposed to a compressing inlet. The first detailed analysis of the incident heat flux on the spacecraft as a result of accelerating the oncoming flow is also included in this work.

Perhaps most importantly, Berner and Camac establish the "weight-doubling time" parameter. This is the amount of time required for the spacecraft to store a surplus of propellant equal to its dry mass. They go on to use this parameter along with the launch vehicle and spacecraft costs to estimate the vehicle lifetime necessary to recover these investments (economic breakeven time) for a propellant-collecting concept. Using this methodology along with data available to the community in 1961, Berner and Camac determined that the economic breakeven time for a propellant-collecting vehicle is less than a year for both nuclear powered and solar powered craft. By establishing the weight-doubling time and using it to arrive at the economic breakeven time, they show that elliptical orbits will take longer to break even economically.

Berner and Camac's work relies on limited atmospheric data which limits its accuracy. Additionally, they fail to factor eclipsing of the sun by the Earth into their analysis for solar powered options. Berner and Camac also fail to consider variation in atmospheric density as a result of solar and geomagnetic activity. These limitations to the Berner and Camac work cast doubt on the validity of their findings. Berner and Camac themselves conclude that limitations in propulsion technology at the time of publishing

are the primary obstacle to feasibility. With 50 years of development in electric propulsion technology since then, this may no longer be the case.

In 1961, Zukerman and Kretshmer considered utilizing energy released from atomic oxygen recombination during compression of incoming air to provide all of the input energy into the flow for acceleration as part of a ramjet system [41]. This work determined that there is insufficient energy from atomic oxygen recombination to enable sufficient thrust to counteract the drag force. However, Zukerman and Kretshmer note that the addition of a fuel into the flow can supply enough energy to overcome drag. This work allows us to exclude chemical propulsion as a sustainable option for propellant-collecting space vehicles.

Reichel et al. expanded on Berner and Camac's work with a paper in 1962 studying the possibility of a nuclear-powered, air-scooping electric propulsion system [36]. Their proposed concept would operate just on the edge of space at 110 km with a 5-MW nuclear power source. At this altitude, their vehicle would be able to collect nearly 60 kg of air per hour. Reichel conducted an analysis of the compression and liquefaction power requirements for his design, and in 1978 Reichel resurrected his proposed concept under the name AIRScoop as a means to deliver the components needed for a 475-GW space solar power plant [37].

The most important contribution of Reichel's work is the simplified analysis he employed for estimating the required power to compress and liquefy the collected air. Collected air must be compressed to a value above the triple point of nitrogen for liquefaction, which is approximately 94 Torr. Eq. (2.21) expresses the energy required per unit mass to accomplish this in an isothermal process, where p_2 is the triple point of nitrogen, p_1 is the pressure at the back of the inlet, T_{LR} is the liquefaction radiator temperature, and η_{comp} is the compressor efficiency.

$$e_{comp} = \frac{1}{\eta_{comp}} RT_{LR} \ln\left(\frac{p_2}{p_1}\right) \quad \textbf{(2.21)}$$

The specific energy required to liquefy the compressed air is a function of the liquefaction radiator temperature and the liquid air temperature T_L as expressed in Eq. (2.22). This equation assumes a Carnot refrigeration cycle for air with constant specific heat at constant pressure c_p and heat of vaporization Δh_{vap}. These equations are useful when determining the total power requirements for a propellant collection system.

$$e_{liq} = \frac{1}{\eta_{liq}} \left[c_p(T_{LR} - T_L) + \Delta h_{vap}\right] \left(\frac{T_{LR}}{T_L} - 1\right) \quad \textbf{(2.22)}$$

Researchers in the Soviet Union also looked at air-breathing concepts in the 1960's. Most of this work is in Russian, but a summary publication by Dolgich in 1969 was translated for researchers in the West. The summary publication details ten other papers published in the Soviet Union with a specific focus on the power requirements for sustainable air-breathing propulsion. Most notably, that work asserts that propellant collection can enable a spacecraft to accommodate as much as 2.5 times the payload as a spacecraft that does not use propellant collection [39]. However, the referenced paper which presumably supports this assertion is not available in English.

In 1975 Cann proposed the Space Electric Ramjet (SERJ) as a form of air-breathing space propulsion [20]. SERJ is effectively an electromagnetic engine with an inlet similar to Demetriades' MHD thruster which ionizes and accelerates the flow through the engine. In a notable shift from previous efforts, Cann studies using a solar power source rather than a nuclear reactor. While he is not the first to mention solar power as an option, he is the first to consider it exclusively. As part of his analysis of the concept, he determines the minimum altitude at which solar power can supply sufficient power to overcome drag. His calculations indicate a minimum altitude of approximately

160 km when the solar panels are parallel to the flow. Unfortunately, Cann's analysis suffers from two deficiencies. First, Cann does not seem to consider the effect of eclipse on his power estimate. In order to maintain orbit the ramjet would have to counteract drag for the entire orbit, not solely when in direct sunlight. Second, his assumptions of solar cell efficiency are outdated when compared with presently available technology. Both of these deficiencies limit the applicability of the findings of the SERJ study when viewed from a modern context.

Minovitch took another look at air-breathing spacecraft concepts in the 1970's and 1980's, culminating in two conference papers in 1983 and 1985. His work refers to such technology as "self-refueling rockets" rather than "air-breathing spacecraft", which effectively communicates the difference in his approach to the concept. In his 1983 paper, Minovitch proposed a system in which solar power generated at a single ground station is transmitted via microwave to orbiting collector vehicles at a total radiated power exceeding 10 GW [9]. For continuous operation, he proposed orbiting an additional "power relay spacecraft" which would effectively act as a reflector for the ground station. This is a completely original approach to addressing the power requirements of an air-breathing spacecraft. It is also the most complex approach, relying on multiple ground and space assets for operation. In his 1983 paper, he proposed a collector craft with a dry mass of 600,000 kg. This is notable because it is roughly five times the payload capacity of a Saturn V, and 150,000 kg more than the International Space Station [42].

The 1985 paper replaces the microwave power system with a nuclear reactor, but is similarly astronomical in its scale to the 1983 concept [38]. Minovitch proposes a 700,000 kg dry mass craft with a 105,000 kg nuclear reactor generating 3,500 MW of power. He justifies this by making the argument that because the propellant is free the spacecraft mass no longer matters. The flaw in this argument is that such a craft still needs to be manufactured, assembled, and launched. This would require an extremely

high up-front cost. Despite the flaws in the economics of the concept, Minovitch succeeds in having vision for the potential of the technology. Minovitch proposes using such a vehicle as an interplanetary transport whereby the vehicle would expend propellant when departing a planet and collect new propellant or "refuel" during an aerocapture maneuver upon arrival. This is the first direct mention of utilizing this technology around other planets. Minovitch would be the final researcher to consider air-breathing concepts for a decade.

2.4.2 Contemporary Work

The conclusion of the Cold War largely marked the end of concepts which rely on massive nuclear powered vehicles and a break in research of air-breathing concepts. The idea was slowly and quietly revived in a series of Master's theses from the Massachusetts Institute of Technology spanning nearly a decade [10, 43, 44]. Renewed interest also brought new focus. Much of the work performed since the 1990's concentrates on a single component of an air-breathing system rather than a full system study. This focus has led to developments in air-breathing electric propulsion and inlet analysis which invalidates the simplistic assumptions made by researchers in the Cold War era. Current efforts are proceeding across the globe with diverse objectives. While the previous section was organized chronologically, this section is organized on a component-by-component basis.

The first documented analysis of an air-breathing spacecraft concept after Minovitch is the 1995 Master's thesis from Buford Ray Conley [43]. Conley's thesis work is the first practical study of utilizing a gridded ion engine in an air-breathing form to counteract atmospheric drag experienced by a spacecraft. This study is unique in that it does not attempt to make use of the gas which is directly impinging with the leading edge of the main vehicle, but rather entrains the wake of the main vehicle in a large gridded ion engine downstream. Figure 11, adapted from Conley's original work, illustrates this concept. While this work gives a detailed treatment of the plasma physics inside the device, it makes several assumptions which negatively impact the quality of the results.

Most important among these is the neglect of drag on the ion engine component even though it accounts for over 99.8 percent of the frontal area of the spacecraft.

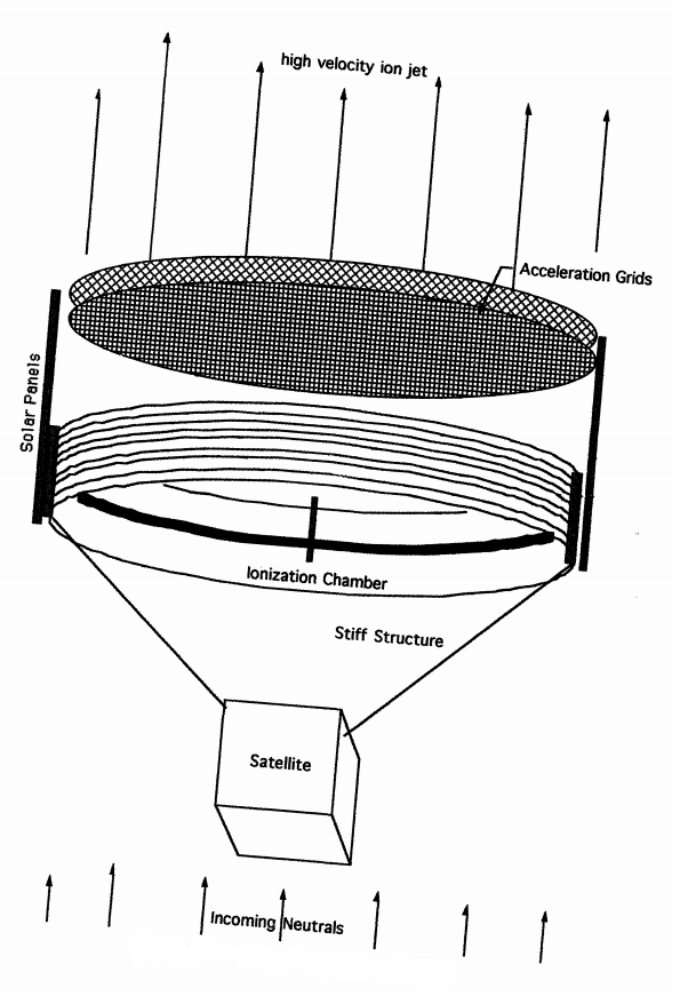

Figure 11. Conley's LEO Ion Thruster Concept [43].

Dressler took a slightly different approach to Conley's LEO ion thruster concept with the Ambient Atmosphere Ion Thruster (AAIT) in 2006 [45]. This device is among the simplest air-breathing thrusters ever proposed. In his original conference paper, the AAIT is simply two grids electrically biased relative to one another and placed perpendicular to the flow as shown in Figure 12. The AAIT concept proposed exploiting the ambient ion populations present in LEO as propellant by electrostatically accelerating those ions which pass through the AAIT to produce thrust. The original concept has no method of producing its own ions. Dressler's analysis indicates an AAIT would have to

be several times the size of the spacecraft in order to counteract aerodynamic drag in circular orbit altitudes ranging from 300-500 km. This is in agreement with Conley's analysis however it is based on two major simplifying assumptions which limit its accuracy.

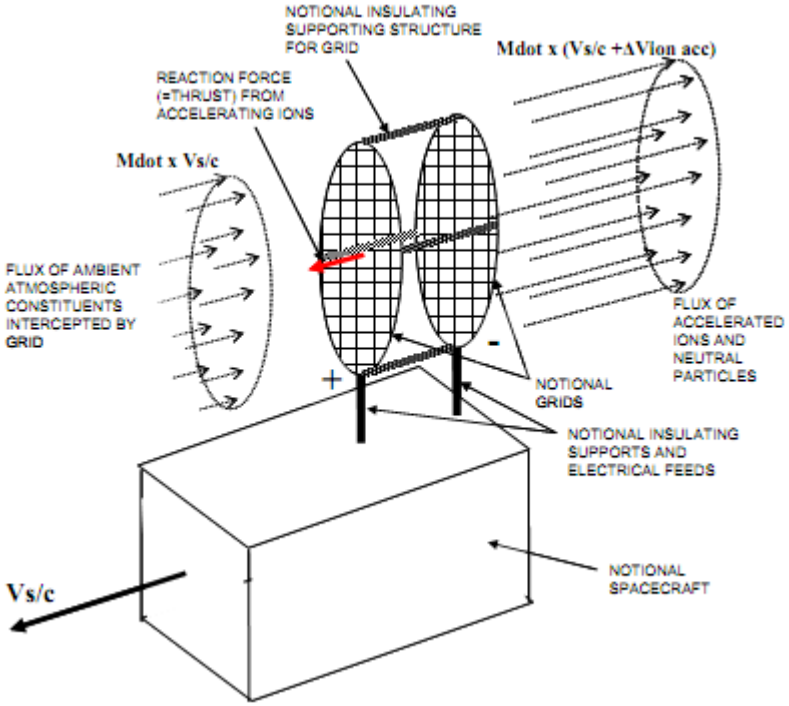

Figure 12. Dressler's AAIT concept [45].

(1) Dressler assumes a constant drag coefficient of 2 with the justification that "this is a free molecular flow regime". Numerous sources dating back to 1959 show that the drag coefficient exceeds 2 and in fact varies with orbital altitude [14, 46-49]. More importantly, (2) Dressler's approach cannot be realized given his original design. The incoming ion population has a potential equal to the local space potential, as does the spacecraft itself. Biasing the two grids relative to one another does not provide a net acceleration because the plasma environment around the grids is at the space potential and no neutralization occurs. Instead, King states that the incoming ion population must be raised in potential by some means in order to lead to net acceleration [50].

King's analysis improves upon Dressler's original design analysis with the help of the Atmospheric Electric Propulsion Mission Performance Tool (AEPMPT) developed at the Georgia Institute of Technology [50]. The AEPMPT allowed King to parametrically search for orbit and AAIT design configurations which produce a thrust-to-drag (*T/D*) ratio equal to or greater than one. He assumed a constant drag coefficient of 2.4, which lies within the results of previous analyses in contrast to Dressler's assumed drag coefficient [14, 49]. He also accounted for additional ionization of the incoming flow required to raise the ion potential above the space potential, though he does not propose a mechanism for accomplishing this. King's high-fidelity analysis finds numerous configurations which provide *T/D* ratio greater than one for circular orbits at altitudes of 500 km and greater. This work proves that drag compensation using atmospheric propellants is possible and in some configurations does not require any sort of compressing inlet, although King himself points out that satellites orbiting at 500 km already have substantial orbit lifetimes.

Japanese researchers have made significant progress with more traditional ion engine designs which include an ionization stage. The Air-Breathing Ion Engine (ABIE) first proposed by Nishiyama in 2003 integrates a novel inlet design with an ECR ion engine [51]. Figure 13 shows a conceptual schematic of the ABIE. Air enters the ABIE inlet from the left side of the page. The inlet provides high transmission probability for the incoming air, but low transmission probability for air attempting to escape. It accomplishes this by collimating the incoming flow with a grid of long and narrow tubes [51]. Incoming air is assumed to be hyperthermal: the bulk velocity of the flow is much greater than the thermal velocity of the flow [46]. The incoming flow is also assumed to be free molecular: the mean free path of the incoming air is much larger than the characteristic length of the device. When the inlet is pointed along the velocity vector of the spacecraft, most of the air passes through the inlet without interacting with the tube walls. Once through the inlet, the air is decelerated out of a hyperthermal free molecular

flow regime with a solid diffuser located aft of the inlet. The much slower and random thermal velocity flow which tries to escape the engine via backflow through the inlet is hindered from doing so by the long, narrow tubes. They have low transmission probability as can be deduced from Clausing's work in conductance of free molecular flow through tubes [52].

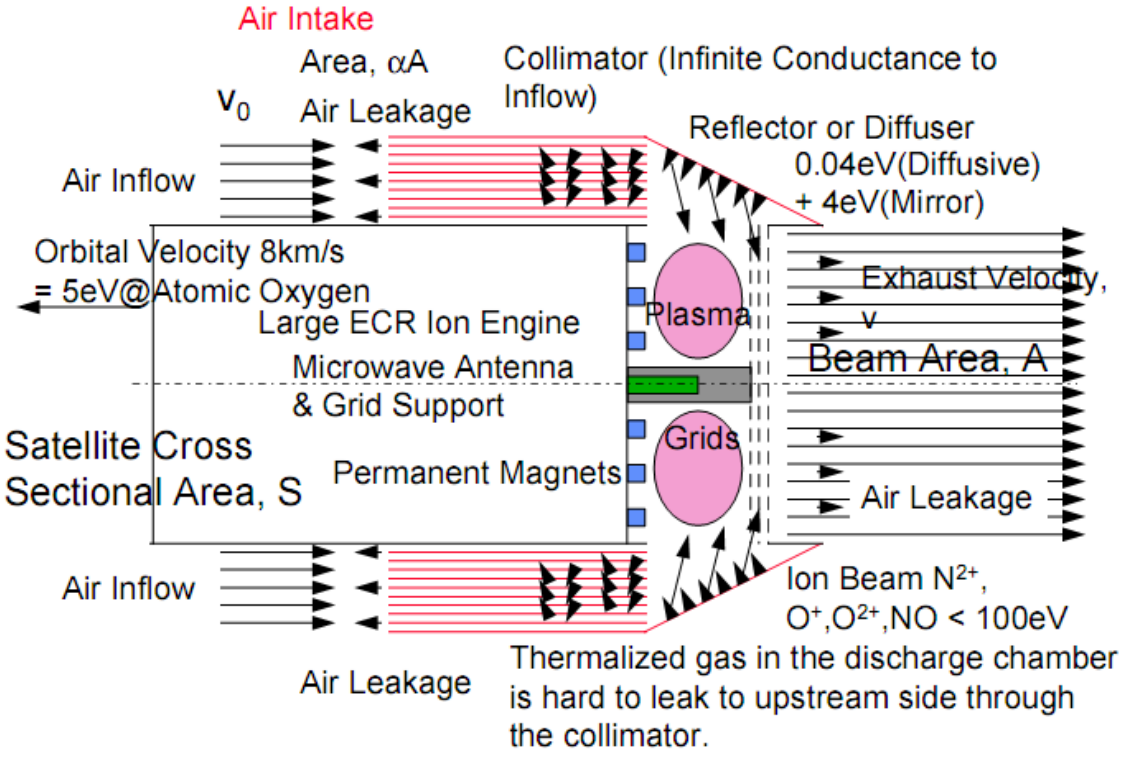

Figure 13. Air breathing ion engine conceptual schematic [51].

Once thermalized by the diffuser, the collected air must be ionized and accelerated to produce thrust. Ionization is accomplished via a microwave electron cyclotron resonance (ECR) ionization source. The ionized air is then accelerated via a series of biased grids as in a typical ion engine. The ABIE is currently the most developed air-breathing concept to have a fully designed, built, and integrated engine and inlet combination. Development of this concept has reached the experimental stage with an integrated design [53]. Researchers simulate the incoming hyperthermal free molecular flow with a pulsed laser detonation beam source operating on either pure

nitrogen or pure oxygen. Peak pressure in the thruster ionization stage has reached as high as 3.6 mTorr, with only ~0.1 mTorr required for thruster operation [53]. These tests have demonstrated the effectiveness of the inlet at preventing captured air from escaping and have successfully demonstrated thrust. However, the ABIE has only been tested in a pulsed mode and without a neutralizer cathode present in the system.

In addition to the Japanese ABIE effort, European researchers have also made progress testing gridded ion engines on atmospheric propellants. Cifali et al. tested the radiofrequency ion thruster (RIT) RIT-10-EBB on pure N_2 and pure O_2 propellants in 2011 [21]. The RIT-10 is a thruster with successful flight heritage on the ARTEMIS spacecraft. Cifali's RIT-10 was modified to operate on atmospheric propellants instead of xenon. Cifali reports using argon to ignite the engine, citing difficulty experienced when trying to ignite using the atmospheric propellants. The cathode used in this work also ran on xenon. Cifali ran the cathode on xenon because traditional thermionic emission sources such as lanthanum hexaboride (LaB_6) are readily oxidized at the temperatures required for electron emission. These difficulties highlight remaining technical issues with operating electric thrusters on atmospheric gases.

Despite these setbacks, Cifali was able to demonstrate thrust levels of 5.25 mN on nitrogen and 6 mN on oxygen at 450 W. This corresponds to a *T/P* of 11.6 mN/kW for nitrogen and 13.3 mN/kW for oxygen. More recent tests of the RIT-10 with a mixture of nitrogen and oxygen demonstrated similar results [54]. Figure 14 shows the RIT-10 operating on the nitrogen/oxygen mixture. Modeling and experimental results produced by Feili et al. demonstrate a lower propellant utilization efficiency and power efficiency for nitrogen and oxygen propellants over xenon propellant. The propellant utilization efficiency is defined as the ratio of the propellant mass flow rate which is ionized to the total propellant mass flow rate. This is an important factor in determining the thruster performance because it is the fraction of the propellant which sees an accelerating force in the electric field. The power efficiency η_e is defined as the ratio of the jet power output

P_{jet} from the flow out of the thruster to the total electrical power input into the thruster P_{input} as given in Eq. (2.23).

Feili predicts a propellant utilization efficiency (η_u) on nitrogen of 35.1 percent for a given set of conditions in comparison to 65.2 percent for xenon. Similarly, he predicts a RIT-10 operating on nitrogen will have a power efficiency of only 63 percent for a given set of conditions in comparison to 76.5 percent if operating on xenon at the same conditions. The difference in these values highlights the trade in performance made when selecting atmospheric propellants over xenon for electric propulsion.

$$\eta_e \equiv \frac{P_{jet}}{P_{input}} \tag{2.23}$$

Figure 14. RIT-10 operating on a nitrogen/oxygen mixture [54].

Cifali's test campaigns with the RIT-10 were performed in support of Di Cara's RAM-EP effort in Europe which first appears in the literature in 2007 [55]. The RAM-EP concept "seeks to enable low altitude missions" below 250 km by developing an air-breathing electric propulsion system. Di Cara's study focused on a hypothetical vehicle with 1 m^2 drag area and a drag coefficient of 2.0. The RAM-EP concept was the first to consider non-continuous thruster strategies by only generating thrust when not in eclipse. In particular, the study looked at two sun synchronous orbits (SSO) with operation during

2/3 and 5/6 of the orbital period. Di Cara's study determines that air-breathing options are not competitive above 250 km because annual propellant requirements to maintain orbit decrease rapidly above this altitude. Most importantly, the RAM-EP concept study identifies power as the primary limiting factor for the concept.

In addition to his gridded ion engine tests with the RIT-10, Cifali also tested a Hall effect thruster (HET) in support of the RAM-EP effort [21]. A Snecma PPS 1350-TSD shown in Figure 15 was tested with pure nitrogen and a nitrogen/oxygen mixture. The thruster was ignited with xenon and the cathode operated on xenon. Results from HET operation on atmospheric propellants indicate lower propellant utilization efficiency in concordance with the RIT-10 results. As expected from an HET, the *T/P* ratio is significantly higher than for the RIT-10. Cifali reports 21 mN/kW on pure nitrogen and 24 mN/kW on the mixture. However, Cifali also reports significant rusting on the anode after operation with the nitrogen/oxygen mixture. This highlights the technical challenges of running an electric propulsion device on oxygen.

Figure 15. Snecma PPS 1350-TSD operating with a N_2/O_2 mixture [21].

The first researchers to propose a HET which ingests ambient gas were Pigeon and Whitaker in 2004 [56]. They proposed a concept whereby ambient gas is ingested via random thermal motion and accelerated to produce thrust. Xenon was used as the ambient gas in their initial experiments, in which they indirectly measured μN levels of thrust. However, later work demonstrates that the performance of such a device is insufficient to compensate for drag on-orbit [57].

Pekker and Keidar proposed a concept similar to Dressler's AAIT concept whereby oncoming flow is fed directly into accelerating grids, but with a Hall acceleration mechanism instead of the aforementioned grids [58]. Like the AAIT, Pekker and Keidar's concept fed oncoming flow directly into the device without any compression mechanism. Most of the work focuses on the design and scaling of the thruster components using a detailed first order analysis. Their analysis indicates effective operation for drag compensation using this concept at altitudes in the range of 90-95 km with 9.1-22 N of thrust for a drag area of 0.1 m^2, although they point out the power requirements for this level of performance are 1.6-2 MW. Power levels of this magnitude are not currently realizable on-orbit. Pekker and Keidar's work confirms that an air-breathing HET should have a mechanism to raise the pressure of the flow prior to injection into the HET to allow for operation at higher altitudes.

Diamant proposed a 2-stage HET called the air-breathing cylindrical Hall thruster (ABCHT) for drag compensation [59]. The two stages consist of an ECR ionization stage similar to that on the ABIE with a traditional HET for acceleration. Diamant built a prototype of this thruster and operated it on xenon. The results of the test indicate the possibility of a lower thrust efficiency as a result of the inclusion of the ECR ionization stage. Like many researchers, Diamant also points out the necessity of using a non-thermionic cathode technology for neutralization [21]. To address this, he has proposed and conducted tests on a microwave cathode for air-breathing propulsion [26]. The results of testing on argon and xenon indicate current-to-power ratios as high as 90 mA/W on xenon and 50 mA/W on argon. While promising, Diamant notes a significant technical challenge may lie in delivering number densities on the order of 10^{20} m^{-3} of atmospheric gas to the cathode.

Shabshelowitz conducted a more detailed study than Diamant in his dissertation looking at rf thruster systems for air-breathing electric propulsion [22]. Shabshelowitz's 2013 dissertation gathered performance data for two thrusters with helicon technology.

The first thruster is called the radiofrequency plasma thruster (RPT). It is a simple helicon plasma device illustrated in Figure 16. Similar devices have produced ion acceleration approaching 30 V on argon [60]. Test results from the RPT indicate low specific impulse on the order of 330 seconds and low rf thrust efficiency on the order of 0.7% on argon. Shabshelowitz ran the RPT on pure nitrogen and air, but was unable to measure any additional thrust from rf power deposition over the cold gas thrust. With no experimentally measurable thrust, Shabshelowitz's results allow us to exclude helicon thrusters from consideration in this work.

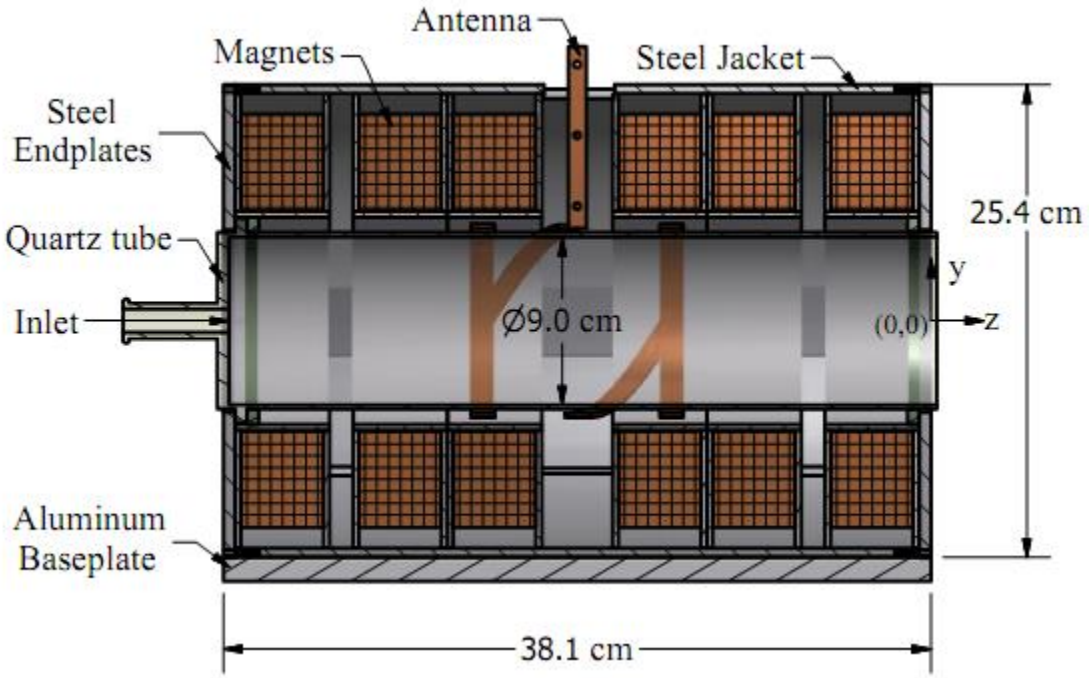

Figure 16. Cross-sectional view of Shabshelowitz's radiofrequency plasma thruster (RPT) [22].

The second thruster tested by Shabshelowitz is the Helicon Hall Thruster (HHT) [61, 62]. The HHT is a 2-stage thruster with a helicon ionization stage and a Hall acceleration stage. Like Diamant's 2-stage thruster, the helicon ionization stage is intended to increase ionization and propellant utilization efficiencies. Figure 17 is a notional schematic of the HHT from Shabshelowitz's dissertation. The helicon ionization stage can be seen closest to the anode while the Hall section is near the thruster exit.

Similar to Cifali, Shabshelowitz operated his thrusters with a cathode operating on xenon rather than atmospheric gases. This limitation in his research further highlights the present deficiency of knowledge in the cathode segment of electric thruster system design for atmospheric constituents.

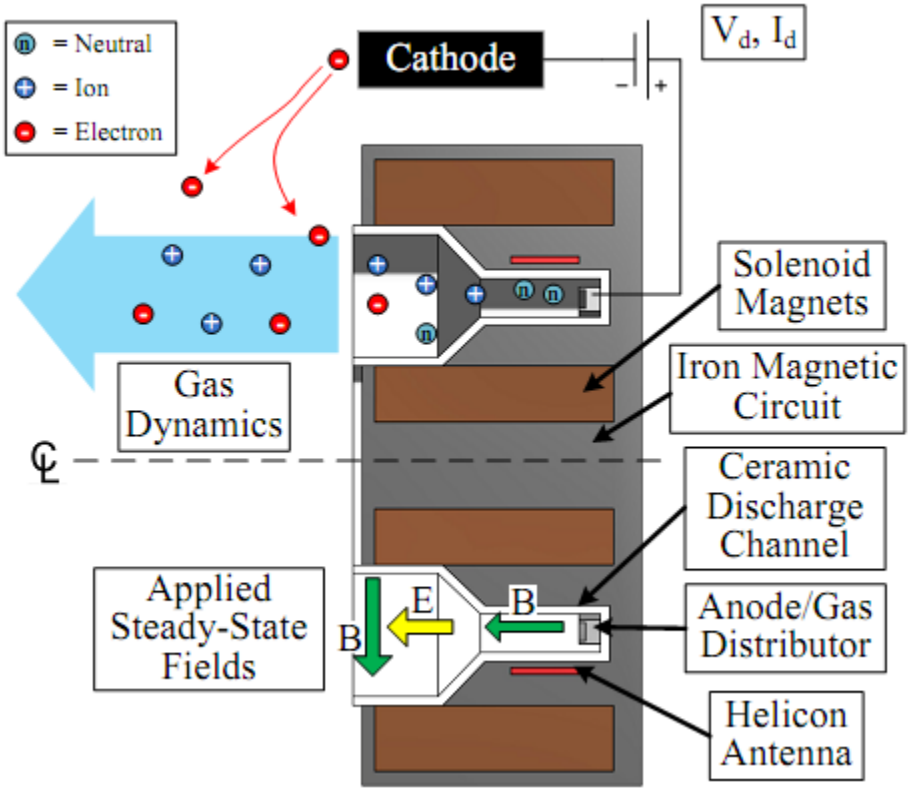

Figure 17. A notional schematic of the HHT from Shabshelowitz's dissertation [22].

Shabshelowitz ran the HHT in 2-stage and Hall-only modes on xenon, argon, and nitrogen propellants. His results show decreasing *T/P* with increasing RF power when running in 2-stage mode. The data demonstrates improved propellant utilization efficiency for all propellant species when using the helicon stage, but the observed improvement is not sufficient for the added power input. In Hall-only mode Shabshelowitz's data demonstrates propellant utilization efficiency on nitrogen of approximately 10%. Unfortunately, Shabshelowitz only ran the HHT at 200 V discharge voltage and 4.8 mg/s for nitrogen propellant, so there is only one data point. *T/P* and propellant utilization efficiency increase with increasing mass flow rate for xenon

according to Shabshelowitz's data, and Shabshelowitz's only flow point on nitrogen is half of the lowest flow rate of xenon.

Where Shabshelowitz used an experimental approach to studying the use of atmospheric propellants in a HET, Garrigues employed a computational approach [63]. Garrigues selected a notional vehicle with drag coefficient of 2, frontal area of 1 m^2, continuous 1 kW available power, and a circular orbit at 250 km altitude. From that notional design, Di Cara's work indicates a maximum thrust of 20 mN is required to counteract aerodynamic drag [55]. Garrigues employs a hybrid axisymmetric model with 2 different thruster channel lengths and a discharge voltage of 300 V to search for configurations which meet that thrust performance target. He also varies magnetic field strength from the nominal field required for xenon and the mass flow rate.

Garrigues' model indicates a mass flow rate greater than the oncoming mass flow rate is required by a HET to provide the required thrust to counteract drag for his notional vehicle. This result occurs because of low propellant utilization efficiency (~10%) and low thrust efficiency (~5%) at the desired thrust performance. However, Garrigues' results also show increasing propellant utilization efficiency and thrust efficiency with increasing mass flow rate, peaking at ~22% and ~7% respectively on molecular nitrogen. While Garrigues correctly concludes that a HET in his design space cannot deliver the necessary performance for a notional vehicle, he fails to consider the possibilities of a larger vehicle, varied discharge voltage, or a sufficient range of magnetic field strengths and channel lengths. Garrigues does succeed in providing some valuable data which roughly agrees with Shabshelowitz's results.

HET technology has also been considered for "air-breathing" applications around Mars. Kurt Hohman from Busek proposed the Martian atmosphere breathing HET (MABHET) concept to reduce propellant delivery requirements to Mars in 2012 [12]. Figure 18 is adapted from Hohman's final report to NASA on the development state of the concept. Like the ABIE, the MABHET concept makes use of the same collimated

inlet design to improve collection efficiency. Hohman performed experiments and analysis using a 1.5-kW HET on a simulated Mars atmospheric mixture. Martian atmospheric make up is composed mostly of CO_2 in contrast to Earth's atmosphere of nitrogen and oxygen, thus data gathered from these experiments is of little use in this work. However, Hohman's work demonstrates encouraging results for such a concept's feasibility around Mars which further emphasizes the potential of air-breathing spacecraft technologies.

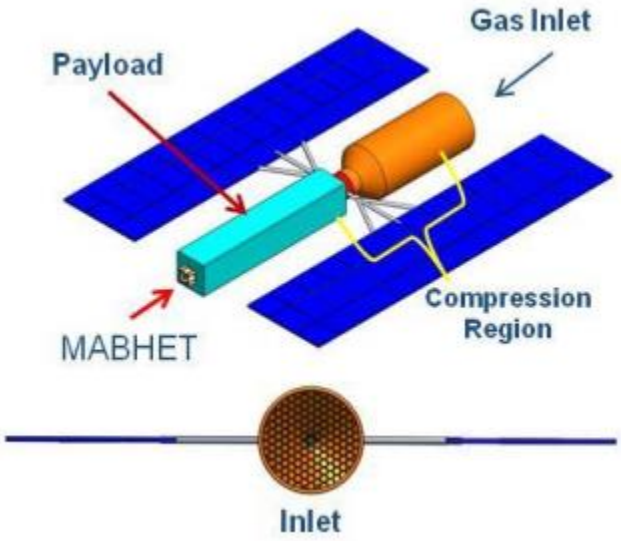

Figure 18. Martian atmosphere breathing hall effect thruster (MABHET) concept proposed by Hohman at Busek [12].

Lamamy's 2004 Master's thesis was the first work in the literature after Minovitch to propose air-breathing concepts around Mars [10]. Lamamy's thesis proposed the propellant production in Mars orbit (PPIMO) concept as a compromise between chemical and electric propulsion options for interplanetary transfer. PPIMO would collect carbon dioxide from the Martian atmosphere and react it with hydrogen carried from Earth to synthesize methane, hydrogen, and oxygen. These propellants would be reacted in a chemical engine to produce the necessary impulse to transfer back to Earth from Mars. While Lamamy made a number of simplifying assumptions in his analysis, he shows the

PPIMO concept can accomplish the same mission as an all chemical option with 30% less mass.

Palaszewski looked to the outer planets in his proposal to mine the atmospheres of gas giants for helium-3 [11]. Figure 19 demonstrates a "scooper" architecture proposed by Palaszewski for use around Uranus. Helium-3 has long held interest in the space and fusion communities for its potential use as nuclear fuel in fusion reactors and relative abundance at extra-planetary destinations. Palaszewski's documentation of his effort is highly theoretical as one would expect from a concept which is second only to Bussard's in its complexity and technical difficulty. While most concepts involving the collection of atmospheric matter are air-breathing types, Palaszewski's is one of the few concepts which considers the storage and separation of the collected gas. Palaszewski's main interest in "atmospheric mining" is the potential to gather nuclear fuel for terrestrial reactors. This is entirely unique and original in that it is the only concept in the literature which proposes the return of a portion of the collected gas to Earth.

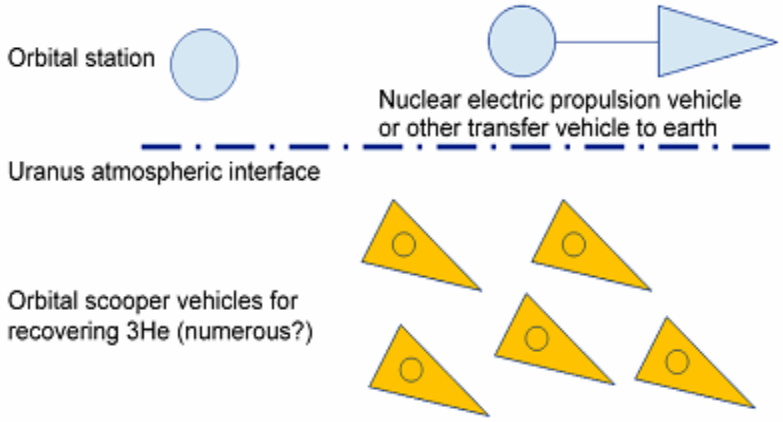

Figure 19. Illustration adapted from Palaszewski demonstrating his system architecture for collecting He-3 around Uranus [11].

One final thruster concept which warrants mention is the field reversed configuration (FRC) electrodeless Lorentz force (ELF) thruster being developed by Kirtley et al. since 2011 [64]. Figure 20 depicts a prototype ELF thruster during operation. Kirtley makes the argument that thruster efficiency is fundamentally a function

of the molecular weight of the propellant, where lower molecular weight propellants lead to lower thruster efficiency. The ELF thruster concept mitigates the poor efficiency of low molecular weight propellants by injecting neutrals into the plasma downstream of the ionization stage. Rather than trying to ionize all propellant, the ELF thruster uses accelerated ions to ionize the injected neutrals via charge exchange interactions. The charge exchange interaction is effectively free in terms of energy, so the newly ionized particle's ionization cost is effectively zero. By reducing the average ionization cost, the thruster efficiency at low specific impulse can be increased. To date, Kirtley has demonstrated operation on neon, but has yet to do so with nitrogen.

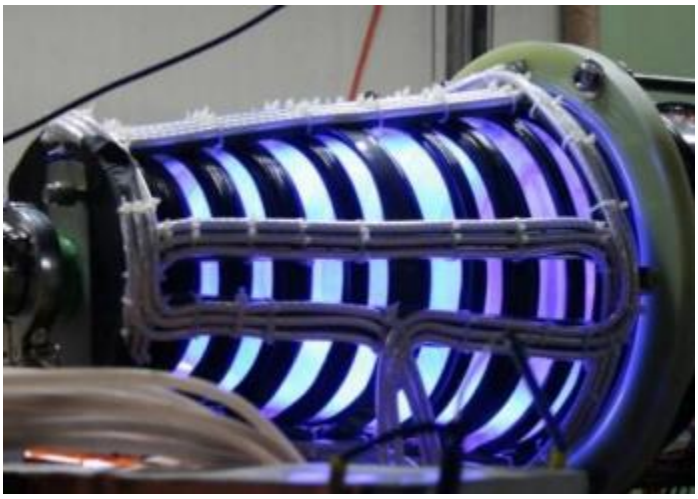

Figure 20. Kirtley's electrodeless Lorentz force thruster (ELF), proposed for use with atmospheric gases. Adapted from [64].

While Kirtley and many others studied the thruster component of propellant collection technology, other researchers studied the inlet component. Prior to Japanese and European studies of air-breathing inlet designs, McGuire performed direct simulation Monte Carlo (DSMC) analysis of a simple conical inlet design as part of his Master's thesis [44]. McGuire proposed a concept called the Aero-Assisted Orbital Transfer Vehicle (AAOTV) demonstrated in Figure 21 which would serve as a space tug system to transfer payloads from LEO to GEO. The DSMC results show a variation in drag coefficient and capture percentage with the angle of the conical inlet and its outer radius.

Notably, none of his designs have a capture percentage greater than 50 percent. His analysis also indicates that smaller inlets will have better capture percentages. This is in agreement with the results of the Japanese with their collimated inlet design, which is effectively an array of small inlets and attains high performance when compared with most simple conical inlet designs. However, this result only holds for hyperthermal free molecular flow. As altitude approaches the Karman line and the flow compresses in the inlet, the flow can undergo a transition to hypersonic continuum flow.

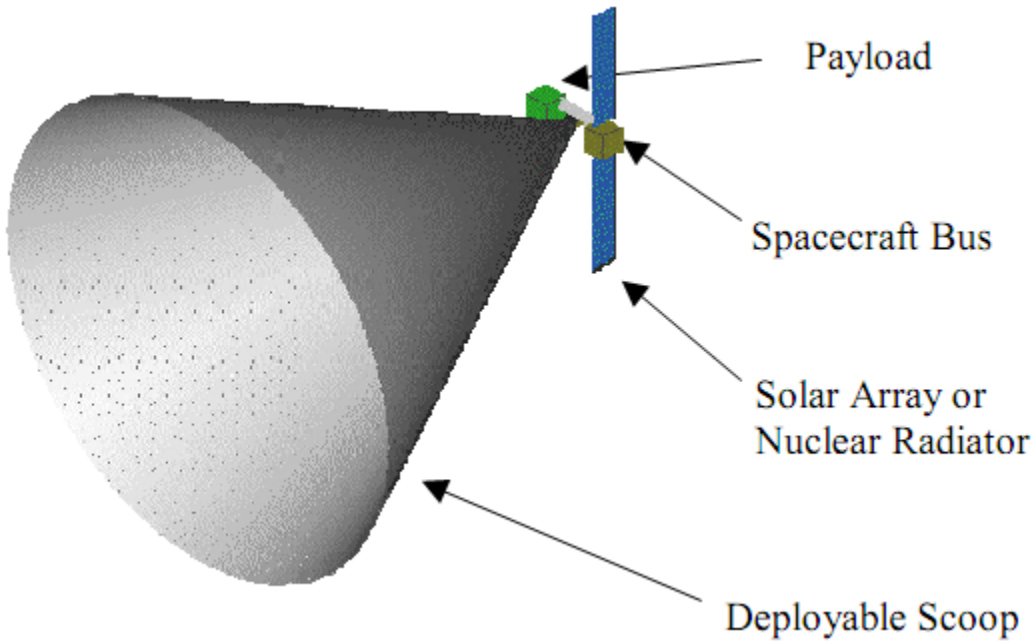

Figure 21. McGuire's Aero-Assisted Orbital Transfer Vehicle (AAOTV) concept. Adapted from [44].

Although generally not perceived as politically realistic in the community today, some researchers are taking a second look at the nuclear-powered concepts of the Cold War era. Jones et al. resurrected the original PROFAC concept in 2010 as a potential option to gather atmospheric propellant for manned exploration of Mars [65]. He performed DSMC analysis of a novel conical inlet design with a diffuser insert to increase the pressure at the back of the inlet. His results confirm an increase in pressure but he does not report on the effect of the diffuser on the percentage of oncoming air that

reaches the back of the inlet. In fact, Jones assumes the capture percentage is one hundred percent. This is in contradiction to McGuire's results, which indicates that an aerodynamic collector cannot collect all of the oncoming flow [44]. Additionally, he does not make any estimates of power requirements which are critical in determining the feasibility of the concept.

2.5 Conclusion

The idea of air-breathing spacecraft is nearly as old as spaceflight. First conceived during the Cold War, pioneering concepts utilized technologies which were available at the time. This meant using nuclear power sources instead of solar photovoltaic power sources. Initial studies like PROFAC looked at the potential system level performance of this technology [19, 32]. These studies outlined the basic physics of propellant collection on-orbit. They considered the power requirements and looked at diverse schemes for collection [32, 33, 35]. Researchers in this period were able to conclusively show that chemical rocketry is not a sustainable option for air-breathing craft [31, 41]. This result led to a focus on EP, which was still in its infancy. The earliest researchers had limited atmospheric models on which to base their analyses. Together, the infancy of EP and limited atmospheric data led to systematic inaccuracy in their evaluation of propellant collection as a concept.

Atmosphere models, computational modeling, and our EP capabilities had advanced tremendously by the time the first researchers after the Cold War resurrected the idea of propellant collection [66]. These advances led to researchers focusing on specific components of propellant collection. While there are recent system level studies [55], a comprehensive review of the available literature reveals no study which performs

a detailed and complete analysis of available orbits and technologies as intended in this work. The component level research conducted over the past 20 years is enabling for the high-fidelity analysis this work will perform. For the first time, all of the resources necessary to achieve the goals of this work are available; however a rigorous and well-documented approach is required to bring these resources together for the stated goals.

CHAPTER 3
APPROACH AND INPUT DATA

As stated in the introductory chapter, the overall objective of this work is to identify where propellant collection is technically feasible. This chapter outlines the approach taken in this work to accomplish this goal. The first section presents the physics model developed from first principles which forms the foundation for this work. Performing a sensitivity analysis on this physics model reveals the major design factors for a propellant collection system in support of the first research goal.

The second section discusses the bounding of the parameter spaces utilized in the model. Selected bounds reflect theoretical and present capability constraints. Unrealizable designs are excluded from consideration as a result of application of the bounds. The remaining design points which satisfy the physics model are those for which propellant collection is technically feasible, thus satisfying the second research goal. Some of the inputs into the physical model are statistical variables which must be determined computationally. This work uses the System Toolkit (STK) from Analytical Graphics Inc. (AGI) to develop these statistical variables for a range of orbit parameters as detailed in the second section.

The third section of this chapter briefly presents the method for conducting a sensitivity analysis on the governing equations for propellant collection in support of the first research goal. The final section outlines the two case studies mentioned in the final research goal and presents the approach to completing them.

Figure 22 illustrates the basic system diagram analyzed in this work. An aerodynamic inlet takes in a fraction of the oncoming flow. Optionally, a compression and condensation system compresses the collected flow and stores it in a propellant storage tank. The propellant tank feeds propellant into the EP thruster. In architectures which do not have compression and storage components, the aerodynamic inlet feeds directly into the EP thruster as in the case of the ABIE [51, 53, 67]. A power source drives the optional compression and condensation system as well as the EP thruster. This diagram forms the basis for the derivation of the physics model in the next section.

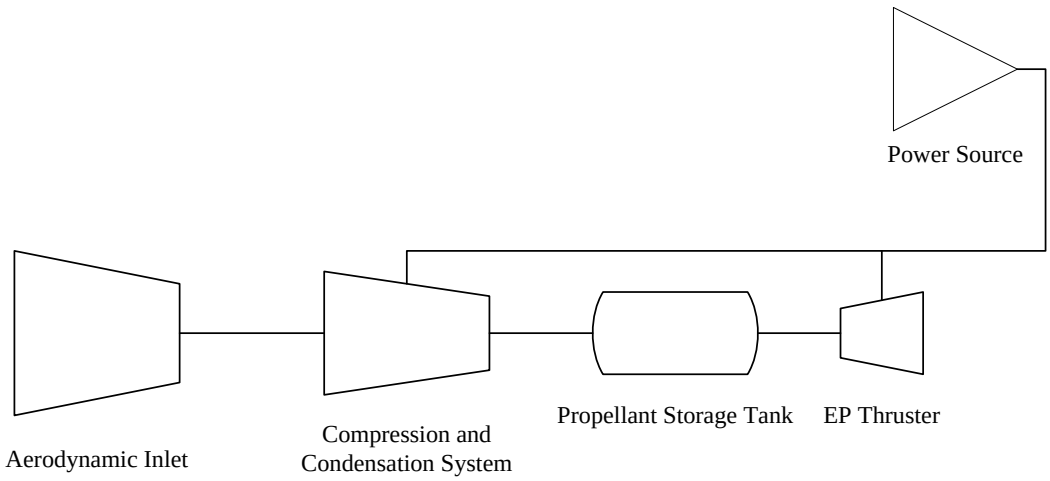

Figure 22. System diagram for a general propellant-collecting system.

3.1 Physics and Assumptions

Eq. (3.1) expresses the instantaneous aerodynamic drag on a propellant collecting vehicle. The drag force consists of two components: a bus component which accounts for the drag on the spacecraft body denoted by the subscript "*s/c*", and a planform area component which accounts for the drag on the planform structures required for power generation. This planform component is denoted by the subscript "*PA*". As can be seen

from Eq. (3.1), both components vary as a function of drag coefficient C_D, density ρ, and the bulk velocity of the oncoming flow v_{bulk}. Each is also a function of a reference area, *A*. The reference area for the spacecraft body is the cross-sectional area perpendicular to the flow, while the area for the planform area component is the planform area. Implicit in this equation are two assumptions:

- Planform areas are infinitely thin flat plates with zero angle of attack and
- The collector vehicle is perfectly aligned to the velocity vector.

$$D = \frac{1}{2} C_{D,s/c} \rho A_{s/c} v_{bulk}^2 + \frac{1}{2} C_{D,PA} \rho A_{PA} v_{bulk}^2 \quad \textbf{(3.1)}$$

These assumptions effectively posit that the vehicle has a fixed planform geometry to minimize net drag and is always perfectly aligned to maximize collector access to the oncoming flow. Section 3.2.3 estimates the validity of the infinitely thin assumption. While Eq. (3.1) perfectly describes the aerodynamic drag for a vehicle under the aforementioned assumptions, one must prescribe numerous design parameters in order to generate a result. Among these parameters are the two reference areas which describe the overall dimensions of the vehicle. One must also prescribe the atmospheric density and the velocity, both of which vary with time and orbital parameters.

For simplicity, we would like to work with the average drag and avoid tying the model to physical size. By dividing Eq. (3.1) by the spacecraft body area and using the time-average of the product of density and the square of velocity we arrive at Eq. (3.2), which expresses the time-averaged area-specific drag as a function of the drag coefficients, the aforementioned time-averaged density-velocity product, and the ratio of

planform and body areas. A time average captures the typical conditions encountered on-orbit and reduces the computational complexity of the problem. However, this comes at the cost of the minimum and maximum conditions. An average is employed in this work rather than minimum or maximum values because minimums and maximums are not coupled to one another: different values reach their limits at different times.

By time-averaging in this fashion, we have assumed the drag coefficients to be time-invariant, i.e. they do not vary appreciably as a result of time variations in orbital location or atmospheric conditions. Results in Section 7.1 indicate the drag coefficients may vary by as much as four percent over the course of an orbit as a result of eclipsing effects on atmospheric conditions, and that this level of variation does not significantly alter the results.

$$\overline{D''} = \frac{1}{2}\overline{\rho v_{bulk}^2}\left[C_{D,s/c} + C_{D,PA}\left(\frac{A_{PA}}{A_{s/c}}\right)\right] \quad \textbf{(3.2)}$$

The collector experiences aerodynamic drag as a result of encountering an oncoming flow. Some of this flow is available for the collector to ingest as expressed in Eq. (3.3), where $A_{collector}$ is the cross-sectional area of the collecting inlet oriented in the direction of the flow. If we assume the entire frontal area of the spacecraft body is part of the inlet, then the collector area equates to the body area and the time-averaged area-specific available mass flow rate becomes the quantity expressed in Eq. (3.4).

$$\dot{m}_{avail} = \rho v_{bulk} A_{collector} \quad \textbf{(3.3)}$$

$$\overline{\dot{m}''}_{avail} = \overline{\rho v_{bulk}} \quad \textbf{(3.4)}$$

Eq. (3.4) accurately describes the average mass flow rate available for collection by the system per unit frontal area, but not all of the available flow will be successfully ingested by the inlet. Some portion of the flow has a potential to backflow out of the inlet rather than being collected by the system. The fraction of the available flow which is actually collected is denoted by η_c, the collector efficiency. Consequently, Eq. (3.5) expresses the time-average area-specific flow rate ingested into the collector system.

$$\overline{\dot{m}''}_{in} = \eta_c \overline{\rho v_{bulk}} \tag{3.5}$$

For a propellant collection system to sustain orbit, at least a portion of the ingested flow must be accelerated to produce thrust. We denote the time-average mass flow rate for thrust as $\overline{\dot{m}''}_{out}$. The usage ratio, ϵ, represents the ratio of the flow used for thrust to the total flow ingested by the vehicle as demonstrated in Eq. (3.6). Usage ratio necessarily takes on a value greater than zero. Vehicles with a usage ratio less than one store or use a fraction of the ingested propellant for some other purpose, while vehicles with usage ratio greater than one contribute additional mass flow from storage into producing thrust.

$$\epsilon \equiv \frac{\dot{m}_{out}}{\dot{m}_{in}} \tag{3.6}$$

Propellant collection designs may incorporate a compressor system to process the ingested flow for storage. Designs have three options for addressing the issue of compression:

- Perform no compression (air-breathing, Figure 23)
- Perform compression, but only on flow destined for storage (diverter, Figure 24)
- Perform compression on all ingested flow (collector, Figure 25)

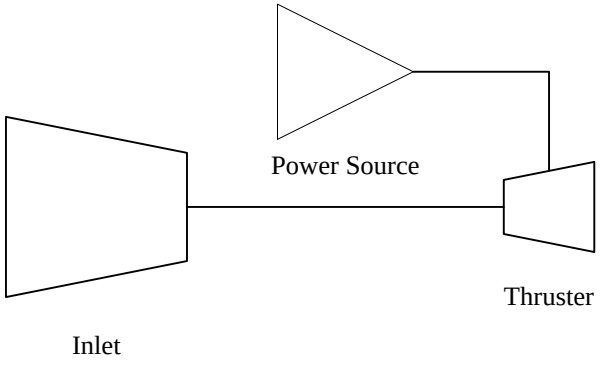

Figure 23. Air-Breathing System Diagram

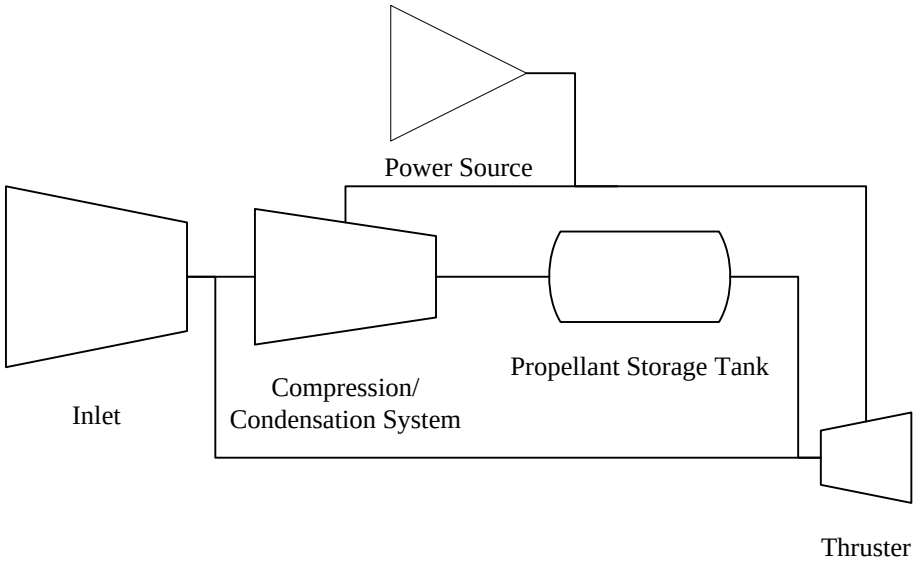

Figure 24. Diverter System Diagram

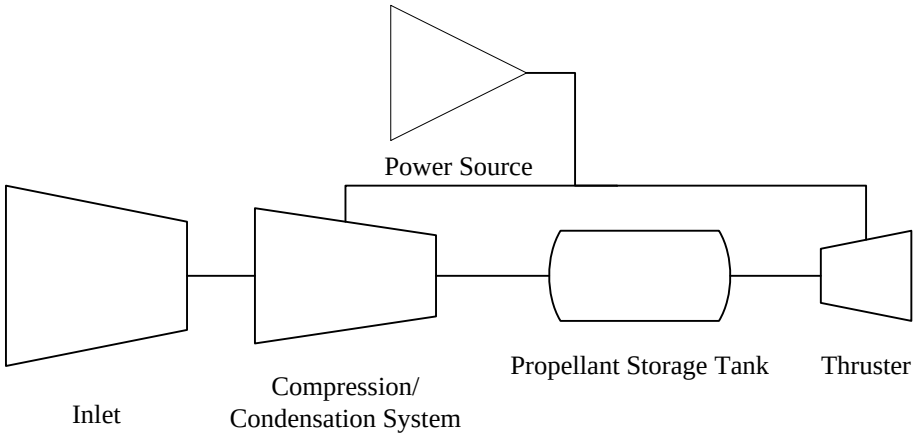

Figure 25. Collector System Diagram

Because of the divergence in possible design paths taken by a propellant collection system, three equations must be prescribed for quantifying the power required for compression. In the case of the first option where no ingested flow is compressed, the compression power is trivially zero as indicated by Eq. (3.7). For the remaining two cases the compression power can be treated as an isothermal compression from the ambient pressure, p_1 to the pressure at the triple point of nitrogen, p_2 with thermodynamic efficiency η_{comp}. Eq. (3.8) describes the time-average area-specific power required for compression for the partial storage case and Eq. (3.9) describes the compression power for the case where all flow undergoes compression.

$$\overline{P''}_{comp} = 0 \tag{3.7}$$

$$\overline{P''}_{comp} = \frac{\eta_c}{\eta_{comp}} \overline{RT_{gas} \ln\left(\frac{p_2}{p_1}\right) \rho v} (1 - \epsilon) \tag{3.8}$$

$$\overline{P''}_{comp} = \frac{\eta_c}{\eta_{comp}} \overline{RT_{gas} \ln\left(\frac{p_2}{p_1}\right) \rho v} \tag{3.9}$$

Contained within Eq. (3.8) is an implicit assumption that the fraction of the oncoming flow being compressed is time-invariant. Any time-variance in the fraction of the oncoming flow would depend on the particular design of the flow diverter system and lies outside the scope of this work. Both Eqs. (3.8) and (3.9) also assume that the gas constant remains invariant over the course of compression at its initial value. While this assumption is almost trivial for most applications due to negligible variation in composition, this effect cannot be ignored here due to the large disparity between initial and final pressure. As the pressure increases in the gas, dissociated species such as atomic oxygen will recombine. This will increase the average molecular weight and thus drive the gas constant down. The effect of a lower gas constant on the required power is obvious from Eqs. (3.8) and (3.9) or from examination of the work integral from which the isothermal compression equation is derived: lower gas constant reduces the required energy to compress. Thus, this assumption leads to an overestimation of the required compression power by a factor on the order of the expected variation in the value of the gas constant.

The presence of operating compression machinery may introduce vibrations into the vehicle which could affect its attitude and thus the quality of data it is able to collect. Some applications might demand interrupted operation of compression machinery to allow for other activities to proceed, which would enhance the demands on the performance of other components of the propellant collection system to accommodate these interruptions. This work only directly considers cases where the propellant collection system continuously operates.

In order to sustain orbit, a propellant-collecting vehicle must at a minimum produce average thrust equal to average drag as expressed in Eq. (3.10). The thrust is a function of the outgoing mass flow rate as well as the specific impulse and the gravitational constant as prescribed earlier in this work. Eq. (3.11) describes the required specific impulse needed to sustain orbit given the encountered area-specific drag and the available mass flow rate for thrust. It arises from combining Eq. (3.10) with the definition of thrust and solving for specific impulse. Most engines are limited to a narrow range of specific impulse for nominal operation, thus the specific impulse can be assumed to be constant. Previous efforts to study propellant collection have looked at two basic strategies for delivering propellant to the engine:

- Propellant delivery with negligible initial bulk motion (rocket)
- Propellant delivery with initial bulk motion equal to the velocity of the vehicle (ramjet)

$$\overline{T''} = \overline{D''} \tag{3.10}$$

$$I_{sp,req} = \frac{\overline{D''}}{\epsilon \eta_c \overline{\rho v} g_0} \tag{3.11}$$

The first option mirrors the situation commonly found in traditional rocket engines whereby the flow enters the engine at a velocity which is negligible when compared with the exit velocity. The second option mirrors that of a ramjet whereby the flow reaches the acceleration region of the engine with most of the velocity with which it entered. By recalling the relation between thrust and power described earlier in this work

and assuming constant thruster efficiency as a result of constant specific impulse, we arrive at Eq. (3.12) which expresses the time-average area-specific power required to produce thrust sufficient to overcome drag under the assumption of the first option.

$$\overline{P''}_{thrust} = \frac{\overline{T''} I_{sp,req} g_0}{2\eta_t} \tag{3.12}$$

Regarding option two for the thrust power, this work assumes negligible velocity loss for thruster flow as it moves from the vehicle inlet to the acceleration region of the thruster. This assumption idealizes the ramjet power requirements to demonstrate the maximum positive effect a ramjet system can have on reducing power over a rocket system. Under this assumption, the area-specific thrust power is a function of the mass flow rate to the thruster, thruster efficiency, and both the initial and exit velocities as presented in Eq. (3.13). The thrust is equal to Eq. (3.14), which accounts for the momentum already contained by the flow as it passes through the thruster. Assuming that the initial velocity is equal to the vehicle velocity, substituting in the relevant parameters for the outgoing mass flow rate, and substituting the specific impulse formulation of exit velocity we arrive at Eq. (3.15). This equation expresses the instantaneous thrust power requirement as a function of the performance of the thruster, the required thrust, the performance of the vehicle inlet, and the ambient conditions. By time-averaging, we arrive at Eq. (3.16), with Eq. (3.17) describing the form of the required specific impulse.

$$P''_{thrust} = \frac{1}{2\eta_t} \dot{m}''_{out} \left(u_{eq}^2 - u_{in}^2 \right) \tag{3.13}$$

$$T'' = \dot{m}''_{out}\left(u_{eq} - u_{in}\right) \tag{3.14}$$

$$P''_{thrust} = \frac{1}{2\eta_t}\left(I_{sp}g_0(T'' + \epsilon\eta_c\rho v^2) - \epsilon\eta_c\rho v^3\right) \tag{3.15}$$

$$\overline{P''}_{thrust} = \frac{1}{2\eta_t}\left(I_{sp}g_0(\overline{T''} + \epsilon\eta_c\overline{\rho v^2}) - \epsilon\eta_c\overline{\rho v^3}\right) \tag{3.16}$$

$$I_{sp,req} = \frac{\overline{D''}}{\epsilon\eta_c\overline{\rho v}g_0} + \frac{\overline{v}}{g_0} \tag{3.17}$$

The nominal operation of many electric propulsion devices is limited by the maximum allowable ambient pressure. At the high pressure limit, collisions can impact acceleration and backpressure can inhibit flow out of the thruster. Research data on facility backpressure effects indicates pressures on the order of those encountered in VLEO can alter the performance and stability of thrusters [68]. At low pressures, the probability of collision declines and adversely impacts the propellant utilization in neutralizer cathodes [26]. Consequently, some thruster designs might require compression even if no flow is being stored in order to meet the minimum pressure requirements. Although these are important considerations for the practical design and selection of an applicable electric propulsion device, the effects of ambient pressure on the thruster system are not considered in this work.

The sum of the required area-specific time-average power for thrust and compression is the total required power as presented in Eq. (3.18). A propellant-collecting vehicle must be capable of supplying sufficient power to meet the required power. This work considers two options for power generation:

- Solar photovoltaic power and
- Nuclear power

$$\overline{P''}_{req} = \overline{P''}_{comp} + \overline{P''}_{thrust} \tag{3.18}$$

These two power source options dominate propellant collection literature and are thus considered here. Of the two, solar power represents the most technically mature option and is employed on a majority of Earth-orbiting craft. Solar power relies on energy gathered from sunlight and thus relies on direct line-of-sight with the sun to effectively generate power. Thus, the performance of solar panels is reliant not only on panel design parameters such as efficiency and area, but also on orbit geometry. Eq. (3.19) expresses the net instantaneous power produced by a solar array as a function of panel area A_{SP}, solar intensity I_0, total panel efficiency η_{SP}, un-eclipsed portion of the solar disk $\mathcal{O}$, and the cosine of the angle between the sun vector and the vector perpendicular to the solar array θ. When considering solar power, the planform area employed in Eq. (3.1) is simply the panel area. Thus, all solar power generation for propellant collection is assumed to occur off of the body.

$$P_{SP} = A_{SP} I_0 \eta_{SP} \mathcal{O} cos\theta \tag{3.19}$$

For simplicity in the derivation moving forward, we will define a factor f as expressed in Eq. (3.20) to represent the orbital geometry terms present in the calculation of solar power. Time-averaging and dividing through by the spacecraft frontal area leads to Eq. (3.21), which expresses the time-average area-specific solar power performance.

Implicit in this formulation is the assumption that both the solar intensity and total panel efficiency are time-invariant. Panel efficiency tends to degrade by a few percent per year over the lifetime of the vehicle, but lifetime effects are not considered in this work [4]. This formulation also neglects any consideration of losses incurred in storing and retrieving solar energy from battery storage.

$$f \equiv \mathcal{O}cos\theta \tag{3.20}$$

$$\overline{P''}_{SP} = \frac{A_{SP}}{A_{s/c}} I_0 \eta_{SP} \overline{f} \tag{3.21}$$

As stated previously regarding the planform component of the vehicle, the solar arrays are assumed to be aligned such that they are parallel to the velocity vector. However, this only provides constraint along the pitch axis of rotation. The roll axis remains unbounded by this assumption, so that a vehicle may adjust its roll attitude to minimize the cosine loss component of *f*.

Figure 26 presents the body-fixed reference coordinates for a spacecraft. The z-axis points in the direction of nadir, the y-axis in the direction opposite of the orbit normal, and the x-axis is mutually orthogonal to the others in a right-handed coordinate system. The velocity vector is perpendicular to the orbit normal by definition but can otherwise have both x and z components. Under the assumption that the collector is always perfectly aligned with the velocity vector, the roll axis aligns perfectly to the velocity vector as well.

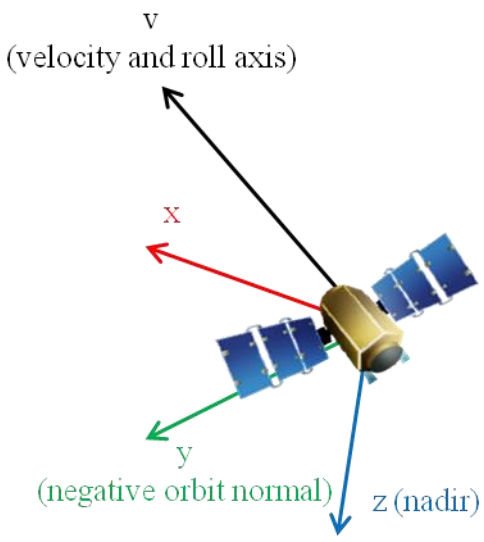

Figure 26. Body-fixed reference frame axes. The velocity vector is perpendicular to the orbit normal and orients along the roll axis of the craft under the assumptions presented in this work.

Let the unit vector $\hat{\boldsymbol{v}}$ represent the unit vector along the direction of the velocity vector, $\hat{\boldsymbol{b}}$ represent the unit vector along the direction of the orbit normal, and $\hat{\boldsymbol{p}}$ represent the unit vector perpendicular to the plane of the solar array. The assumption of zero angle of attack constrains $\hat{\boldsymbol{p}}$ to be perpendicular to $\hat{\boldsymbol{v}}$. One possible orientation of $\hat{\boldsymbol{p}}$ is the orientation in which it is mutually orthogonal to both the velocity and the orbit normal as prescribed in Eq. (3.22). Eq. (3.23) enumerates the form of both $\hat{\boldsymbol{v}}$ and $\hat{\boldsymbol{b}}$. Computing the cross product and recognizing its magnitude to be unity, Eq. (3.24) expresses one acceptable value for $\hat{\boldsymbol{p}}$.

$$\hat{\boldsymbol{p}} = \frac{\hat{\boldsymbol{v}} \times \hat{\boldsymbol{b}}}{\left\| \hat{\boldsymbol{v}} \times \hat{\boldsymbol{b}} \right\|} \tag{3.22}$$

$$\hat{\boldsymbol{v}} = [v_x, 0, v_z]; \hat{\boldsymbol{b}} = [0, -1, 0] \tag{3.23}$$

$$\hat{\boldsymbol{p}} = [v_z, 0, -v_x] \tag{3.24}$$

Eq. (3.25) expresses the cosine loss as a function of both $\hat{\boldsymbol{p}}$ and the sun-vector $\hat{\boldsymbol{S}}$, which points in the direction of the sun. For simplicity we assume the sun vector to be formatted in body-fixed coordinates similar to the solar array vector. The solar array vector may be rotated by an angle ϕ such that the cosine loss is minimized ($cos\theta$ is maximized). A rotation about the roll axis is equivalent to a general rotation about the velocity unit vector with rotation matrix $\boldsymbol{R}(\phi)$. Simplifying leads to Eq. (3.26), which is optimized by taking the derivative with respect to ϕ and setting the result equal to zero. Eq. (3.27) thus expresses the optimum angle with which to roll to minimize the cosine loss for the solar arrays. This work assumes that this optimum roll is always executed to maximize solar power.

$$\left|\hat{\boldsymbol{p}} \cdot \hat{\boldsymbol{S}}\right| = cos\theta \tag{3.25}$$

$$\boldsymbol{R}(\phi)\hat{\boldsymbol{p}} \cdot \hat{\boldsymbol{S}} = (v_z S_x - v_x S_z)cos\phi + (v_x^2 + v_z^2)S_y sin\phi \tag{3.26}$$

$$\phi = \tan^{-1}\left(\frac{(v_x^2 + v_z^2)S_y}{v_z S_x - v_x S_z}\right) \tag{3.27}$$

A nuclear reactor does not rely on line-of-sight with the sun to produce power, but must exhaust the considerable waste heat generated by the reactor to maintain acceptable temperatures onboard the vehicle. Thus whereas a solar power architecture has solar arrays, a nuclear power architecture has radiators which will contribute to the drag of the vehicle. Eq. (3.28) expresses the radiative performance of a radiator system with radiator

area A_{rad} at temperature T_R and emissivity ε. The quantity σ is the Stephan-Boltzmann constant. In contrast with the solar power case, the radiator area is equivalent to the twice the planform area in this formulation. A radiator can radiate from both sides of the planform area whereas a solar array can only direct one side of the planform area towards the sun.

$$P_{rad} = A_{rad}\sigma\varepsilon T_R^4 \tag{3.28}$$

Note that the formulation of Eq. (3.28) assumes that both sides of the radiator transmit energy into space with no reflected sources. A real radiator on a propellant-collecting vehicle would likely have one or both sides partially viewing the sun or Earth. Data from Gilmore indicates that Earth albedo and infrared sources can contribute between 100-300 W/m^2 of return heat, depending on a number of time-varying conditions [69]. In contrast, the heat rejection performance values studied in this work range from 15,000-150,000 W/m^2, thus the maximum contribution of other heat sources is on the order of one to ten percent.

We can couple the radiative performance to the electrical power generation of the reactor with the aid of Eq. (3.29) which expresses the relationship between the reactor thermal efficiency η_R and the net thermal and electrical powers, P_t and P_e respectively. Recognizing the net thermal power is the sum of the radiated power and the electrical power, Eq. (3.30) expresses the electrical power a radiator system can accommodate given the radiator area and temperature as well as the reactor thermal efficiency. Assuming the reactor and radiator performance parameters are all time-invariant and dividing by the spacecraft body area leads to Eq. (3.31). Note that surface finish

properties can vary by a few percent over the vehicle lifetime, but lifetime effects are not considered in this work.

$$\eta_R = \frac{P_e}{P_t} \tag{3.29}$$

$$P_e = \frac{\eta_R}{1-\eta_R} A_{rad} \sigma \varepsilon T_R^4 \tag{3.30}$$

$$\overline{P''}_e = \frac{2\eta_R}{1-\eta_R} \frac{A_{PA}}{A_{s/c}} \sigma \varepsilon T_R^4 \tag{3.31}$$

As derived in this work, propellant collection systems can be categorized into one of ten types as summarized in Table 1. Designs for some categories have never been reported in the literature until this work.

Table 1. Taxonomy of propellant collection systems

Name	**Compression Scheme**	**Thrust Scheme**	**Power Scheme**
Solar Air-breathing Rocket	No Compression	Rocket	Solar
Solar Diverter Rocket	Only on Storage	Rocket	Solar
Solar Collector Rocket	All	Rocket	Solar
Solar Air-breathing Ramjet	No Compression	Ramjet	Solar
Solar Diverter Ramjet	Only on Storage	Ramjet	Solar
Nuclear Air-breathing Rocket	No Compression	Rocket	Nuclear
Nuclear Diverter Rocket	Only on Storage	Rocket	Nuclear
Nuclear Collector Rocket	All	Rocket	Nuclear
Nuclear Air-breathing Ramjet	No Compression	Ramjet	Nuclear
Nuclear Diverter Ramjet	Only on Storage	Ramjet	Nuclear

Note in both Eq. (3.21) and Eq. (3.31) the presence of an area ratio term which is equivalent to the ratio of the planform area and the body area as derived in Eq. (3.2). This term couples the power production to the aerodynamic drag and effectively closes a

design loop on the propellant collection system. Consider the case of a solar air-breathing rocket, similar to the RAM-EP or ABIE concepts. Such a vehicle has a thrust power requirement of the form presented in Eq. (3.12). Imposing the condition that average thrust equals average drag as expressed in Eq. (3.10) and substituting in the formulation for required specific impulse results in Eq. (3.32). Further substituting in the long-form of the drag as derived in Eq. (3.2) and noting that the required thrust power is equal to the total required power results in Eq. (3.33). Eq. (3.33) expresses the required time-average area-specific thrust power as a function of the area ratio term. The thrust power is effectively a quadratic function with respect to the area ratio term, while the solar power as derived in Eq. (3.21) is a linear function with respect to the area ratio term.

$$\overline{P''}_{thrust} = \frac{\overline{D''}^2}{2\eta_t \eta_c \epsilon \overline{\rho v}} \tag{3.32}$$

$$\overline{P''}_{req}\left(\frac{A_{PA}}{A_{s/c}}\right) = \frac{\left(\frac{1}{2}\overline{\rho v^2}\right)^2}{2\eta_t \eta_c \overline{\rho v}}\left[C_{D,s/c}^2 + 2C_{D,PA}C_{D,s/c}\left(\frac{A_{PA}}{A_{s/c}}\right) + C_{D,PA}^2\left(\frac{A_{PA}}{A_{s/c}}\right)^2\right] \tag{3.33}$$

A solar air-breathing rocket propellant collection design will close if, given its performance parameters (efficiencies, drag coefficients, geometry) and orbit conditions (velocity, density, solar geometry), a value of the area ratio exists such that the average area-specific power required is less than or equal to the average area-specific solar power generated. A nuclear air-breathing rocket propellant collection design will close with the same conditionality applied to the linear curve for the radiator. Variations on this solution have been derived for the other design categories and are included below.

Diverter Rocket:

$$\overline{P''}_{req}\left(\frac{A_{PA}}{A_{s/c}}\right) = \frac{\left(\frac{1}{2}\overline{\rho v^2}\right)^2}{2\eta_t\eta_c\epsilon\overline{\rho v}}\left[C_{D,s/c}^2 + 2C_{D,PA}C_{D,s/c}\left(\frac{A_{PA}}{A_{s/c}}\right) + C_{D,PA}^2\left(\frac{A_{PA}}{A_{s/c}}\right)^2\right] + \frac{\eta_c}{\eta_{comp}}\overline{RT_{gas}\ln\left(\frac{p_2}{p_1}\right)\rho v}(1-\epsilon) \quad \textbf{(3.34)}$$

Collector Rocket:

$$\overline{P''}_{req}\left(\frac{A_{PA}}{A_{s/c}}\right) = \frac{\left(\frac{1}{2}\overline{\rho v^2}\right)^2}{2\eta_t\eta_c\epsilon\overline{\rho v}}\left[C_{D,s/c}^2 + 2C_{D,PA}C_{D,s/c}\left(\frac{A_{PA}}{A_{s/c}}\right) + C_{D,PA}^2\left(\frac{A_{PA}}{A_{s/c}}\right)^2\right] + \frac{\eta_c}{\eta_{comp}}\overline{RT_{gas}\ln\left(\frac{p_2}{p_1}\right)\rho v} \quad \textbf{(3.35)}$$

Air-breathing Ramjet:

$$\begin{aligned}\overline{P''}_{req}\left(\frac{A_{PA}}{A_{s/c}}\right) = {} & \frac{\left(\frac{1}{2}\overline{\rho v^2}\right)^2}{2\eta_t\eta_c\overline{\rho v}}\left[C_{D,s/c}^2 + 2C_{D,PA}C_{D,s/c}\left(\frac{A_{PA}}{A_{s/c}}\right) + C_{D,PA}^2\left(\frac{A_{PA}}{A_{s/c}}\right)^2\right] \\ & + \frac{\overline{\rho v^2}}{4\eta_t}\left(\frac{\overline{\rho v^2}}{\overline{\rho v}} + \overline{v}\right)\left(C_{D,s/c} + C_{D,PA}\left(\frac{A_{PA}}{A_{s/c}}\right)\right) \\ & + \frac{\eta_c}{2\eta_t}\left(\overline{\rho v^2}\,\overline{v} - \overline{\rho v^3}\right)\end{aligned} \quad \textbf{(3.36)}$$

Diverter Ramjet:

$$\begin{aligned}\overline{P''}_{req}\left(\frac{A_{PA}}{A_{s/c}}\right) = {} & \frac{\left(\frac{1}{2}\overline{\rho v^2}\right)^2}{2\eta_t\eta_c\epsilon\overline{\rho v}}\left[C_{D,s/c}^2 + 2C_{D,PA}C_{D,s/c}\left(\frac{A_{PA}}{A_{s/c}}\right) + C_{D,PA}^2\left(\frac{A_{PA}}{A_{s/c}}\right)^2\right] \\ & + \frac{\overline{\rho v^2}}{4\eta_t}\left(\frac{\overline{\rho v^2}}{\overline{\rho v}} + \overline{v}\right)\left(C_{D,s/c} + C_{D,PA}\left(\frac{A_{PA}}{A_{s/c}}\right)\right) \\ & + \frac{\epsilon\eta_c}{2\eta_t}\left(\overline{\rho v^2}\,\overline{v} - \overline{\rho v^3}\right) + \frac{\eta_c}{\eta_{comp}}\overline{RT_{gas}\ln\left(\frac{p_2}{p_1}\right)\rho v}(1-\epsilon)\end{aligned} \quad \textbf{(3.37)}$$

This section identifies numerous vehicle design parameters which factor into design closure and performance. The next section develops ranges of study for them.

3.2 Ranges of Study

This section presents the ranges of study for each of the parameters considered in the previous section. Some parameters such as the usage ratio are constants which depend on the design of the vehicle while other values such as the time-average parameters depend on underlying information such as the vehicle orbit. This section consists of seven subsections, which each detail a different set of parameters considered in this work.

3.2.1 Time-Average Parameters

The previous section identifies six time-averaged parameters as being important to the performance of a propellant collecting vehicle, as listed in Table 2. Table 2 also includes two other time-average terms, the temperature and the speed ratio. Their importance will become apparent later in this section. These terms depend on the parameters of the orbit the propellant-collecting vehicle occupies. Orbit periapsis altitude, eccentricity, inclination, and the year are all factors which affect the value of these averages. However, not all time-average parameters are important to all vehicle types.

This work employs the Systems Toolkit (STK) from Analytical Graphics, Inc. (AGI) to produce high-fidelity estimates of many of the contributing factors in the time-average parameters. STK is a commercially available software package used by spacecraft designers and operators. Among its numerous features, STK has a high precision orbit propagator (HPOP) which contains the functionality for modeling central body gravity, aerodynamic drag, solar radiation pressure, third-body terms, and eclipsing

bodies. This work utilizes HPOP solely with central body gravity modeling, third-body contributions from the Sun and Moon and eclipsing to produce detailed orbit data for an ideal propellant-collecting vehicle which exactly counteracts the other perturbing terms.

Table 2. Summary of Time-Average Parameters.

Parameter Symbol	Parameter Name
$\overline{v}$	Velocity (m/s)
$\overline{\rho v}$	Area-Specific Mass Flow Rate (kg/m^2-s)
$\overline{\rho v^2}$	Area-Specific Force (Pa)
$\overline{\rho v^3}$	Area-Specific Flow Energy (W/m^2)
$\overline{RT_{gas} \ln\left(\frac{p_2}{p_1}\right) \rho v}$	Compression Energy (W/m^2)
$\overline{f}$	Solar Viewing Factor
$\overline{T_{gas}}$	Temperature (K)
$\overline{s}$	Speed Ratio

Atmospheric density is common to four of the eight time-average parameters summarized in Table 2. Numerous atmospheric models estimate the atmospheric density as a function of time, location, and space weather conditions. This work uses NRLMSISE-00 (Naval Research Laboratory Mass Spectrometer and Incoherent Scatter Radar Exosphere Model). NRLMSISE-00 is a standard atmosphere model developed by the United States Naval Research Laboratory in 2001 to model the atmosphere from sea level to 1,000 km [66]. While there are atmosphere models such as the updated Jacchia model JB2006 that better predict ambient density, NRLMSISE-00 is the highest fidelity model which contains atmospheric composition information. Composition information is necessary in this work to predict the compression energy, because variations in composition result in variation in the gas constant term.

Solar and geomagnetic activity can dramatically affect the composition and density of the upper atmosphere [50, 55]. These phenomena are often referred to as part of space weather. Numerous ground facilities and spacecraft have performed

measurements of space weather, leading to a rich historical dataset. Researchers have found that in recent history the Sun has operated on roughly an 11-year cycle of repeating activity [70]. In order to fully understand the effect of variations in space weather on a propellant-collecting vehicle, the analysis must span at least one half of a solar cycle to capture minimum and maximum solar activities. Figure 27 illustrates the last complete solar cycle: solar cycle 23, which spanned from May 1996 to January 2008. The historical data gathered during the years of 1996, 1999, and 2001 provide a baseline for minimum, average, and maximum solar activity. The specific data source for this information is the space weather file compiled by the Center for Space Standards and Innovation (CSSI).

STK propagates an orbit over an entire year and outputs numerous raw data products to Matlab for post-processing. These products include the time, classical orbital elements, Sun vector, velocity vector, visible percentage of the solar disk, latitude, longitude, and altitude. Matlab code developed for this work decimates the raw data by sampling one orbit period at 00:00 UTC every fifth day to reduce computational load. The Matlab code processes the results from STK and interfaces with NRLMSISE-00 to generate the time-average parameters. These parameters are determined over a variety of orbits with varying year, inclination, eccentricity, and periapsis altitude.

Table 3 lists the full parameter set and provides the test matrix this work uses to calculate the time-average parameters. Eccentricity is varied between values of 0.0, 0.1, and 0.2. Periapsis altitude is varied between 100 km and 300 km, with varying increment between data points. Altitude varies by 2 km between 100 km and 120 km, by 5 km between 120 km and 150 km, and by 10 km between 150 km and 300 km for a total of 32 data points. Inclination values of 0, 5, 10, 28.5, 53.5, 75, 80, 85, and 90 degrees are chosen to capture the inclination of equatorial orbits, orbits at launch from Kennedy Space Center (KSC), ISS orbit, sun synchronous orbits, and polar orbits. Together these parameter variations result in a test matrix consisting of 2,592 orbits.

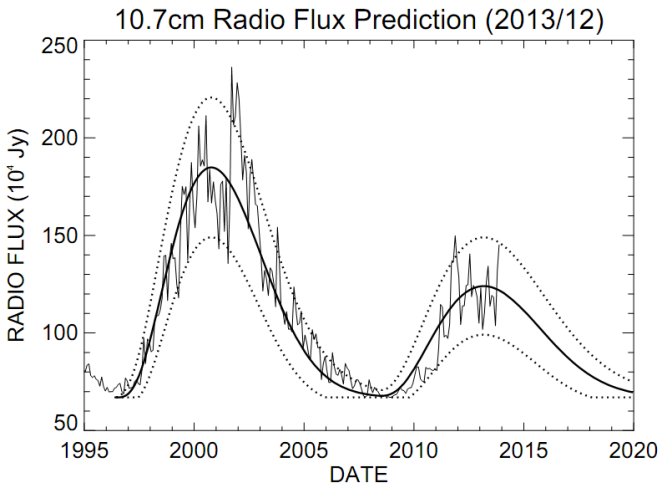

Figure 27. Map of solar radio flux, which plays an important role in atmospheric conditions. This figure shows solar cycle 23 on the left. Courtesy NASA MSFC.

Table 3. Test matrix for modeling time-average parameters.

Parameter	Minimum	Maximum	Total
Inclination (deg)	0	90	9
Eccentricity	0	0.2	3
Periapsis Altitude (km)	100	300	32
Year	1996	2001	3

3.2.2 Usage Ratio

The usage ratio is an important parameter for vehicles of the Diverter and Collector types, and can take any value from zero to one. Usage ratio contributes explicitly through its appearance in the derivations of the previous section, and also through its implicit contribution to the spacecraft body drag coefficient. This is demonstrated in the following section. This work considers the entire applicable range of usage ratio when considering Diverter and Collector vehicles.

3.2.3 Drag Coefficients and Collector Efficiency

The drag coefficients $C_{D,s/c}$ and $C_{D,PA}$ both contribute to the overall aerodynamic drag on a propellant collecting vehicle. This work makes use of the analytical drag coefficient derivations from Sentman to estimate the drag coefficient as a function of the orbit, the collector efficiency, and the usage ratio [47]. Sentman's analysis makes the assumption of free-molecular flow and diffuse reflection of particles. Recalling the assumption that the planform area is an infinitely thin flat plate with zero angle of attack, Sentman's derivation for the drag on a flat plate becomes:

$$C_{D,PA} = \frac{2}{s\sqrt{\pi}} \tag{3.38}$$

where s is the aforementioned speed ratio. The speed ratio is the ratio of the bulk velocity of the flow to the random thermal velocity of the flow and acts as a self-similarity parameter for the hyperthermal free-molecular flow regime. Eq. (3.39) describes the time-average speed ratio in terms of the spacecraft velocity, the local gas constant, and the local gas temperature. As the speed ratio changes due to variation in these parameters during an orbit, so too will the drag coefficient. This work makes the assumption that the drag coefficient corresponding to the time-average speed ratio accurately represents the drag coefficient for the vehicle on an average basis. This work also assumes that there is negligible variation in planform area drag coefficient away from Sentman's analytical result. Results presented in Section 7.1 as Figure 97 for a specific vehicle design demonstrate the validity of these assumptions.

$$\overline{s} = \frac{\overline{v}}{\sqrt{2RT_{gas}}} \tag{3.39}$$

The drag coefficient for the spacecraft body takes a more complicated form as the shape and sources of drag gain variability. Where the planform area essentially has a skin friction drag contribution term under the infinitely thin assumption, the body has a contribution from the inlet in addition to skin friction. This work makes use of two equations which place bounds on the upper and lower limits of the drag coefficient while accounting for the variability from design. Eq. (3.40) represents the lower bound for the body drag coefficient.

The first term in Eq. (3.40) represents the drag coefficient due to the portion of the flow which is not stopped by the vehicle. Eq. (3.40) neglects skin friction. Note that this work assumes the planform area is always visible to the flow. γ_c is a conditional term which takes on the values denoted in Eq. (3.41). It represents the drag coefficient for the portion of the flow which is stopped inside of the vehicle. Finally, $C_{D,min}$ represents a drag coefficient on the order of that attained through investigation of the *Viking* aeroshell at the continuum limit with margin for improvement [71]. $C_{D,min}$ is thus selected to be 1.5. The collector efficiency appears in both terms, and can take any value from zero to one in this work.

$$C_{D,s/c,min} = C_{D,min}(1 - \eta_c) + \gamma_c \eta_c \tag{3.40}$$

$$\gamma_c \equiv \begin{cases} 0, Air - Breathing\ Ramjet \\ 2(1-\epsilon), Diverter\ Ramjet \\ 2, Rocket \end{cases} \tag{3.41}$$

Eq. (3.42) prescribes the upper limit of the body drag coefficient, and consists of three terms. The first term is the skin friction contribution, which is taken to be equal to that of Sentman's analytical solution for a cylinder as prescribed in simplified form in Eq. (3.43). The drag coefficient of a cylinder depends on the length-to-diameter ratio which is nominally selected as three for an upper limit. Also present in Eq. (3.42) is an inlet term analogous to the first term in Eq. (3.40), which represents the drag contribution from the portion of the flow which is not collected by the inlet. $C_{D,FP}$ represents Sentman's analytical solution for the drag on a flat plate perpendicular to the flow as given in Eq. (3.44). $T_{s/c}$ is the spacecraft temperature under the assumption that the oncoming flow perfectly accommodates to the inlet. This is assumed to have a temperature of 298 K. The final term in Eq. (3.42) is analogous to the second term in Eq. (3.40) and accounts for the portion of the flow which is stopped inside the vehicle. Figure 28 represents each of the drag coefficient components and the maximum body drag coefficient as a function of periapsis altitude for a polar circular orbit during peak solar activity.

$$C_{D,s/c,max} = C_{D,cyl} + (1 - \eta_c)C_{D,FP} + \gamma_c\eta_c \tag{3.42}$$

$$C_{D,cyl} = \frac{4}{s\sqrt{\pi}}\left(\frac{L}{D}\right) \tag{3.43}$$

$$C_{D,FP} = \left(1 + \frac{1}{2s^2}\right)(1 + \mathrm{erf}(s)) + \sqrt{\frac{T_{s/c}}{T_{gas}}}\left[\frac{\sqrt{\pi}}{2s}(1 + \mathrm{erf}(s))\right] \tag{3.44}$$

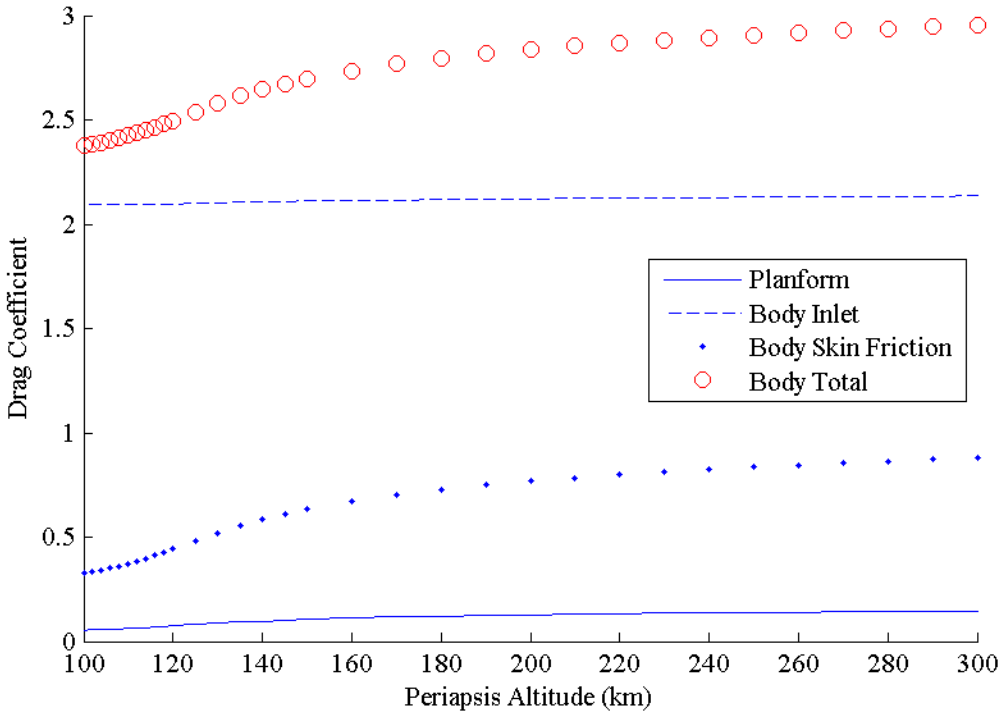

Figure 28. Drag coefficient components and maximum body drag coefficient for a polar circular orbit during peak solar activity.

The infinitely thin flat plate assumption relies on the thickness of the planform areas being sufficiently small to not significantly alter the total drag coefficient. Eqs. (3.38) and (3.44) allow for quantification of the effect of the frontal area of the planform components on the total drag coefficient as a function of length dimension as expressed in Figure 29. Different types of solar arrays and radiators have different thicknesses based on their deployment strategy and structural requirements. The thickness of a typical rigid plate solar panel is on the order of 15 mm [72]. Assuming this thickness, a gas temperature of 1,100 K, and a speed ratio of 8.1 consistent with a circular 85° inclination orbit in 2001 yields the relationship between drag coefficient ratio and panel thickness demonstrated in Figure 30. The frontal drag drops below five percent of the skin friction

drag at 5 meters length. This indicates that the infinitely thin flat plate assumption is valid for large vehicles, but loses validity for smaller vehicles.

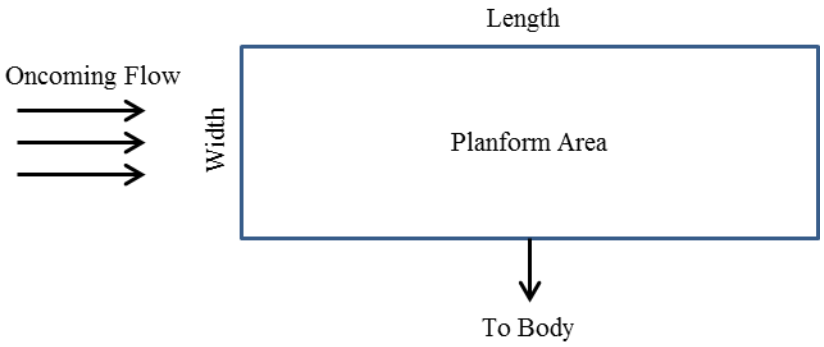

Figure 29. Flow diagram of planform areas.

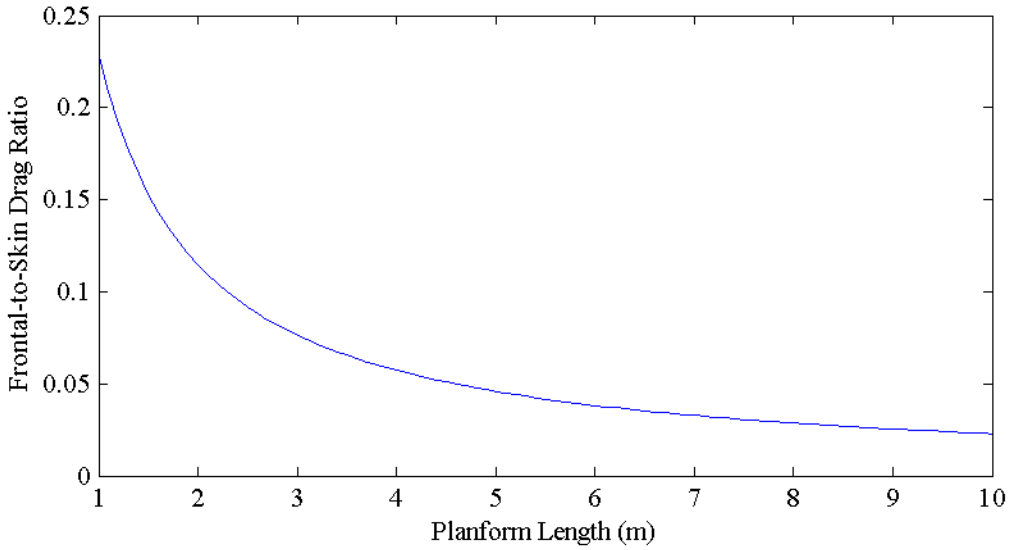

Figure 30. Ratio of frontal drag due to thickness to skin drag on the planform area as a function of length.

3.2.4 Compressor Efficiency

In order to compress the oncoming flow for storage, the compressor system must operate over several orders of magnitude of pressure. Systems capable of achieving the high compression ratios necessary to perform this function exist in the form of vacuum pumps. The most likely analog to a notional compression system for a propellant-

collecting vehicle is the turbomolecular pump. Turbomolecular pumps are turbomachinery devices which utilize a rotating blade assembly over several stages to mechanically compress ingested gas. Thermodynamically, turbomolecular pumps are inefficient because they ingest a small mass flow rate and must combat comparatively large friction and backflow losses [73]. Hablanian estimates turbomolecular pump thermodynamic efficiency to be "only a few percent." Thus compressor efficiency in this work is taken to vary between one and ten percent.

3.2.5 Thruster Efficiency

In an ideal thruster, the energy consumed goes towards accomplishing two tasks: ionizing the propellant and accelerating the propellant. The cost of ionization is considered a loss of energy because the energy spent to ionize propellant does not produce thrust. Thus, as the exit velocity increases a larger portion of the energy goes towards generating thrust rather than ionization. This drives an increase thruster efficiency; this is made evident by Eq. (3.45) which relates the thruster efficiency to the specific impulse and other thruster performance parameters for a gridded ion engine. η_u is the propellant utilization efficiency, γ is the beam divergence and double-ionization factor, ε_i is the ion production cost, V_{NC} is the neutralizer coupling potential, and m_i is the mass of the ion.

$$\eta_t = \frac{\eta_u \gamma^2}{1 + \frac{\varepsilon_i + V_{NC}}{\frac{m_i}{2q}(I_{SP} g_0)^2 + V_{NC}}} \tag{3.45}$$

This work uses Cifali et al.'s experimental results operating the RIT-10-EBB on pure nitrogen as the baseline of thruster performance [21]. Adapting the data presented in their 2011 publication with a second-order polynomial fit results in Eq. (3.46). Eq. (3.46) relates the thruster efficiency to the specific impulse with a R^2 value of 0.9997. Note that this curve fit is quadratic in nature and thus only useful for extrapolation to specific impulse of 9,500 seconds, after which the function begins to fall back towards zero in contradiction to the real behavior. To account for this limitation, the efficiency is assumed to level off at the efficiency value for 9,500 seconds which corresponds to 36.9%.

$$\eta_t = -4.606 \times 10^{-9}(I_{SP})^2 + 8.667 \times 10^{-5}(I_{SP}) - 3.876 \times 10^{-2} \qquad \textbf{(3.46)}$$

The upper bound of thruster performance used in this work is an adaptation of Eq. (3.45) under the idealized assumption that operation on nitrogen can ideally be made to be analogous to operation on xenon. Specifically, the upper bound model assumes that the ratio of ionization cost and ionization energy for nitrogen can reach parity with the equivalent ratio for xenon. Table 4 presents the values utilized in Eq. (3.45) to produce the "ideal" upper bound case for thruster efficiency.

Figure 31 illustrates the performance curves for both the ideal case and the experimental results of Cifali et al. [21]. The data points from the RIT-10-EBB experiment demonstrate the aforementioned relationship between efficiency and specific impulse. Recalling back to the first section in this chapter, the required specific impulse is a function of the time-average area-specific drag force. The drag is a function of the planform/body area ratio, and thus so is the thruster efficiency. Thruster efficiency

consequently represents a hidden, but important contribution of area ratio variability in the required power equations developed in the previous section. These equations serve to reduce the rate of increase of required power with respect to increasing area ratio.

Table 4. Performance values used to generate theoretical upper bound of ion thruster performance on nitrogen.

Description	Value	Unit
Molar Mass (N_2)	28.01	g/mol
Ionization Energy (N_2)	15.5	eV
Approximate Ionization Cost (N_2^+)	155	eV
Cathode-to-Ground Potential	15	V
Propellant Utilization	0.9	-
Beam Divergence	0.95	-

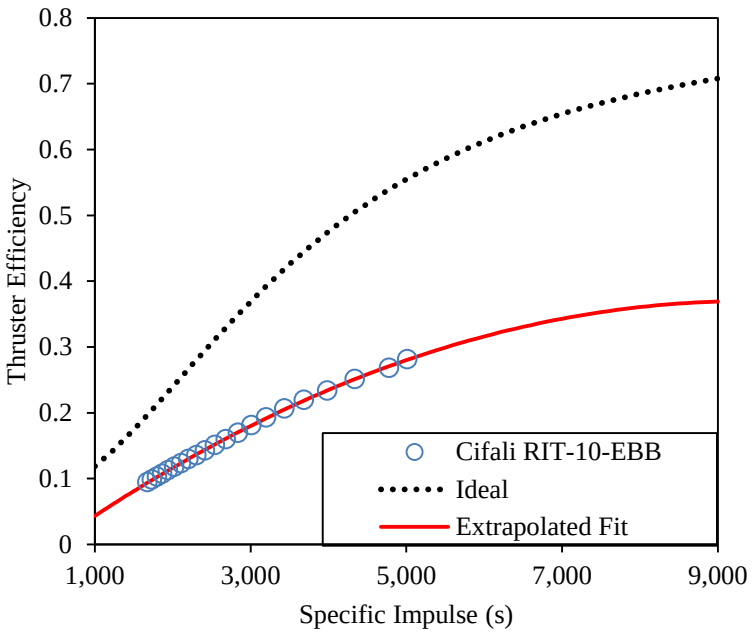

Figure 31. Illustration of the lower and upper bound cases for thruster efficiency as a function of specific impulse.

3.2.6 Solar Panel Efficiency

Panel efficiency continues to improve with continued development of solar technology as a renewable energy option for terrestrial needs. Solar panel efficiency varies by both cell and array design. Presently available solar panels from Spectrolab attain beginning-of-life performance of 366 W/m^2 under peak sunlight, equating to an efficiency of 26.8% [74]. This efficiency value is the baseline of performance used for solar power generation in this work. The upper limit is 68.2%, which corresponds to the theoretical limit calculated by De Vos for a cell of infinitely many layers with continuously-varying, infinitely-thin band gaps [75]. De Vos' limit forms the theoretical bound for tandem-type solar cell technology.

3.2.7 Nuclear Power Parameters

Nuclear reactor power sources have only been used once on a demonstration spacecraft in the West. Despite their rarity, researchers have continued developing nuclear reactors for space. The most recent models include the SAFE-400 and HOMER-15 reactors. The HOMER-15 design has attractive published specifications listed in Table 5 [76].

Table 5. HOMER-15 performance data [76].

Thermal Power Output	15 kW_t
Electrical Power Output	3 kW_e
Total Reactor Mass	416 kg
Power-Specific Mass, K	139 kg/kW
Thermal Efficiency, η_R	20%
Discharge Temperature, T_R	~900 K

Eq. (3.31) reveals three reactor and radiator performance parameters which drive the electrical power output: emissivity, radiator temperature, and thermal efficiency.

Emissivity is a material property which is easily identified and documented for a variety of spacecraft materials [4]. A value of 0.8 is assumed for this work, which is attainable with a variety of surface finishes. Thermal efficiency is demonstrated by the HOMER-15 reactor at approximately 20%, which consequently forms the baseline value for this parameter. Commercial scale nuclear plants typically have somewhat low efficiency on the order of 33% because they are unable to produce the same temperature of steam as fossil fuel plants while ensuring fuel integrity [77]. Thus, the upper limit considered for thermal efficiency of space nuclear reactors is 30%.

The final parameter, radiator temperature varies with the core temperature T_c and the thermal efficiency as demonstrated in Eq. (3.47). Thus, in order to describe a range of radiator temperatures one must actually describe a range of core temperatures. Using Eq. (3.47), the core temperature of the HOMER-15 reactor is an estimated 1,125 K which forms the baseline for this work. Increasing radiator temperature serves to decrease the necessary radiator area by increasing the area-specific radiated power. Molten salt reactors which operate with fuel and coolant salts are thus an attractive option for continued space reactor development because the salts can accommodate large core temperatures. Table 6 documents the boiling points for selected fuel/coolant salts under consideration in the literature for advanced reactor designs. Given the range of boiling points available, 1950 K is selected as the upper limit of core temperature considered in this work.

$$T_R = (1 - \eta_R)T_c \tag{3.47}$$

Table 6. Selected fuel/coolant salt boiling points [78].

Salt	Boiling Point (K)
NaF	1,977
PuF_3	2,270
LiF	1,949
ThF_4	1,953

3.3 Sensitivity Analysis Methodology

Section 3.1 presents the fundamental equations of this work. These are the equations for required and generated power, which include Eq. (3.21), Eq. (3.31) and Eqs. (3.33)-(3.37). These equations depend on a number of design parameters. We must determine the importance of each of these parameters to the result of each of the functions to satisfy the first objective of this work. This is done with a sensitivity analysis around a common set of "nominal" parameters based on values available in the literature. Table 7 lists the nominal parameter values used for the sensitivity analysis.

Table 7. Nominal parameters for the baseline case. The sensitivity analysis varies each individual parameter while holding the rest constant at these values.

Parameter Name	Symbol	Nominal Value
Periapsis Altitude	h	200 km
Orbit Inclination	i	0°
Orbit Eccentricity	e	0.0
Year	N/A	2001
Collector Efficiency	η_c	0.4
Drag Coefficient	$C_{D,s/c}, C_{D,PA}$	Sentman's Result
Usage Ratio	ϵ	0.5
Compressor Efficiency	η_{comp}	0.01
Thruster Efficiency	η_t	Cifali's Result
Solar Panel Efficiency	η_{SP}	0.268
Emissivity	ε	0.8
Thermal Efficiency	η_R	0.2
Core Temperature	T_c	1,125 K
Area Ratio	$\frac{A_{PA}}{A_{s/c}}$	1

The sensitivity of a function *A(x)* with respect to *x* is just the partial derivative of *A* with respect to *x*. However, this form of sensitivity is not suitable for comparing different types of parameters and does not capture the relative ability of each parameter to change. As an example, consider the factors of radiator temperature and emissivity in Eq. (3.31). The partial derivative of the function with respect to either parameter describes the effect of changing each parameter by one on the power. This is deceptive, because changing temperature by one Kelvin is insignificant compared to changing emissivity by one.

Another issue is dimensionality: the partial derivative of power with respect to temperature has different units than the partial derivative with respect to emissivity. In order to compare the sensitivity of a function relative to dissimilar parameters, a formulation must be used which non-dimensionalizes the sensitivity. The elasticity of *A* with respect to *x*, $E_{x,A}$ as defined in Eq. (3.48) presents a unit-less form of sensitivity which allows for comparison between dissimilar parameters. The value of the elasticity at a specific value of *A* represents the local order of *A* with respect to *x* and is easily applied both analytically and numerically. This work uses elasticity to determine the parameters which drive propellant collection system design.

$$E_{x,A} \equiv \frac{x}{A}\frac{\partial A}{\partial x} \tag{3.48}$$

3.4 Case Studies

The third research goal presented in Section 1.2 is to apply the results of the sensitivity and technical feasibility analyses to two mission types and identify potential

designs for presently available technology. The two mission types include a VLEO science craft whose mission is reliant on flying at the lowest possible altitude, and a modern version of a collector vehicle whose mission is to supply long range missions with as much propellant as possible. Studies of these two mission types are widely reported in the literature. Studying them in this work provides verification of the quality of the results from satisfying the first two research goals.

The first case study is the VLEO science mission. This mission is intended to repeat the measurements performed by GOCE with improved fidelity. Vehicle size is restricted to fit within a SpaceX Falcon 9 payload fairing, and the thruster employs solar power. Vibration requirements restrict the use of compression equipment, thus constraining the vehicle to be an air-breathing rocket. The objective of this case study is to identify the vehicle design which allows operation in the lowest stable orbit while providing global coverage at a constant altitude.

Case study two is a propellant depot which collects its payload on-orbit and provides it to vehicles at the beginning of their missions. The collector vehicle may employ nuclear power. Additionally, the collector vehicle must be capable of being lifted into orbit aboard a SLS Block II launch vehicle. This constrains not only the vehicle dimensions but also the reactor mass, which has been budgeted to no more than 60 percent of the launch mass. The vehicle must be placed into a 28.5° inclination orbit to facilitate direct rendezvous for missions launched from Cape Canaveral. The objective of this case study is to identify the design and orbit parameters which allow the collector vehicle to maximize the propellant collection rate while assuring the vehicle does not undergo unplanned reentry.

3.5 Conclusion

This chapter sets the mathematical foundation for this work. Section 3.1 begins with basic equations and derives the fundamental equations for propellant collection. These equations express the generated and required power as a function of the input design parameters, and form the basis of this work. Section 3.2 looks at the relationships between the input design parameters which is not captured by the initial high-level physics treatment in the prior section. In particular, the thruster efficiency depends on numerous other input parameters as a result of its dependence on required specific impulse, and thus on drag. This section also describes the ranges of each input parameter with justification to exclude large regions of physically impossible or improbable design space. Finally, this section details the mechanism for determining the time-average parameters determined to be factors in the fundamental propellant collection equations in Section 3.1. High-fidelity data is obtained from STK and then decimated and time-averaged over a period of one year to arrive at the time-average parameters. Chapter 4 discusses the results of this effort.

Section 3.3 provides the nominal baseline case parameters against which comparisons are made. These parameters represent presently available technology and baseline values of performance. Section 3.3 also presents the mathematics for the sensitivity analysis performed in this work. The propellant collection equations vary with a number of dissimilar parameters. Thus, the sensitivity is non-dimensionalized to permit comparison between them. This non-dimensionalized sensitivity is called the elasticity,

which is studied for each of the input parameters to the propellant collection equations. Chapter 5 presents the results of the sensitivity analysis.

The final section in this chapter presents the two case studies conducted in this work. These studies include a VLEO science mission and a propellant depot mission. Studies of these types have been widely reported in propellant collection literature. Conducting similar studies in this work verifies the quality of the results and demonstrates the benefit of this improved approach.

CHAPTER 4
SUMMARY OF TIME-AVERAGE PARAMETERS

Section 3.2.1 develops the methodology for building the time-average parameters used throughout the propellant collection performance equations derived in Chapter 3. This chapter reports how each of those parameters varies with the orbital test matrix given in Table 3 and is divided into two sections: density-independent parameters, and density-dependent parameters. This division is made because density experiences the greatest overall variation with orbit conditions which drives the value and trends of the density-dependent parameters.

4.1 Density-Independent Parameters

Four of the eight time-average parameters presented in Section 3.2.1 are not directly dependent on density: velocity, temperature, speed ratio, and solar viewing factor. The average velocity varies with the periapsis altitude and eccentricity as demonstrated in Figure 32. The variation with eccentricity presents the expected trend, with higher eccentricity resulting in a lower average velocity. Similarly, increasing periapsis altitude serves to reduce orbit velocity. As expected, Figure 33 shows negligible variation in velocity with inclination. The minor variation exhibited results from Earth oblateness.

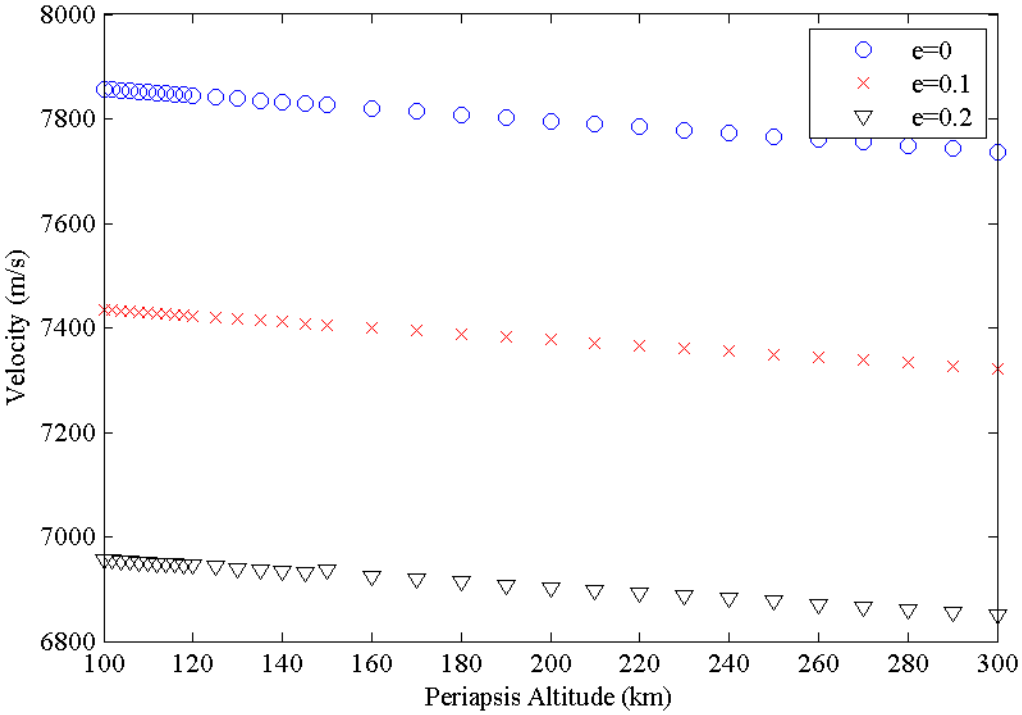

Figure 32. Average orbital velocity with varying periapsis altitude and eccentricity.

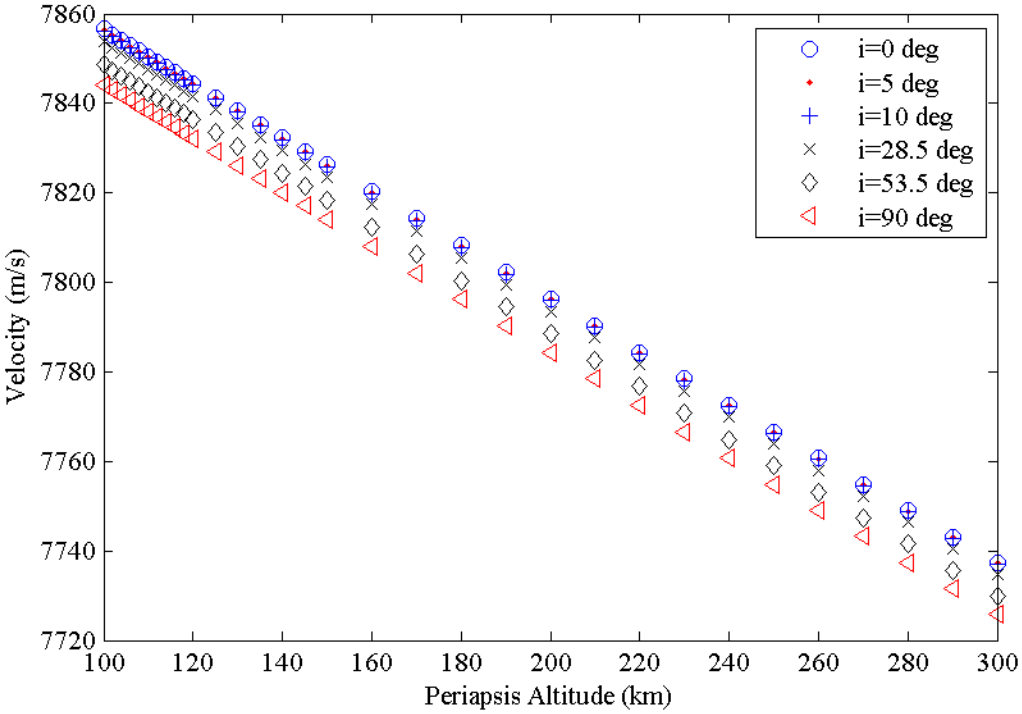

Figure 33. Variation of velocity with inclination for a range of periapsis altitude. As expected, variation with inclination is very small, on the order of 20 m/s.

The ambient temperature varies with altitude and solar activity because it is driven by solar radiation flux. Figure 34 demonstrates the variation with periapsis altitude

for different eccentricities averaged over the year 1996 for equatorial orbits. The expected altitude variation is present which can be seen to be the cause of the variation with eccentricity. Eccentric orbits make excursions out to higher altitudes, which leads them into higher temperature regions, thus driving up the average temperature.

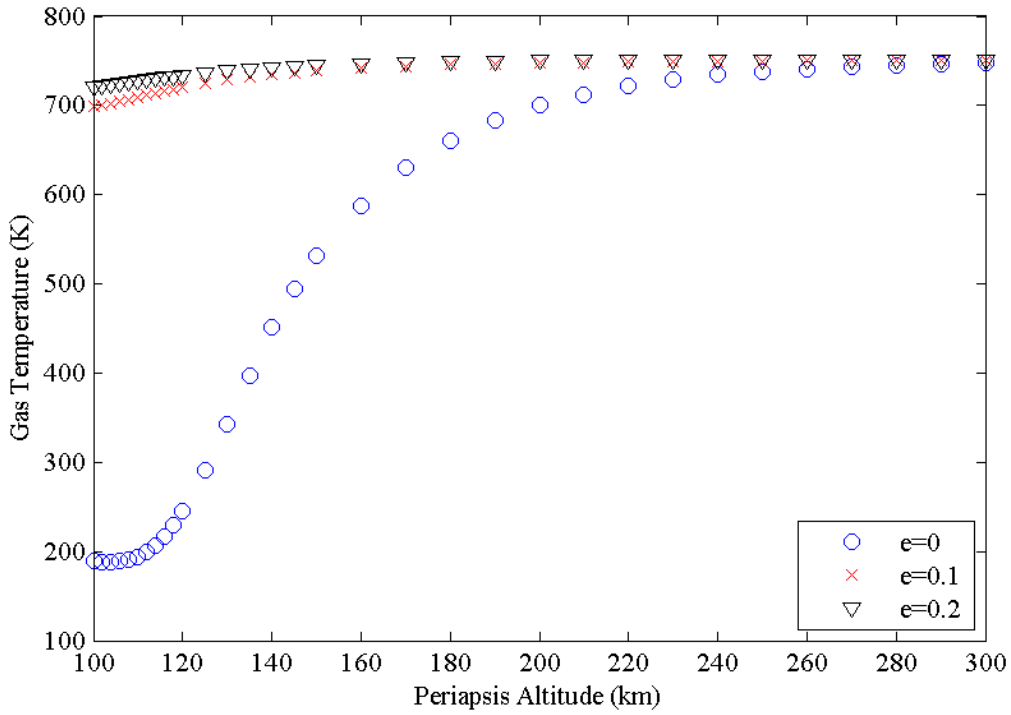

Figure 34. Variation of ambient temperature with altitude for three eccentricity cases. Data is averaged over the year 1996 for equatorial orbits. Note the expected large variation in temperature with altitude.

Figure 35 demonstrates variation of average temperature with inclination. Intuition based on experience on the ground says that, since orbits with higher inclination pass over higher latitudes, they should have lower average temperature. This is in fact the opposite of the trend revealed in Figure 35, indicating that the upper atmosphere does not share the behavior of the lower atmosphere.

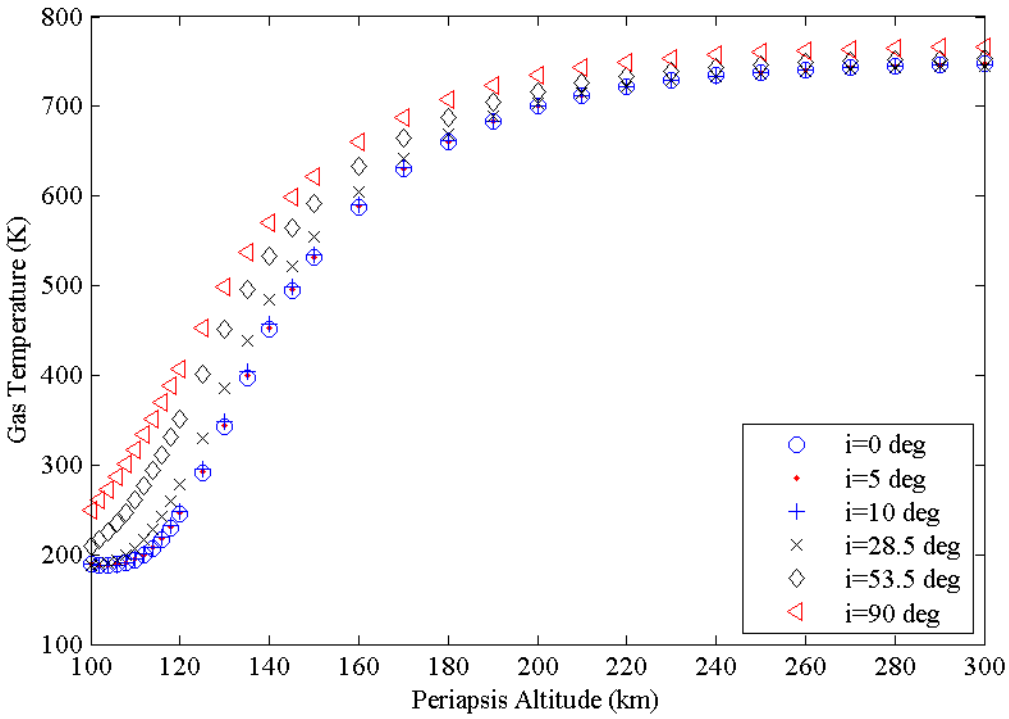

Figure 35. Variation of temperature with periapsis altitude and inclination. Data is averaged from the year 1996 for circular orbits. Increasing inclination serves to marginally increase average temperature, especially at lower altitudes.

Figure 36 demonstrates the expected variation of temperature with solar activity. Periods of high solar activity drive up the temperature in high altitude regions. This effect is less pronounced at low altitudes because lower altitudes have better access to the rest of the atmosphere for use as a heat sink.

As demonstrated in Eq. (3.39), the speed ratio is a function of both the orbital velocity and the temperature. It is worth mentioning that it is also slightly dependent on density as a result of the inclusion of the average gas constant term in the denominator, although this variation is far less pronounced than for the parameters which directly incorporate the density. Figure 37 demonstrates the variation of the speed ratio as a function of the periapsis altitude and eccentricity for the year 1996 and equatorial orbits. The variation in speed ratio is dominated by temperature effects, as seen by the dramatic

variation with eccentricity. This is despite Eq. (3.39), which shows that the speed ratio varies linearly with velocity and as the inverse square root of temperature. Temperature experiences larger overall variations as a result of changing orbit parameters which overrides the more sensitive, but smaller velocity variations.

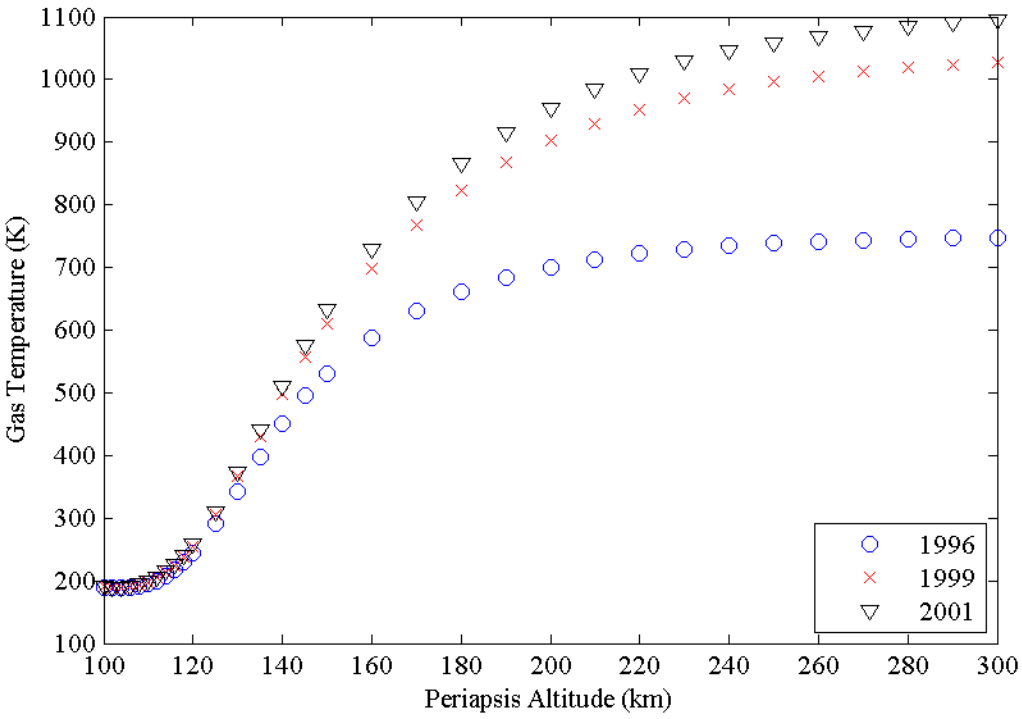

Figure 36. Variation of temperature with periapsis altitude and solar activity. Data is averaged for circular, equatorial orbits. As expected, increasing solar activity produces pronounced temperature increases in the upper atmosphere.

The reduction of speed ratio with increasing altitude as demonstrated by the circular orbit case in Figure 37 is corroborated by the results of other researchers which demonstrate drag coefficient increases with altitude [49]. Sentman's equations generally indicate an inverse relationship between speed ratio and drag, and thus predict that the drag coefficient should increase with decreasing speed ratio.

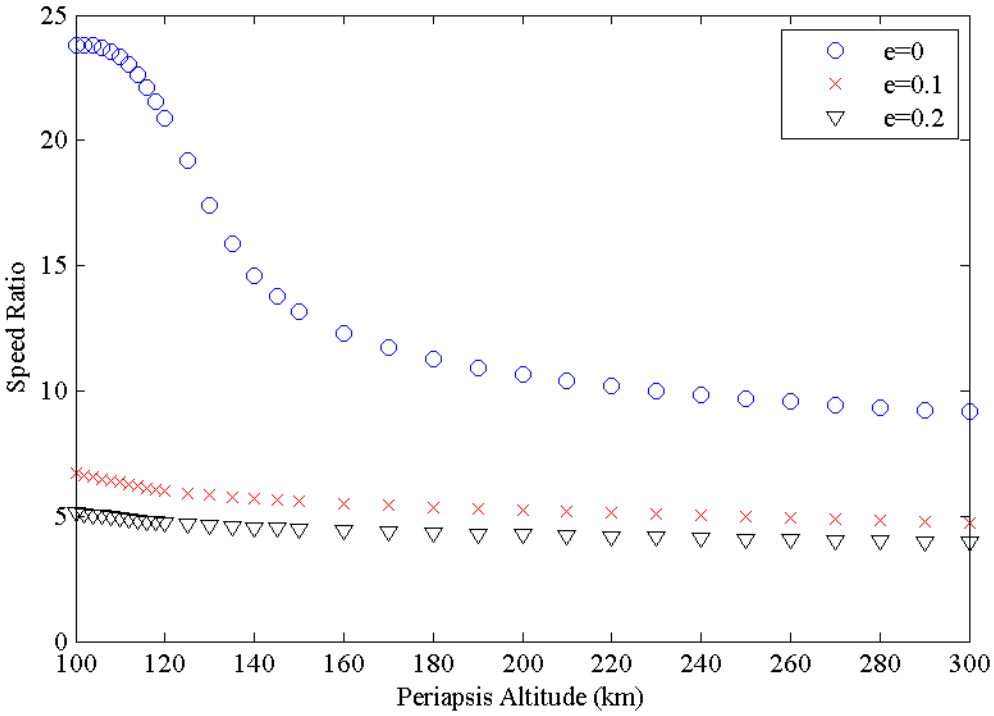

Figure 37. Variation of the speed ratio with periapsis altitude and eccentricity for the year 1996 and zero inclination. The temperature dominates the variation in speed ratio as demonstrated by the circular orbit case, with velocity producing a less pronounced effect.

The final density-independent time-average parameter used in this work is the solar viewing factor as derived in Section 3.1. To review, the average solar viewing factor is a measure of the average fraction of solar energy which is accessible to solar arrays and accounts for both eclipsing and cosine losses. It is thus a lumping of the geometrical loss terms in the calculation of solar power. The viewing factor exhibits the largest variation as a result of changing eccentricity or inclination, as demonstrated in Figure 38. Figure 38 reports the variation of solar viewing factor with eccentricity and periapsis altitude for equatorial orbits. The aforementioned behavior with respect to eccentricity is the result of the coupling of altitude and eclipsing, with higher orbits experiencing less eclipsing than lower orbits. Eccentric orbits make excursions away from the planet which reduces the effect of eclipsing.

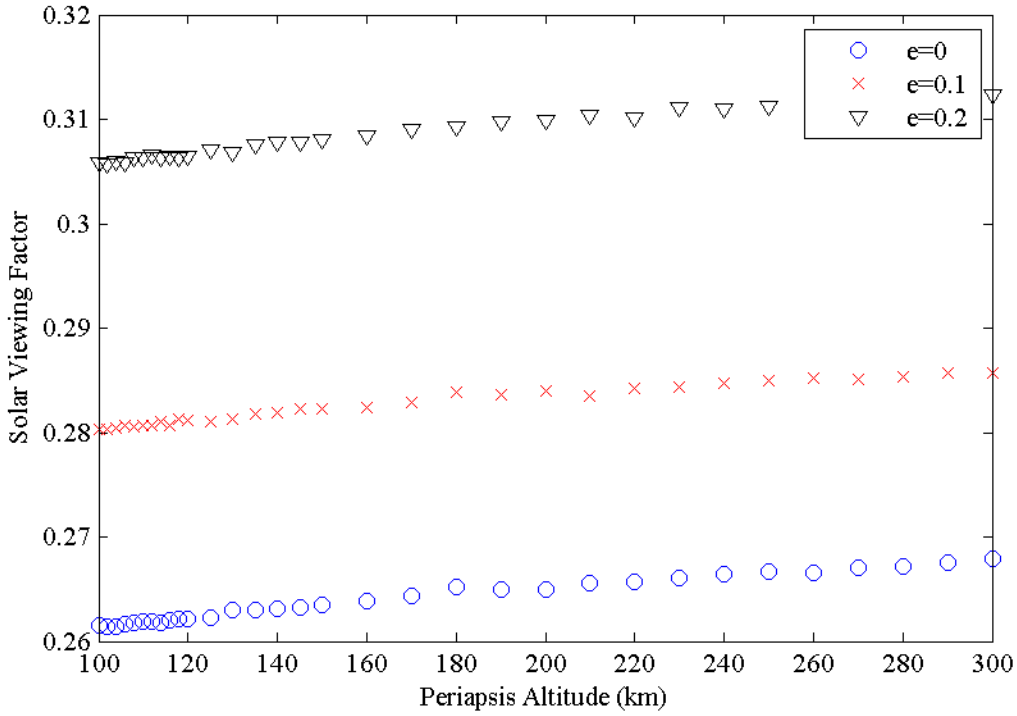

Figure 38. Variation of solar viewing factor with periapsis altitude and eccentricity for equatorial orbits.

A similar result is seen in Figure 39, this time for polar orbits. Polar orbits produce higher viewing factors than equatorial orbits as a result of orbit geometry under the attitude constraints developed in Section 3.1. The effect of increasing periapsis altitude on the viewing factor is especially pronounced for the polar circular orbit configuration which shows a linear 2 percent increase for 200 km of altitude rise. These results indicate that, for spacecraft in VLEO, the average solar viewing factor may vary from 25 to 45 percent. Peak average solar viewing factors can be attained by selecting a sun-synchronous orbit with high eccentricity, with increasing altitude providing a marginally smaller benefit.

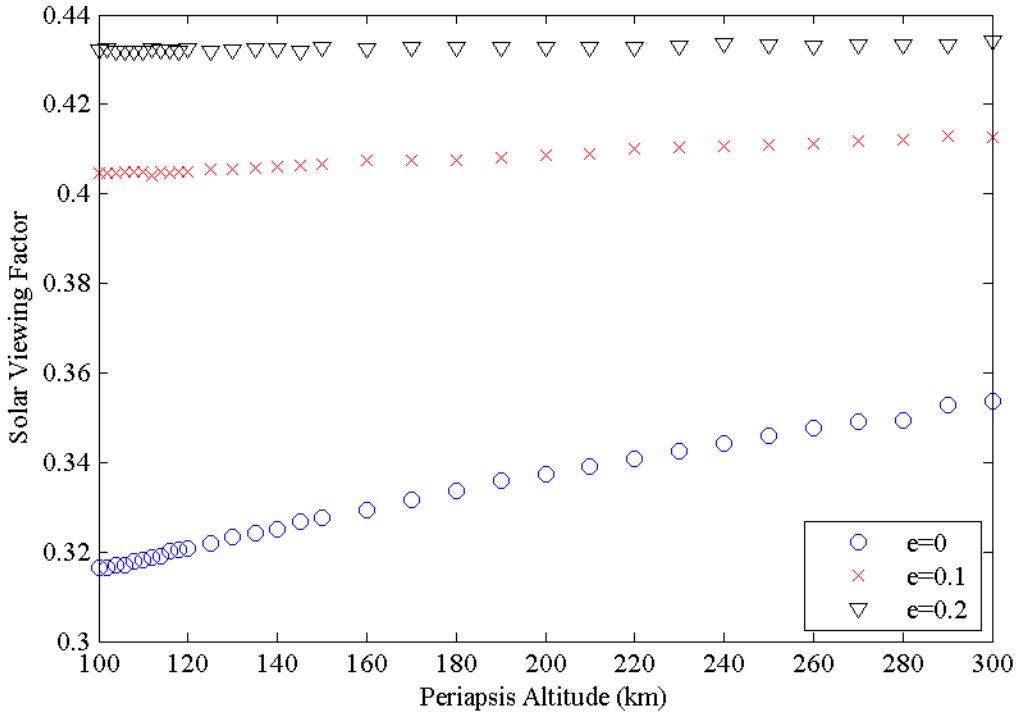

Figure 39. Variation of solar viewing factor with varying periapsis altitude and eccentricity for polar orbits. Note the larger values of viewing factor for polar orbits over equatorial orbits.

4.2 Density-Dependent Parameters

As stated in the introduction of this chapter, the density term in the density-dependent parameters drives the value and trends of these time-average parameters with respect to the orbit parameters. These time-average parameters include the area-specific mass flow rate, area-specific force, area-specific flow energy, and area-specific compression energy.

Figure 40 presents the variation of the mass flow rate term with periapsis altitude for each of the three years considered, for zero inclination and zero eccentricity. The exponential variation in density with altitude dominates the behavior of all three curves, with the flow rate at 100 km altitude reaching as high as 60 g/m^2-s and as low as 0.1 mg/m^2-s at 300 km. Recalling back to Section 3.2.1, the year of 1996 represents the minimum of the solar cycle while 2001 represents the maximum of the solar cycle. The

mass flow rate at low altitudes is unchanged by variation in year, while at higher altitudes it can vary by approximately 50 percent between minima and maxima years.

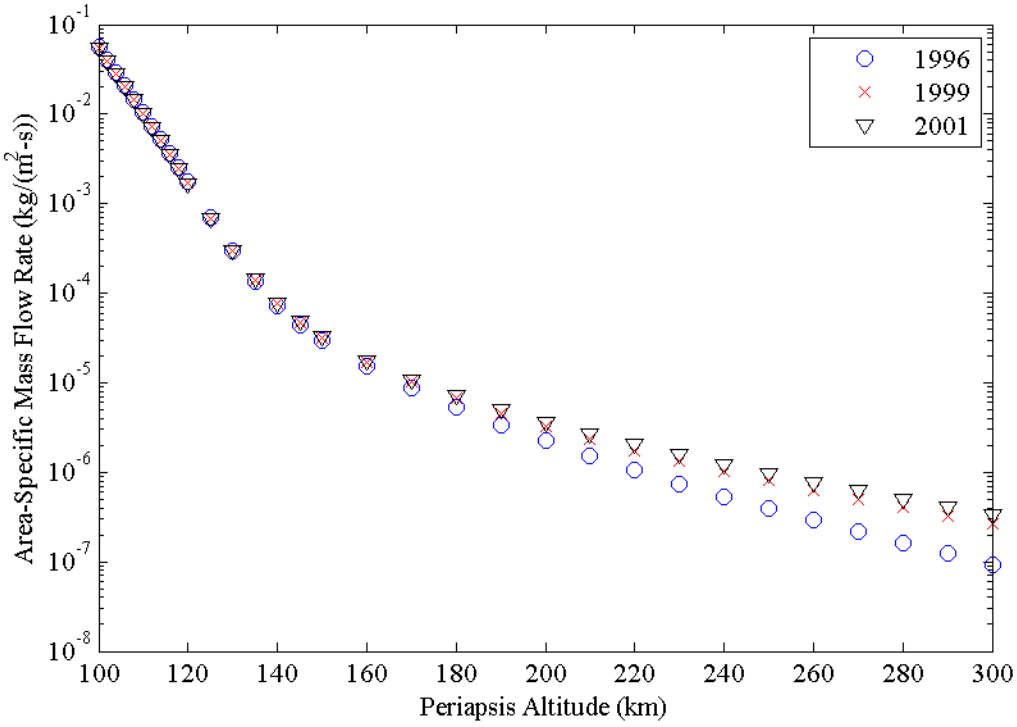

Figure 40. Variation of the mass flow rate term with periapsis altitude for three years. The orbit is taken to be equatorial and circular. The largest variation with solar activity is seen at the high range of altitudes considered.

Although less dramatic than altitude, the mass flow rate term also varies with inclination as indicated in Figure 41. This figure plots data for the year 1996 and zero eccentricity. The variation is noticeable at all altitudes and can account for as much as an order of magnitude change in mass flow rate between equatorial and polar orbits. The area-specific mass flow rate appears to decline with increasing inclination, which implies that lower altitudes may be reached with propellant-collecting vehicles by operating in polar orbits rather than equatorial orbits. This is further supported by the results of the previous section for solar viewing factor, which indicates that propellant-collecting vehicles also gain better access to sunlight when operating in polar orbits.

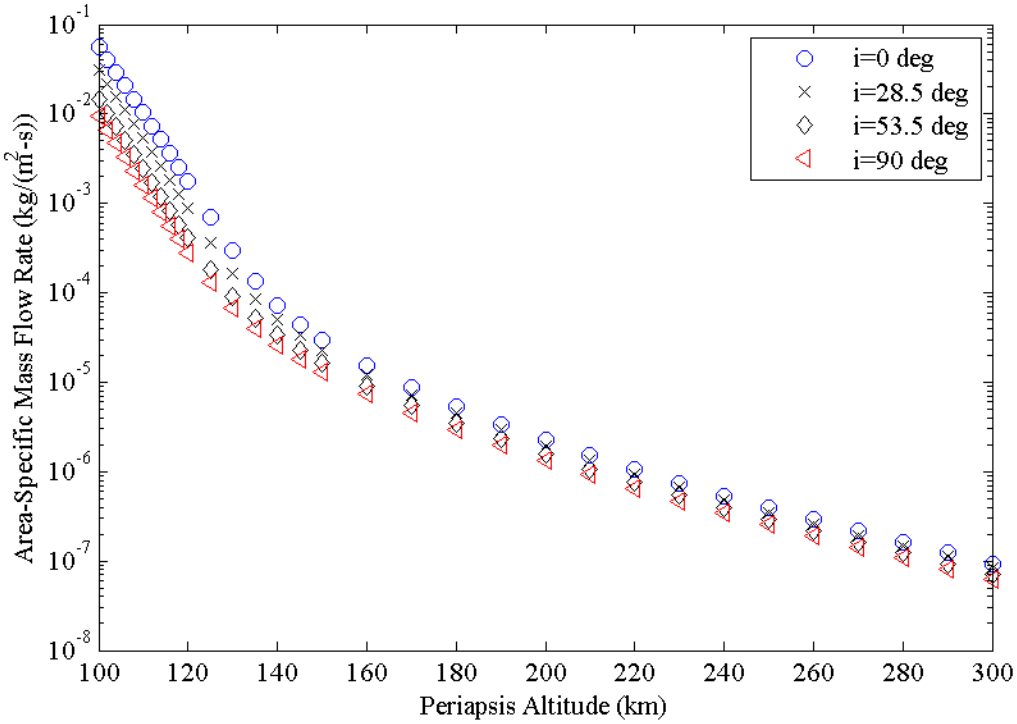

Figure 41. Variation of mass flow rate term with altitude for different inclinations. Data is averaged over the year 1996 for circular orbits.

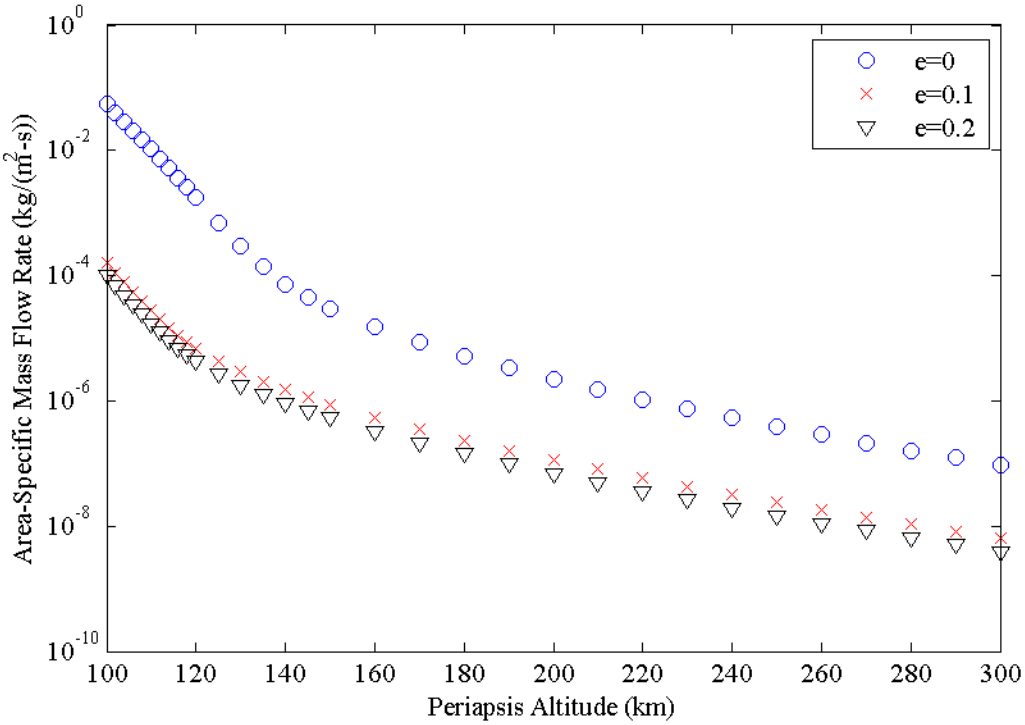

Figure 42. Area-specific mass flow rate with varying periapsis altitude and eccentricity. Data is averaged over the year 1996 for equatorial orbits.

Figure 42 demonstrates that eccentricity is second only to altitude in is effect on the density-dependent parameters. This figure plots data for the year 1996 at zero inclination. Changing eccentricity from 0.0 to 0.2 results in a reduction in mass flow rate by a factor of a thousand at 100 km periapsis altitude. This result occurs because eccentric orbiting craft spend considerable time at higher altitudes when compared with circular orbits at the same periapsis altitude. At 300 km, the area-specific mass flow rate reaches as low as ~1 μg/m^2-s: a full 8 orders of magnitude difference from the highest mass flow rates calculated in this work.

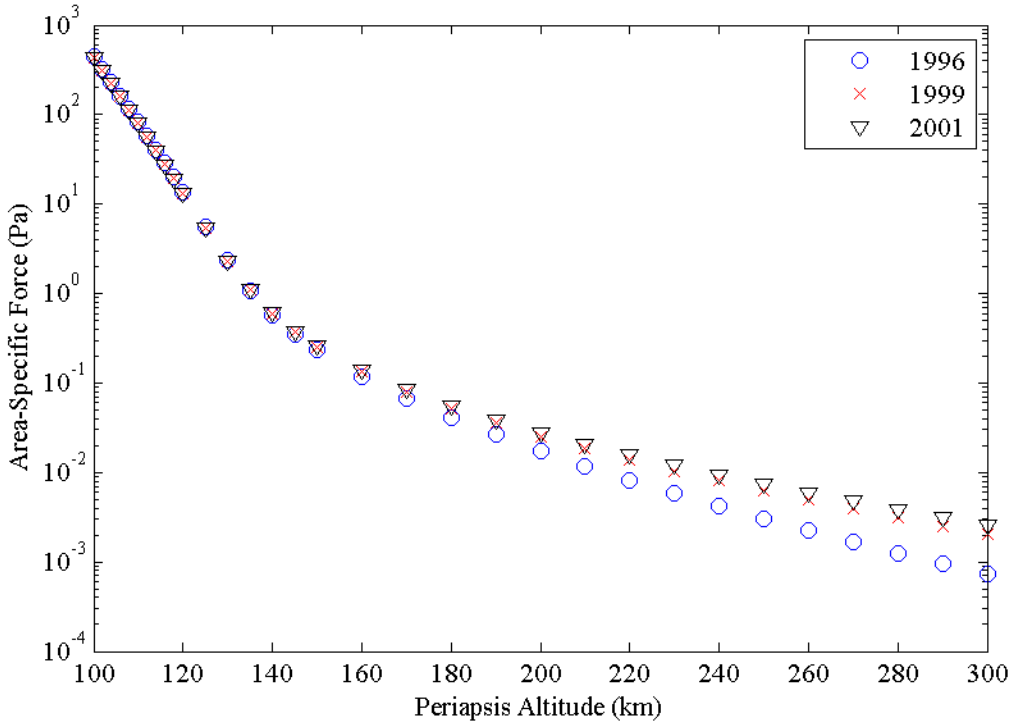

Figure 43. Area-specific force with varying periapsis altitude and year. Orbits are equatorial and circular.

The area-specific force is a measure of the momentum transfer the flow makes to the vehicle as demonstrated by its prevalence in the Eq. (3.2). Figure 43 demonstrates that similar behaviors exist for the area-specific force as for the mass flow rate. This figure plots the force as a function of altitude with varying year, zero inclination and zero

eccentricity. At 100 km, the force reaches as high as 400 Pa, while it is as low as 1 mPa at the higher altitude required for circular, equatorial orbits. Despite the squared velocity term, the variation in density still drives the value of the force. Note that both this term and the mass flow rate term appear to be insensitive to solar activity at low altitudes, suggesting that the physics of propellant collection becomes insensitive to solar activity when sufficiently low orbits are selected.

The area-specific flow energy represents the amount of energy contained in the oncoming flow. This is an important parameter for ramjet-type designs. Figure 44 demonstrates the variation of this parameter with altitude for three different values of eccentricity over the year 1996 at zero inclination. Flow energy varies exponentially with periapsis altitude as expected from the first two density-velocity products, but does so with less overall change in magnitude. The presence of the cubed velocity term dampens the effect of the density component because higher eccentricity orbits have higher velocity at periapsis. This drives up the flow energy despite the fact that more time is spent in lower density regions of the atmosphere.

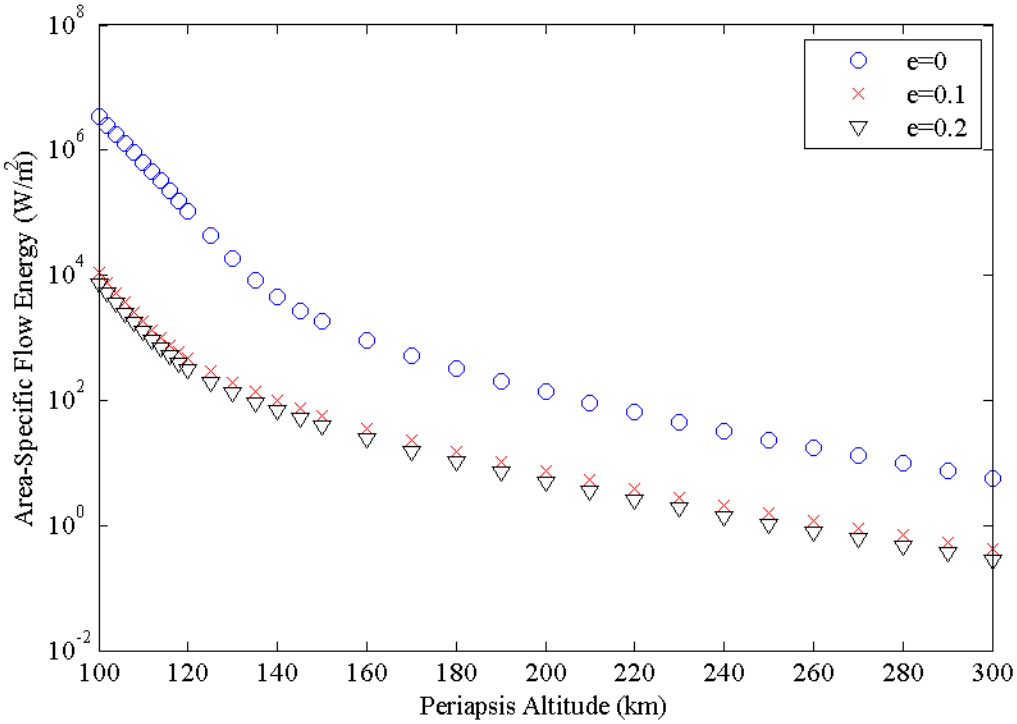

Figure 44. Flow energy with varying periapsis altitude and eccentricity. Data is averaged for the year 1996 and equatorial orbits. Note the reduced variation when compared to the mass flow rate term.

The final density-dependent time-average term is the area-specific compression energy. This term represents the ideal energy required to compress the oncoming flow for storage. As expected, the compression energy presents the same behavior with respect to periapsis altitude as the other density-dependent terms. Figure 45 demonstrates this variation for different values of inclination averaged over the year 1996 for circular orbits. The absolute magnitude of this term varies by an order of magnitude with varying inclination. Even so, a perfect compressor in a 100 km circular, polar orbit in a solar minimum year requires 6 kW/m^2 of continuous power to compress all of the incoming flow. This power requirement is likely beyond the capability of solar power generation.

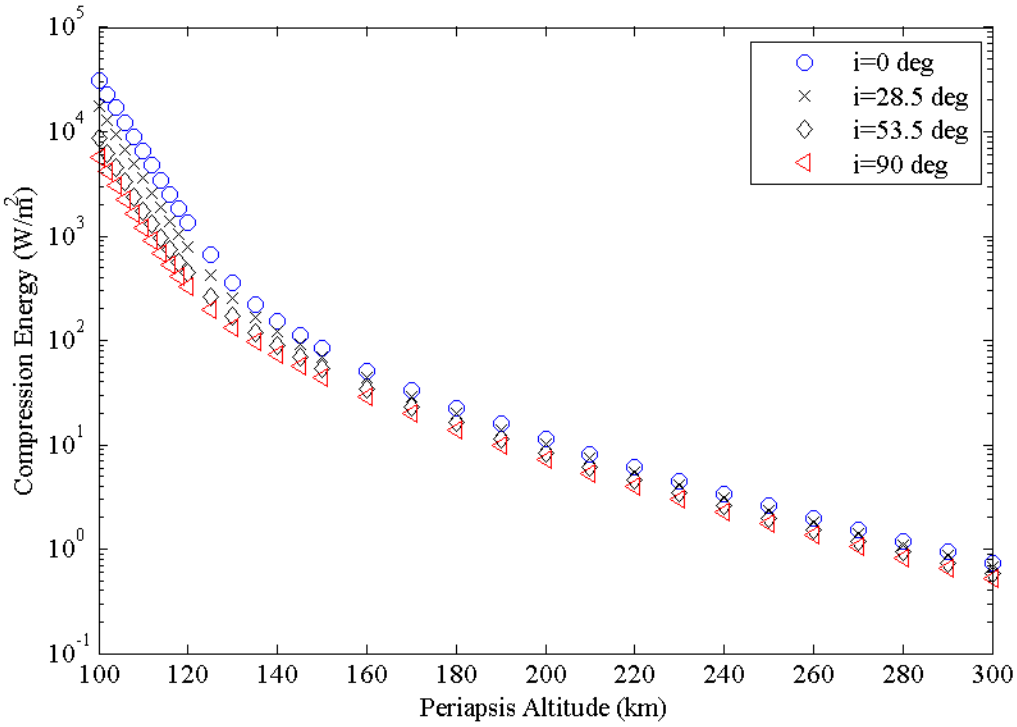

Figure 45. Compression energy with varying periapsis altitude and inclination for the year 1996 and circular orbits. This term represents the power required by an ideal compressor working on all of the oncoming flow.

4.3 Summary

This chapter demonstrates the variation of the time-average parameters derived in Chapter 3 with orbit conditions. The density-dependent parameters all exhibit a notable exponential relationship with periapsis altitude which is expected given the exponential relationship density has with altitude as demonstrated in Figure 3. The density-dependent parameters indicate that the flow rates, forces, and energies grow dramatically at low altitudes, perhaps beyond the ability of spacecraft to overcome.

Some variation with inclination also occurs, with higher inclination orbits generally having smaller values than equatorial orbits. Similarly, increasing eccentricity serves to reduce the magnitude of density-dependent terms by sending the orbit out to higher average altitudes. For a propellant-collecting spacecraft designed to minimize the

value of the density-dependent parameters without varying altitude, one should select an orbit with high inclination and eccentricity.

Solar activity also presents variation in the density-dependent terms, as expected. The solar cycle cannot be avoided, thus propellant collection spacecraft designers should consider the maximum solar activity condition rather than the nominal solar activity. Alternatively, they may develop procedures to alter the orbit parameters in response to changing solar activity.

The density-independent parameters exhibit far less variation with altitude and far less variation overall when compared with the density-dependent parameters. Compared with density, the average orbital velocity changes only slightly with orbit parameters for any of the VLEO cases studied in this work. For propellant-collection spacecraft design, velocity may be effectively treated as a function only of eccentricity without appreciable loss in fidelity. Like density, temperature does exhibit variation based on not only inclination and altitude, but solar activity as well. As stated for the density-dependent terms, spacecraft designers should consider the temperature at the peak of the solar cycle in order to accurately estimate the speed ratio, and thus the drag coefficient of a design.

Average solar viewing factor is an important parameter for solar-powered designs. The data presented in this chapter suggests that this function can be designed through smart selection of orbit parameters. A design which seeks to maximize solar viewing factor for a given altitude should seek the large inclination and eccentricity. As stated in Section 3.2.1, the data presented in this chapter is the result of averaging raw data from STK which was decimated down to one orbital period every five days. This simplification made the calculations tractable with the resources available, but it remains

to be seen how much fidelity is sacrificed in the process. Table 8 indicates the accuracy of the decimated values against the non-decimated values for the 100 km, zero inclination and zero eccentricity orbit of 1996. The results indicate the decimated averages produce results which lie within 0.2% of the non-decimated averages, which is of sufficient accuracy for this work.

Table 8. Accuracy of calculations performed with decimated data. Each of the time-average parameters varies from the non-decimated averages by 0.2% or less. Data from calculation for year 1996, 100 km, circular, equatorial orbit.

Parameter	Decimated Value	Non-decimated Value	% Difference
$\overline{v}$	7,856.6 m/s	7,856.6 m/s	0.00
$\overline{\rho v}$	0.0560 kg/m^2-s	0.0559 kg/m^2-s	0.18
$\overline{\rho v^2}$	440.0993 Pa	439.7317 Pa	0.08
$\overline{\rho v^3}$	3.4613 MW/m^2	3.4584 MW/m^2	0.08
$\overline{RT_{gas} \ln\left(\frac{p_2}{p_1}\right) \rho v}$	31.208 kW/m^2	31.146 kW/m^2	0.20
$\overline{f}$	0.2615	0.2617	0.08
$\overline{T_{gas}}$	189.9133 K	189.8522 K	0.03
$\overline{s}$	23.7732	23.7749	0.007

CHAPTER 5
SENSITIVITY ANALYSIS RESULTS

This chapter presents the results of the sensitivity analysis performed on the governing equations for propellant collection derived in Chapter 3. Section 3.3 outlines the method for conducting the sensitivity analysis. This chapter divides the sensitivity analysis into two sections. Section 5.1 presents and discusses the results of the sensitivity analysis for the power generation equations. Section 5.2 presents and discusses the results of the sensitivity analysis for the required power equations for each of the propellant collection architectures.

5.1 Generated Power

Eqs. (3.21) and (3.31) in Section 3.1 present the power generation capability of a propellant-collecting spacecraft under the assumptions discussed in Chapter 3 as a function of the performance parameters of the power system and the planform area-to-body area ratio. In Eq. (3.21), the time-average area-specific solar power $\overline{P''}_{SP}$ is shown to be a function of the time-average solar viewing factor $\overline{f}$, the solar panel efficiency η_{SP}, and the area ratio $A_{SP}/A_{s/c}$.

The elasticity of the solar power with respect to the panel efficiency and the area ratio is easily determined analytically by applying Eq. (3.48) and found to be one. The orbit parameters of periapsis altitude, eccentricity, and inclination also contribute to the value of the solar viewing factor. However, they do so in a manner which is not easily prescribed in an analytical way, and thus the elasticity of the solar power with respect to the orbit parameters is determined numerically. Figure 46 plots the elasticity with respect

to each of the parameters. The abscissa plots the normalized domain of the parameter of interest while the ordinate plots the elasticity of the solar power with respect to that parameter. The area ratio is studied over the range [0, 100], the solar panel efficiency over the range [0.268, 0.682], and the orbit parameters over the test matrix provided in Table 3.

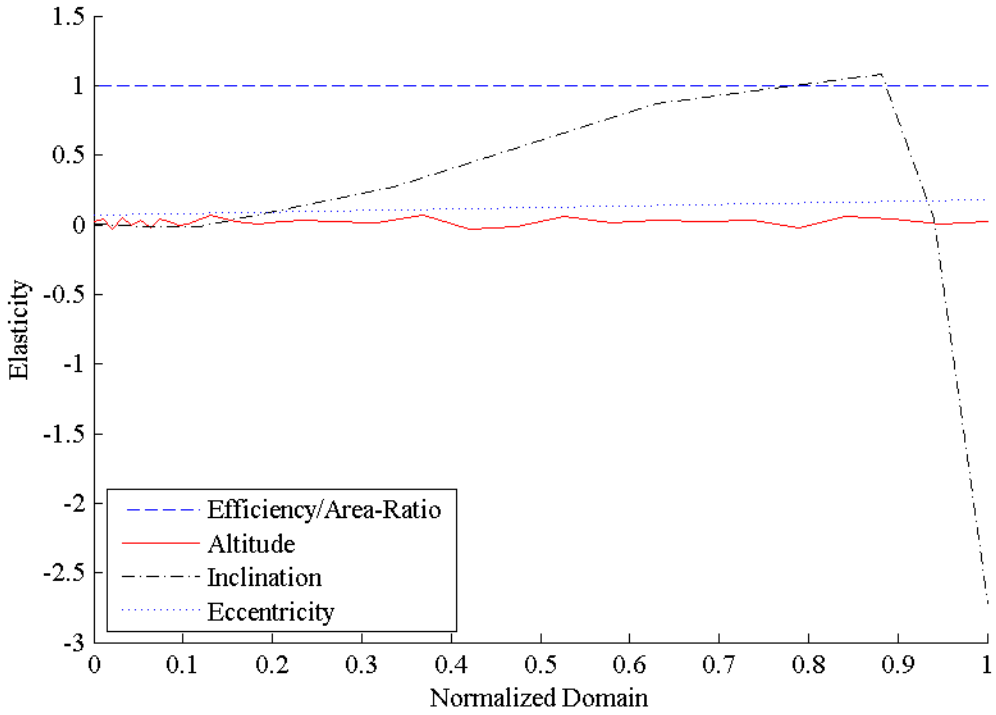

Figure 46. Elasticity of the time-average area-specific solar power. The abscissa plots the normalized domain of each parameter as given in the text, and the ordinate plots the elasticity as derived in Eq. (3.48).

The results of this analysis indicate that the solar power is insensitive to the selection of periapsis altitude and eccentricity, with both displaying only a slightly positive elasticity. Altering inclination has a far more dramatic effect on the performance of a solar power system over the range of orbit parameters studied. Solar power is insensitive to inclination near zero inclination, but displays a positive elasticity for mid-range values. Crossing over at zero near the edge of the normalized domain indicates that

a slightly sub-polar orbit, likely a sun-synchronous orbit, is optimal for maximizing solar power. Recalling from Section 3.2.1, sun-synchronous orbit inclinations are not specifically targeted in this section of the work. The inclination for sun-synchronicity is a function of the other orbital parameters and its inclusion would thus impact the consistency of the inclination data points at high inclinations.

As can be analytically determined from applying Eq. (3.48) to Eq. (3.21), the elasticity of solar power with respect to both panel efficiency and area ratio is exactly one. This result demonstrates the anticipated linear relationship between solar power and the design parameters of the solar array.

Eq. (3.31) demonstrates that the nuclear electrical power $\overline{P''}_e$ is a function of the radiator temperature T_R, the thermal efficiency η_R, radiator emissivity ε, and the area ratio. In the case of radiator temperature, Eq. (3.47) further shows that it is a function of both the thermal efficiency and the core temperature T_c. Thus, the elasticity of the nuclear electrical power is a simply analyzed by applying Eq. (3.48) to each parameter.

Figure 47 plots the results of the elasticity analysis of the nuclear electrical power. Thermal efficiency is studied over a range of [0.2, 0.3] and the elasticities for the other parameters are all constant. Core temperature dominates the design of nuclear systems for propellant-collecting craft with an elasticity of four. Increasing core temperature dramatically improves the heat rejection performance of the radiator, which couples the performance of the nuclear system to the overall performance of a propellant-collecting vehicle. With lesser effect, the emissivity and area ratio both have constant elasticity equal to one which denotes a directly proportional relationship between nuclear electrical power and these parameters.

Finally, thermal efficiency has the smallest impact on the electrical power over the range studied, and its elasticity crosses through zero. This suggests that there is an ideal thermal efficiency for a nuclear system from a radiator perspective which is not necessarily the maximum attainable efficiency. Specifically, the ideal thermal efficiency is demonstrated analytically to be 25 percent. This effect results from the thermal efficiency's tendency to lower the radiator temperature. Reducing the temperature is seen to have a far more significant impact on the radiation performance than the modest increase in net electrical power generation from increasing the efficiency affords.

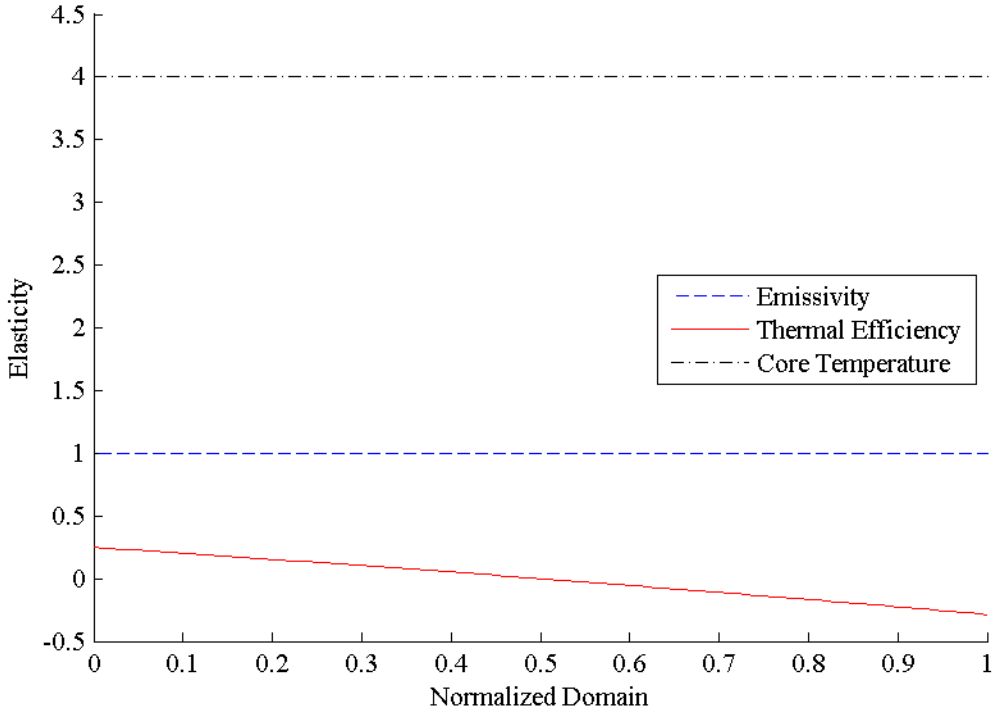

Figure 47. Elasticity of the area-specific nuclear electrical power with respect to the emissivity, thermal efficiency, and core temperature.

5.2 Required Power

Eqs. (3.33)-(3.37) at the end of Section 3.1 are the required power equations for each type of propellant-collecting architecture. Numerous parameters contribute to the required power in different ways depending on the vehicle. Furthermore, many of these

parameters have implicit coupling with one another as demonstrated in Section 3.2. The implicit relationships between the parameters make analytical determination of the elasticities impractical. They are thus determined numerically from the baseline case data as provided in Table 7. The following figures plot the elasticity of each of the parameters with which the required power is dependent upon. The abscissa axis plots the normalized domain of each parameter studied, where zero is the minimum value studied and one is the maximum value studied. To review from Section 3.2:

- Collector Efficiency and Usage Ratio vary from zero to one
- Compressor Efficiency varies from 0.01 to 0.1
- Thruster Efficiency varies from Eq. (3.46) to Eq. (3.45)
- Body Drag Coefficient varies from Eq. (3.40) to Eq. (3.42)
- The orbital parameters vary over the test matrix described in Table 3

Figure 48 plots the elasticity results for the case of the Air-Breathing Rocket. The elasticity of the required power with respect to the body drag coefficient is nearly constant over the range of studied drag coefficients with value slightly less than one. At first glance of Eq. (3.33), one might expect the elasticity to be near two. However, the drag coefficient also affects the thruster efficiency by varying the specific impulse. This implicit relationship drives down the order of the response of the required power to the drag coefficient. Additionally, the presence of the planform term reduces the elasticity by adding a term to the required power which is independent of the body drag coefficient.

The elasticity with respect to the collector efficiency is also affected by thruster efficiency dependence. At the low range of collector efficiency, the elasticity is flat at negative one, indicating an inverse linear relationship. The low collector efficiency in this range serves to restrict most of the oncoming flow from use by the thruster, which drives up the required specific impulse and thus the thruster efficiency. However, the model used in this work restricts the thruster efficiency above 9,500 seconds to a flat 0.3699, effectively removing the implicit thruster efficiency relationship. Beyond a collector efficiency of 0.15, the elasticity increases due to the rising influence of the thruster efficiency. Raising collector efficiency provides the thruster with higher mass flow which reduces the required specific impulse and thus the attainable thruster efficiency.

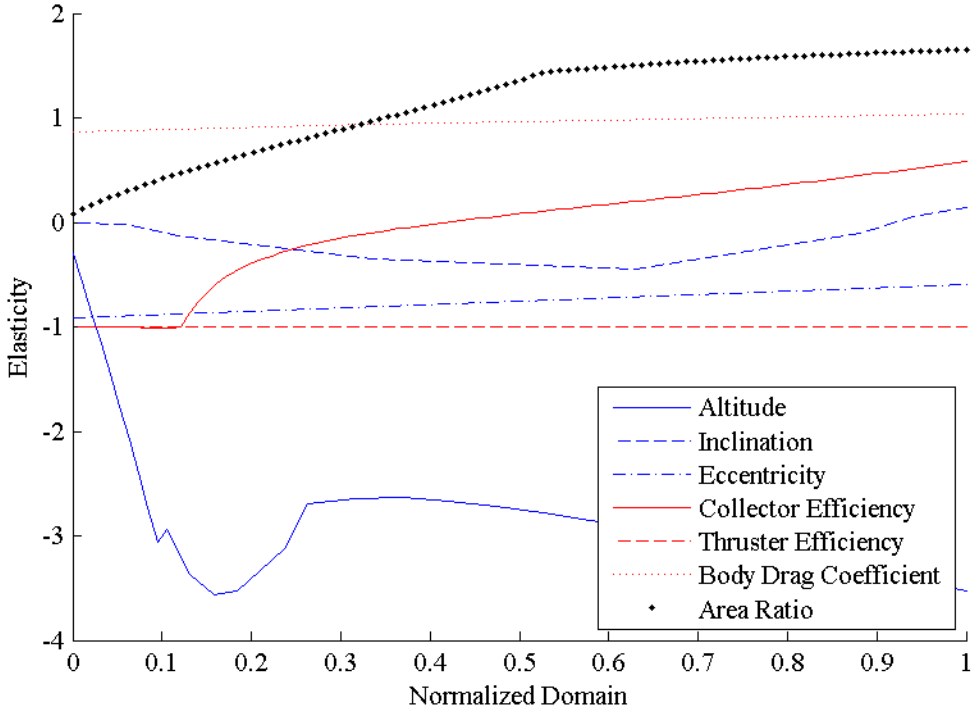

Figure 48. Elasticity of the required power for an air-breathing rocket with respect to the input parameters.

For this particular case, the elasticity crosses zero at ~0.45. This suggests that there exists an optimum portion of the flow used to generate thrust while minimizing

power. At higher collector efficiencies the decreasing thruster efficiency serves to drive up the required thrust power because more of the thrust power must be devoted to ionizing the flow rather than accelerating it. Smart design may avoid this result by restricting the flow into the thruster for higher collector efficiency designs. It is worth noting however that 0.45 is very near the maximum collector efficiency reported by McGuire and Fujita independently [44, 79].

The thruster efficiency itself does not affect any of the other input parameters of the required power equation, and thus its elasticity is shown analytically to be equal to negative one for the air-breathing rocket case. The result seen in Figure 48 confirms this numerically. Improving the thruster efficiency through improvements in thruster design linearly affects the required power for this propellant-collecting architecture.

As expected, the required power has positive elasticity with respect to area ratio, which indicates that the required power increases for increasing area ratio. Like the drag coefficient, at first glance it appears the value of the elasticity should be in the area of two as a result of the quadratic area ratio term. However, the area ratio also implicitly contributes to the determination of the thruster efficiency. Increasing area ratio forces specific impulse to also increase in order to accommodate the increase in planform drag. This in turn increases the thruster efficiency. The kink in the area ratio elasticity occurs for the case where the thruster efficiency has reached its maximum modeled value of 0.3699. As area ratio increases, the planform component of drag begins to dominate over the body-component. This explains the more gradual increase in elasticity tending toward two as area ratio continues to rise beyond the fixed thruster efficiency point.

The required power has negative elasticity with respect to eccentricity and inclination which results from the effect of these two orbit parameters on the density-dependent terms from Chapter 4. Increasing inclination and eccentricity generally serves to reduce the magnitude of the density-dependent terms, thus directly affecting the required power. As expected, the required power has a highly negative elasticity with respect to periapsis altitude which results from the high order of dependency between altitude and density. Periapsis altitude thus appears to be the single most important consideration for an air-breathing rocket design.

Figure 49 plots the elasticity of the diverter rocket required power with respect to the input parameters. Careful examination of both Figure 48 and Figure 49 reveals some differences in elasticity for select parameters. The elasticity with respect to the body drag coefficient appears to increase slightly for the diverter rocket case over the air-breathing rocket case. This is the result of the presence of the usage ratio and its effect on thruster efficiency. The usage ratio reduces the mass flow rate to the thruster which serves to shift the thruster efficiency and thus alter the coupling with the drag coefficient.

This upward shift in thruster efficiency and specific impulse also explains the changes in the elasticity with respect to collector efficiency. The collector efficiency elasticity departs from its initial thruster efficiency-limited value of negative one at a higher value than for the air-breathing rocket. Similarly, it crosses zero at a higher value as well. Diverting some flow to storage reduces the rapidity with which increasing collector efficiency reduces required specific impulse, thus reducing the rate at which thruster efficiency declines. Thruster efficiency itself becomes less important to the required power for a diverter rocket because of the introduction of the compression

power term. This drives a slight decline in the elasticity of the required power with respect to thruster efficiency when compared with the air-breathing rocket case.

Compressor efficiency is unimportant to the required power for the diverter rocket at the stated baseline case studied. It remains relatively constant near zero across the entire range of compressor efficiency studied. This result indicates that the required power is dominated by the thrust term rather than the compression term.

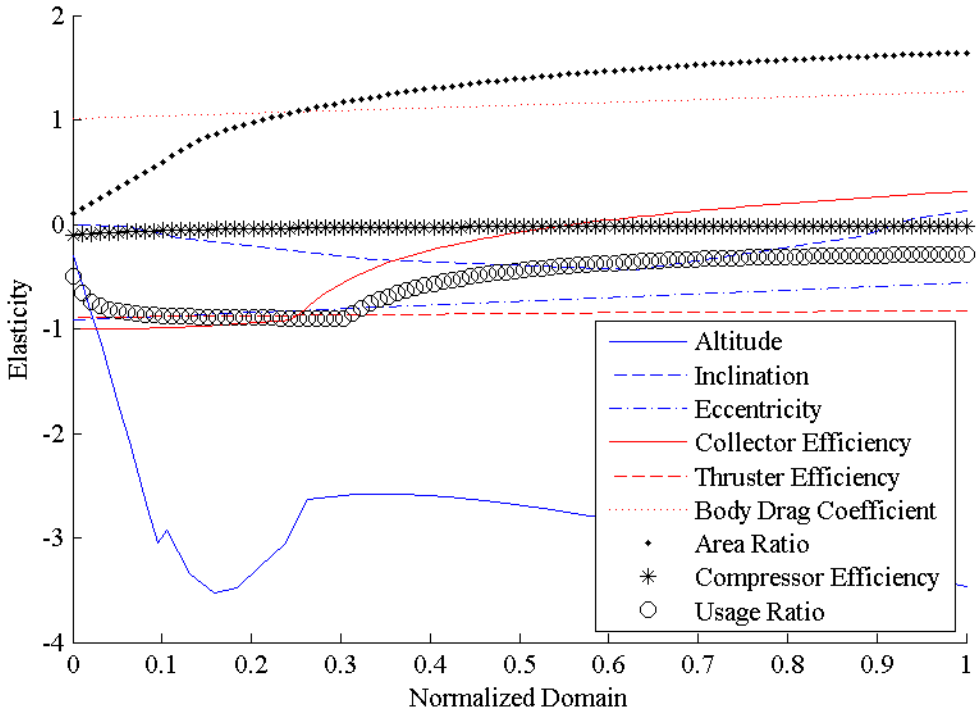

Figure 49. Elasticity plot for the diverter rocket required power equation. Note the inclusion of the compressor efficiency and usage ratio curves.

The elasticity with respect to usage ratio demonstrates a complex behavior which is divisible into three regimes. Near zero, the compression term dependence of the usage ratio dominates because the thruster efficiency is fixed at the model limit. This occurs because almost no flow is available to the thruster for low usage ratios. The elasticity flattens out at negative one as usage ratio increases due to the thruster efficiency remaining fixed as the compression power and thrust power diverge. The behavior of the

usage ratio after the specific impulse drops below the model limit is analogous to that of the collector efficiency. Increasing usage ratio increases the mass flow to the thruster, reducing the required specific impulse and thus the thruster efficiency.

The final parameter with notable differences is the area ratio. The elasticity for the area ratio kinks earlier for the diverter rocket than for the air-breathing rocket due to the aforementioned shift upward in thruster efficiency caused by the usage ratio. Elasticity with respect to periapsis altitude, inclination, and eccentricity does not appear to vary between the air-breathing rocket and diverter rocket architectures.

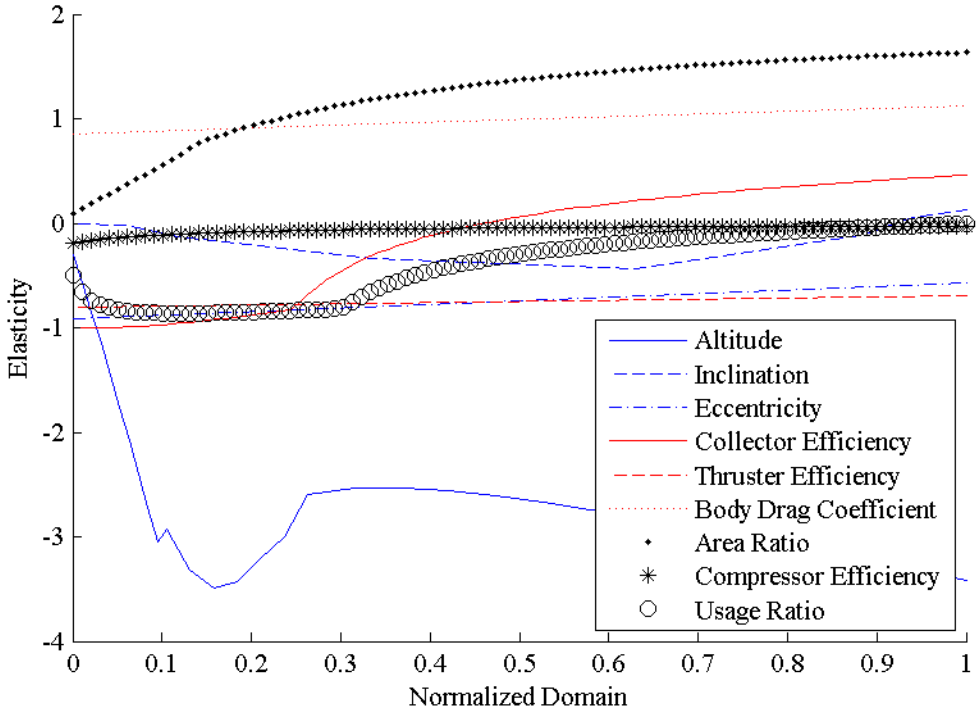

Figure 50. Elasticity plot for the collector rocket required power equation.

Figure 50 shows the elasticity of the required power for the collector rocket architecture with respect to the input parameters. Elasticity with respect to the drag coefficient is smaller for the collector rocket than the diverter rocket as a result of the increased importance of the compression power term. The compression power term is

more important for the collector rocket because all of the oncoming flow is compressed, contrasting with the diverter rocket where only the stored flow is compressed. Compressing all of the collected flow also leads to a minor change in the magnitude of the compression efficiency elasticity, although the required power remains insensitive to it. Thruster efficiency is also affected by this change in behavior. As the relative size of the compression term increases, the magnitude of the elasticity with respect to thruster efficiency decreases.

The elasticities with respect to the collector efficiency and usage ratio both rise faster for the collector rocket than for the diverter rocket. The relative importance of the usage ratio decreases as a result of its removal from the compression term, thus driving the usage ratio elasticity toward zero for smaller values of usage ratio. Increasing the mass flow rate into the compressor also drives up the compressor power, which leads to the aforementioned rise in collector efficiency when compared with the diverter rocket.

Figure 51 plots the elasticity of the required power for an air-breathing ramjet as a function of the input parameters. Like the addition of a compressor term in the diverter and collector rocket cases, the ramjet introduces terms which are independent of the body drag coefficient. This serves to reduce the elasticity of the required power with respect to the body drag coefficient as demonstrated by comparing Figure 48 and Figure 51. The only other parameter whose elasticity deviates from the air-breathing rocket case is the collector efficiency term. The collector efficiency elasticity initially behaves similar to the air-breathing rocket case at low values, but its behavior changes as it approaches one.

Specific impulse remains somewhat high when compared with the air-breathing rocket case due to the addition of the second term in the ramjet required specific impulse

equation, Eq. (3.17). This keeps the thruster efficiency from declining as severely as in the air-breathing rocket case. The ultimate cause for the inflection point in the collector efficiency elasticity however is the dramatic reduction in drag with increasing collector efficiency. Recalling Eq. (3.41), γ_c is zero for the air-breathing ramjet case. Consequently, as the collector efficiency increases, the portion of the flow which contributes to spacecraft-body drag declines. At one, the only contribution to the body drag coefficient is from skin friction.

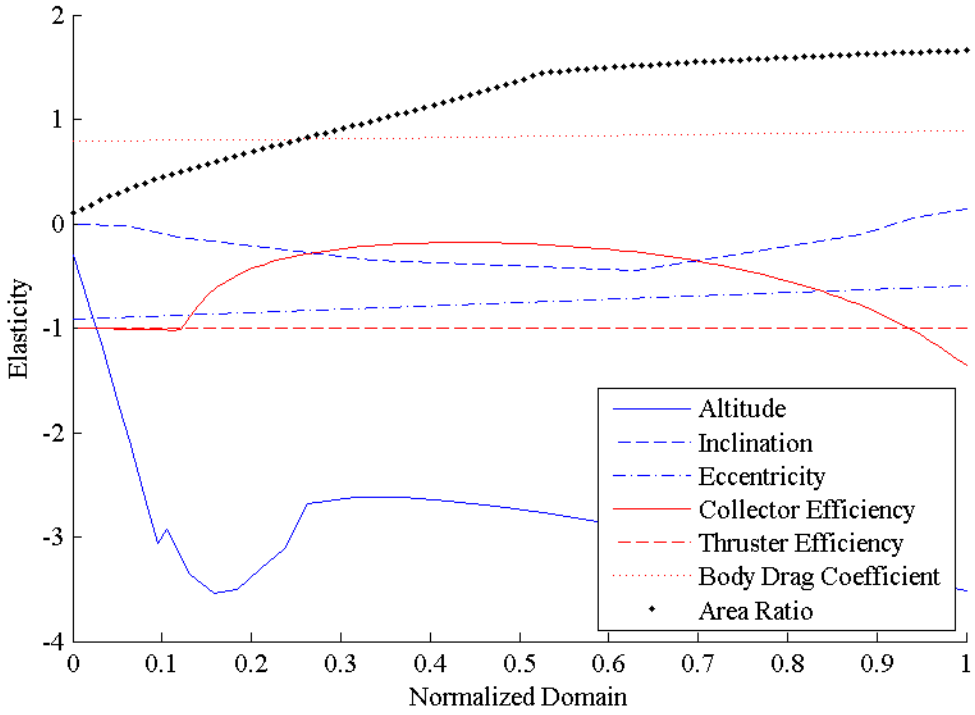

Figure 51. Elasticity plot for the air-breathing ramjet required power equation.

Figure 52 plots the elasticity of the required power function for the diverter ramjet architecture with respect to the input parameters. Many of the same changes in the behavior of the elasticities occur between the air-breathing and diverter ramjets as between the air-breathing and diverter rockets. One noticeable change is in the collector efficiency elasticity. Collector efficiency elasticity presents a form similar to a rocket

rather than the air-breathing ramjet as a result of the modification of the γ_c term. A diverter ramjet stops some of the oncoming flow to store it. This reduces the magnitude of the reduction in body drag coefficient. It does however still partly affect the required power, as the collector efficiency elasticity rises slower for the diverter ramjet than for the diverter rocket.

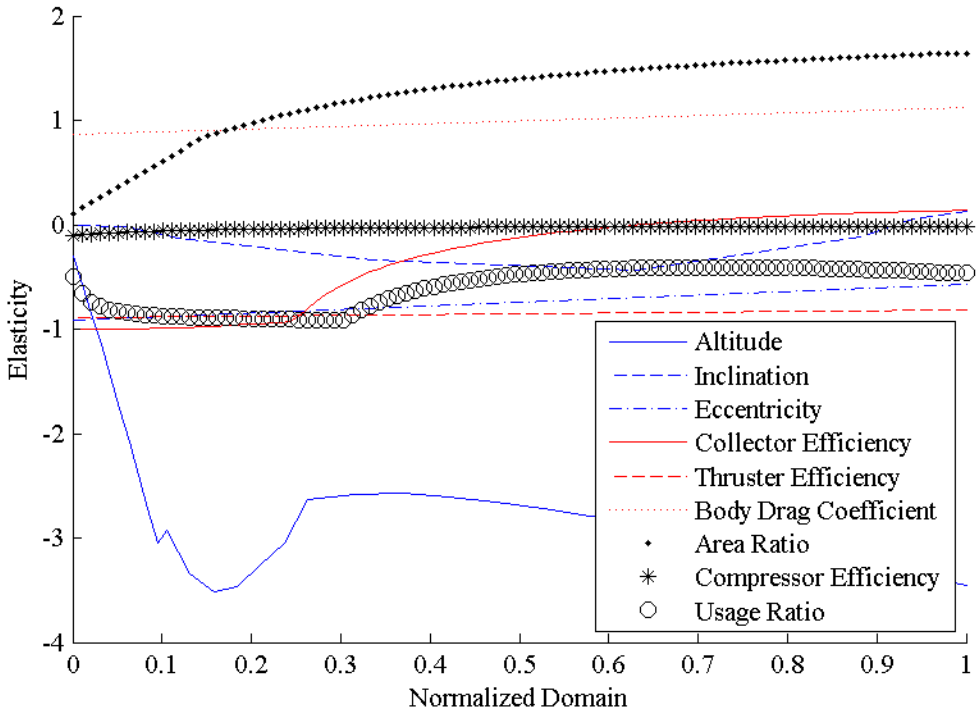

Figure 52. Elasticity plot for the diverter ramjet required power equation.

The preceding plots demonstrate the elasticity at 200 km periapsis altitude. Varying the baseline case changes many of the elasticities. Figure 53 shows the elasticity of the collector rocket required power equation evaluated at 100 km instead of 200 km. Comparison with Figure 50 reveals numerous changes as a result of selecting a different altitude. The compressor efficiency which is already unimportant at 200 km becomes completely negligible at 100 km. This results from the thrust power dominating the compressor power by an even wider margin in the 100 km case than in the 200 km case.

This result is further confirmed by the increase in the magnitude of the elasticity with respect to the thruster efficiency when transitioning to 100 km.

In contrast with the compressor efficiency, the elasticity with respect to the body drag coefficient appears to increase. The reason for this change is two-fold. First, as stated above for the compressor efficiency, the compression energy term is totally dominated by the thrust term. This increases the importance of the drag coefficient in the equation. Second, recalling back to Figure 33 and Figure 37 from Section 4.1, reducing the periapsis altitude has the effect of both increasing the speed ratio and reducing the ambient temperature. These changes create variation in the relative importance between the planform and spacecraft-body drag coefficients, because the body drag coefficient varies with temperature whereas the planform drag coefficient does not.

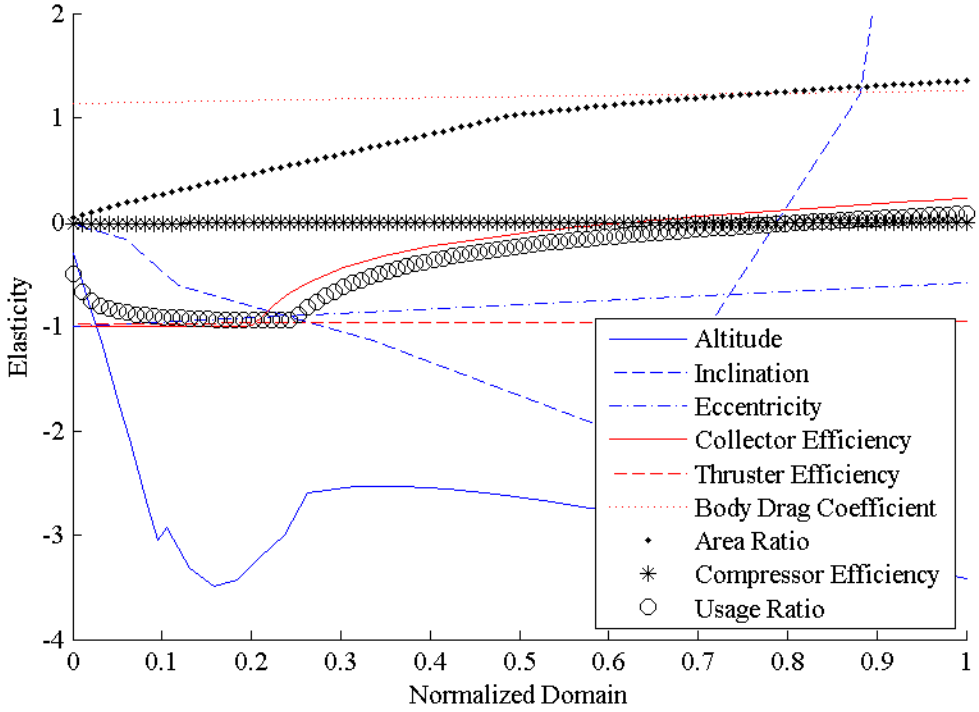

Figure 53. Elasticity plot for the collector rocket required power equation, evaluated at 100 km.

Altering the speed ratio also serves to reduce the value of the drag coefficients overall. This leads to a reduction in the ratio of the time-average area-specific drag force and the time-average area-specific mass flow rate term present in the required specific impulse as described in Eq. (3.11). Reducing this term leads to a reduced required specific impulse, and a more gradual variation in thruster efficiency. These effects are apparent in the area ratio elasticity. Changing to 100 km results in a reduced elasticity which kinks later when compared with the 200 km case. The lower overall elasticity is a result of the reduction in the drag coefficients, while the lower specific impulse leads to the kink for maximum thruster efficiency being pushed to higher area ratio values.

The usage ratio and collector efficiency both diverge sooner from negative one as a further result of the more gradual change in thruster efficiency. Collector efficiency peaks lower at the high range as a result of the reduced importance of the compression term. Since the linearly-varying compression term has reduced importance, the collector efficiency consequently has less importance to the overall required power.

The final and most dramatic change between the two altitude cases is the change in the elasticity with respect to inclination. The required power is significantly more sensitive to inclination at 100 km than at 200 km. All density-dependent parameters experience more variation with inclination at 100 km. Additionally, the minimum for the density-dependent parameters shifts downward in inclination when transitioning from 200 km. This effect causes the transition from negative elasticity to positive elasticity near polar inclinations.

The aforementioned variations with altitude of the elasticity with other design parameters highlights an important point. Elasticity with respect to one parameter can

vary with changes to another parameter (cross-terms). The elasticity results presented in this chapter thus present only a cross-section of the multidimensional elasticity functions at the baseline case.

Figure 54 plots the elasticity of the required power for an air-breathing rocket with varying input parameters once again. However, the results presented in this figure are based on an area ratio of 50 instead of one. At this higher area ratio the required power becomes less sensitive to body drag coefficient, eccentricity, and altitude. However, the most notable shift is in the elasticity with respect to collector efficiency. The collector efficiency maintains an elasticity of one until ~0.4 rather than ~0.15 in this higher area ratio case, and does not cross zero. This indicates that, while collector efficiency had a point of diminishing returns for the original set of parameters, at higher area ratio this is no longer the case. Similar results of varying area ratio can be seen in the results for the other required power equations as well, as demonstrated in Figure 55 for the collector rocket.

The cross-term describing the variation of elasticity of one parameter with regards to the variation of another parameter becomes non-trivial when the two parameters are dependent on one another. In addition to those demonstrated here, cross-term variation occurs for the required power elasticity with thruster efficiency for a number of parameters (orbital parameters, collector efficiency, usage ratio, area ratio).

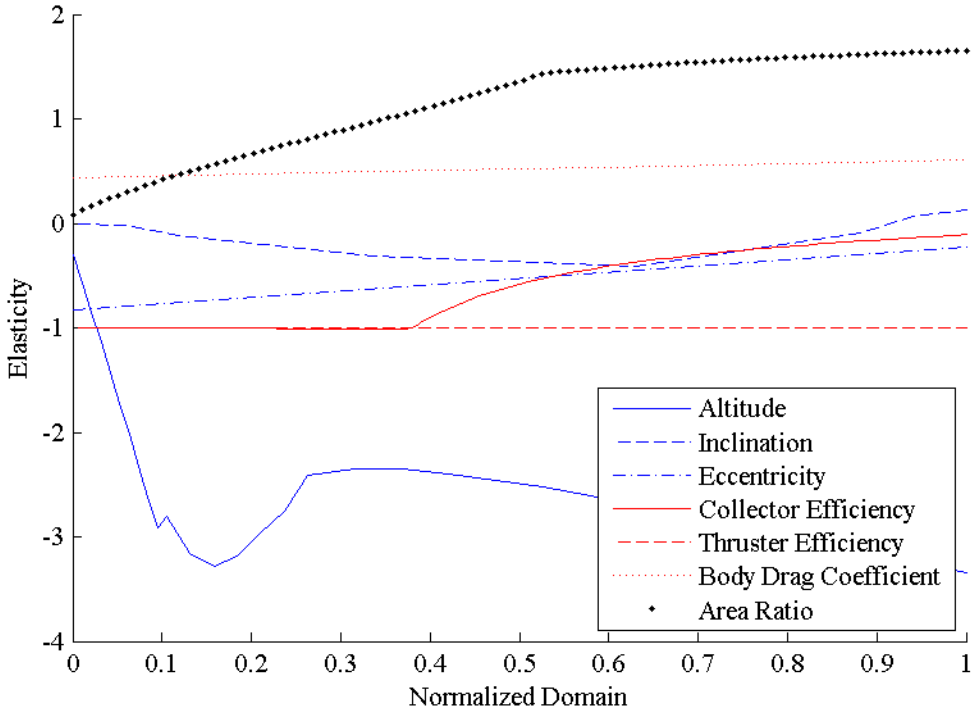

Figure 54. Elasticity of the required power for an air-breathing rocket with respect to the input parameters, calculated for an area ratio of 50 instead of one.

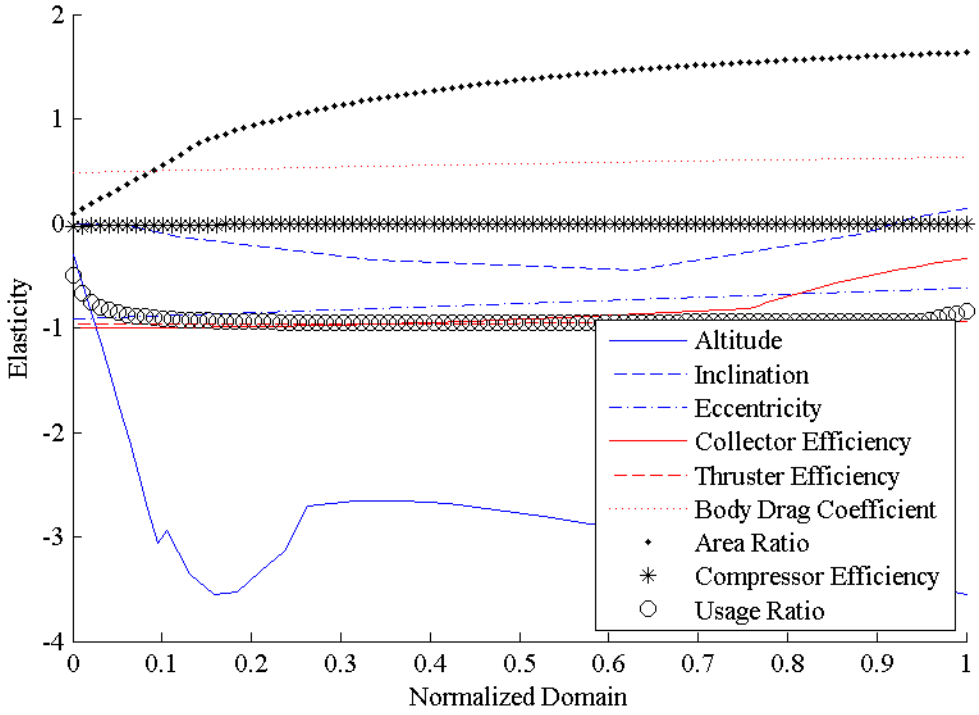

Figure 55. Elasticity of the required power for a collector rocket with respect to the input parameters, calculated for an area ratio of 50 instead of one.

5.3 Summary

Section 5.1 reports the results for the sensitivity analysis performed on the power generation equations. The solar power presents the anticipated sensitivity to the array design parameters, with both the area ratio and panel efficiency elasticities analytically determined to be one. Solar power is relatively insensitive to periapsis altitude and eccentricity, but is very sensitive to inclination. The results demonstrate that peak solar power can be attained for orbits with high inclination but which are sub-polar. Peak solar power is likely attained at the inclination corresponding to a sun-synchronous orbit. In contrast, nuclear electrical power does not depend on orbit conditions. It does however heavily depend on core temperature, with elasticity analytically determined to be equal to four. Thermal efficiency is found analytically to have an optimum value of 25 percent for maximizing electrical power generation with minimum radiator area. Increasing thermal efficiency beyond this value serves to reduce radiator heat rejection performance faster than it increases electrical power.

The sensitivity analysis for the required power performed in Section 5.2 is conducted over the range of parameters given in Section 3.2 with the baseline case provided in Table 7. The results of this section indicate mostly minor variation in the relative importance of the input parameters as a function of propellant collection architecture. For every case the periapsis altitude proves to be the dominant factor governing the required power. Periapsis altitude is thus the single most important design factor for propellant collection.

Factors of lesser importance include the thruster efficiency, eccentricity, and body drag coefficient. The required power equations show similar levels of sensitivity for each of these parameters. As seen from the 100 km case presented in Figure 53, required

power can be very sensitive to the selection of orbit inclination. However, the analyses conducted for the 200 km baseline case indicate that the required power is not always sensitive to inclination. This result occurs because the variation of atmospheric density with inclination varies with altitude.

The required power is sensitive to both usage ratio and collector efficiency for low values of either. In contrast, at values near one the required power equations lose sensitivity to these values or the elasticity changes sign. Changing sign in elasticity corresponds to a minimum or maximum design point, which is normally present for collector efficiency at the baseline design point selected. These results indicate that increasing collector efficiency and usage ratio presents diminishing returns as they approach one from a power minimization perspective.

The only value found to be unimportant by the sensitivity analysis on the required power equations is the compressor efficiency. The elasticity for compressor efficiency lies very near to zero in all circumstances, which indicates that compression power is of secondary concern to thrust power. As defined, the elasticity of a function with respect to one parameter can be dependent on the value of other parameters as well. The elasticity results presented are only cross-sections of the elasticity function, which has dimensionality equal to that of the design problem. The results presented in this chapter demonstrate this effect by altering the periapsis altitude and area ratio upon which the elasticity calculations are performed.

CHAPTER 6
TECHNICAL FEASIBILITY ASSESSMENT

This chapter presents the results of the technical feasibility assessment conducted in support of the second of this work's three research goals. In Section 6.1, the shape and behavior of the region of technical feasibility for a design are presented in terms of area ratio. The area ratio is the term which couples the required and generated power equations, and thus is a suitable parameter with which to analyze technical feasibility. Chapters 4 and 5 both demonstrate the importance of periapsis altitude to propellant collection. Thus, Section 6.2 focuses primarily on the location and variation of the minimum periapsis altitude which presents a technically feasible selection of area ratio. Propellant throughput provides an estimate of the benefit of propellant collection, especially for storage or propellant depot-type applications. Section 6.3 presents estimates of the propellant throughput at various design conditions and presents the results of an effort to determine the optimum usage ratio for collector-type vehicles to maximize the rate of propellant storage. The final section, Section 6.4, summarizes the findings of this chapter.

6.1 Area Ratio Solution Spaces

As stated in Section 3.1, the minimum condition for technical feasibility is that the time-average area-specific required power must be less than the time-average area-specific generated power. Eqs. (3.21) and (3.31) describe the generated power for solar and nuclear power sources respectively, while Eqs. (3.33) - (3.37) describe the required power for each of the propellant collection architectures. Careful examination of these equations leads to the realization that the one parameter which they all depend upon is the body-to-planform area ratio. The generated power equations both vary linearly with area

ratio, while the required power equations all vary as the square of area ratio to first order. Thus, the range of technically feasible area ratios consists simply of the intersection of a concave-up parabolic curve with positive y-intercept, and a line with positive slope which intersects the origin. Some propellant collection designs may include some power generation area on the body itself. The effect of this will be to raise the y-intercept of the generated power curve above zero, although the overall shape of the curve will not change. This effect is not considered in this work. Feasible solutions are those for which the required power lies below the generated power.

Figure 56 demonstrates this relationship for the baseline case provided in Table 7 from Section 3.3. As anticipated, the air-breathing ramjet power requirement is the smallest, although it is not significantly smaller than the air-breathing rocket. The ramjet does not experience loss from slowing the oncoming flow, however it must impart momentum to flow which is already in motion. This partly counteracts the energy savings. Diverter vehicles have higher required power than air-breathing vehicles because some of the collected flow is saved for storage. This drives up the specific impulse, as demonstrated in Figure 57. Finally, the collector vehicle has the highest power requirement because it must compress all of the collected flow.

For this particular case, it is clear that the solar power generated will never exceed any of the required powers. This is one possible solution to the curve-line intersection problem present in propellant collection. Another is demonstrated by the significantly more capable nuclear power option, where it overtakes the required power. A third, negligible solution type is the one for which the generated power is tangent to the required power. In this baseline case, solar power proves to be non-viable for propellant collection whereas nuclear power in this case can easily accommodate propellant collection.

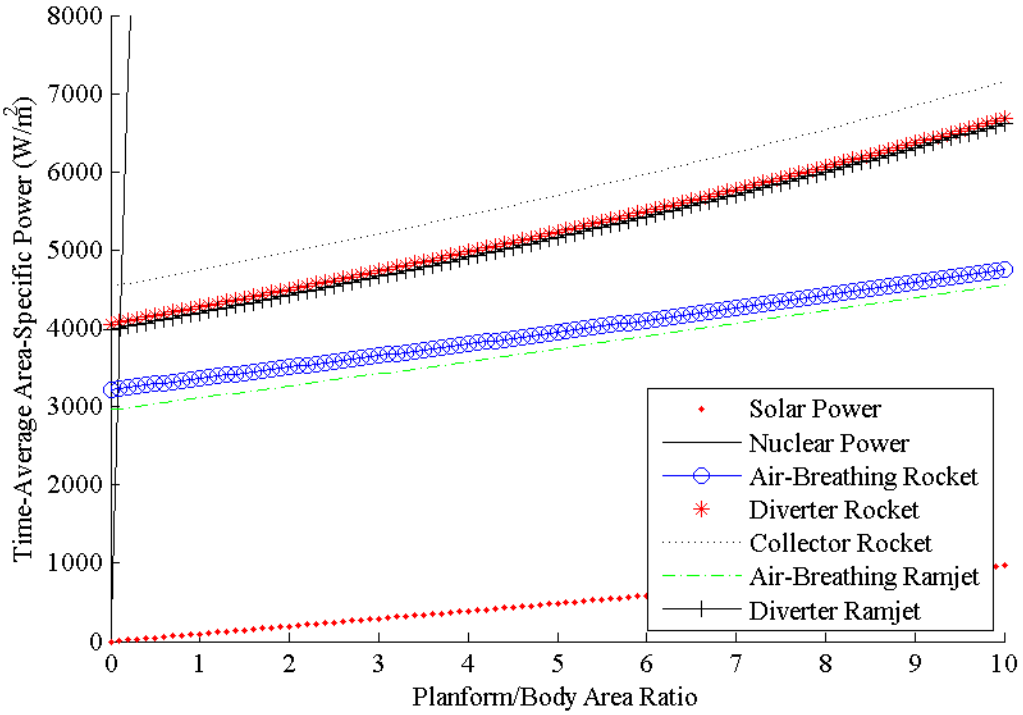

Figure 56. Plot of the required and generated powers with varying area ratio for the baseline case.

As noted before, Figure 57 plots the required specific impulse for each vehicle type as a function of area ratio for the baseline case. The vehicle types collapse into two groupings: those which store propellant (non-airbreathers) and those which do not (air-breathers). The air-breathing vehicles have the same specific impulse, despite the air-breathing ramjet required specific impulse having an additional velocity term. This result arises from the mutual counteraction of the reduction of drag and the initial velocity term addition to the ramjet specific impulse equation, Eq. (3.17). Similar reasoning governs the behavior of the non-airbreathing vehicle types, with the difference in specific impulse between the air-breathers and non-airbeathers governed by the reduction in mass flow to the thruster due to diversion to storage.

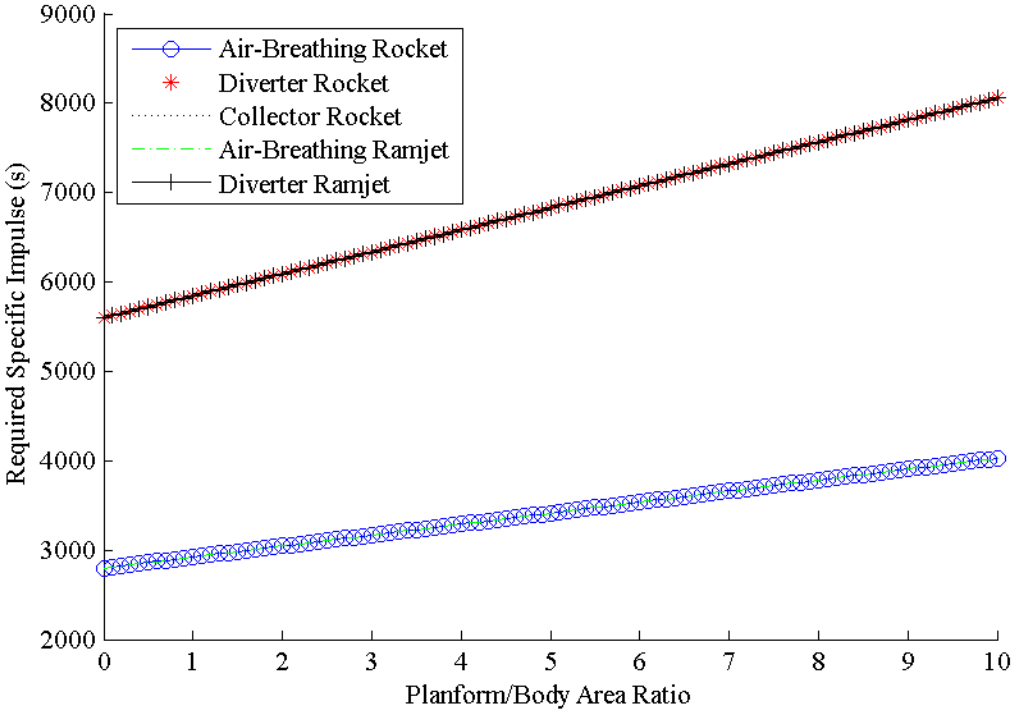

Figure 57. Required specific impulse with varying area ratio.

Figure 58 demonstrates the relationship between required power and solar activity for an air-breathing rocket. Solar power experiences very little variation with year and is thus plotted only once. Power requirements can vary dramatically based on solar activity, with the required power during a solar maximum being fifty percent higher than during a solar minimum. As noted previously, solar activity is a fact which cannot be changed; only adapted to. Thus, designers should take care when designing propellant collection systems to plan for solar activity and its effects on the power requirements of the vehicle. What may lead to a closed design in one year could be a flawed design in another year. One possible strategy stated earlier in this work is to adapt the periapsis altitude of the vehicle to the present level of solar activity.

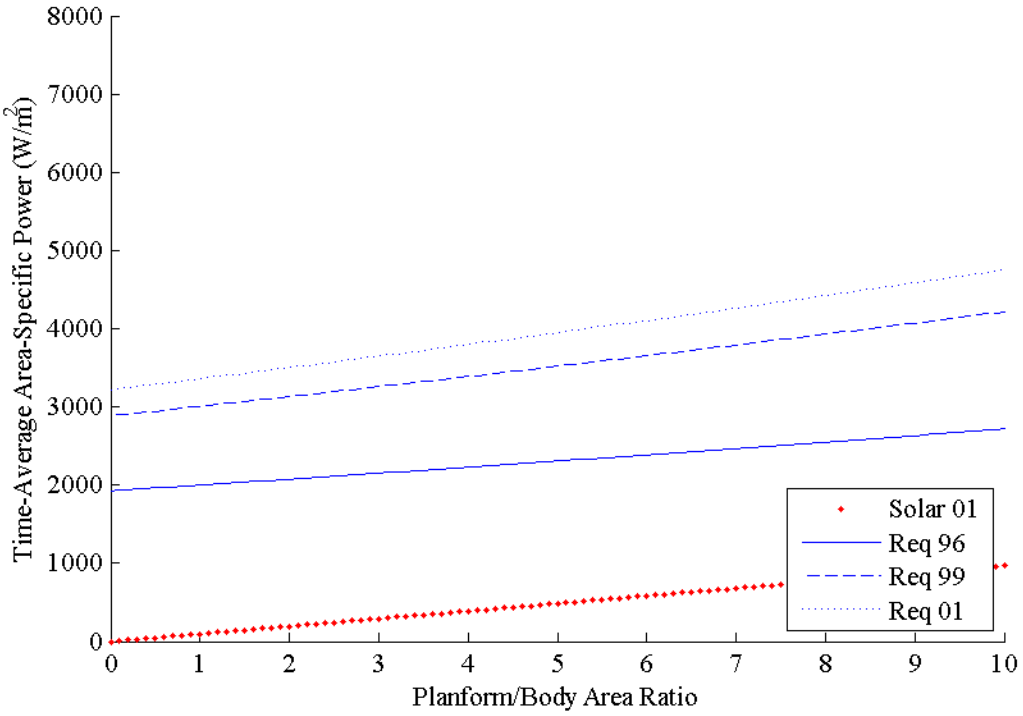

Figure 58. Air-breathing rocket required power for varying area ratio and three different levels of solar activity.

The results in Figure 59 demonstrate anticipated relationships from the sensitivity analysis results presented in Chapter 5. Increasing eccentricity serves to increase the available solar power, as demonstrated by the relevant elasticity curve in Figure 46. Similarly, increasing eccentricity serves to reduce the required power as indicated by the relevant elasticity curve in Figure 48. To review, increasing eccentricity drives up the solar power by driving up the average solar viewing factor. Higher eccentricity orbits travel out to higher altitudes where the effect of Earth eclipsing is not as great. These excursions to higher altitude also serve to reduce the drag force present on the vehicle, which drives down the required power.

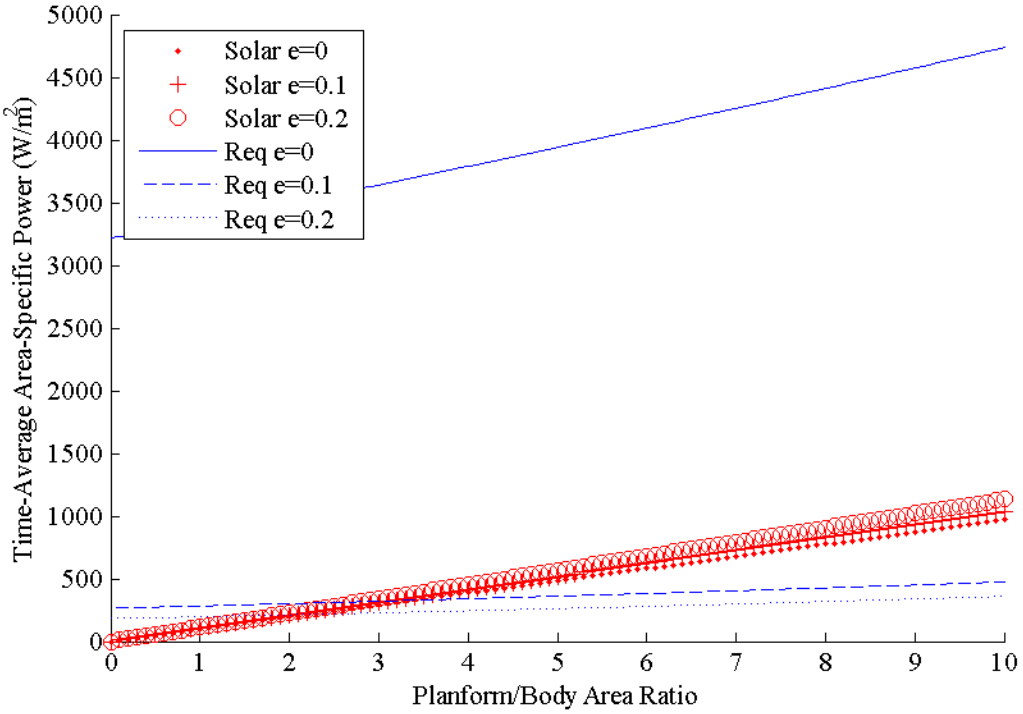

Figure 59. Required and generated power for a solar air-breathing rocket with varying area ratio at different eccentricities for the baseline case.

As demonstrated previously, nuclear power is far more capable than solar power on a power-per-planform area basis. Figure 60 demonstrates this by plotting eccentric 100 km orbit power lines for a nuclear air-breathing rocket. While not present in this figure, an upper limit exists to area ratio for closure. This upper limit is present for any case where the generated power exceeds the required power. Generated power varies linearly with area ratio, whereas required power varies roughly as the square. The result is that at some area ratio, the added benefit to the generated power by increasing area ratio is outweighed by the corresponding increase in required power. This upper limit is inevitable, and its presence cannot be forgotten by designers.

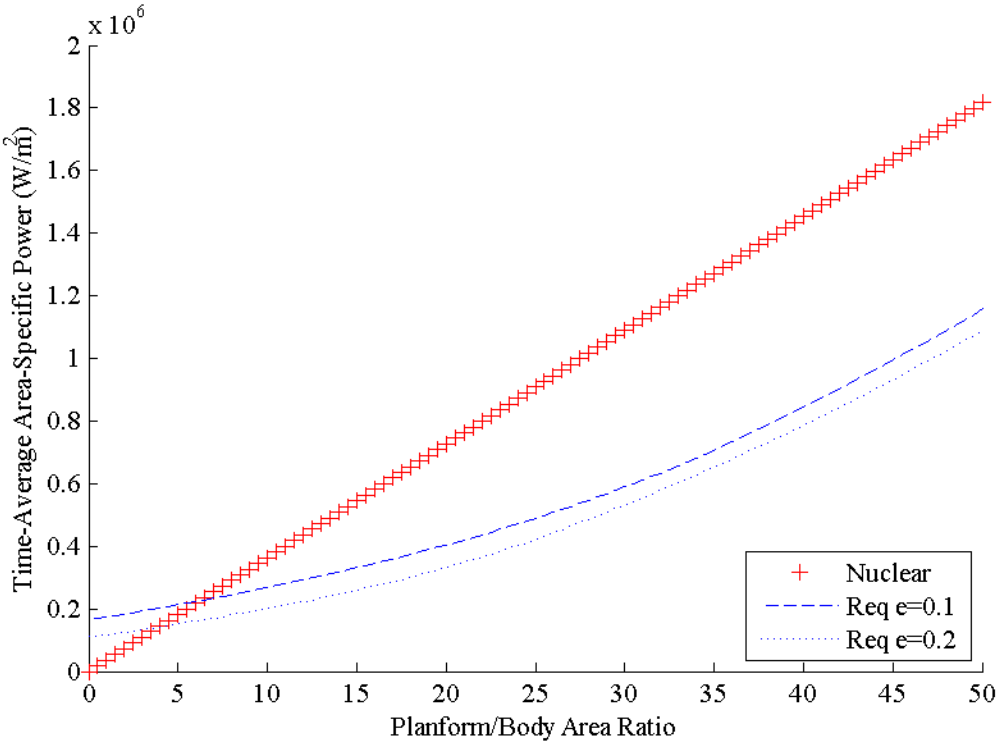

Figure 60. Power lines for a nuclear air-breathing rocket at 100 km periapsis altitude, for varying eccentricity.

At a sufficiently low altitude, even nuclear power is incapable of delivering the required power to sustainably operate a propellant-collecting vehicle. Figure 61 demonstrates this for the extreme case of 100 km periapsis altitude, circular orbits. The power requirement varies with inclination as predicted by Figure 48, with increasing inclination driving a reduction in the required power. However, even in a polar orbit the required power for this case dominates the available nuclear power. The required power is on the order of one to tens of MW/m^2, whereas the nuclear power available is on the order of 100's of kW/m^2. This result demonstrates that, contrary to the results of previous researchers, nuclear power is not presently capable of operating propellant-collection devices at the extremely low altitudes they considered [9, 32, 35, 36].

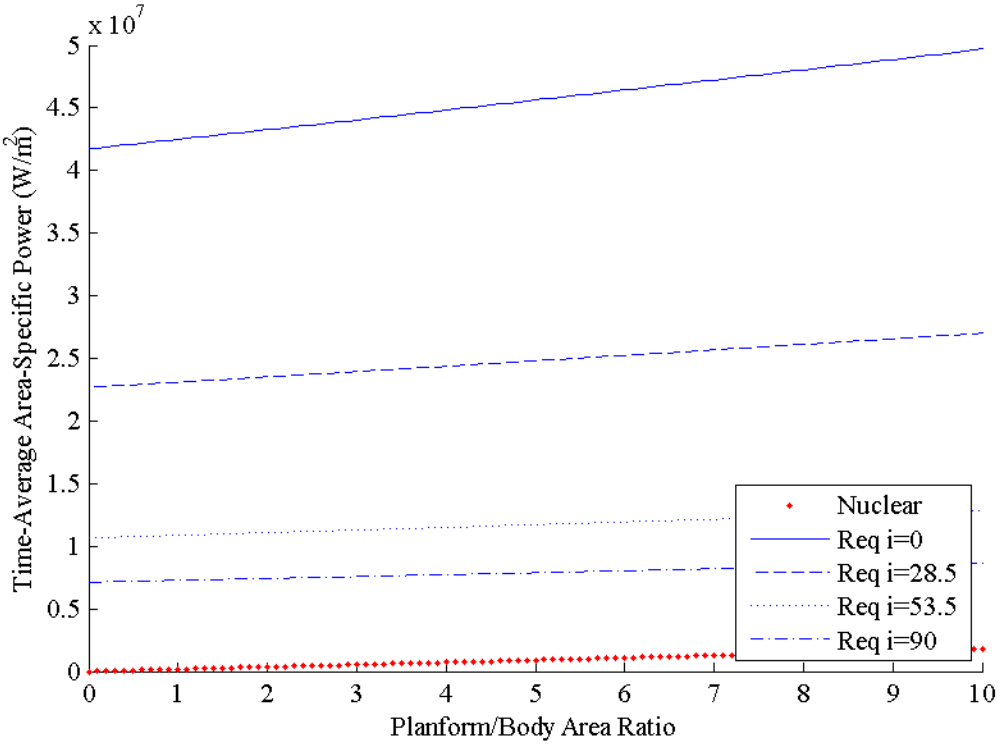

Figure 61. Nuclear air-breathing rocket power lines for varying inclination in a 100 km circular orbit.

6.2 Regions of Technical Feasibility

As demonstrated in Chapter 5, the required power equations are dominated by the selection of periapsis altitude. Thus, it makes sense to consider the "where" in the second research goal as the minimum periapsis altitude where closure can be attained as a function of the input parameters. Area ratio free to vary between zero and 100 in this analysis, which is justified later in this section. The regions of technical feasibility presented in this section are those regions which lie above the minimum altitude lines indicated in the figures that follow.

The aforementioned results are calculated for two cases: the baseline case as described in previous sections and detailed in Table 7, and an "ideal" case which assumes the highest performance on many of the design parameters as summarized in Table 9. Considering each case provides an understanding of what is presently technically feasible, and what may become technically feasible with continued development. The

minimum altitude is also calculated for a varying set of inclination/eccentricity combinations, as denoted in the legend of the relevant figures. This provides an understanding of the effect orbital configuration has on technical feasibility.

Table 9. Summary of design parameters for the "ideal" case.

Parameter Name	Symbol	Nominal Value
Orbit Inclination	i	0°
Orbit Eccentricity	e	0.0
Year	N/A	2001
Collector Efficiency	η_c	0.95
Drag Coefficient	$C_{D,s/c}, C_{D,PA}$	Jones' Result
Usage Ratio	ϵ	0.5
Compressor Efficiency	η_{comp}	0.1
Thruster Efficiency	η_t	Ideal Case
Solar Panel Efficiency	η_{SP}	0.628
Emissivity	ε	0.8
Thermal Efficiency	η_R	0.3
Core Temperature	T_c	1950 K

6.2.1 Baseline Case – Presently Available Technology

Figure 62 presents the minimum periapsis altitude for closure as a function of varying collector efficiency for a baseline solar air-breathing rocket. The results are also presented for a range of inclination and eccentricity. To reiterate, the technically feasible regions on the plot for a given orbital configuration are those designs which lie above the relevant minimum altitude line in altitude space. Minimum altitude asymptotes near zero collector efficiency as a result of low collector efficiency restricting mass flow to the thruster, thus driving up the required specific impulse. The results tend to cluster into two distinct groups as demonstrated in this figure, with circular orbit cases inhabiting the upper cluster and eccentric orbit cases inhabiting the lower cluster. Eccentricity serves to reduce the density-dependent time-average products while increasing the solar viewing factor, thus permitting lower orbits. This behavior with regards to eccentricity is consistent with that observed both in Chapter 5 and in Section 6.1.

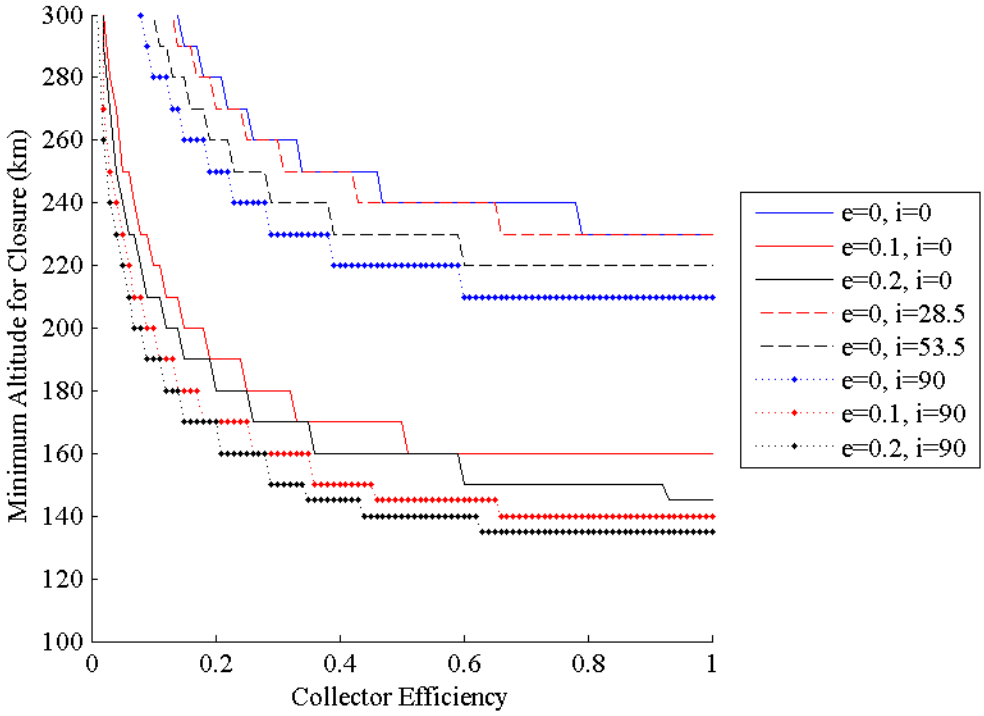

Figure 62. Minimum periapsis altitude for closure for a baseline solar air-breathing rocket with varying collector efficiency for a range of inclination/eccentricity combinations.

Each cluster of results further subdivides on the basis of inclination. Altering inclination has a smaller effect on the minimum altitude than eccentricity, as is expected given the results in Figure 48 from Section 5.2. As stated previously in this work, an informed selection of inclination can have a beneficial effect on propellant collection. In this context, inclination can affect as much as a 30 km impact on the minimum periapsis altitude for system closure. The results from Figure 48 in the previous chapter indicate that the minimum periapsis altitude for closure should increase at high values of collector efficiency. Recall however, that the elasticity values calculated in that figure are made with an area ratio of one. The elasticity of required power with increasing collector efficiency is different at high area ratios than it is at one, as demonstrated in Figure 54. Thus, the behaviors present in the elasticity plots do not universally extend to minimum altitude plots.

Figure 63 shows the same results as Figure 62, but for a solar-powered collector rocket instead of an air-breathing rocket. The higher power requirement for the collector

rocket drives the minimum altitude curves upward and to the right. The diverter vehicles both exhibit a similar range as the collector rocket, as do the air-breathing vehicles with one another. This highlights the clustering of required power curves seen in Section 6.1.

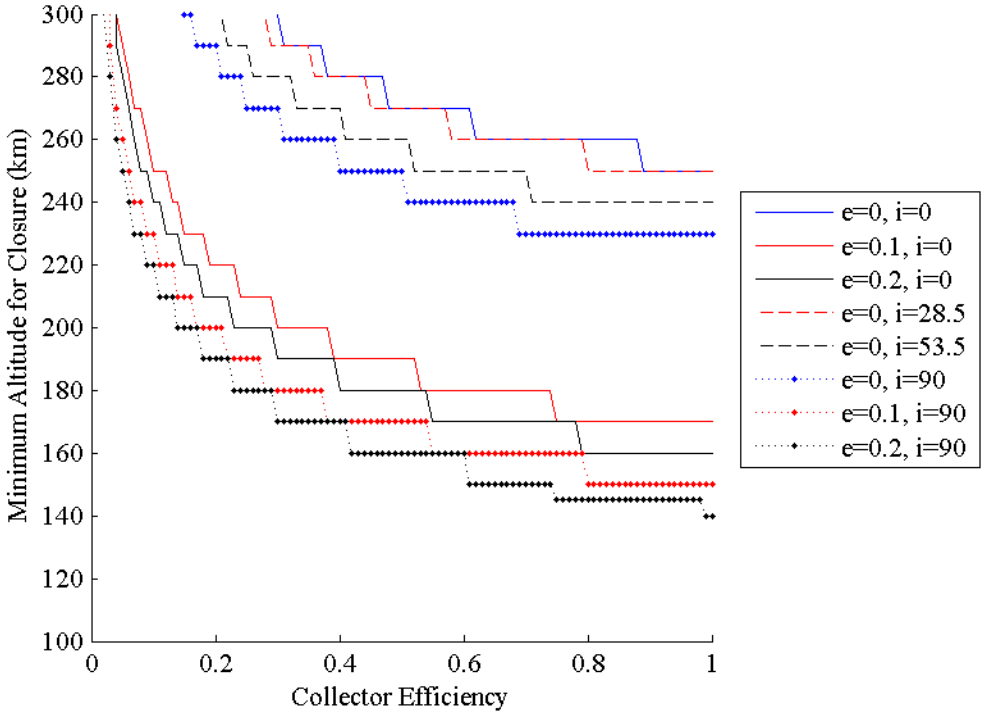

Figure 63. Minimum periapsis altitude for closure for a baseline solar collector rocket with varying collector efficiency for a range of inclination/eccentricity combinations.

The results of varying the thruster efficiency are more linear in the range studied than for the collector efficiency. Figure 64 presents the minimum periapsis altitude for a solar air-breathing rocket as a function of relative thruster efficiency for varying cases of eccentricity and inclination. The results are plotted in terms of relative thruster efficiency, where the left side of the plot represents the thruster performance predicted from Cifali et al.'s experimental results. The right side of the plot represents the thruster performance as predicted for the "ideal" thruster case [21]. According to the results, improvement of air-compatible thruster technology to improve efficiency can affect a 20- 30 km impact to the minimum periapsis altitude attainable for a solar powered air-breathing rocket in a circular orbit. Eccentric orbits experience a similar effect, although the change in

periapsis altitude is reduced because their periapsis altitudes are already lower and thus in a higher density region. Analysis of the results of modifying thruster efficiency for other solar powered vehicle types indicates this result is independent of vehicle type.

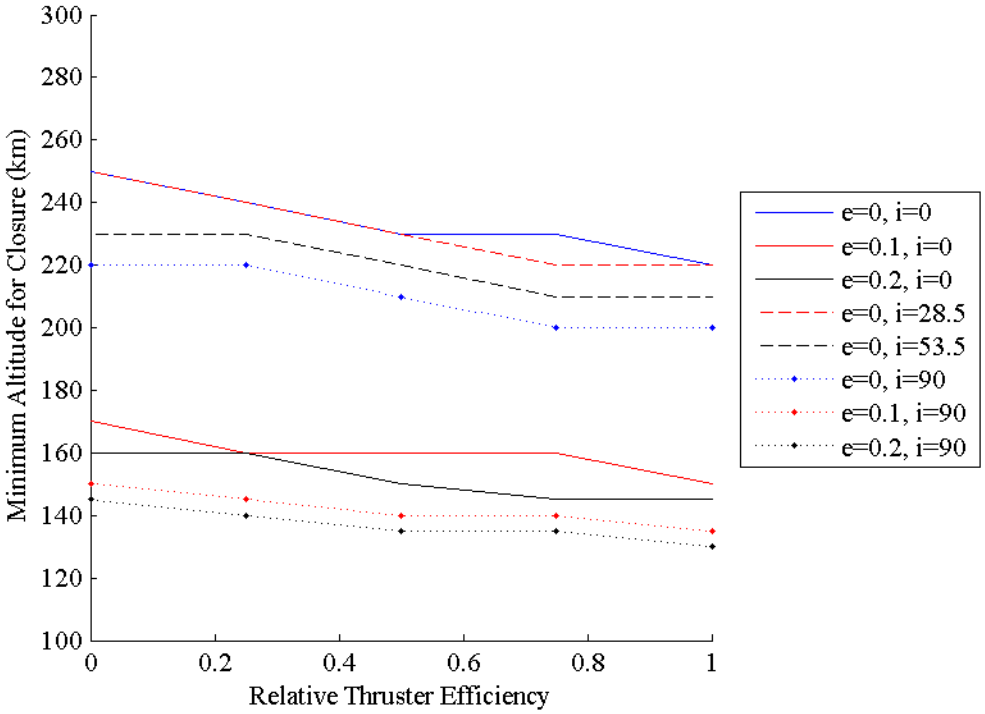

Figure 64. Minimum periapsis altitude for closure for a baseline solar air-breathing rocket with varying thruster efficiency for a range of inclination/eccentricity combinations. Values on the left represent Cifali's result, while the values on the right represent the "ideal" thruster case.

Figure 65 presents the minimum altitude as a function of varying drag coefficient for a solar air-breathing rocket. Values at zero relative drag coefficient represent the minimum drag coefficient as described in Section 3.2.3 whereas the values at relative spacecraft-body drag coefficient of one represent Sentman's analytical result [47]. As one would expect, increasing the drag coefficient drives up the required power, resulting in an increase in the minimum attainable periapsis altitude. However, the effect of changing the drag coefficient over the range studied appears to have a smaller effect than changing the thruster or collector efficiencies.

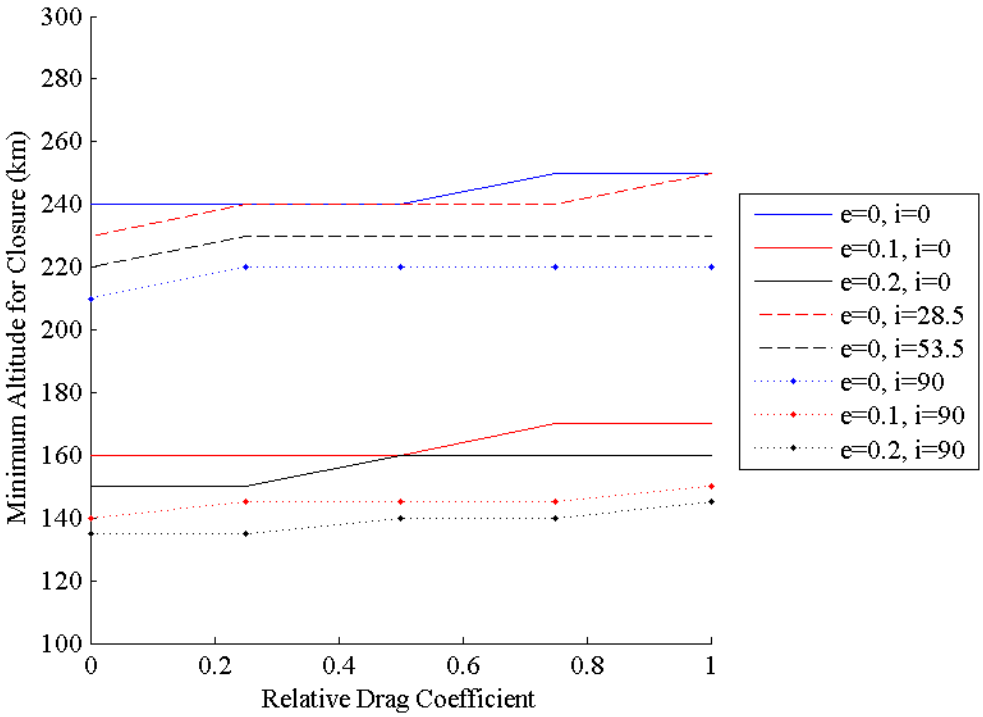

Figure 65. Minimum periapsis altitude for closure for a baseline solar air-breathing rocket with varying drag coefficient for a range of inclination/eccentricity combinations. Values on the left of the plot represent drag coefficients for the minimum case whereas drag coefficients on the right represent Sentman's result.

Figure 66 presents the same results, although for a solar diverter ramjet vehicle. The effect of modifying the selection of drag coefficient on minimum altitude is increased in this case when compared with the solar air-breathing rocket. Minimum periapsis altitude for air-breathing vehicles appears to have reduced sensitivity to body drag coefficient when compared to non-air breathing vehicles. This result is roughly consistent with the elasticity results from Chapter 5. However, despite a minor difference in the magnitude of its effect, drag coefficient is of secondary concern when designing to minimize the altitude of operation. These results indicate only 10-20 km of variation in minimum altitude over the range of body drag coefficient studied.

Improving solar panel efficiency can potentially lead to dramatic reductions in minimum periapsis altitude. Figure 67 plots the results for the solar air-breathing rocket as a function of varying solar panel efficiency. The results indicate approximately 10 km of improvement in minimum periapsis altitude with ten percent improvement in panel

efficiency for both circular and eccentric orbits. This result is consistent for every solar-powered vehicle type using the baseline case parameters. Solar panels remain an ongoing area of research, which is promising given the potential improvements in minimum feasible altitude improved panel efficiency affords.

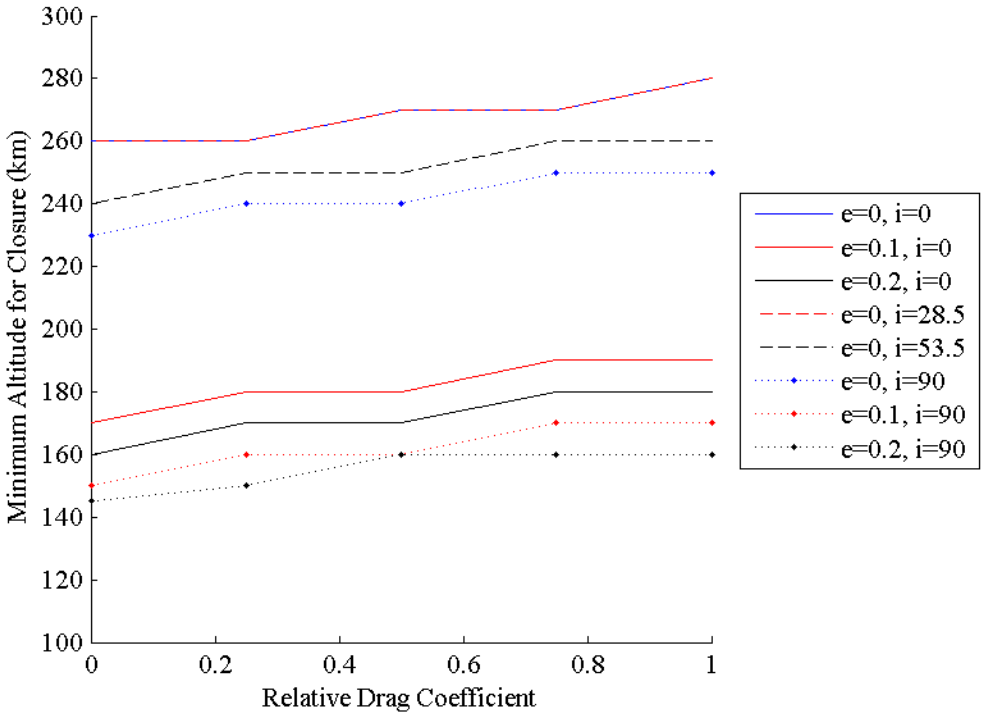

Figure 66. Minimum periapsis altitude for closure for a baseline solar diverter ramjet with varying drag coefficient for a range of inclination/eccentricity combinations. Values on the left of the plot represent drag coefficients for the minimum case whereas drag coefficients on the right represent Sentman's result.

The final parameter considered for the solar-powered baseline case is usage ratio. Note that compressor efficiency is not considered in this chapter because the sensitivity analysis in Chapter 5 determines it is not an important parameter to the overall design. Figure 68 plots the minimum periapsis altitude as a function of usage ratio for the solar-powered diverter ramjet case. For similar reasons as for the collector efficiency, the minimum altitude asymptotes as usage ratio approaches zero. This effect appears for both the circular and eccentric orbit cases. As usage ratio approaches one, the results for the diverter ramjet approach the results for the baseline case for a solar air-breathing ramjet.

This result occurs because an air-breathing ramjet is effectively a special type of diverter ramjet where usage ratio is unity.

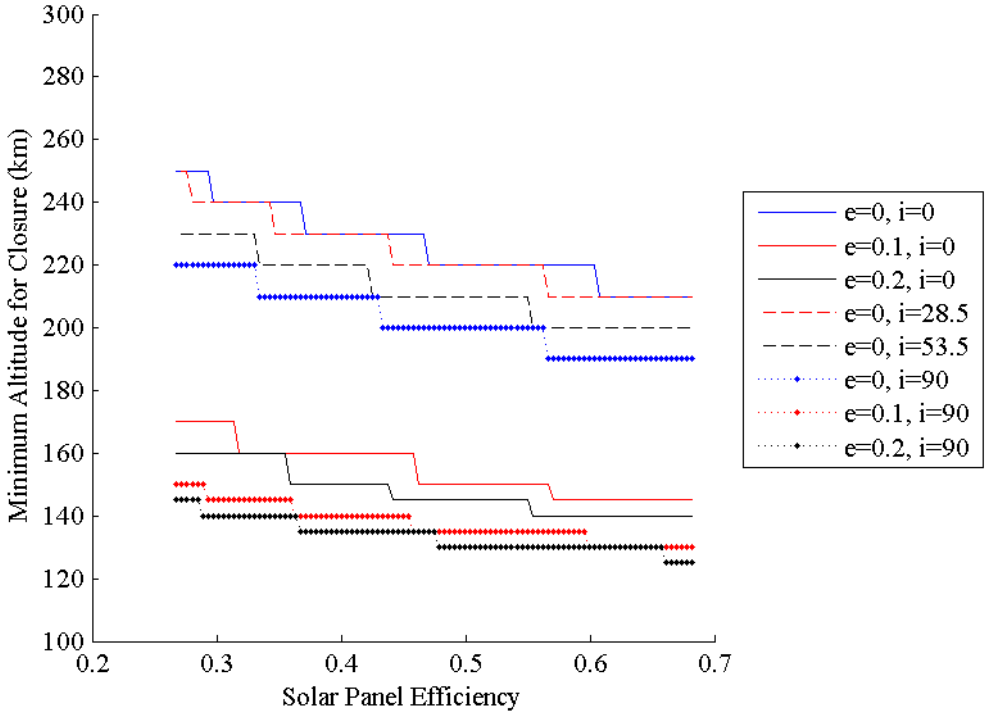

Figure 67. Minimum periapsis altitude for closure for a baseline solar air-breathing rocket with varying solar panel efficiency for a range of inclination/eccentricity combinations.

For the baseline case, the preceding figures show solar-powered vehicles are capable of operating as low as 250 km when in an equatorial, circular orbit to as low as 220 km when in a polar, circular orbit. Eccentricity reduces this range to 140-170 km as a result of reducing the magnitude of the density-dependent time-average parameters. Di Cara et al. suggest in the RAM-EP study that propellant collection does not offer a benefit above 250 km for average satellite lifetimes, because the required propellant budget above this altitude is sufficiently low that it can be accommodated in a design. GOCE operated in a circular, near-polar orbit at 255 km altitude for 4.5 years during a period of unusually low solar activity with only 60 kg of xenon propellant. However, this propellant budget would have only lasted 24 months under normal solar activity.

Although most of the preceding analysis focused on circular orbits in order to demonstrate trends in other parameters, introducing eccentricity also has a beneficial effect which is potentially advantageous for some applications. Eccentricity significantly reduces the minimum altitude attainable for the vehicle while extending the apoapsis out to a higher altitude. This combination could be potentially valuable for reconnaissance vehicles because it affords such vehicles the advantage of low altitude for high resolution imagery over a target while reducing the cost for plane-change maneuvers. It appears then that, for the present level of technology, solar-powered propellant collection may be a viable method for counteracting drag in VLEO circular orbits and may present desirable advantages to satellite designers. The next chapter performs a more exhaustive search to determine the technical feasibility for this particular application.

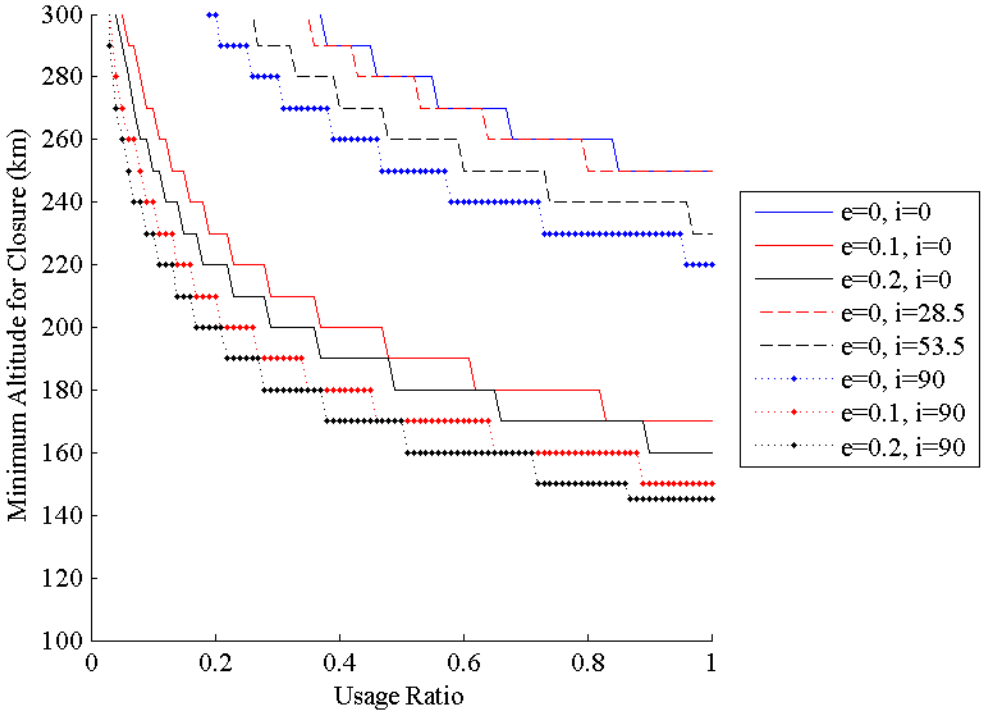

Figure 68. Minimum periapsis altitude for closure for a baseline solar diverter rocket with varying usage ratio for a range of inclination/eccentricity combinations.

The other power source considered in this work, nuclear power appears well suited to providing for the power needs of a propellant collection system. Figure 69 plots results identical to those of Figure 62, but for a nuclear-powered air-breathing rocket as

opposed to a solar-powered air-breathing rocket. Most notably among the differences between these two figures is the significantly lower altitude attainable for nuclear power as opposed to solar power. Nuclear power produces far more power per unit planform area than solar power collects, which allows for propellant-collecting vehicles to operate at lower altitudes where power requirements are higher. Circular orbit operation can be maintained at altitudes as low as 118-130 km, depending on inclination. Contrasted with the same limits for solar power at 220-250 km, the advantage of nuclear power is clear for this application.

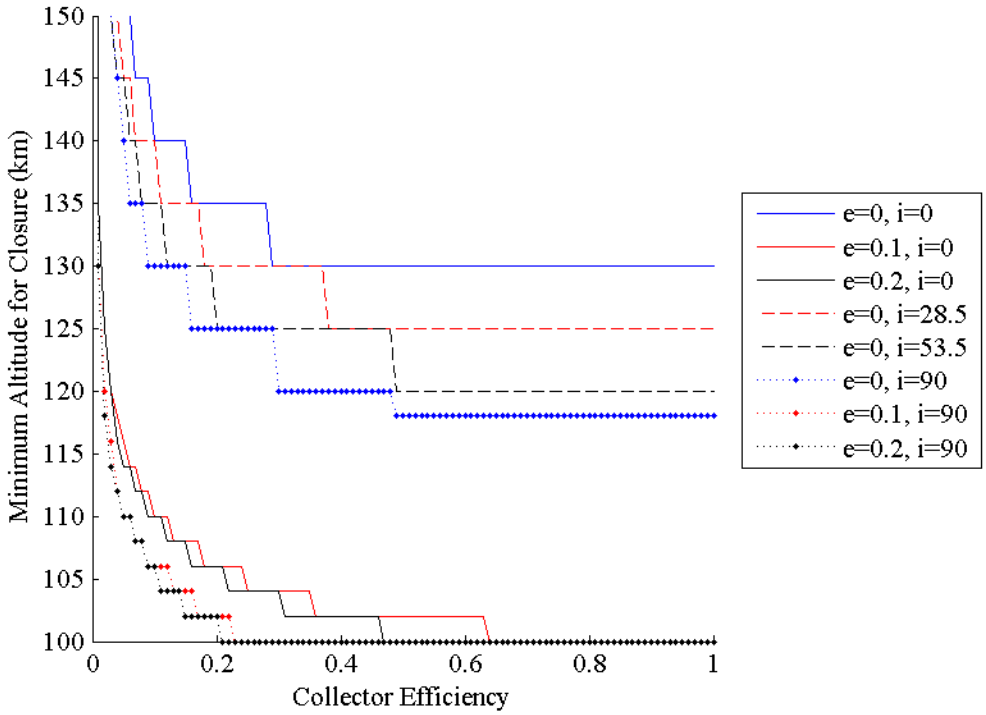

Figure 69. Minimum periapsis altitude for closure for a baseline nuclear air-breathing rocket with varying collector efficiency for a range of inclination/eccentricity combinations.

Also note the appearance of clustering of the results as found for solar-powered vehicles. Like the solar power cases, increasing eccentricity serves to reduce the magnitude of the density-dependent time-average parameters which permits lower periapsis altitudes for operation. For nuclear power, moderate collector efficiency allows the baseline case eccentric orbits to reach the 100 km altitude modeling limit at the Karman line. Eccentricity permits nuclear-powered propellant-collecting vehicles to

operate as true aerospace vehicles and regularly cross the classical boundary of aeronautics and astronautics. However, it is important to note that aerodynamic heating will become very significant at these low altitudes due to the high density and with the increased velocity associated with an eccentric orbit at periapsis.

The response of the minimum periapsis altitude to collector efficiency appears to diminish at high values for the nuclear case in contrast with the solar case. The minimum altitude lines become flat beyond 0.5 collector efficiency. The eccentric orbits experience this as a result of hitting the modeling limit of altitude. However, the circular cases do not reach this limit. Instead, the circular cases experience the interrelationship between the required specific impulse and the thruster efficiency. As collector efficiency increases, the amount of flow available to the thruster increases and the required specific impulse declines. However, this serves to lower the thruster efficiency which reduces the positive effect lowering the required specific impulse otherwise has on the required power.

Figure 70 presents the results for varying thruster efficiency on a nuclear-powered air-breathing rocket. Thruster efficiency at first appears to be far less important for nuclear-powered vehicles than for solar-powered vehicles from the perspective of minimum periapsis altitude. Figure 70 indicates only 5 km of variation with thruster efficiency from the baseline case to the ideal case for nuclear power as opposed to 20 km with solar power. However, this result is misleading. On the basis of density, altering the altitude by 5 km at 130 km is far more significant than altering the altitude by 20 km at 250 km. Figure 3 from Section 2.1 demonstrates the more rapid decrease of density with increasing altitude at low altitudes as opposed to high altitudes. Consequently, improving thruster efficiency remains an important area of continued development for nuclear-powered systems.

Similar to the solar-powered baseline cases, the nuclear-powered vehicles demonstrate almost no variation in minimum periapsis altitude as a result of varying the body drag coefficient. Figure 71 shows the results of varying the body drag coefficient

between the minimum value and Sentman's analytical result for a nuclear collector rocket. The circular orbit cases demonstrate no variation with varying drag coefficient for nuclear-powered vehicles, which is a result of operating at lower altitudes than their solar power counterparts.

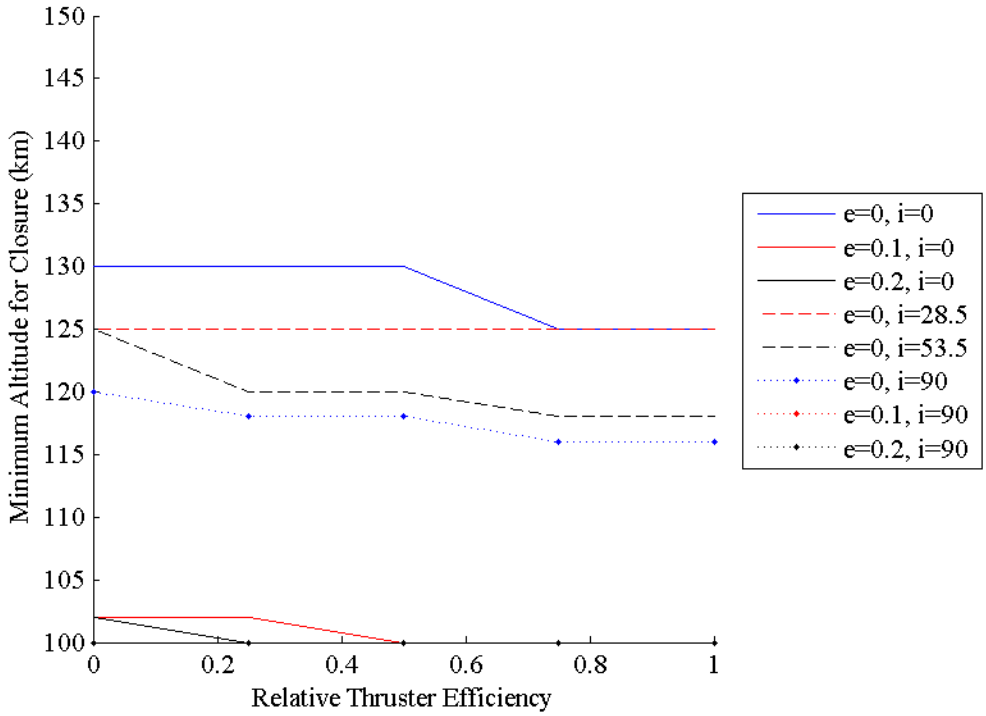

Figure 70. Minimum periapsis altitude for closure for a baseline nuclear air-breathing rocket with varying thruster efficiency for a range of inclination/eccentricity combinations. Values on the left represent Cifali's result, while the values on the right represent the "ideal" thruster case.

Recalling from Figure 37 in Section 4.1, as altitude decreases so too does speed ratio. Reducing the speed ratio serves to reduce Sentman's analytical drag coefficients, whereas the minimum case studied does not depend on speed ratio and remains constant. Consequently, the absolute range of body drag coefficient contracts as altitude declines. Some effect remains for the eccentric cases because they experience less change in speed ratio with varying periapsis altitude. Even so, the effect of varying the body drag coefficient for eccentric orbits remains very small. This result suggests that the body drag coefficient is not a major factor in dictating the minimum feasible periapsis altitude of nuclear-powered propellant collection concepts.

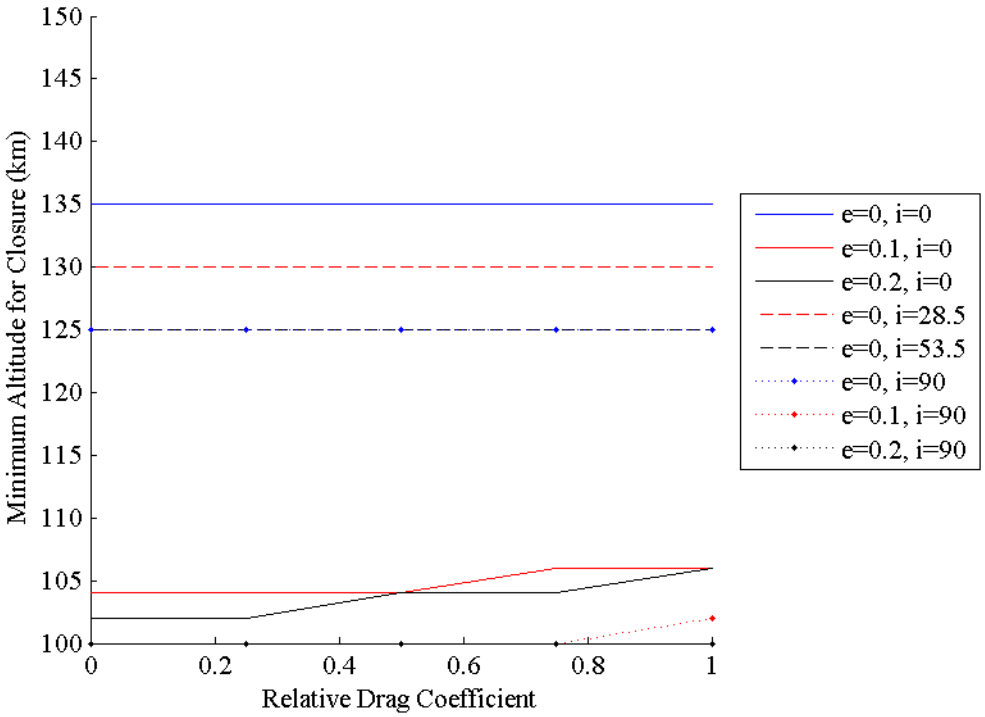

Figure 71. Minimum periapsis altitude for closure for a baseline nuclear collector rocket with varying drag coefficient for a range of inclination/eccentricity combinations. Values on the left of the plot represent drag coefficients for the minimum case whereas drag coefficients on the right represent Sentman's result.

Unique to nuclear-powered craft are the thermal efficiency and core temperature design parameters. Figure 72 demonstrates the effect of varying thermal efficiency on the minimum periapsis altitude for a nuclear-powered air-breathing rocket. The results indicate no dependence; this result is consistent across all nuclear-powered vehicle types in the baseline case. Recalling Figure 47 from Section 5.1, the nuclear electrical power generated is least sensitive to thermal efficiency as confirmed by this result.

The second nuclear-specific parameter is the core temperature, for which Figure 73 plots results for a nuclear air-breathing rocket. As expected from Section 5.1, varying core temperature has a dramatic effect on the minimum periapsis altitude for closure over the range of temperature considered, with diminishing returns at higher temperatures. The circular orbit cases presented see ~15 km of reduction in periapsis altitude by transitioning from the lowest temperature to the highest temperature, whereas the eccentric orbits rapidly hit the modeling limit of 100 km at the Karman line. Higher core

temperatures serve to reduce the amount of radiator area required to generate the same amount of power, which reduces the drag and thus the minimum attainable altitude of the vehicle. The results demonstrated in Figure 73 are consistent with the same results for the other baseline nuclear-powered cases. This demonstrates that, if nuclear-powered propellant-collecting vehicles are developed, increasing core temperature should be the primary area of development.

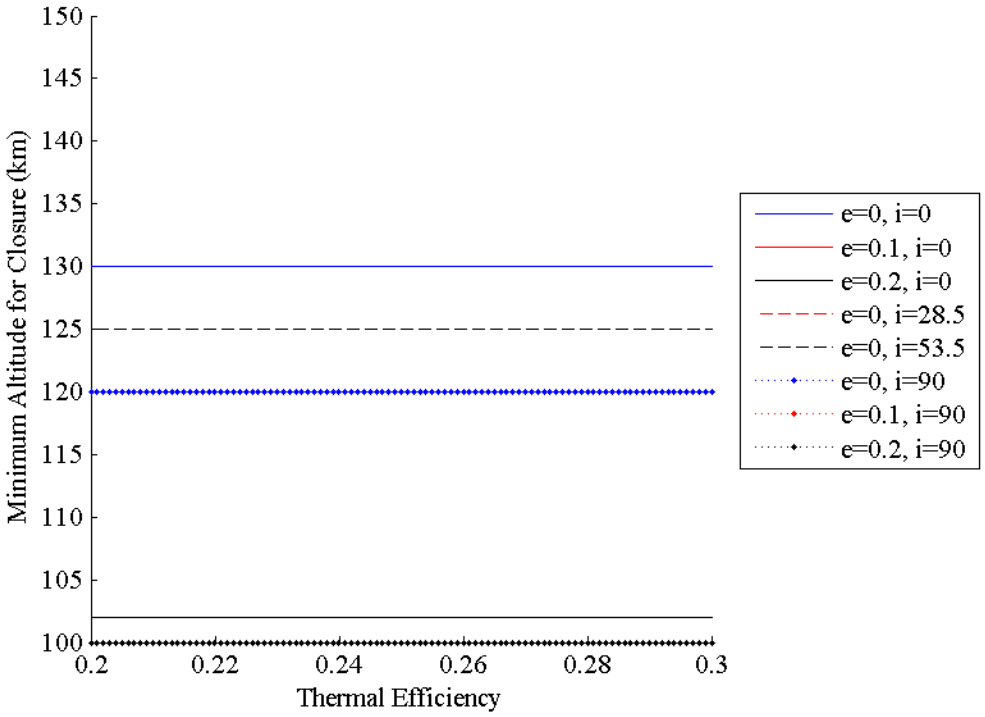

Figure 72. Minimum periapsis altitude for closure for a baseline nuclear air-breathing rocket with varying thermal efficiency for a range of inclination/eccentricity combinations. Many of the results overlap with one another.

Figure 74 plots results for usage ratio for the case identical to that presented in Figure 68, but for a nuclear-powered diverter rocket rather than a solar-powered rocket. Minimum altitude predictably asymptotes near zero usage ratio, as seen in Figure 68. While the altitudes are lower for the nuclear case as opposed to the solar case, the behavior is nearly identical.

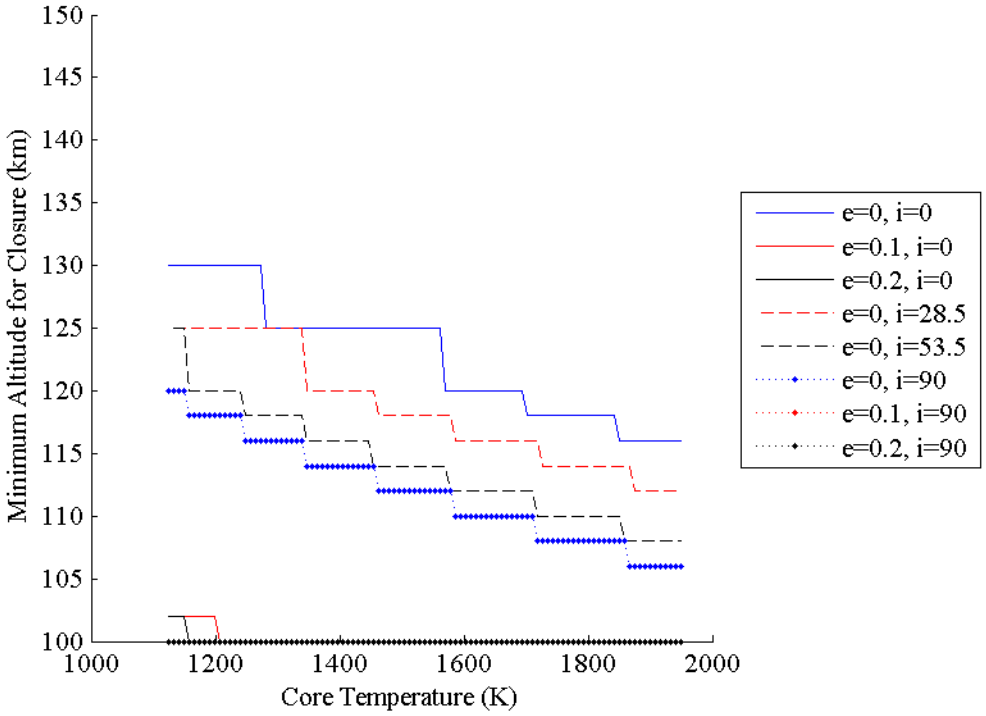

Figure 73. Minimum periapsis altitude for closure for a baseline nuclear air-breathing rocket with varying core temperature for a range of inclination/eccentricity combinations.

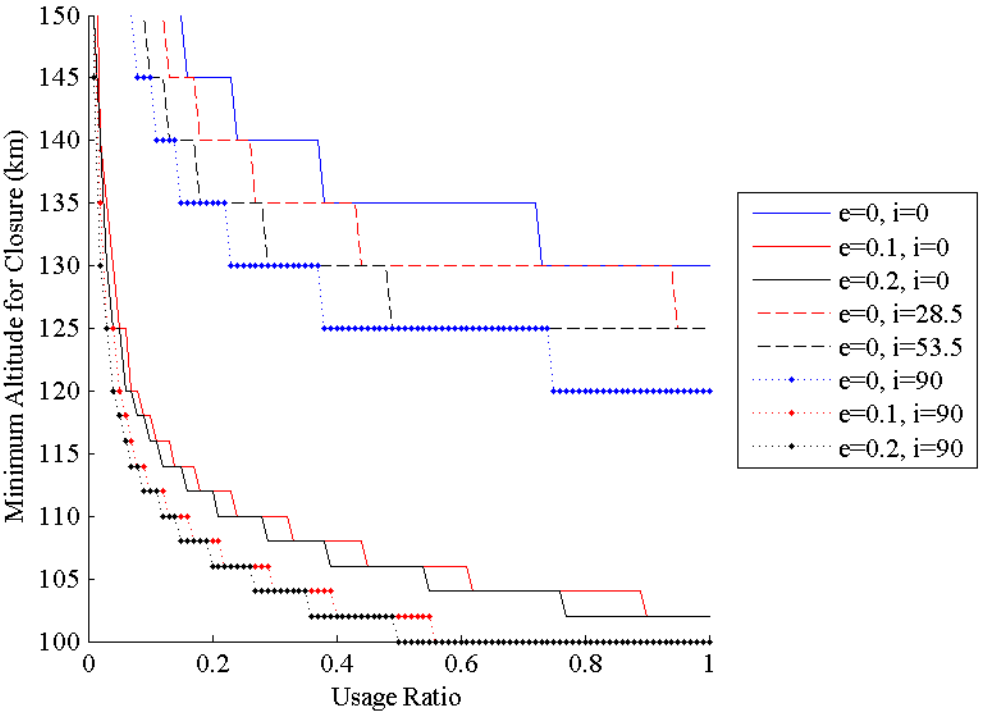

Figure 74. Minimum periapsis altitude for closure for a baseline nuclear diverter rocket with varying usage ratio for a range of inclination/eccentricity combinations.

Nuclear-powered propellant-collecting vehicles exhibit far larger regions of feasibility in periapsis altitude space for the baseline case than solar-powered vehicles. Circularly-orbiting nuclear-powered vehicles may occupy altitudes as low as 118-130 km, in contrast with 220-250 km for the equivalent solar-powered options. While presently available solar technology does not appear sufficient to allow propellant-collecting vehicles to store a sizeable surplus of propellant for later use on the basis of its altitude limitations, nuclear-powered vehicles can perhaps operate low enough in the atmosphere to make this option viable.

6.2.2 Ideal Case – Potentially Achievable Technology

The results presented in the previous subsection suggest presently available solar technology may support propellant collection, and future developments may improve its applicability. Figure 75 presents the minimum periapsis altitude for closure for an ideal solar collector rocket with varying collector efficiency. This figure presents results which are analogous to those presented in Figure 63 for the baseline case. The plot contains the anticipated asymptote near zero as in the baseline case, however the ideal results experience a significant downward shift in minimum periapsis altitude for closure. An ideal circular-orbiting collector may operate as low as 160-180 km depending on inclination, whereas a baseline case collector in the same circular orbit may operate only as low as 220-250 km. A similar downward shift occurs for eccentric orbits as well, and these shifts are consistently present among all of the solar-powered vehicle types.

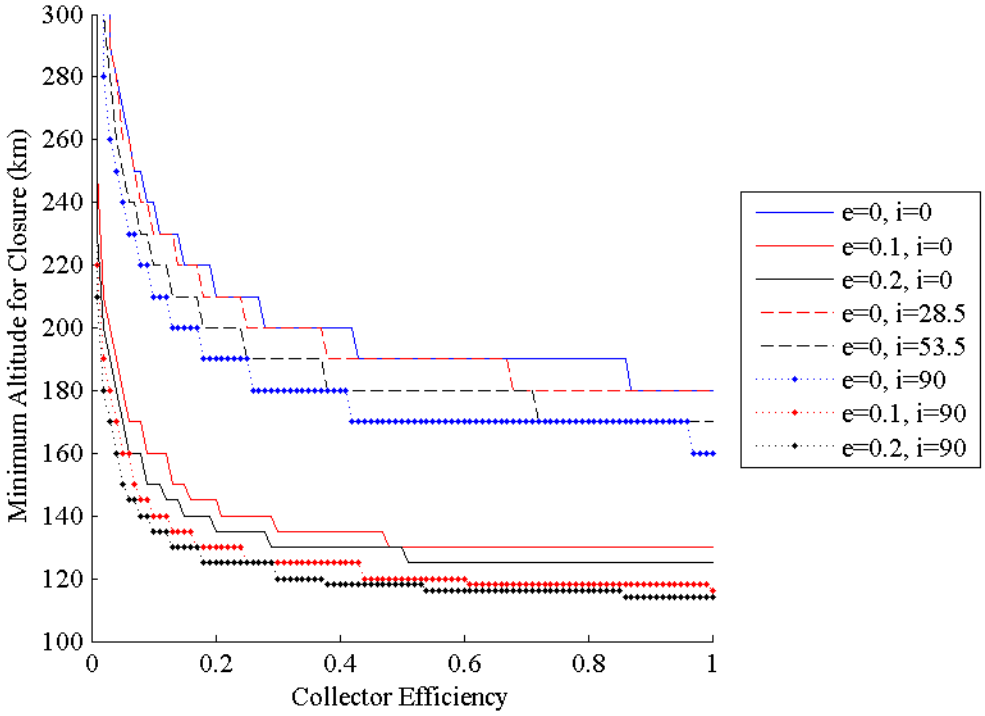

Figure 75. Minimum periapsis altitude for closure for an ideal solar collector rocket with varying collector efficiency for a range of inclination/eccentricity combinations.

Improving thruster efficiency appears to have the same magnitude of effect for both the ideal and baseline cases. Figure 76 plots the evolution of the minimum periapsis altitude for closure for a solar air-breathing rocket with varying thruster efficiency. Both the results from Figure 64 and Figure 76 indicate approximately 20-30 km of altitude reduction as a result of improving thruster efficiency from the Cifali result to the ideal result. This result is consistent among the other vehicle types as well. The difference between the Cifali result and the ideal result indicate the relative contribution fully developing air-compatible thruster technology has when compared with the other developments.

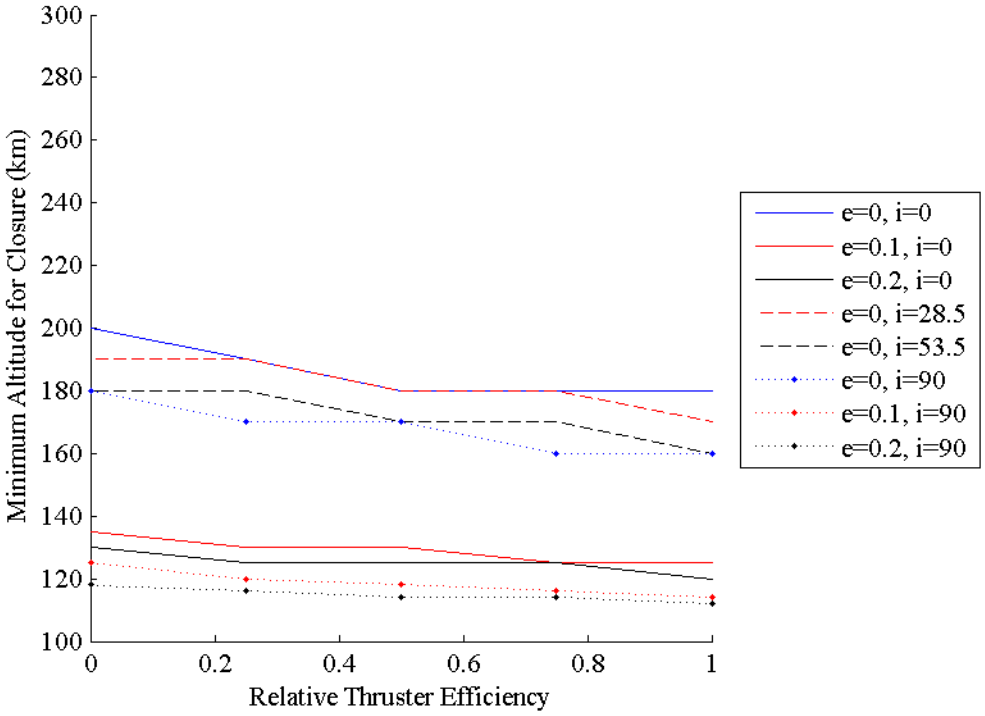

Figure 76. Minimum periapsis altitude for closure for an ideal solar air-breathing rocket with varying thruster efficiency for a range of inclination/eccentricity combinations. Values on the left represent Cifali's result, while the values on the right represent the "ideal" thruster case.

Consider the effect of improving solar panel efficiency to the theoretical limit in the ideal case as a competing contribution. Figure 77 plots the result of improving panel efficiency on the minimum periapsis altitude for closure for the ideal case. Like the thruster efficiency, the circular orbit cases exhibit a nearly linear decrease in minimum altitude by 30 km over the range of efficiency studied. This indicates that thruster efficiency and panel efficiency are approximately equivalent paths forward to improve solar propellant collection capability from a performance improvement perspective. The sensitivity analysis results from Chapter 5 support this point: the required and generated powers for a solar air-breathing rocket have an equivalent magnitude of elasticity with respect to thruster efficiency and solar panel efficiency, respectively.

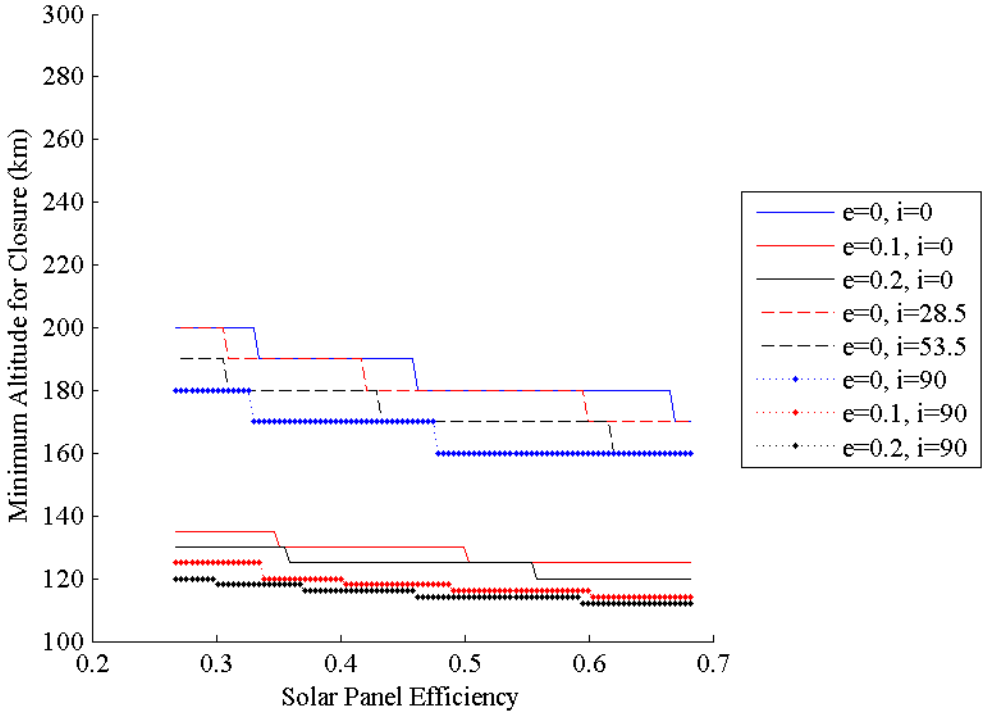

Figure 77. Minimum periapsis altitude for closure for an ideal solar air-breathing rocket with varying solar panel efficiency for a range of inclination/eccentricity combinations.

Because the body drag coefficient results do not exhibit any changes between the baseline and ideal solar cases, these results are not presented here. Thus, the final remaining parameter to consider is the usage ratio, as plotted in Figure 78 for an ideal solar collector rocket. As anticipated from previous figures plotting usage ratio and minimum periapsis altitude for closure, an asymptote is present near zero usage ratio. Similarly, the range of minimum altitude is shifted downward for the ideal case in relation to the baseline case. Unlike in the baseline case however, the effect of increasing usage ratio on the minimum periapsis altitude appears to decline at high usage ratios.

Figure 68 shows that usage ratio continues to affect the periapsis altitude in the baseline case, whereas minimum feasible altitude largely stabilizes beyond a usage ratio of 0.5 for circular orbits in the ideal case. This flattening of the response is a result of the behavior of the ideal specific impulse/thruster efficiency curve. For the moderate usage ratios and enhanced collector efficiency of the ideal case, the thruster efficiency

decreases at a rate similar to the rate of increase of the usage ratio. In some cases, this can even lead to increasing power requirements.

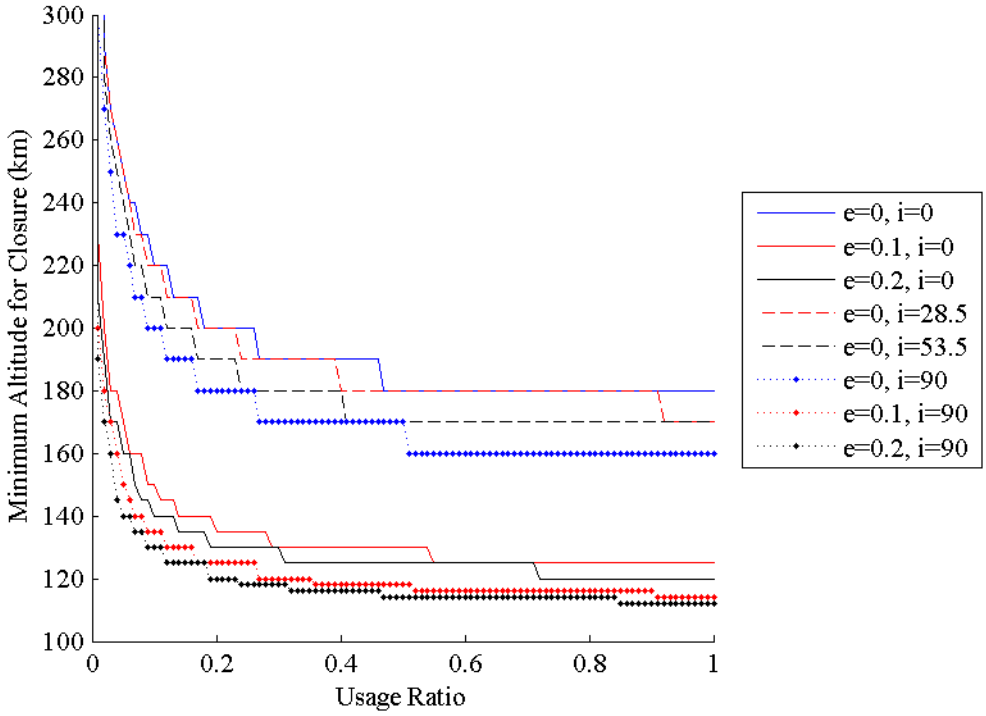

Figure 78. Minimum periapsis altitude for closure for an ideal solar collector rocket with varying usage ratio for a range of inclination/eccentricity combinations.

To review, the ideal case is superior to the baseline case in that it has: higher thruster efficiency, higher collector efficiency, higher solar panel efficiency, and lower body drag coefficient. Together, these advantages sum to deliver a noticeable and enabling improvement for solar-powered vehicles. As demonstrated in the preceding figures, an ideal circular-orbiting collector may operate as low as 160-180 km depending on inclination, whereas a baseline case collector in a circular orbit may operate only as low as 220-250 km. In both cases the minimum periapsis altitude for closure lies well below the altitude at which GOCE demonstrated VLEO operation for 4.5 years. Furthermore, ideal case non-air breathing vehicles can occupy altitudes where they may be able to collect a sizeable amount of ambient gas. This potential capability of an ideal solar propellant collection vehicle is assessed in the next section of this chapter in more detail.

The ideal nuclear power cases exhibit a similar amount of improvement in minimum altitude as the solar power cases, as demonstrated in the following results. Figure 79 presents the minimum periapsis altitude for closure for the ideal nuclear collector rocket with varying collector efficiency and orbit conditions. Circular orbits achieve closure as low as <100-110 km, depending on inclination. Eccentric orbits also experience improvement in minimum altitude when transitioning to the ideal case. The altitude appears to drop below the modeling limit imposed in this work, with most collector efficiency values closing at 100 km. Although not as severe as in the baseline case, the effect of collector efficiency on the minimum periapsis altitude also diminishes at high values for the ideal case. As with before, this result occurs because of the aforementioned relationship between specific impulse and thruster efficiency.

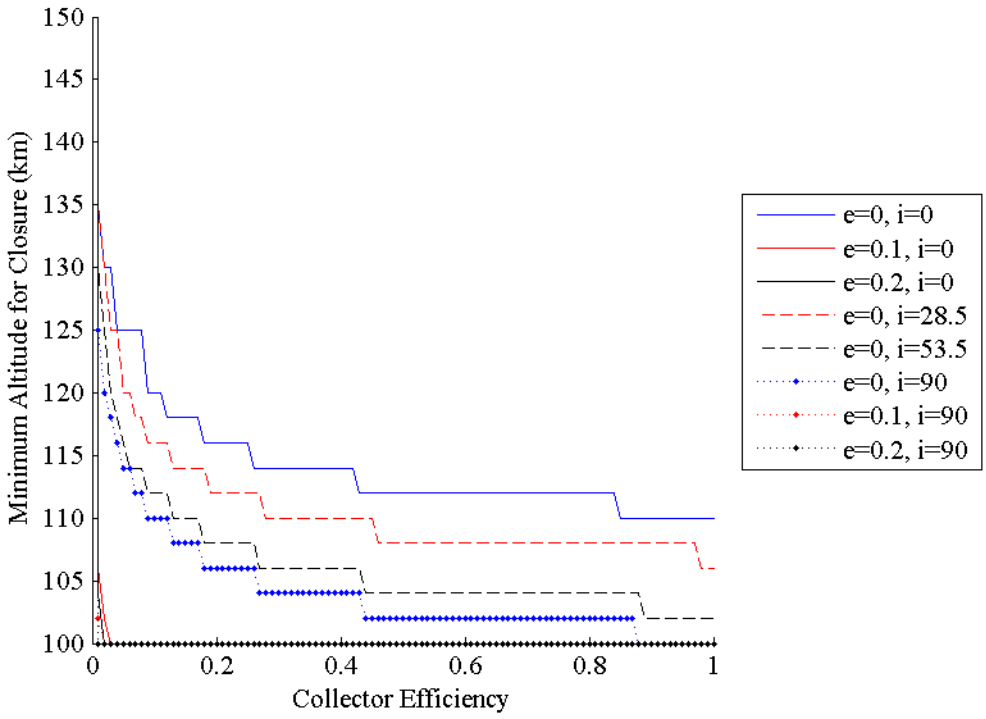

Figure 79. Minimum periapsis altitude for closure for an ideal nuclear collector rocket with varying collector efficiency for a range of inclination/eccentricity combinations.

In addition to generally reducing the minimum altitude for closure, some other behavior changes when transitioning from the baseline cases to the ideal cases. Figure 80 plots the altitude results for varying collector efficiency on a nuclear air-breathing ramjet.

The transition in drag coefficient from Sentman's analytical result to the minimum case leads to a condition where the effective body drag coefficient approaches zero at unity collector efficiency, which leads to the minimum altitude approaching the modeling limit at unity collector efficiency. This is an artifact of the modeling, which is not physically realizable because collector efficiency can never reach unity. Specifically, it results from the assumption that the flow into the vehicle encounters no losses, an assumption which loses validity at very high collector efficiency.

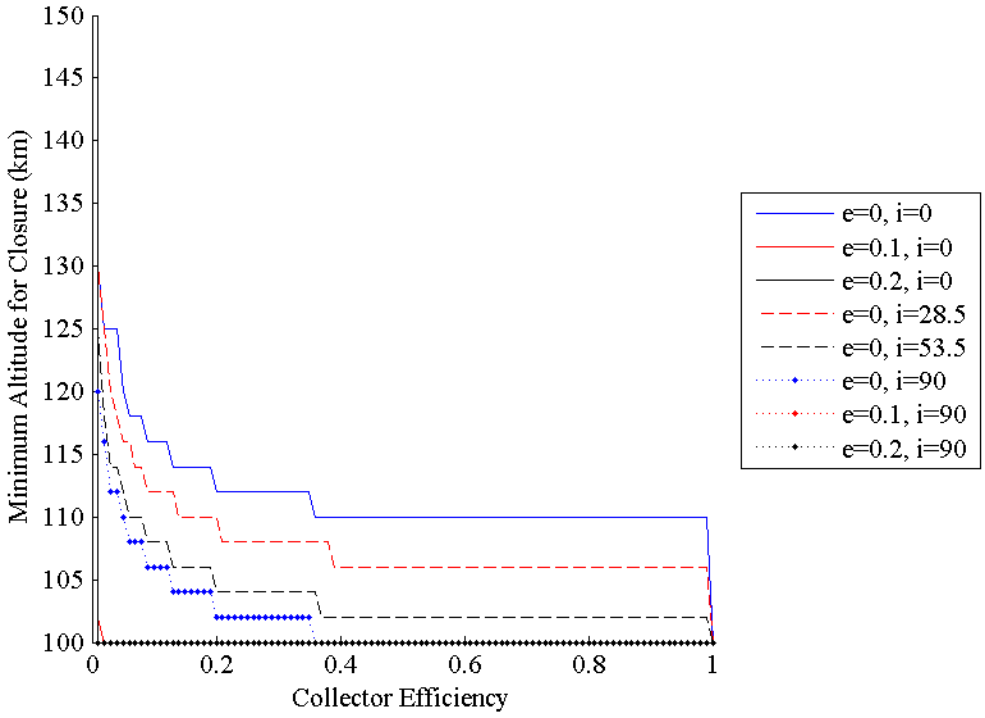

Figure 80. Minimum periapsis altitude for closure for an ideal nuclear air-breathing ramjet with varying collector efficiency for a range of inclination/eccentricity combinations. Note the drop-off in altitude as collector efficiency approaches unity.

In the ideal nuclear cases, the minimum altitude for closure becomes very insensitive to drag coefficient and thruster efficiency. Additionally, it becomes less sensitive to usage ratio as well. Figure 81 plots the minimum altitude results for an ideal nuclear collector rocket as usage ratio varies from zero to one. Similar to the collector efficiency, the effect of increasing the usage ratio diminishes after exceeding ~0.45.

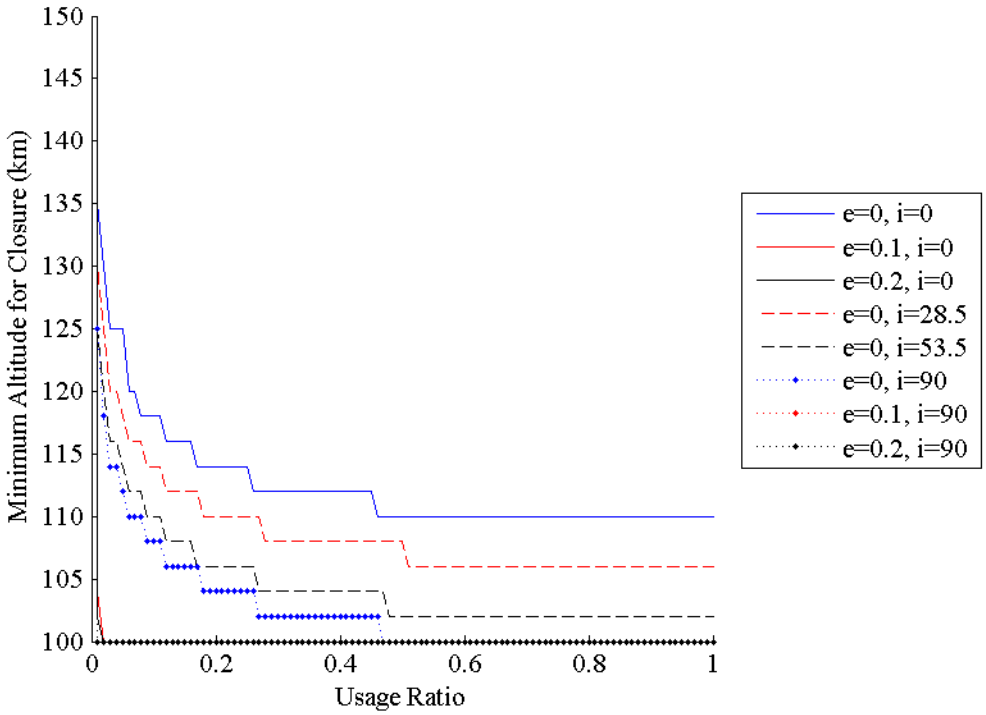

Figure 81. Minimum periapsis altitude for closure for an ideal nuclear collector rocket with varying usage ratio for a range of inclination/eccentricity combinations.

The preceding results for the ideal nuclear cases effectively indicate that an ideal nuclear propellant-collecting vehicle can operate anywhere above 110 km in effectively any orbit. With the careful selection of orbit, even the present level of nuclear technology appears capable of supporting operation both at, and even below the Karman line. However, other issues become important at these low altitudes. Heating, the rapid growth of aerodynamic forces, and orbit stability all become critical design considerations. Thus, although feasible solutions exist in power-space for propellant collection, these additional considerations not addressed in this work may otherwise prohibit operation at these altitudes.

6.2.3 Area Ratio Plots

The results from the previous subsection result from optimizing periapsis altitude while leaving the area ratio free to vary. Varying the area ratio thus allows the design to

accommodate minor changes in required power without changing altitude. This leads to variations in area ratio like those plotted in Figure 82, which provides the minimum area ratio for a baseline solar air-breathing rocket as a function of varying solar panel efficiency and a variety of orbit configurations. These area ratios correspond to the results plotted in Figure 67 for the minimum periapsis altitude for closure. Examination of the figure reveals a minimum and maximum value of area ratio for which closure is possible as a function of the orbit conditions.

The vehicle types again cluster into groups of non-air breathers and air-breathers with regards to the maximum value of area ratio seen in the plots. Air-breathers have a peak closeable area ratio around ~35 as demonstrated in Figure 82. In contrast, non-air breathers peak at only ~22. Careful examination of the required power equations leads to a geometric explanation of this difference. The required power equations for non-air breathers include a compression term which serves to shift the required power curve upward. They also include the usage ratio multiplier on the front of the area ratio terms which increases the slope of the required power curve. Thus, the non-air breather curves increase more rapidly which leads to the tangent point with the generated power shifting to lower values of area ratio. Beyond these values closure is no longer possible due to the curvature of the required power lines for the solar-powered vehicles, and so the vehicle must move to a higher altitude to attain closure instead.

The baseline nuclear-power cases show a similar result, with maximum area ratio reaching approximately 50 for air-breathers and 25 for non-air breathers. The higher performance of the nuclear system drives up the maximum attainable area ratio for closure by increasing the slope of the generated power line. The effect of improved performance also influences the maximum area ratio for the ideal cases. Ideal solar power systems can attain area ratios as high as ~65 for air-breathers and ~35 for non-air breathers. Similarly, ideal nuclear air-breathers can operate at area ratios as high as ~95 for air-breathers and ~75 for non-air breathers.

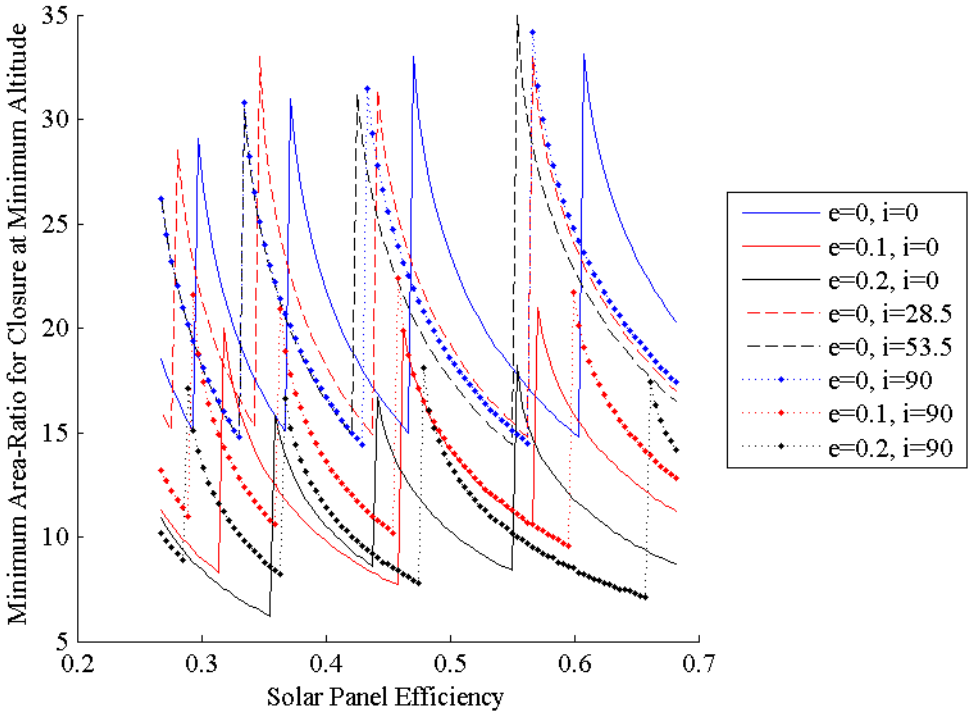

Figure 82. Variation of minimum area ratio for closure with varying solar panel efficiency for the baseline case solar air-breathing rocket.

6.3 Propellant Throughput

One way to quantify the benefit of propellant collection is by examining the propellant throughput. Assuming an identical value of specific impulse, thruster efficiency, and drag; the collected mass flow rate or propellant throughput provides an order-of-magnitude estimate of the quantity of propellant required to maintain an orbit for both a propellant-collecting vehicle and a non-propellant collecting vehicle.

Propellant throughput is highly dependent on orbital parameters, as demonstrated in Table 10. Table 10 presents the minimum periapsis altitude and time-average area-specific propellant throughput for a baseline air-breathing ramjet with varying power source, inclination, and eccentricity. As demonstrated in Chapter 4, periapsis altitude drives the value of the oncoming mass flow rate which in turn drives the value of the propellant throughput. For constant eccentricity, the data presented in Table 10 follows this behavior.

The effect of inclination is noticeable when comparing the zero and 28.5 degree inclination circular orbit cases for solar power. Both inclinations have the same minimum periapsis altitude, but the 28.5 degree case has a slightly reduced propellant throughput. Recalling the results from Chapter 4, the average mass flow rate term experiences variation with inclination in addition to altitude. Additionally, the location of the minimum mass flow rate in inclination-space varies with altitude. This variation leads to the polar orbits having higher propellant throughput in the solar case whereas the equatorial orbits have higher propellant throughput in the nuclear case.

Table 10. Minimum periapsis altitude and propellant throughput for a baseline air-breathing ramjet with varying power source, inclination, and eccentricity.

Inclination (degrees)	Eccentricity	Solar h_{min} (km)	Solar $\overline{\dot{m}''}_{in}$ (mg/m^2-s)	Nuclear h_{min} (km)	Nuclear $\overline{\dot{m}''}_{in}$ (mg/m^2-s)
0	0	250	0.384	130	117.5
0	0.1	170	0.221	102	43.6
0	0.2	160	0.19	102	26.5
28.5	0	250	0.354	125	144
53.5	0	230	0.487	125	73.5
90	0	220	0.552	120	109
90	0.1	150	0.338	100	26.5
90	0.2	145	0.257	100	16.0

Eccentricity also contributes to the propellant throughput, with eccentric orbits experiencing lower average throughput than circular orbits. As stated in previous chapters, increasing eccentricity drives the orbit out to higher altitudes where the atmospheric density is reduced. Thus, although the eccentric orbits have a lower minimum periapsis, their higher apoapsis tends to counteract any potential benefit in propellant throughput.

Table 11 presents the minimum periapsis altitudes and propellant throughputs for propellant-collecting vehicles operating with the baseline parameters and for the ideal parameters in a polar, circular orbit. As demonstrated in the previous section, the minimum periapsis altitude is minimized for the nuclear-powered ideal vehicles. The data

indicates very little variation in either the minimum altitude or the throughput for different vehicle types with the same power source and design parameters. However, air-breathing vehicles can generally reach slightly lower altitudes than the other vehicles as a result of having a lower specific impulse requirement.

Table 11. Minimum altitude and propellant throughput for baseline and ideal vehicles operating in a polar, circular orbit.

Vehicle Type	Baseline h_{min} (km)	Baseline $\overline{\dot{m}''}_{in}$ (mg/m^2-s)	Ideal h_{min} (km)	Ideal $\overline{\dot{m}''}_{in}$ (mg/m^2-s)
Solar Air-breathing Rocket	220	0.56	160	8.9
Solar Diverter Rocket	250	0.27	170	5.9
Solar Collector Rocket	250	0.27	170	5.9
Solar Air-breathing Ramjet	220	0.56	160	8.9
Solar Diverter Ramjet	250	0.27	170	5.9
Nuclear Air-breathing Rocket	120	110	100	8794
Nuclear Diverter Rocket	125	52	100	8794
Nuclear Collector Rocket	125	52	100	8794
Nuclear Air-breathing Ramjet	120	110	100	8794
Nuclear Diverter Ramjet	125	52	100	8794

The propellant throughput values presented in Table 10 and Table 11 are in units of mg/m^2-s. For reference, 1 mg/m^2-s is approximately equal to 3.15 kg/m^2-yr. For non-air breathing vehicles, the propellant throughput values provide an estimate of how much propellant is available for collection. Baseline solar collector vehicles have as much as 851 g/m^2-yr of mass flow available for collection whereas baseline nuclear vehicles may have as much as 164 kg/m^2-yr available. Ideal designs support larger throughputs, with solar-powered vehicles having as much as 18.6 kg/m^2-yr and nuclear-powered vehicles having as much as 27,700 kg/m^2-yr available for collection. It is clear from these values alone that solar power does not have sufficient performance to operate a collector rocket for a propellant depot application, nor will it ever have sufficient performance.

However, nuclear-powered vehicles support much larger throughputs than solar-powered vehicles. Thus, nuclear-powered vehicles may yet support a propellant depot

application. Absent from the throughput values presented in Table 11 is any consideration of usage ratio. A propellant-collecting vehicle must use a portion of the throughput for drag-compensating thrust, thus reducing the fraction of the throughput available for collection. Eq. (6.1) describes the time-average area-specific propellant storage rate as a function of the propellant throughput and the usage ratio. The optimum usage ratio to maximize the propellant storage rate is the usage ratio which minimizes the energy cost to store the propellant. This minimum is located where the partial derivative of the energy cost with respect to the usage ratio is equal to zero, as expressed in Eq. (6.2).

$$\overline{\dot{m}''}_{store} = (1-\epsilon)\overline{\dot{m}''}_{in} = (1-\epsilon)\eta_c\overline{\rho v} \tag{6.1}$$

$$\frac{\partial\left(\frac{\overline{P''}_{req}}{\overline{\dot{m}''}_{store}}\right)}{\partial\epsilon} = 0 \tag{6.2}$$

If one neglects the compression energy term and holds thruster efficiency constant, then the value of usage ratio which satisfies Eq. (6.2) is 0.5 for all non-air breathing vehicles, which is the value stated by Demetriades [32]. Earlier discussions in this work demonstrate that the compression energy term is in fact small compared with the thrust term, and likely negligible.

Continuing to assume the thruster efficiency is constant; the effect of the compression term on the location of the optimum usage ratio can be determined as a function of the ratio of the compression and thrust terms for the collector rocket. Figure 83 plots this function, where the result on the left edge is the ideal "compression neglected" result and the result on the right edge is the optimum usage ratio for compression power equal to thrust power. Even at compression/thrust power parity the optimum shifts by less than 0.1, indicating the inclusion of compression power has little

effect on the optimum usage ratio. However, as seen numerous times in the preceding results, the relationship between thruster efficiency and required specific impulse can introduce unanticipated behavior into propellant collection physics.

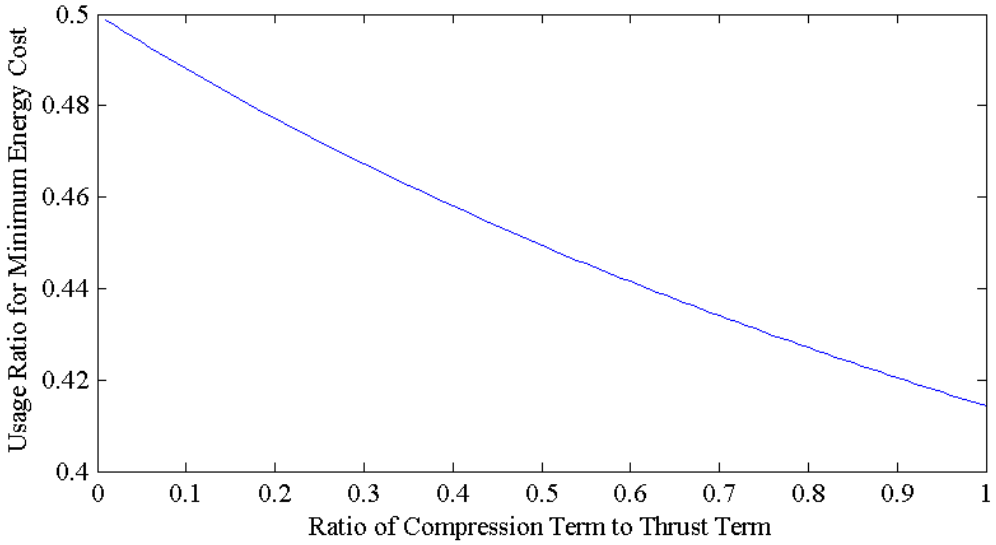

Figure 83. Optimum usage ratio as a function of the ratio of the compression and thrust terms in the collector rocket required power equation.

Figure 84 plots the maximum time-average area-specific mass storage rate for a baseline nuclear collector rocket as a function of varying usage ratio and orbit inclination/ eccentricity. The data curves exhibit a saw-tooth-like variation as a result of the numerical discretization of altitude performed to improve the computational tractability of the model. The result of the discretization is that small increases in usage ratio do not permit a jump to a new altitude to take advantage of the reduced thrust power, but do reduce the mass storage rate, leading to a monotonic decrease towards the point (1,0) on the plot within each saw-tooth.

Despite this limitation in the quality of the data, the general behavior remains identifiable. A peak in mass storage rate occurs around a usage ratio of 0.45 for both circular and eccentric orbit cases. The quality of the data is insufficient to elucidate any dependence the peak mass storage rate may have with inclination. A peak around 0.45 is close to the 0.5 result from Eq. (6.2), although some deviation is present. The

compression power is approximately ten percent of the total power for the circular, equatorial orbit condition at the peak mass storage rate. Thus, the presence of the compression term causes a downward shift in optimum usage ratio by 0.012 from the Eq. (6.2) result. The remainder of the shift in usage ratio must then result from the variation of thruster efficiency with specific impulse.

Increasing the usage ratio serves to reduce the required specific impulse by allowing a larger portion of the flow to be utilized by the thruster. However, reducing the specific impulse reduces the thruster efficiency. The result of this behavior is an upward shift in required power beyond what it would be absent the presence of the thruster efficiency variation. Increasing the required power with increasing usage ratio serves to skew the optimum usage ratio to lower values.

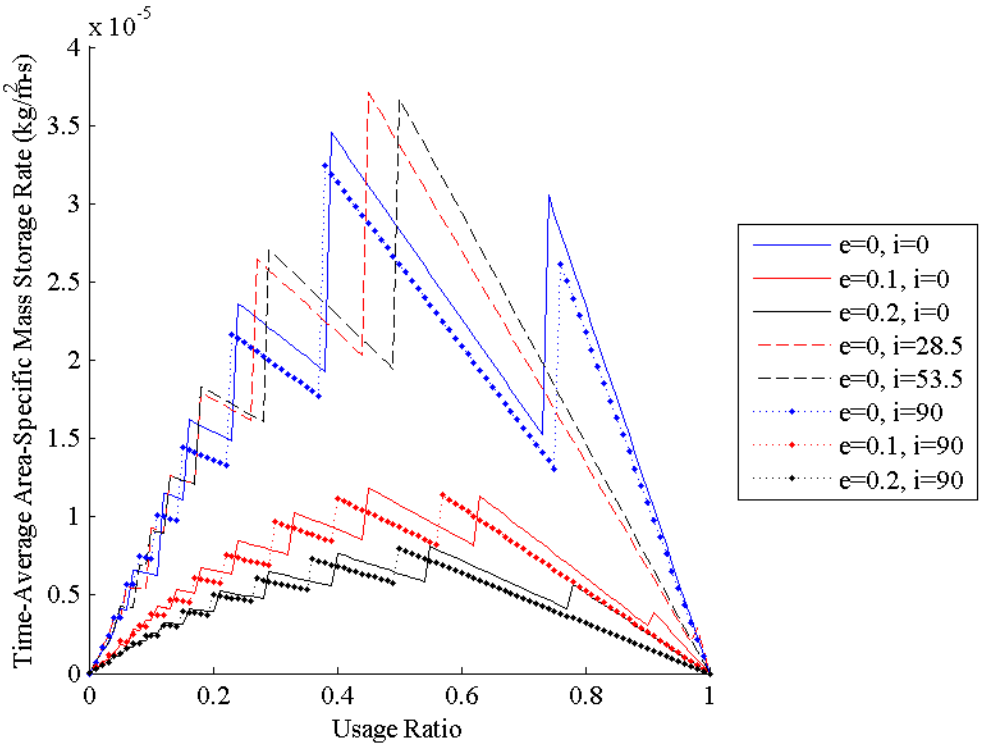

Figure 84. Maximum mass storage rate for a baseline nuclear collector rocket as a function of varying usage ratio and orbit.

Despite this shift from thruster efficiency, the optimum usage ratio still occurs at the minimum energy cost condition. Figure 85 presents the energy cost for the conditions

presented in Figure 84. Again, the saw-tooth pattern present in the data results from the discretization of the altitude. However, the plot indicates the minimum energy cost is located near a usage ratio of 0.45, consistent with the location of the optimum usage ratio.

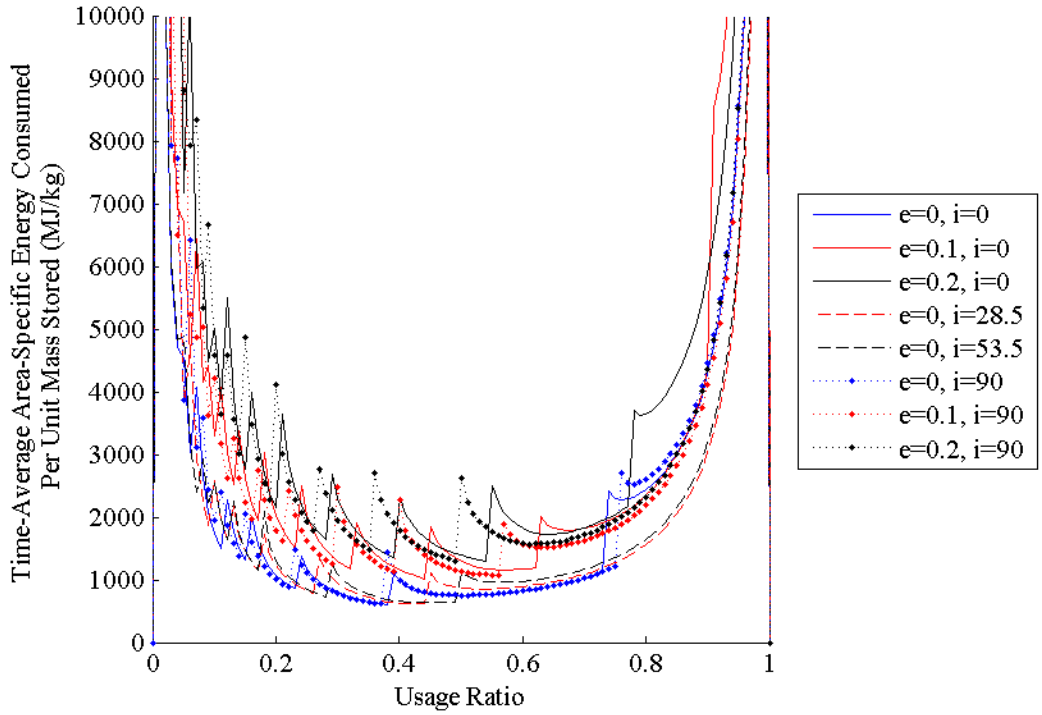

Figure 85. Energy consumed per unit mass stored for a baseline nuclear collector rocket as a function of varying usage ratio and orbit.

As anticipated, the energy cost asymptotes near a usage ratio of zero and one. As usage ratio approaches zero, the thrust power increases because of restricted mass flow to the thruster. Zero mass is stored by definition at the unity usage ratio condition, which leads to the singularity at unity usage ratio. Neglecting the saw-tooth variations, the minimum energy cost for the baseline nuclear collector rocket appears to vary between 1 and 2 GJ/kg. Eccentric orbits require more energy because they have a lower periapsis altitude where the majority of collection occurs.

Figure 86 for the ideal nuclear collector rocket case exhibits numerous differences in behavior when compared with Figure 84 for the baseline case. The optimum usage ratio shifts much lower, to about 0.25 for the circular orbit cases. Eccentric orbits exhibit an even larger shift, but this is an artifact from reaching the 100 km altitude modeling

limit. The compression power is only ~6% of the total power for the peak mass storage rate condition on the circular orbits, which results in a deviation in the optimum usage ratio of only 0.007. Clearly, the cause of the shift is the implicit variation of thruster efficiency with usage ratio. To review, the ideal case makes use of the ideal thrust curve as defined in Eq. (3.45) and displayed in Figure 31 from Section 3.2.5. As can be seen from that figure, the ideal thruster efficiency is far more sensitive to variation in specific impulse than the experimental result from Cifali et al. [21]. This increased sensitivity results in a stronger shift in optimum usage ratio. This once again illustrates the importance of the implicit relationship between the required specific impulse and the thruster efficiency.

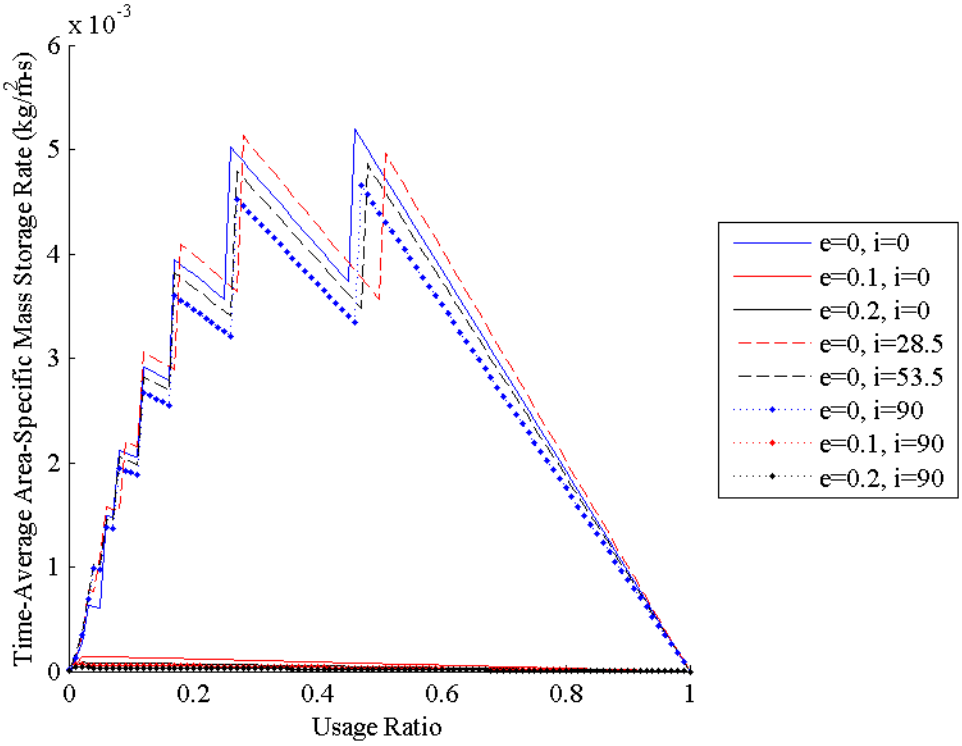

Figure 86. Maximum mass storage rate for an ideal nuclear collector rocket as a function of varying usage ratio and orbit.

Figure 87 demonstrates that the minimum energy cost for the ideal case also lies at the optimum usage ratio. Whereas the eccentric cases exhibited a higher energy cost in the baseline case results, in the ideal case they appear to have a lower energy cost. This

result is an artifact of the eccentric cases reaching the 100 km periapsis altitude modeling limit. However, careful observation of the magnitude of the energy costs in Figure 85 and Figure 87 reveals that the energy cost in the ideal case is significantly lower than in the baseline case. The ideal case benefits from several improved efficiency terms, each of which contributes to reducing the energy cost.

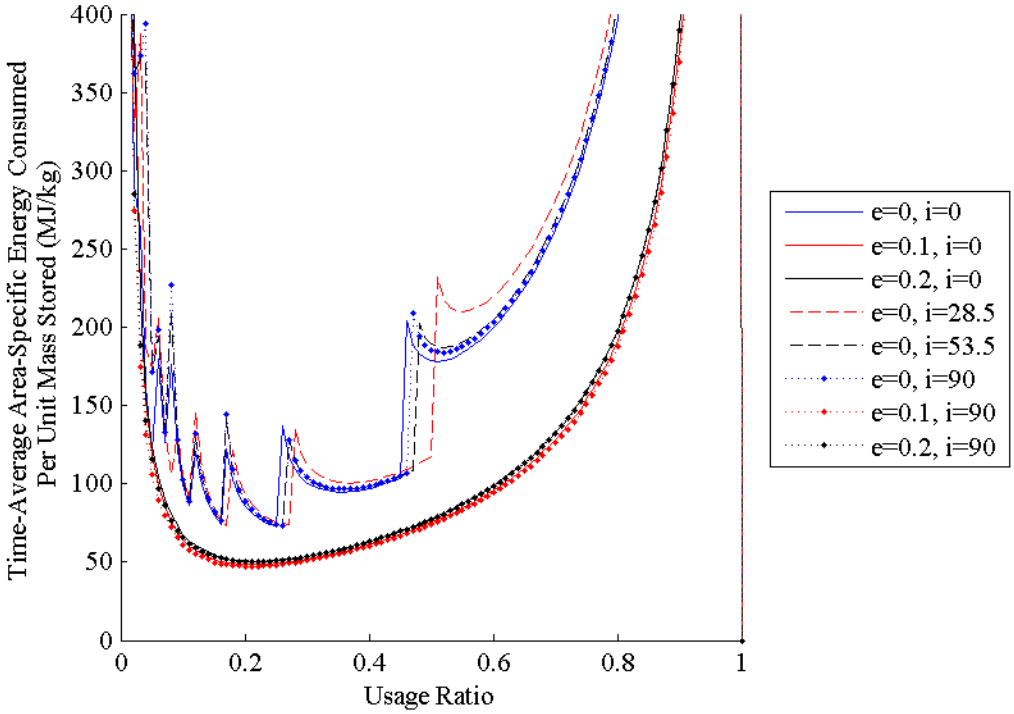

Figure 87. Energy consumed per unit mass stored for an ideal nuclear collector rocket as a function of varying usage ratio and orbit.

The results from this analysis indicate that a baseline case nuclear collector rocket can attain a time-average area-specific mass storage rate as high as 37 mg/m^2-s, equating to 117 kg/m^2-yr. In contrast, an ideal nuclear collector rocket may attain a time-average area-specific mass storage rate as high as 5,100 mg/m^2-s, equating to 16,100 kg/m^2-yr. Such a mass storage rate is likely sufficient to enable the servicing of numerous vehicles per year. As a final note, this section presents results relating to a nuclear collector rocket vehicle type. The results are nearly identical for diverter vehicles as well, varying by only a few percent.

6.4 Summary

The preceding sections in this chapter identify where propellant collection technology can sustain an orbit, and where it can store a specified portion of the ingested flow as a function of relevant design factors. The standard applied to develop this "region" of technical feasibility is the average power standard: the required power must on average be less than the generated power. Whereas the solar and nuclear generated power equations from Section 3.1 vary linearly with the spacecraft body-to-planform area ratio, the required power equations vary as the square of the area ratio to first order. Consequently, the propellant collection problem takes the form of the intersection of a line and a parabolic curve as demonstrated in Section 6.1.

Plotting the required power curves for different vehicle types at identical design points demonstrates the difference in power and specific impulse requirements between the vehicle types. Under the assumptions made in this work, the required power curves for the vehicle types cluster into two groups. The group with the lower power requirement consists of the air-breathing vehicle types, and the higher power requirement group consists of the non-air breathing vehicle types. Both ramjet variants have slightly reduced power requirements when compared to their rocket counterparts. However, this reduction is small compared with the reduction which is afforded by not storing propellant.

Section 6.2 identifies the regions of technical feasibility for solar and nuclear-powered vehicles for two cases. The first case is the baseline case, which represents presently available technology and capability. The second case is the "ideal" case, which represents the potentially achievable or theoretical limit of technology and capability. Section 6.2 presents the minimum periapsis altitude for closure as a function of varying design and orbit parameters to identify the regions of technical feasibility for each of these cases. Periapsis altitude is selected as the main parameter of interest because Chapter 5 identifies it as the parameter that the required power equations are most

sensitive to. Technical feasibility is realizable at altitudes above the minimum periapsis altitude for closure, given the selected design parameters.

The results indicate a solar-powered propellant collection vehicle operating with presently available technology can inhabit circular orbits as low as 220-250 km in altitude, depending on inclination. Di Cara et al. suggests that propellant collection application does not offer a significant benefit above 250 km altitude because propellant requirements for counteracting drag rapidly decline above this altitude [55]. The design specifications of GOCE, which operated successfully in a 260 km sun-synchronous orbit for over four years, support this assertion. Thus, solar power may accommodate the power requirements for propellant collection at a beneficial altitude below the design orbit of GOCE.

Future developments have the potential to improve the applicability of this technology. The ideal-case solar power results present a vastly improved range of minimum altitude, between 160 and 180 km depending on inclination. This result is for a propellant collection vehicle with theoretically perfect solar arrays and a thruster which operates on the collected propellant as well as presently available thrusters operate on xenon. Thus, this minimum range represents the best possible altitude where a solar-powered vehicle can continuously operate.

Nuclear power appears far more suitable to accommodating the power requirements for propellant collection. With presently available technology, nuclear-powered propellant-collecting vehicles may continuously operate as low as 118-130 km while in a circular orbit, depending on inclination. Nuclear power has superior performance to solar power on an area-specific basis, with presently attainable nuclear power far exceeding even the theoretical limit of solar power performance. The performance of a nuclear propellant-collecting vehicle is heavily reliant on core temperature. Increasing core temperature not only increases the available electrical power, but also improves the heat rejection performance of the radiators, thus decreasing

their size and reducing drag. Consequently, the results of this chapter demonstrate that improvements to core temperature have the greatest effect on the range of feasibility for nuclear propellant-collecting vehicles.

The ideal nuclear case demonstrates performance far in excess of the baseline case, highlighting the potential for improvement of capability in this area. In a circular orbit, ideal nuclear propellant-collecting vehicles may operate as low as 100-110 km, depending on inclination. Eccentric orbits hit the Karman line at the 100 km modeling limit for most variations of the ideal design parameters.

Section 6.3 considers the propellant throughput as a measure of the potential benefit propellant collection can provide. Propellant throughput is a suitable order-of-magnitude estimate of the propellant budget required to maintain a given orbit. The results indicate that orbit parameters affect the amount of throughput a propellant-collecting vehicle may encounter. Altitude has a dominant effect, with reductions in altitude rapidly increasing the throughput. This result is anticipated, given the density-dependent parameter data presented in Chapter 4. Although eccentricity serves to reduce the periapsis altitude, it also tends to reduce throughput. This result is also anticipated given the results from Chapter 4.

The type of vehicle appears to have little effect on the throughput at the minimum altitude for closure. However, the method of power generation and the design parameters have a major effect. The propellant throughput results for the baseline and ideal solar cases indicate that solar power is not suitable for a propellant storage application, and never will be. In the baseline case, solar power can support only 851 g/m^2-yr of throughput. In the ideal case, it can support up to 18.6 kg/m^2-yr. Section 6.2 demonstrates that solar power may have an application in propellant collection for VLEO orbit maintenance, however it cannot provide the performance necessary to store propellant for a propellant depot-type application.

In contrast, nuclear power shows promise for a depot application. In the baseline case, nuclear power can support as much as 117 kg/m^2-yr of mass storage. In the ideal case, a nuclear-powered collector vehicle may store 16,100 kg/m^2-yr of propellant. These levels of performance are attained by operating at the optimum usage ratio, which is located at the value of usage ratio for which the mass-specific energy cost of storing propellant is minimized. Demetriades' analysis indicates this value to be equal to 0.5. The results in Section 6.3 demonstrate that this is not always the case. Compression power requirements contribute in a minor way to the optimum point for usage ratio, driving it down slightly to lower values. The major contribution is from the required specific impulse/thruster efficiency relationship, which also serves to shift the optimum point downward. The thruster efficiency relationship shifts the optimum usage ratio point as low as 0.25 in the ideal case results presented in this chapter, highlighting the significance of this effect.

As is evident in the results from Chapter 5 and the present chapter, the presence of the required specific impulse/thruster efficiency relationship leads to unanticipated results. This relationship has never before been factored in to propellant collection design analysis, and so its effects have never been quantified. Optimum usage ratio shifts dramatically from the first order result towards storing a higher fraction of the oncoming flow. Collector efficiency can have a point of diminishing returns. These results contradict intuition absent the thruster efficiency relationship. Propellant collection analyses must account for the coupling of thruster efficiency and required specific impulse in order to accurately predict the response of a design to variation of its performance parameters.

CHAPTER 7
CASE STUDY RESULTS

This chapter presents the case study results in support of the third research objective of this work. The two case studies examined include a VLEO science mission and a propellant collector mission to gather propellant for use by other missions. Conducting these case studies with the data from the previous chapters demonstrates the utility of those results, further validates them, and simultaneously assesses the potential benefit of propellant collection in either of these applications. Section 7.1 presents the results of the VLEO science mission analysis. Section 7.2 similarly presents the results of the collector mission analysis, and Section 7.3 summarizes the major findings in this chapter.

7.1 VLEO Science Mission

To review from Chapter 3, the VLEO science mission case study considers a solar-powered air-breathing rocket which seeks to minimize orbit altitude as an ends to maximizing scientific results. This mission is effectively a propellant-collection analog of the GOCE mission. Reducing orbital altitude in that mission allowed researchers to take measurements of the gravity field with improved accuracy over previous missions. For this study, the vehicle is assumed to make use of presently available technology, and launch on a Falcon 9 v1.1 into a high inclination orbit in order to maximize coverage. Table 12 summarizes the fixed parameters selected given the assumption of presently available technology.

Table 12. Fixed parameters for the VLEO science mission case study.

Parameter Name	Symbol	Nominal Value
Orbit Eccentricity	e	0.0
Year	N/A	2001
Collector Efficiency	η_c	0.4
Drag Coefficient	$C_{D,s/c}, C_{D,PA}$	Sentman's Result
Thruster Efficiency	η_t	Cifali's Result
Solar Panel Efficiency	η_{SP}	0.268

The first objective of the analysis is to find the minimum feasible altitude at which a solar air-breathing rocket can operate in near-polar inclinations. Subsequently, 80°, 85°, and 90° are studied as potential options. The minimum altitude given the fixed parameters at which the average required power exceeds the average generated power is 220 km. An inclination of 85° minimizes the area ratio for feasibility, as demonstrated in Figure 88. The difference in required power between inclinations is on the order of Watts; however generated power varies significantly between the polar orbit and the others.

At this altitude, specular reflection begins to exert an influence on the reaction of gas particles with a vehicle's surface. The drag coefficient can thus be driven up 10 percent or more when compared with Sentman's analytical result [49]. Figure 89 demonstrates the effect of increasing the body drag coefficient by ten percent over the nominal Sentman calculation. The required power not only begins at a higher value, but rises faster in area ratio space as well. A small increase in area ratio is sufficient to accommodate the increase in required power that the inaccuracy in drag coefficient may cause.

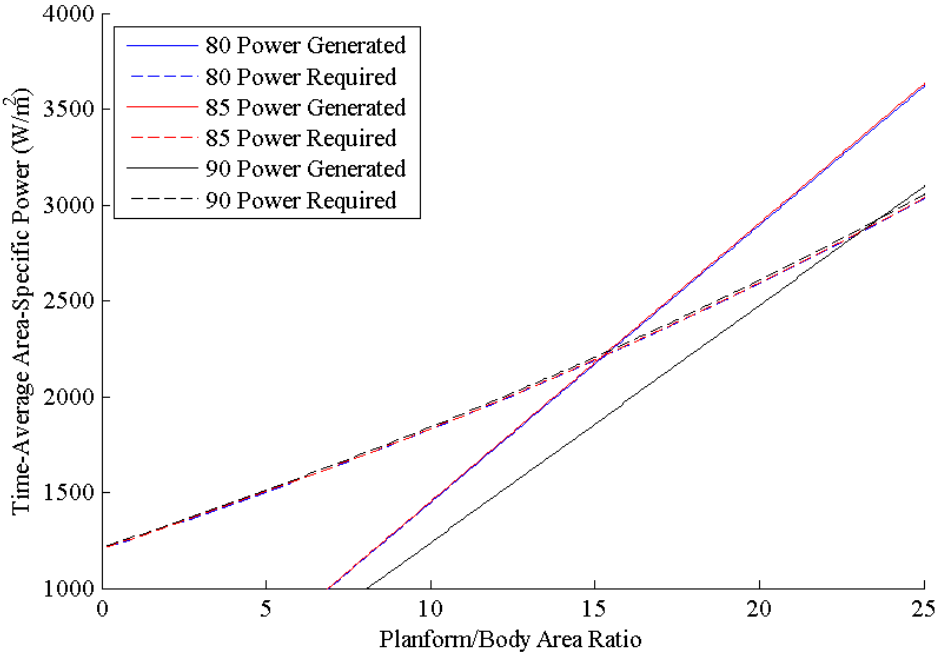

Figure 88. Required and generated power lines for a solar air-breathing rocket with the given design parameters in a 220 km, circular orbit at varying inclinations.

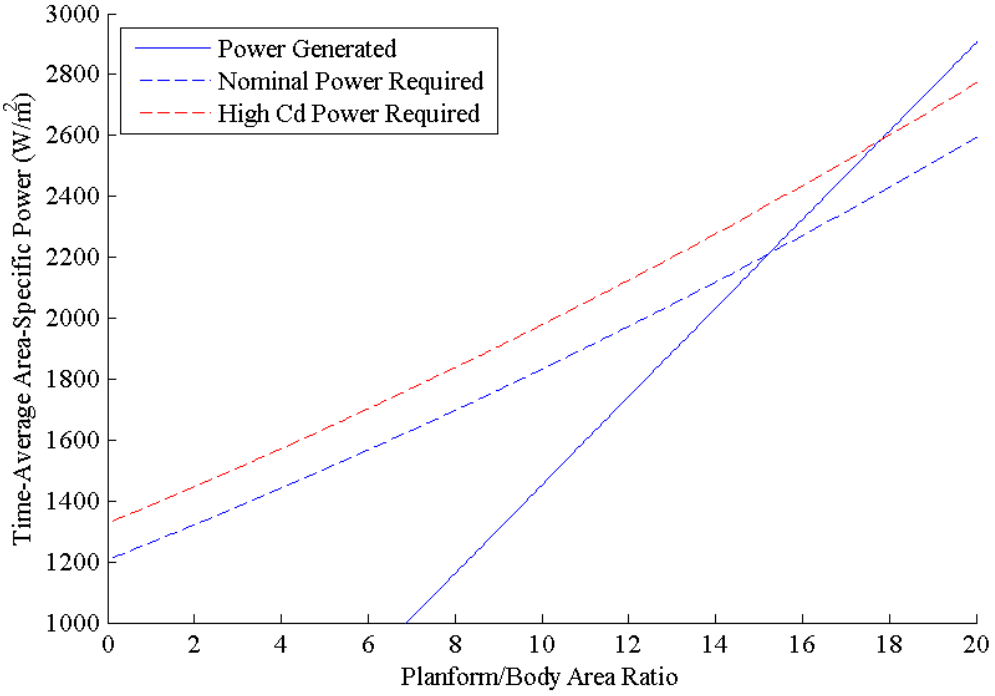

Figure 89. Effect of increasing the drag coefficient by 10 percent over the nominal value.

Figure 90 demonstrates the effect of solar activity on the range of feasible area ratios. Reducing solar activity, or in the case of this data moving back in time, has the

effect of increasing both the minimum and maximum feasible area ratios. Thus, if an area ratio closes the design at the peak of solar activity, it will also do so at any other point in the solar cycle. This is a generally applicable result: reducing solar activity reduces density, thus reducing both the area ratio-independent term and the growth rate of the area ratio-dependent terms with increasing area ratio.

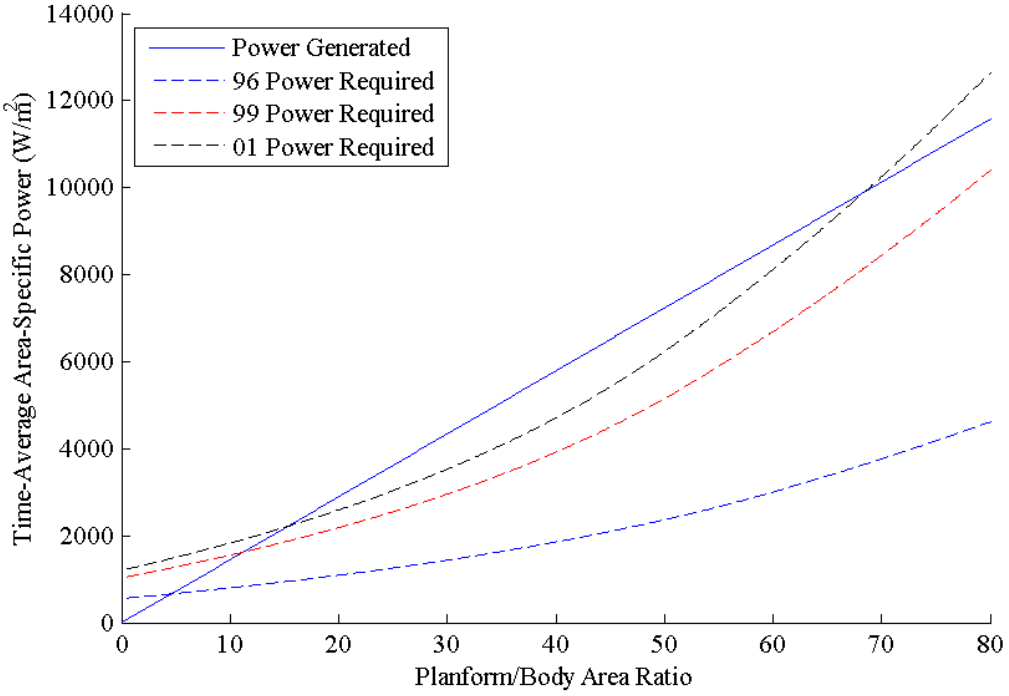

Figure 90. Required and generated power curves with varying year at the minimum feasible periapsis altitude.

However, propellant collection is an inherently unstable concept. If the required power ever exceeds the supplied power, the thrust from the vehicle becomes insufficient to completely overcome the aerodynamic drag. The remaining component of drag reduces altitude, which in turn further drives up the required power. A vehicle may be able to accommodate such a deficiency in the event that the deficiency is sufficiently temporary that the vehicle can regain a surplus in supplied power and work its way back to its operating altitude. This is further studied in the next section.

Furthermore, note the usage of the term "supplied power", rather than "generated power". This selection of words is intentional, and these two values are not equal. Internal vehicle losses between the solar arrays and the power loads/batteries can significantly reduce the power which is actually available for use. Some loss results from line resistance, but the majority of loss arises from converting and conditioning the power generated by the solar arrays into a usable form. Normally, these losses are lumped into a day loss factor and an eclipse loss factor [4]. Whereas the day loss factor accounts for losses between the solar array and the loads directly, the eclipse loss factor accounts for the losses between the solar array to the loads through the batteries. To accommodate these effects, a factor of safety is required to produce a more robust criterion for design closure. This work proposes a multiplier of two be added, such that the average generated power must double the average required power.

Imposing this revised condition on the propellant collection equations results in a shift in minimum periapsis altitude up to 250 km from the aforementioned 220 km. Figure 91 plots the ratio of generated to required power at 250 km for varying inclination and area ratio. As demonstrated from the indicated point on the figure, an area ratio of 15.3 at 85° inclination results in a ratio of generated-to-required power of two as desired. Figure 91 serves a secondary purpose of demonstrating once again the diminishing returns increasing area ratio can have. The power-ratio reaches a peak, but ultimately declines as a result of the additional planform area increasing the drag faster than it increases generated power.

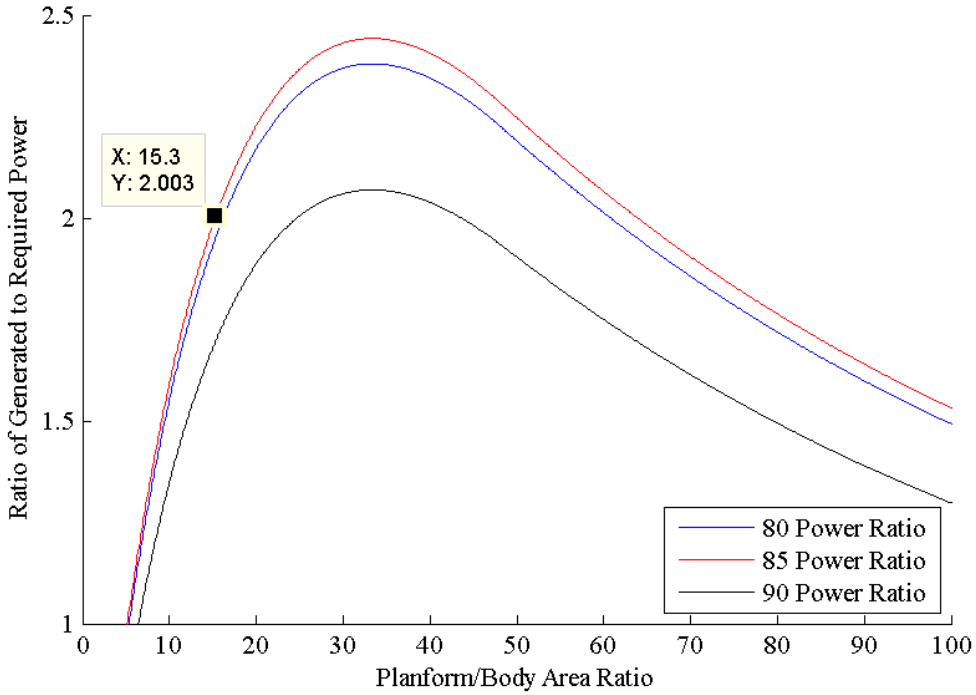

Figure 91. Ratio of generated and required power with varying area ratio and inclination for a circular, 250 km orbit in 2001.

Even with a factor of safety of two, periods of extreme solar activity may still be sufficient to drive the instantaneous supplied power below the instantaneous required power. A direct calculation of the instantaneous supplied and required powers on non-decimated STK data using the stated design parameters tests this assertion. Figure 92 plots the area-specific available excess energy for storage over the year for the case of a factor of safety equal to two in kW-hr/m^2. At first glance, the data appears to indicate that with the stated factor of safety the vehicle is overdesigned. Over 5,000 kW-hr/m^2 of energy is available for storage by the end of the year, and the energy available for storage never drops below zero.

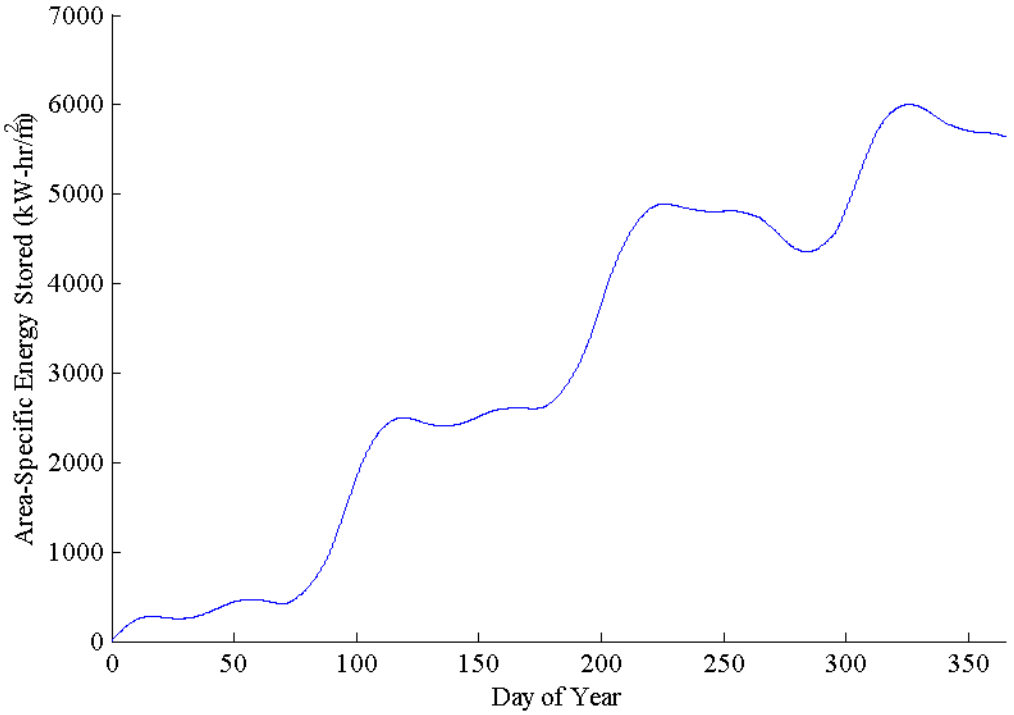

Figure 92. Area-specific energy available for storage as a function of time for a 250 km, circular, 85 degree inclination orbiting solar air-breathing rocket in 2001.

However, the data is deceptive because it does not factor in the storage capacity requirement for this quantity of energy. A conservative estimate of energy density for space-rated lithium-ion (Li-ion) batteries is 110 W-hr/kg, or 250 W-hr/L [4]. In order to actually store 5,000 kW-hr of energy, a spacecraft would have to accommodate 50,000 kg or 22 m^3 of batteries for every square meter of frontal area. These are intuitively impractical values.

The non-monotonicity of the available energy for storage in Figure 92 indicates the presence of regions where the orbit-average required power temporarily exceeds the orbit-average supplied power from the solar arrays. Figure 93 plots the area-specific energy stored by the spacecraft under the assumption that it has 1,000 kg/m^2 of Li-ion batteries, corresponding to ~50 kW-hr/m^2 of energy storage capacity. Note the presence of local minima in the data. These indicate "power droughts" as a consequence of

enhanced solar activity, where the orbit-average required power exceeds the orbit-average supplied power for several days. It is clear that, for three to four periods during the solar maximum year, activity can become so great that even a factor of safety of two can be insufficient to guarantee stable operation in a given orbit.

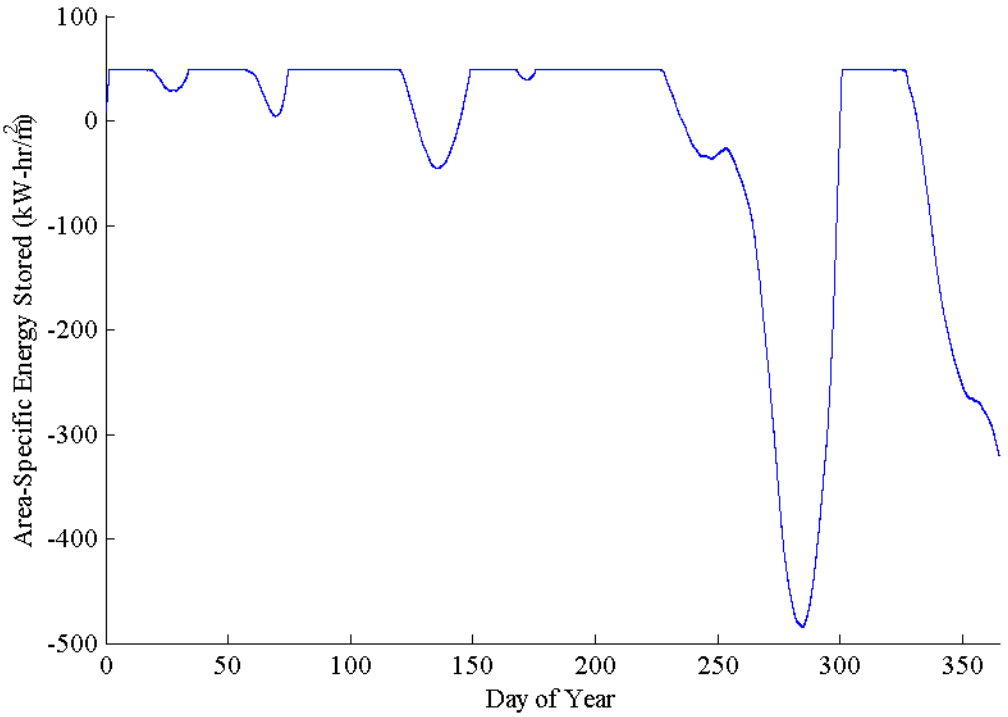

Figure 93. The area-specific energy stored by the spacecraft assuming it has 1,000 kg of batteries per square meter of frontal area.

A closer view of the plotted data in Figure 93 reveals the normal eclipse-to-day cycle of charge and discharge on the batteries. Figure 94 focuses on the beginning of the final dip in stored energy seen in Figure 93. The small oscillations present in the data represent the aforementioned charge/discharge cycle, and indicate only 1-1.5 kW-hr/m^2 is consumed in a normal discharge cycle for a such a vehicle configuration. The figure also demonstrates the timescale over which the solar activity can change the required power. Net energy stored per orbit does not radically change in a single orbit. Rather, it slowly drops over the course of several orbits.

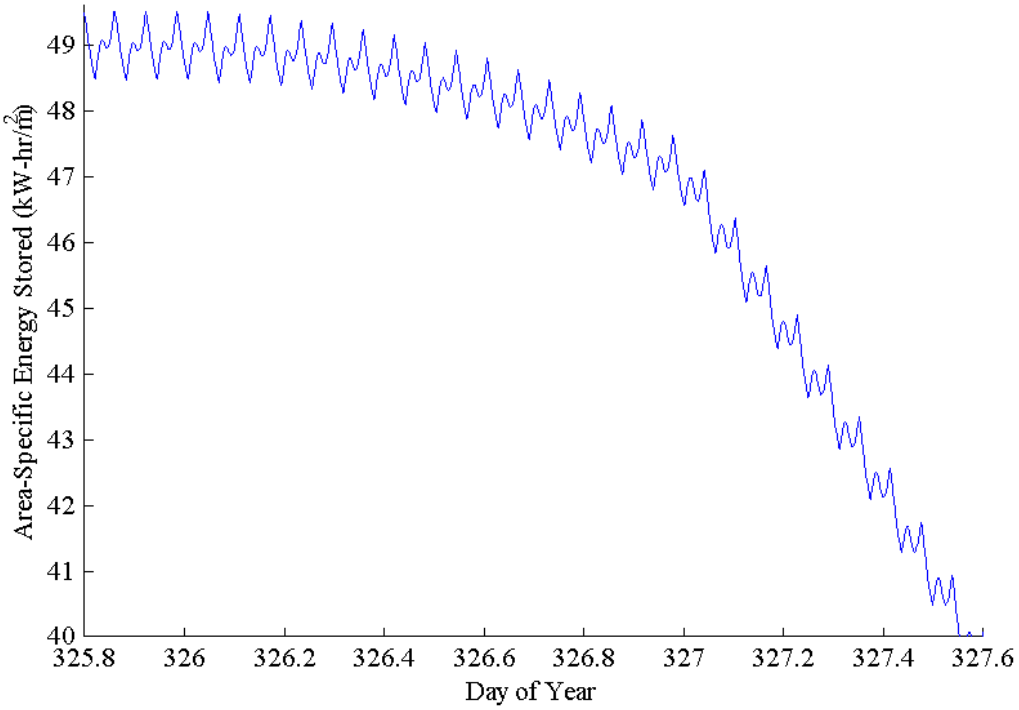

Figure 94. A closer view of the beginning of the final dip in stored energy from Figure 93.

Figure 94 demonstrates that a battery capacity of 10 kW-hr/m^2 with 90 percent depth of discharge is sufficient to provide over 36 hours of delay before the vehicle can no longer continue to occupy the design orbit. A contingency strategy for these rare occurrences during solar maxima can likely be enacted with such a warning to prevent the vehicle's orbit from destabilizing due to insufficient thrust power. This work proposes three contingency options, the first two of which include:

1. Fire an emergency chemical rocket to quickly increase the eccentricity of the orbit, thus reducing the required power and providing additional time to recharge batteries at apogee.
2. Use the reserve energy capacity to transition to a higher orbit by increasing the specific impulse above the required value (active orbit control).

The first option is low risk, but increases the mass of the vehicle and reintroduces a propellant budget. In contrast, the second option does not reintroduce a propellant budget, but is high risk. Although a more detailed trade study of these two options is beyond the scope of this work, the second option presents a notable advantage in that it would also permit the vehicle to transition to lower orbits when solar weather permits.

A potential third option lies in more carefully designing the orbit. The present 85° inclination orbit under consideration experiences considerable variation in the generated power depending on the time of year. Figure 95 demonstrates this variation by plotting the raw required and supplied power data over the course of the year. Whereas the bottom borders of the shaded areas represent the orbit-minimum power, the upper borders represent the orbit-maximum. Figure 95 demonstrates that, at some points during the year the orbit geometry is such that no eclipsing occurs. These periods occur around 100, 200, and 300 days in this particular case.

Figure 95 also demonstrates the variation in instantaneous required power over the course of the year. The results indicate that the instantaneous required power can vary by more than 100 percent in either direction of the average required power. Eclipsing has a noticeable effect on the required power as well, causing it to vary by as much as 1,500 W/m^2 in this data. The portion of the atmosphere under eclipse contracts, reducing the density and thus aerodynamic drag. Consequently, solar-powered propellant collectors fortuitously require peak power at roughly the same time they generate peak power.

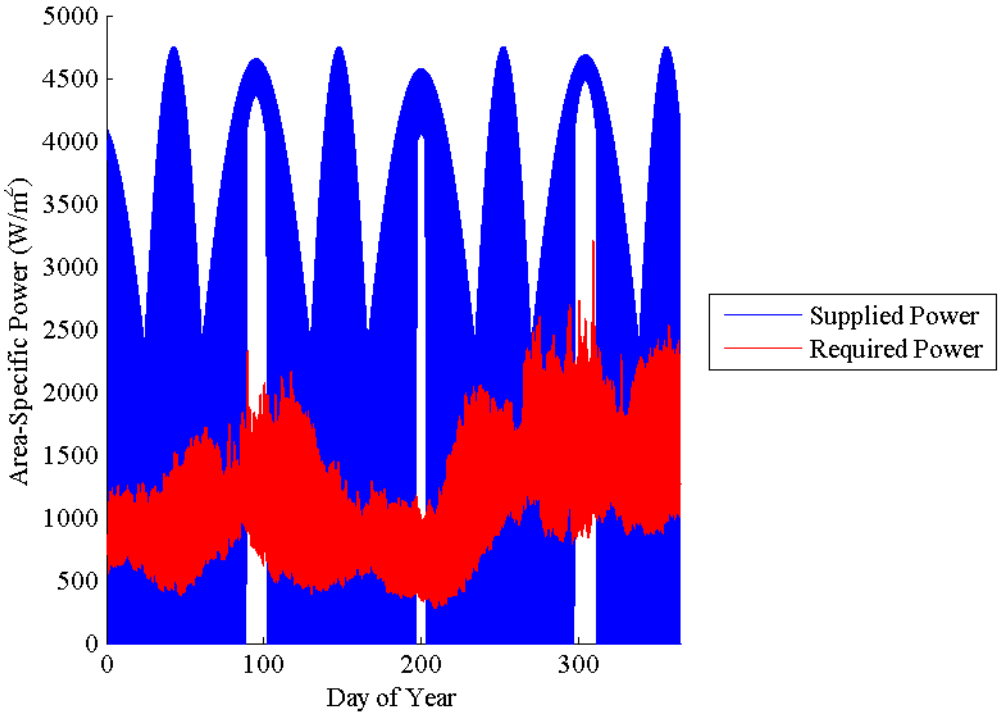

Figure 95. Plot of supplied and required power as a function of time. The upper bounds of the shaded areas represent the orbit-maximum values, whereas the bottom represents the orbit-minimum.

Regardless, reducing the variations in supplied power reduces the factor of safety required to ensure stable operation. One approach to accomplishing this is by selecting a sun-synchronous orbit, in particular a dawn-dusk sun-synchronous orbit. Sun-synchronous orbits take advantage of the natural precession caused by Earth oblateness to rotate the RAAN about the Earth at a rate of once per year. This precession rate leads to objects in that orbit passing over a given latitude at the same local solar time. A dawn-dusk orbit is a special case which uses the precession to lock the motion of the RAAN such that the vehicle rides the terminator between day and night. Consequently, the vehicle gains constant access to sunlight for large portions of the year and short eclipse periods otherwise. Notably, Di Cara et al. selected dawn-dusk sun-synchronous orbits as a preferred orbit in their 2007 work [55].

The inclination of a circular sun-synchronous orbit at 250 km is 96.5°. Figure 96 plots the instantaneous required and supplied powers as in Figure 95, but for the aforementioned dusk-dawn sun-synchronous orbit. An identical vehicle design to that designed for the 85° inclination case is used in the calculation in order to permit a direct comparison. The advantage is dramatic. The sun-synchronous orbit-maximum supplied power varies smoothly by only 15 percent over the course of the year. Periods without eclipsing are more substantial, and eclipses are otherwise short. Consequently, whereas the energy storage varied by 1-1.5 kW-hr/m^2 in the original case, in the dusk-dawn sun-synchronous case it never varies by more than 0.5 kW-hr/m^2. The "power droughts" experienced by the original case vanish in the sun-synchronous case, removing the need for reserve power in case of heightened solar activity. Energy storage requirements are thus reduced by a factor of 20 simply by more carefully designing the orbit.

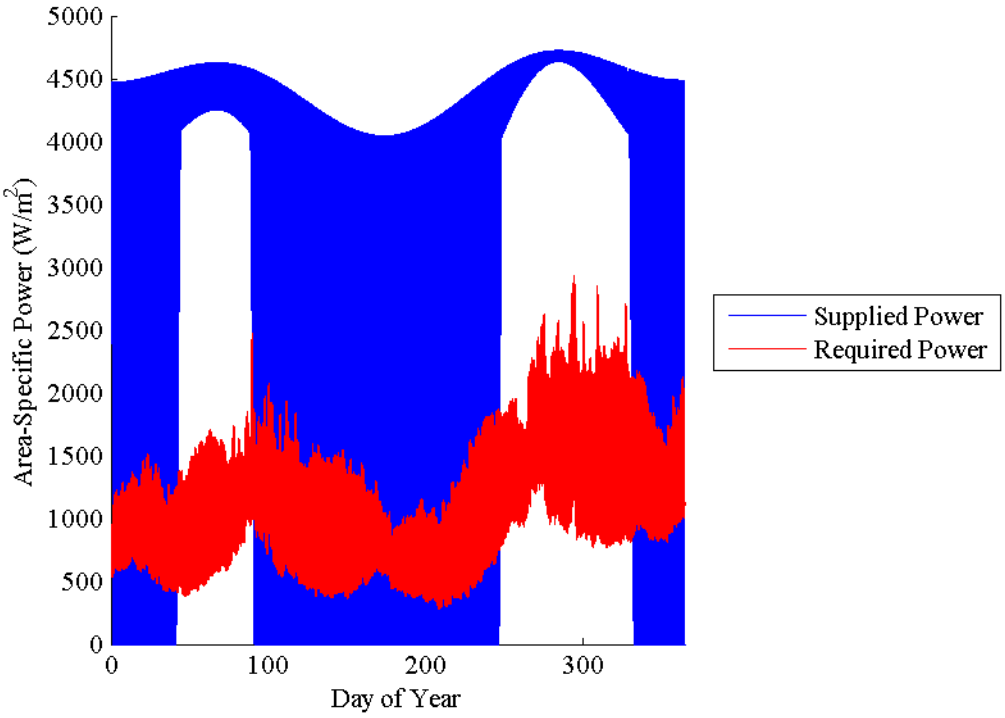

Figure 96. Sun-synchronous orbit supplied and required powers. The same vehicle parameters, including area ratio are used to generate this plot.

Conducting the preceding analysis on the raw STK data presents an opportunity for secondary analyses as well. Figure 97 plots the instantaneous body drag coefficient over the course of three orbits for the 85° inclination case. The analytical drag coefficient varies by 0.04 as a result of temperature variations around the orbit. These results are similar to those presented by King, and serve to validate the code [50].

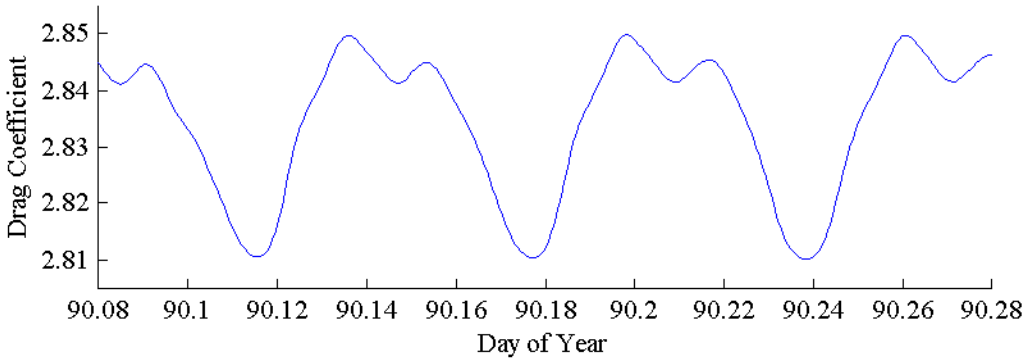

Figure 97. Plot of the instantaneous body drag coefficient over the course of three orbits.

The preceding analysis also presents an opportunity to once again quantify the effect of decimation and averaging on the quality of the results. Table 13 presents the calculated values of average required and generated power with both the direct calculations and the calculations conducted with time-averaged parameters. The difference in power in both cases is on the order of one percent, indicating that sampling and averaging the raw data does not significantly affect the fidelity of the results.

The preceding analysis leads to a preliminary set of design specifications given in Table 14. Battery sizing assumes a factor of safety of two over the predicted energy storage requirements, with 60 percent depth of discharge. Such a vehicle would be capable of launch aboard a Falcon 9 v1.1 and able to operate at 250 km altitude even during peak solar activity. This orbit is lower than that occupied by GOCE during the majority of its mission in a period of higher solar activity, indicating that propellant

collection can be enabling for operating in VLEO orbits. Using an optical mission as demonstration, such a reduction in altitude corresponds to a reduction in aperture diameter or improvement in resolution of four percent.

Table 13. Difference in the average required and generated power between the directly calculated average, and the average calculated from sampled, time-averaged parameters.

	Direct Calculation (kW/m^2)	Averaged Calculation (kW/m^2)	Difference (%)
Required Power	1.141	1.129	1.05
Generated Power	2.239	2.262	1.03

Table 14. Design specifications for a preliminary propellant-collecting VLEO science mission concept.

Diameter	3 m
Length	7.5 m
Total Battery Energy Capacity	7.06 kW-hr at 60% DOD
Total Battery Mass	107 kg
Solar Array Area (Deployed)	110 m^2
Orbit	6:00 AM Sun-Synchronous @ 250 km

7.2 Collector Mission

To review again from Chapter 3, the collector mission intends to store a surplus of collected ambient propellant which can then be given to other vehicles for their missions. The vehicle is a nuclear-powered collector rocket with assumed specifications listed in Table 15. Additionally, the vehicle must launch on a Block 2 SLS, and only sixty percent of the system mass can be taken up by the reactor. Thus, the maximum total reactor mass is 81,000 kg for this study. Like the previous case study, the nuclear collector rocket is constrained in its eccentricity, collector and thruster efficiencies, and reactor performance.

Table 15. Nominal parameters for the collector rocket mission study.

Parameter Name	Symbol	Nominal Value
Orbit Eccentricity	e	0.0
Orbit Inclination	i	28.5°
Year	N/A	2001
Collector Efficiency	η_c	0.4
Drag Coefficient	$C_{D,s/c}, C_{D,PA}$	Sentman's Result
Thruster Efficiency	η_t	Cifali's Result
Thermal Efficiency	η_R	0.2
Core Temperature	T_c	1125 K
Power Specific Mass	K	139 kg/kW

The previous case study revealed that a factor of safety of two placed on the minimum condition for feasibility is sufficient to ensure operation of a VLEO solar vehicle during most of the solar maximum. However, this factor of safety proves insufficient for a nuclear collector rocket. Figure 98 plots the ratio of generated-to-required power for a collector at 135 km as a function of area ratio. The results from this calculation indicate an area ratio of 31.7 and a usage ratio of 0.61 provide the maximum area-specific mass storage rate, while satisfying the design condition with the desired factor of safety. Usage ratio appears optimum above 0.5 for this and other cases in this section as a result of the numerical discretization of the applicable altitude data points from the STK portion of this work.

Although nuclear power does not suffer from the same limitation in available power generating time that solar power does, it must still contend with the significant fluctuations in power demand caused by location and time-dependent variations in density. Figure 99 indicates the required and supplied power over the course of the year. The thickness of the required power band indicates the magnitude of the effect of eclipsing on the required power, and the magnitude of orbit-to-orbit variations. Figure 99 shows that even with a factor of safety of two, the required power will frequently overcome the supplied power available for brief periods each orbit.

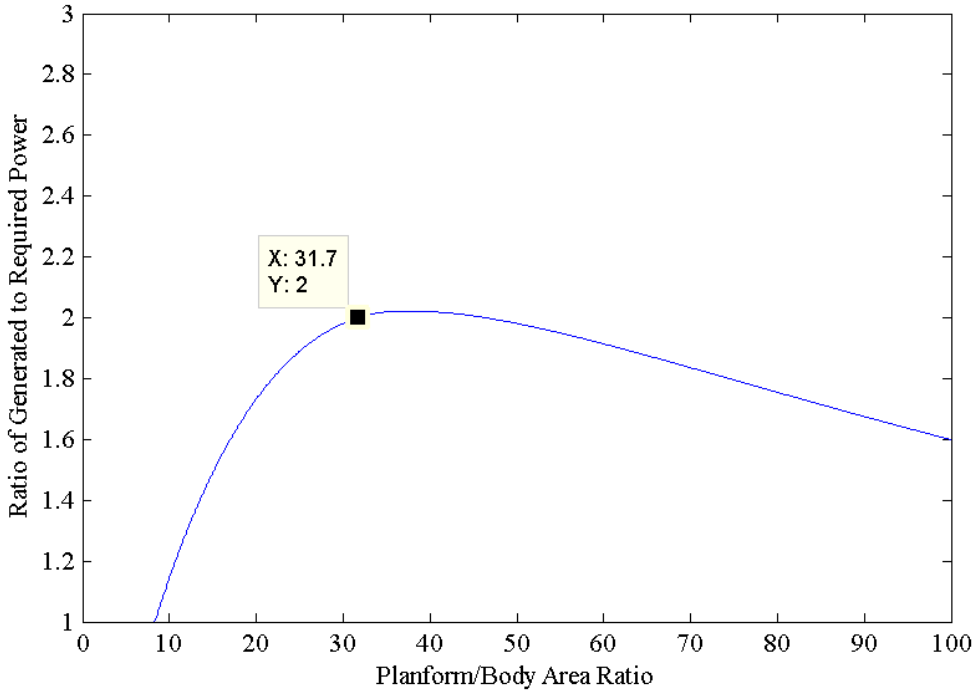

Figure 98. Power ratio plot for the collector at 135 km as a function of area ratio. The design condition is indicated in the figure to be satisfied for area ratio equal to 31.7.

The effect of these variations on the orbital motion is observable through the delta-v deficit developed as a result of insufficient thrust power. Figure 100 plots this deficit as a function of time. These values are calculated assuming a worst-case scenario of area-to-mass ratio. The full 8m diameter frontal area which can be accommodated by the SLS is the area selected and the full payload mass is the mass selected. Furthermore, this calculation neglects thrust vectoring components and gravity loss components of the delta-v. Finally, it does not track the orbit changes which would develop as a result of experiencing the delta-v. Despite these limitations, this plot has use in providing an indication as to the stability of the vehicle orbit at this design condition. This plot indicates a deficit reaching as high as 1.4 m/s, which corresponds to a change in periapsis altitude of ~5 km. Although the results show that the reactor is always able to recover this deficit within half an orbit, the cumulative effect of the perturbations may ultimately destabilize the orbit and force reentry.

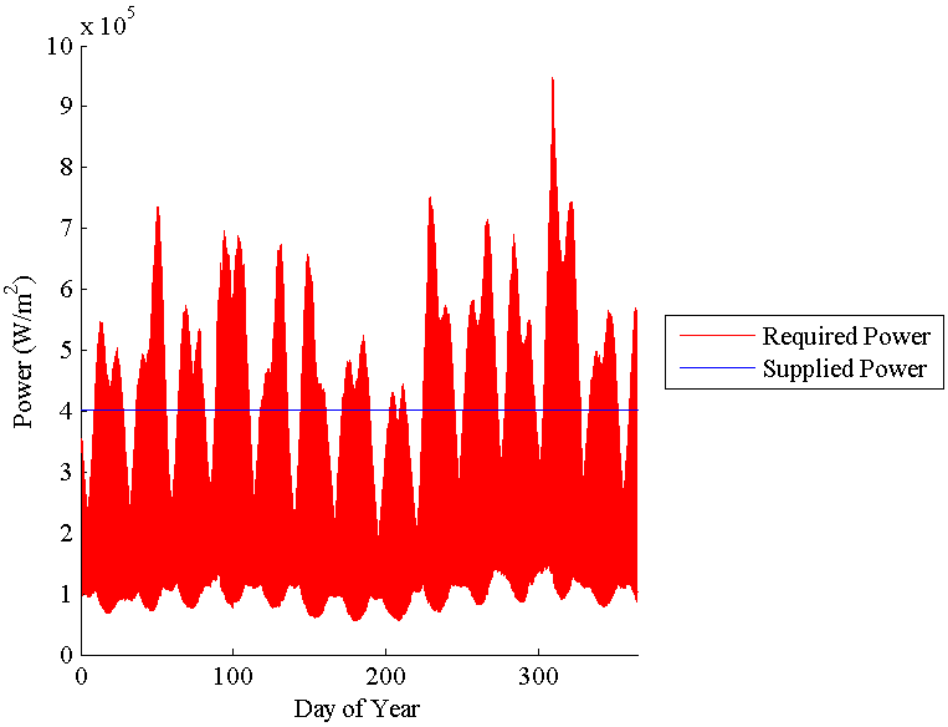

Figure 99. Required and supplied power over the course of the year for the nuclear collector rocket.

Since the collector stores some propellant for future use, it has different options to mitigate the effect of solar activity on the performance than the VLEO mission. One notable option is to overcome temporary deficiencies by expending some stored propellant to increase thrust at a cost of specific impulse. Another option is to conduct active orbit control as is suggested with the first case study. In the absence of these mitigating strategies, a factor of safety of two is not sufficient to maintain orbit for a nuclear collector.

In contrast, a factor of safety of three readily supplies sufficient power to maintain orbit for all but brief periods during the year. The following figures present results for a vehicle which operates at 140 km with a usage ratio of 0.61 and an area ratio of 31. Figure 101 presents the supplied and required power for these design parameters over the course of the year 2001. The supplied power exceeds the orbit-peak required power for all but a few days of the year.

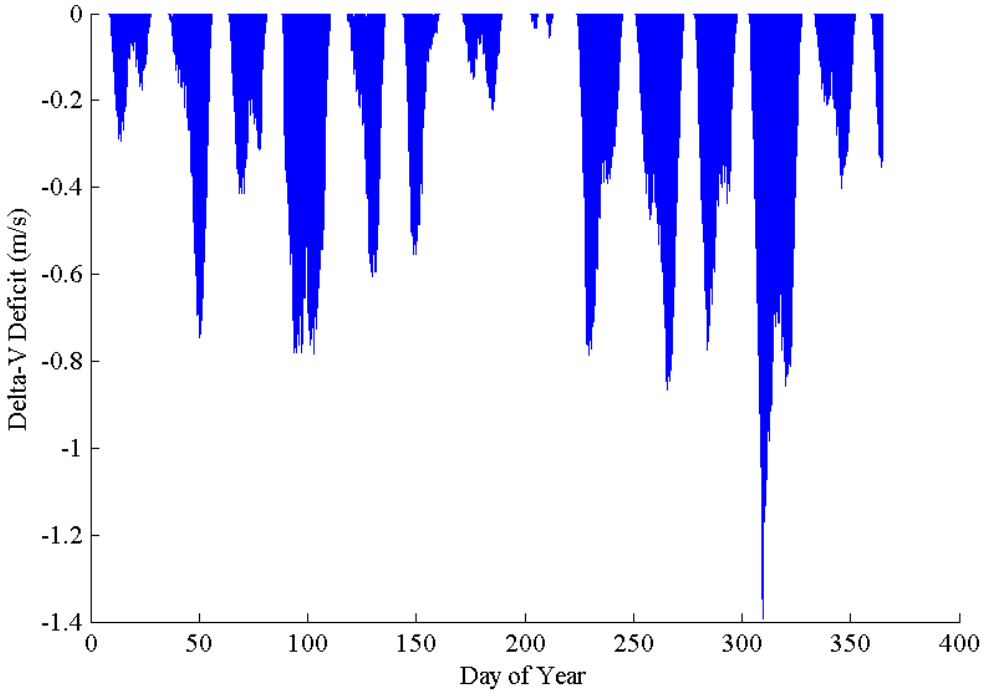

Figure 100. Delta-V deficit accumulated by the vehicle as a result of insufficient thrust power over the course of the year.

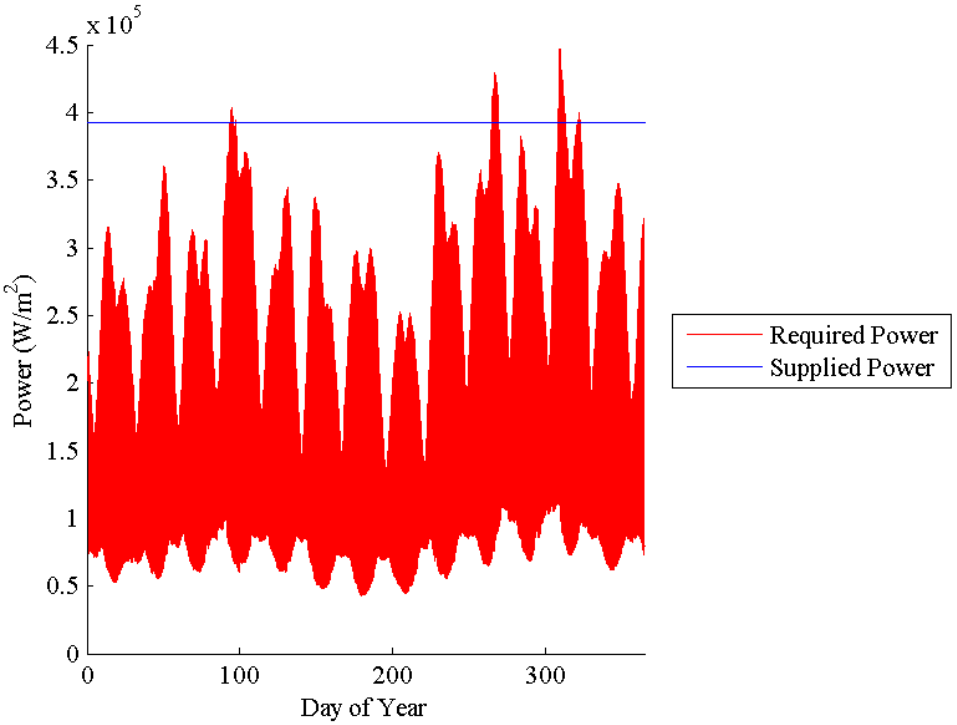

Figure 101. Supplied and required power for a nuclear collector rocket with a factor of safety of three. The reactor supplies sufficient power to accommodate peak demands for all but a few days of the year.

The rare periods of deficiency which are present last only a few minutes per orbit. Consequently, the delta-v deficit developed over the course of the power deficiency is small when compared to the previous design case. Figure 102 shows the delta-v deficit for the case where the factor of safety is three. Peak deficit exceeds 6 cm/s for a single orbit in the year, despite the numerous spikes in required power revealed in Figure 101. In contrast with the previous design case, 6 cm/s of peak delta-v deficit corresponds to only ~200 m in periapsis altitude change, which is quickly recoverable during the rest of the orbit.

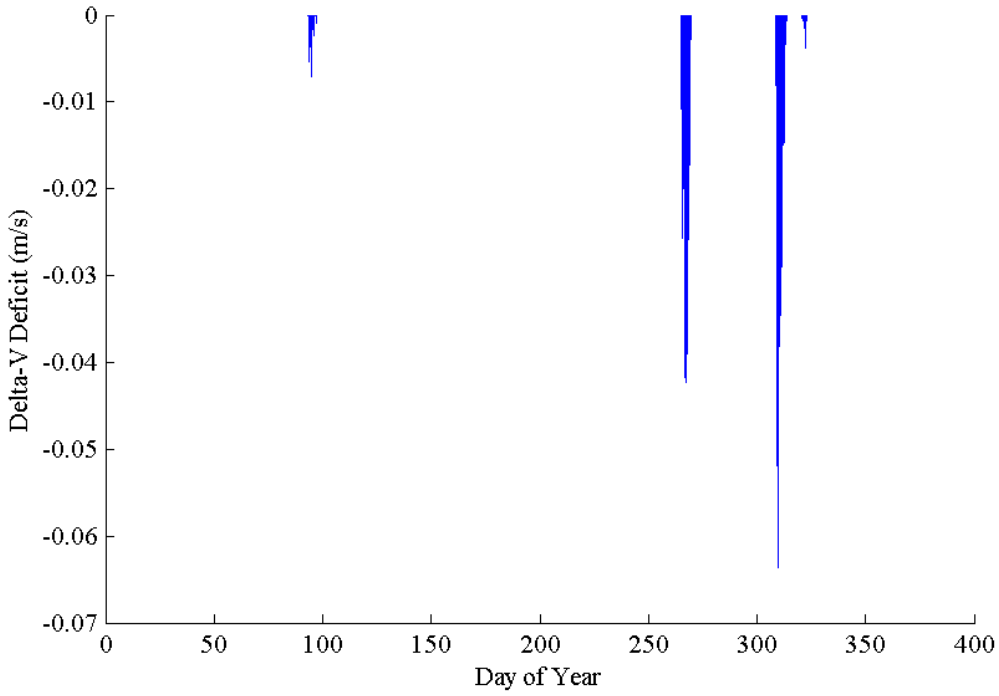

Figure 102. Delta-v deficit as a function of time for the factor of safety of three case.

Figure 103 confirms this notion by plotting the energy deficit for the peak power deficiency identified in Figure 101. The plot covers an entire orbit, and demonstrates both the brevity and the triviality of the deficiency. Recalling the battery discussions in Section 7.1, a peak deficiency of 5kW-hr/m^2 which occurs once during the year is easily accommodated by batteries. The deficiency could also be easily overcome with any of the

aforementioned mitigating strategies. However, employing such strategies may not even be necessary given its magnitude. Thus, it appears a factor of safety of three is sufficient to guarantee operation in a desired orbit for a nuclear collector vehicle. Moreover, such a large factor of safety appears sufficient to guarantee the stability of the vehicle's orbit against all but the most intense effects of solar weather.

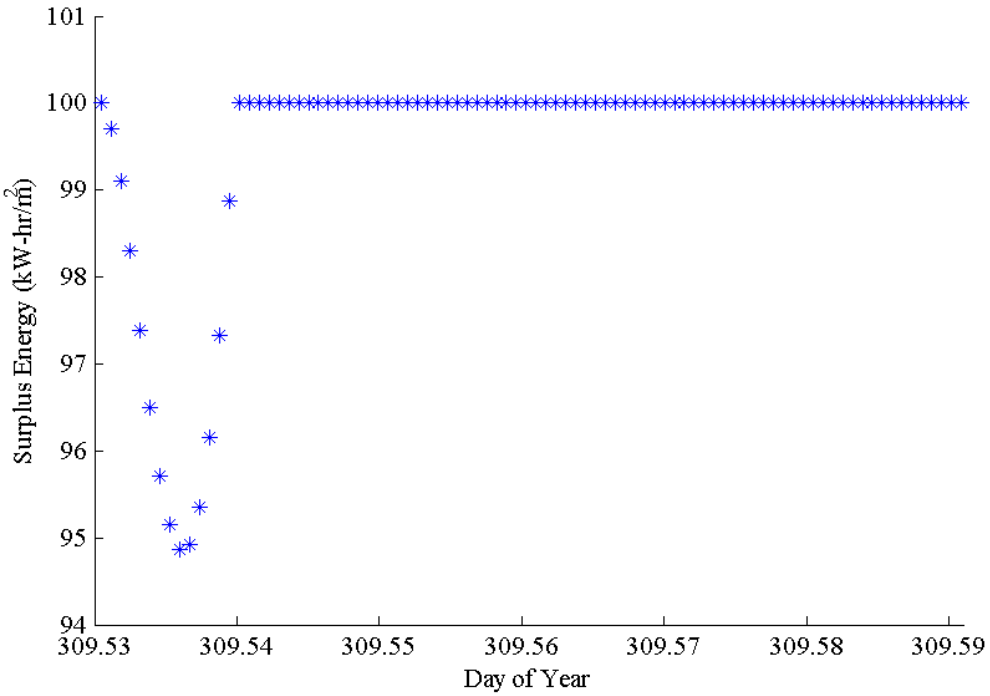

Figure 103. Energy deficit for the peak power deficiency presented in the results.

The preceding results in this section identify the maximum area-specific mass storage rate attainable with presently available technology. However, operating at the design point which results in this maximum area-specific rate does not necessarily result in an maximum net mass storage rate. Furthermore, it does not factor in the limiting factors of reactor specific mass and vehicle density. Sizing a vehicle for the aforementioned design point supports this assertion. Table 16 provides the specifications for a vehicle which operates at the maximum area-specific mass storage rate design point. The sizing of the vehicle assumes it fully uses the payload capacity of the SLS, and has a reactor mass fraction of 0.6. The reactor specific power performance is 139 kg/kW as

reported in Section 3.2.7. Finally, the length-to-diameter ratio of the vehicle is assumed to be equal to five.

Table 16. Vehicle specifications for operation at the maximum area-specific mass storage rate design point given design parameters for presently available technology.

Diameter	1.27 m
Length	6.3 m
Volume	8 m^3
Usage Ratio	0.61
Total Generated Power	583 kWe
Total Reactor Mass	81,000 kg
Vehicle Dry Mass	135,000 kg
Vehicle Density	16,875 kg/m^3
Radiator Area (Deployed)	39 m^2
Orbit	140 km, 28.5° Inclination, Circular
Annual Mass Surplus	340 kg/year

At first glance these specifications appear reasonable. The vehicle has dimensions which allow it to fit within the predicted dimensions of an SLS payload shroud, and has a mass which the SLS can deliver to orbit. However, the vehicle density reveals the infeasibility inherent in this concept: at 16,875 kg/m^3, this vehicle would be ~1.5 times the density of lead. This density value does not account for the empty volume of storage tanks such a vehicle would need to accommodate stored propellant. This result highlights the presence of another design constraint when sizing a vehicle: the specific power reactor performance. This additional constraint places further limitations on the results by limiting the area-specific power generation.

Moreover, peak area-specific mass storage at the minimum periapsis altitude does not translate to peak net mass storage. A trade exists between inlet area and density for the net mass storage rate. The maximum attainable spacecraft inlet area under a given mass constraint decreases with decreasing altitude. Conversely, density increases with decreasing altitude. Allowing the area-specific reactor mass, altitude, and usage ratio to

vary under dimensionality, reactor mass, and feasibility condition constraints in a parametric analysis leads a design that maximizes the net mass storage rate.

Table 17 tabulates the design specifications for such a vehicle. This vehicle operates 20 km higher, and is larger than the previous design. Furthermore, the annual mass surplus is much lower at only 79.3 kg/year during the solar maximum. Assume for the sake of argument that the same mass storage is achievable during other periods of solar activity with active orbit control, and neglect all other decaying factors. This vehicle would then have to operate for nearly 1,100 years in order to collect propellant mass equal to the reactor mass.

Table 17. Specifications for a collector design which meets the dimension and reactor mass constraints in addition to the feasibility condition.

Diameter	3.89 m
Length	19.4 m
Volume	230.6 m^3
Usage Ratio	0.43
Total Generated Power	583 kWe
Total Reactor Mass	81,000 kg
Vehicle Dry Mass	135,000 kg
Vehicle Density	585 kg/m^3
Radiator Area (Deployed)	39 m^2
Orbit	170 km, 28.5° Inclination, Circular
Annual Mass Surplus	79.3 kg/year

With the stated length, this vehicle could carry as much as 47,500 kg of gaseous propellant stored at 180 atm or 185,000 kg of liquid propellant. Thus, the storage of the propellant is unlikely to alter the drag area of the vehicle. This demonstrates the effect of propellant storage phase state on the amount of storable propellant given dimensionality constraints for aerodynamic considerations. Additional capacity forces an increase in the dimensions of the vehicle, thus increasing the total drag force it must overcome. When compared with the alternative of simply launching the necessary propellant at mission start, the limitations of this concept become clear. With presently available technology,

propellant collection as defined in this work with the intent to produce an on-orbit reserve of propellant is not competitive with launching the equivalent mass of propellant from the surface.

Given this result, the question then remains as to whether propellant collection can ever be a competitive method for producing an on-orbit propellant reserve. Repeating the previous analysis for an ideal case provides insight into this question. Table 18 details specifications for a collector with ideal performance capability. This analysis assumes a reactor specific power of 25 kg/kW, ideal thruster efficiency and drag coefficients, 90 percent collector efficiency, 25 percent reactor efficiency, and the peak studied core temperature of 1,950 K. Reducing the reactor specific power significantly improves the net power available to the vehicle. The ideal design has 3.24 MW available whereas the baseline design only has 0.58 MW. The orbit altitude reduces by 30 km between the two cases as a result of a higher attainable power density, and the vehicle density reduces by a factor of two.

Table 18. Specifications for a collector design in the ideal case which meets the design constraints.

Diameter	3.96 m
Length	19.8 m
Volume	244 m^3
Usage Ratio	0.26
Total Generated Power	3,240 kWe
Total Reactor Mass	81,000 kg
Vehicle Dry Mass	135,000 kg
Vehicle Density	553 kg/m^3
Radiator Area (Deployed)	23.4 m^2
Orbit	130 km, 28.5° Inclination, Circular
Annual Mass Surplus	4,367 kg/year

Most important however is the annual mass surplus. An ideal vehicle might feasibly collect 4,367 kg/year under the previously discussed design and performance assumptions. While this is a dramatic improvement over the design which assumes presently available technical capability, such a vehicle would still take 19 years to collect

propellant mass equivalent to the reactor mass. The potential benefit of this level of performance is arguable, and likely dependent on the specifics of the overall mission architecture for which propellant collection is being considered. Even so, it is clear that propellant collection is not a panacea for avoiding the launch of propellant from the surface.

7.3 Summary

This chapter identifies designs and orbit configurations for a VLEO science mission and a collector mission. The VLEO science mission case study finds that a factor of safety of two over the minimum feasibility condition presented in previous chapters is sufficient to ensure orbit stability with an easily accommodated battery capacity. Specifically, a design employing a 250 km dusk-dawn sun-synchronous orbit with a factor of safety of two with regards to the minimum feasibility condition remains stable during even the most extreme solar activity recorded in 2001. This factor of safety is included to account for variations in instantaneous required power which exceed the average required power. Propellant collection is inherently unstable as a result of operation in low altitudes with high drag. Thus, a relatively minor deficiency in power over a short duration can be sufficient to lead the vehicle into irrecoverable orbit decay.

250 km is notably 10 km lower than the operational orbit of GOCE, which itself operated during a period of unusually low solar activity. In contrast, the propellant-collecting design stably operates at 250 km during even the most severe solar activity recorded in 2001. If active orbit control and other mitigating measures proposed in Section 7.1 are employed by such a vehicle, the average altitude of the vehicle over its operational lifetime is likely significantly lower.

The VLEO case study in this chapter also provided another opportunity to quantify the accuracy of the averaged results. The average required and generated power values appear to vary by only one percent between the results from the averaged and raw

data sets. This indicates that the mechanisms for averaging conducted in this work are robust and valid for the high-level systems analysis conducted. Ultimately, the results of the VLEO case study demonstrate that propellant collection can be beneficial when one is interested in minimizing altitude while preserving lifetime. As discussed in the introductory chapter, such a capability has significant potential impact on the science and observations we can conduct.

The collector case study attempted to identify a design point where propellant collection is potentially beneficial over equivalent propellant depot architectures, but failed to do so. While the solar-powered VLEO science mission could operate stably with a factor of safety of two on the minimum feasibility condition, the nuclear collector rocket could not. This is a result of operating at a lower altitude, where the magnitude of the variations in density is much greater, leading to increased instability and intolerance to power deficiency. However, a factor of safety of three proves to be sufficient, as demonstrated by the analysis of the delta-v deficit and the energy surplus. With the aforementioned factor of safety, a nuclear-powered collector can recover from even the most severe effects of solar activity witnessed in 2001.

However, the collector case study also identifies additional constraints. The power density and overall vehicle density must also be considered when sizing a potential design. Absent these considerations, the net vehicle density can become arbitrarily high. Inclusion of these constraints raises the design altitude and increases the vehicle size. The final proposed design has a predicted mass collection rate during the solar maximum of 79.3 kg/year. Clearly, this collection rate is insufficient to justify the launch of a 135,000 kg vehicle as it would take eleven centuries to collect a propellant mass equivalent to the nuclear reactor mass. A case study with ideal parameters exhibits far better performance at 4,367 kg/year, although even this level of performance lies in a gray area with regards to its potential benefit. Regardless, the ideal case study result demonstrates that propellant collection is not suitable to replace all launched propellant. Thus, it appears that

propellant collection as defined and studied in this work is suitable for "personal use" applications such as VLEO orbiting, but not for providing other missions with propellant.

CHAPTER 8
CONCLUSIONS

As stated in the first pages of this work, the goal of this dissertation was to learn where propellant collection technology can sustain a VLEO orbit and where it can store a surplus of atmospheric gases for other applications. The preceding chapters build the necessary tools and report on the analysis conducted to address this aim by completing the three intermediate research goals presented in the introduction. Thus, this work identifies the major design factors for propellant collection from first principles in Section 3.1, and applies an elasticity analysis to determine the relative importance of these factors in Chapter 5. It identifies where propellant collection is technically feasible in altitude-space in Chapter 6, and it determines designs for two mission types using presently available technology in Chapter 7. These final sections summarize and consolidate the conclusions already drawn throughout the preceding chapters, identify the major contributions made to the body of knowledge, and propose areas for future work.

8.1 Contributions

This work makes six major contributions to the body of knowledge. The first three contributions are those presented in the introduction. The final three contributions arise from the analysis conducted in support of accomplishing the first three. These six contributions include:

- ***Identification of major design factors for propellant collection***

The elasticity plots in Chapter 5 reveal the design factors to which propellant-collecting concepts are most sensitive. Altitude dominates the required power as a result of its exponential effect on density. Many of the other parameters have similar levels of importance, although collector efficiency and usage ratio exhibit diminishing returns as they approach unity. This effect results from the implicit coupling between thruster efficiency and specific impulse. Compressor efficiency is unimportant for propellant collection because the thrust power requirement dominates the compression power requirement by at least an order of magnitude.

The nuclear power generation equation does not exhibit dependence on altitude, but is instead highly reliant on the core temperature of the reactor. Increasing core temperature ultimately improves the area-specific heat rejection performance of the radiators which contribute to the overall drag of the vehicle. The nuclear generated power is least sensitive to thermal efficiency, although its dependence on the core temperature leads to an optimum thermal efficiency of 25 percent. Solar power is most sensitive to panel efficiency and area ratio, as anticipated.

- ***Determination of where propellant collection is technically feasible from a propulsion perspective***

Because altitude dominates the required power equations, it forms the basis for demarking the locations of technical feasibility. With presently available technology, solar-powered vehicles can be feasible as low as 220-250 km during the solar maximum. Similarly, nuclear-powered vehicles can be feasible as low as 118-130 km, with variation

to account for the selection of other orbital parameters. In an ideal case, solar vehicles may operate as low as 160-180 km and nuclear vehicles may operate as low as 100-110 km. The most notable result from identifying these altitude ranges is that solar-powered vehicles cannot feasibly operate low enough in the atmosphere to be suitable for propellant depot-type applications. Additionally, the type of propellant-collecting vehicle has little effect on the minimum attainable altitude.

- ***Determination of the suitability of propellant collection for applications***

The basic design developed in Chapter 7 for a VLEO science mission with presently available technology demonstrates the potential utility of propellant collection in enabling VLEO operation. At peak solar activity, the presented design maintains a stable orbit at 250 km. In contrast, the recent GOCE mission operated stably at 260 km during only moderate solar activity. Chapter 6 demonstrates that eccentrically orbiting propellant collectors can reach lower into the atmosphere than circularly orbiting collectors, which could aid vehicles in rapid reposition and high resolution reconnaissance.

The designs developed for a nuclear collector mission demonstrate the limited utility of propellant collection in replacing surface-launched propellant. With presently available technology, the proposed collector design would take centuries to collect a reserve of propellant mass equal to its nominal reactor mass. Even with ideal considerations, the same accomplishment takes on the order of 20 years. This application may be beneficial for some specific mission architectures, but is not generally applicable.

- ***Derivation of fundamental propellant collection equations***

The first section of Chapter 3 presents the derivation of fundamental propellant collection equations which can be applied to any internally-powered propellant-collecting vehicle that sustainably counteracts drag. These equations arise from first principles and are not presented at the same level of detail elsewhere in the literature. The fundamental propellant collection equations derived in this work form the foundation upon which the rest of these contributions are built.

- ***Development of a taxonomy of collectors***

The development of the fundamental propellant collection equations demonstrated numerous approaches and choices designers might make when designing a propellant collection concept. Enumeration of each of these leads to the taxonomy of collectors as presented in Chapter 3. Under the assumptions made in this work, any propellant-collecting vehicle can be categorized as one of the vehicle types in the taxonomy. Notably, some of the vehicle types are not reported elsewhere in the literature. This is thus the first time they have been studied in a documented manner.

- ***Development of a minimum condition for propulsion technical feasibility***

The final major contribution made in this work is the development of the minimum condition for propulsion technical feasibility. This condition is the average power standard: the average generated power must exceed the average required power for a concept to be technically feasible. Previous efforts have alluded to a requirement such

as this, but it has never before been explicitly identified and rigidly applied as it has in this work.

8.2 Future Work

With the analysis conducted in this work complete, new areas for continued research in propellant collection arise. Obvious areas include ways to improve the various design parameters which are important to propellant collection. In addition, areas of future work include:

- ***Further investigate VLEO applications and advantages***

The analysis conducted in this work demonstrates that this broad area of application is where propellant collection can have the most immediate impact. Presently available technology could feasibly lead to new satellite designs which operate in VLEO to realize improved measurements and reduced costs. However, some questions remain unanswered. Further optimization is likely possible over the design proposed in this work with additional study. Integration of payloads into a propellant-collecting vehicle is something which is insufficiently studied in the literature, especially given the coupling of vehicle geometry and propellant collection performance. Further challenges await in implementing the space weather-mitigating strategies proposed in this work. Finally, developing thrust control algorithms to accurately counteract the drag instantaneously, or otherwise regularly correct for orbit perturbations due to the time-varying acceleration applied to the vehicle will be necessary before this technology can be employed on-orbit.

- ***Improve air-compatible thruster technology***

This work employed Cifali et al.'s experimental results on the RIT-10 to predict thruster performance. This thruster has not been optimized for operation on atmospheric

propellants, and the development of air-compatible thrusters is an ongoing and active area of research. Given the potential impact improving thruster efficiency has on a propellant collection design, it should remain an active area of research. Many researchers have correctly pointed out the need to quantify the effect of operating on atmospheric constituents on lifetime. Others have noted the need to improve the ionization process and propellant utilization efficiency on these devices. Finally, some have identified the need for air-compatible cathodes and have made progress in their development.

- ***Investigate the application of propellant collection around other planetary bodies***

Although propellant collection is demonstrated in this work to be presently unsuitable for propellant depot-type applications around Earth, it may yet be suitable for such an application around other planets. As one travels farther away from the surface in terms of delta-v, the cost of propellant delivered rises. Thus, it may be worthwhile to send a propellant-collecting depot vehicle to a planet like Mars. This could enable manned and sample return missions to replenish their propellant supplies at their destination before returning home. Such an application may be enabling for future interplanetary exploration.

REFERENCES

[1] Saleh, J. H., Hastings, D.E., Newman, D.J. "Spacecraft design lifetime," *Journal of Spacecraft and Rockets* Vol. 39, No. 2, 2002, pp. 244-257.

[2] Wallace, N., Jameson, P., Saunders, C., Fehringer, M., Edwards, C., Floberghagen, R. "The GOCE Ion Propulsion Assembly - Lessons Learnt from the First 22 Months of Flight Operations," *32nd International Electric Propulsion Conference*. Wiesbaden, Germany, 2011. IEPC-2011-327.

[3] Krueger, J. "CLOSeSat: Perigee-Lowering Techniques and Preliminary Design for a Small Optical Imaging Satellite Operating in Very Low Earth Orbit," *Department of Aeronautics and Astronautics*. Vol. Master of Science, Massachusetts Institute of Technology, 2010.

[4] Wertz, J. R., Larson, W.J. *Space Mission Analysis and Design*. Hawthorne, CA: Microcosm Press, 2007.

[5] van Belle, G. T., Meinel, A.B., Meinel, M.P. "The Scaling Relationship Between Telescope Cost and Aperture Size for Very Large Telescopes," *SPIE* Vol. 5489, 2004, pp. 563-570.

[6] Drinkwater, M. R., Haagmans, R., Muzi, D., Popescu, A., Floberghagen, R., Kern, M., Fehringer, M. "The GOCE Gravity Mission: ESA's First Core Earth Explorer," *3rd International GOCE User Workshop*. ESA, Frascati, Italy, 2006, pp. 1-8.

[7] Klaus, K., Elsperman, M.S., Rogers, F. "Mission Concepts Enabled by Solar Electric Propulsion and Advanced Modular Power Systems," *44th Lunar and Planetary Science Conference*. The Woodlands, TX, 2013.

[8] "The Role of Small Satellites in NASA and NOAA Earth Observation Programs." Space Studies Board: National Research Council, 2000.

[9] Minovitch, M. A. "Solar Powered, Self-Refueling, Microwave Propelled Interorbital Transportation System," *AIAA 18th Thermophysics Conference*. Montreal, Canada, 1983. AIAA-83-1446.
doi: 10.2514/6.1983-1446

[10] Lamamy, J. A. "Enhancing the science return of Mars missions via sample preparation, robotic surface exploration, and in orbit fuel production," *Aeronautics and Astronautics*. Massachusetts Institute of Technology, 2004.

[11] Palaszewski, B. "Atmospheric Mining in the Outer Solar System," *41st AIAA/ASME/SAE/ASEE Joint Propulsion Conference and Exhibit*. Tuscon, AZ, 2005. AIAA 2005-4319.
doi: 10.2322/jjsass.52.514

[12] Hohman, K. "Atmospheric Breathing Electric Thruster for Planetary Exploration." Busek Co. Inc., Natick, MA, 2012.

[13] "The Earth's Ionosphere." NASA GSFC, 1971. NASA SP-8049.

[14] Vallado, D. A., Finkleman, D. "A Critical Assessment of Satellite Drag and Atmospheric Density Modeling," *AIAA/AAS Astrodynamics Specialist Conference and Exhibit*. Honolulu, HI, 2008. AIAA 2008-6442.
doi: 10.2514/6.2008-6442

[15] Humble, R. W., Henry, G.N., Larson, W.J. *Space Propulsion Analysis and Design*. New York: McGraw-Hill, 1995.

[16] Schonherr, T., Komurasaki, K., Herdrich, G. "Analysis of Atmosphere-Breathing Electric Propulsion," *33rd International Electric Propulsion Conference*. Washington, D.C., 2013. IEPC-2013-421.

[17] Zakrzwski, C., Benson, S., Sanneman, P., Hoskins, A. "On-Orbit Testing of the EO-1 Pulsed Plasma Thruster," *38th AIAA/ASME/SAE/ASEE Joint Propulsion Conference and Exhibit*. Indianapolis, IN, 2002. AIAA 2002-3973.
doi: 10.2514/6.2002-3973

[18] Schonherr, T., Nees, F., Arakawa, Y., Komurasaki, K., Herdrich, G. "Characteristics of plasma properties in an ablative pulsed plasma thruster," *Physics of Plasmas* Vol. 20, No. 3, 2013.

[19] Demetriades, S. "A Novel System for Space Flight Using a Propulsive Fluid Accumulator," *Journal of the British Interplanetary Society* Vol. 17, 1959, pp. 114-119.

[20] Cann, G. L. "A Space Electric Ramjet," *AIAA 11th Electric Propulsion Conference*. New Orleans, LA, AIAA 75-377, 1975.
doi: 10.2514/6.1975-377

[21] Cifali, G., Misuri, T., Rossetti, P., Andrenucci, M., Valentian, D., Feili, D. "Preliminary characterization test of HET and RIT with Nitrogen and Oxygen," *47th AIAA/ASME/SAE/ASEE Joint Propulsion Conference and Exhibit*. San Diego, CA, 2011. AIAA 2011-6073.
doi: 10.2514/6.2011-6073

[22] Shabshelowitz, A. "Study of RF Plasma Technology Applied to Air-Breathing Electric Propulsion," *Aerospace Engineering*. University of Michigan, Ann Arbor, MI, 2013.

[23] Goebel, D. M., Katz, I. *Fundamentals of Electric Propulsion: Ion and Hall Thrusters*. Pasadena, CA: California Institute of Technology, 2008.

[24] Degeling, A. W., Mikhelson, N., Boswell, R.W., Sadeghi, N. "Characterization of Helicon Waves in a Magnetized Inductive Discharge," *Physics of Plasmas* Vol. 5, No. 3, 1998, pp. 572-579.

[25] Rauf, S., Bera, K., Collins, K. "Self-consistent Simulation of Very High Frequency Capacitively Coupled Plasmas," *Plasma Sources Science and Technology* Vol. 17, No. 3, 2008.

[26] Diamant, K. D. "Microwave Cathode for Air Breathing Electric Propulsion," *31st International Electric Propulsion Conference*. Ann Arbor, Michigan, 2009. IEPC-2009-015.
doi: 10.2514/6.2009-15

[27] Raitses, Y., Ashkenazy, J., Guelman, M. "Propellant Utilization in Hall Thrusters," *Journal of Propulsion and Power* Vol. 14, No. 2, 1998, pp. 247-253.

[28] Keidar, M., Gallimore, A.D., Raitses, Y., Boyd, I.D. "On the Potential Distribution in Hall Thrusters," *Applied Physics Letters* Vol. 85, No. 13, 2004, pp. 2481-2483.

[29] King, L. B. "A Re-examination of Electron Motion in Hall Thruster Fields," *29th International Electric Propulsion Conference*. Princeton, NJ, 2005. IEPC-2005-258.

[30] Vallado, D. A. *Fundamentals of Astrodynamics and Applications*. El Segundo, CA: Microcosm Press, 2004.
[31] Demetriades, S. T., Kretschmer, C. "The Use of Planetary Atmospheres for Propulsion." United States Air Force, Office of Scientific Research, 1958.
[32] Demetriades, S. T. "Preliminary Study of Propulsive Fluid Accumulator," *Journal of the British Interplanetary Society* Vol. 18, 1962, pp. 392-402.
[33] Bussard, R. W. "Galactic Matter and Interstellar Flight," *Astronautica Acta* Vol. 6, 1960, pp. 179-194.
[34] Anderson, P. *Tau Zero*: Doubleday, 1970.
[35] Berner, F., Camac, M. "Air Scooping Vehicle," *Planetary and Space Science* Vol. 4, 1961, pp. 159-183.
doi: 10.1016/0032-0633(61)90130-1
[36] Reichel, R. H., Smith, T.L., Hanford, D.R. "Potentialities of Air-Scooping Electrical Space Propulsion Systems," *ARS Electric Propulsion Conference*. Berkeley, CA, 1962.
[37] Reichel, R. H. "The Air-Scooping Nuclear-Electric Propulsion Concept for Advanced Orbital Space Transportation Missions," *Journal of the British Interplanetary Society* Vol. 31, 1978, pp. 62-66.
[38] Minovitch, M. A. "Self-Refueling Rocket Propulsion for Future Space Travel," *AIAA/SAE/ASME/ASEE 21st Joint Propulsion Conference*. Monterey, CA, 1985. AIAA-85-1370.
doi: 10.2514/6.1985-1370
[39] Dolgich, A. "Soviet Studies on Low-Thrust Orbital Propellant-Scooping Systems," *Foreign Science*, 1969.
[40] Berner, F., Camac, M. "Air Scooping Vehicle." Research Report 76, AVCO Everett Research Laboratory, AFBMD TR 59-17, 1959.
[41] Zukerman, A., Kretschmer, C.B. "A Study of the Feasibility of an Atomic Oxygen Ramjet," *Planetary and Space Science* Vol. 4, 1961, pp. 60-76.
[42] Mendell, W. W., Hoffman, S. "Strategic considerations for cislunar space infrastructure," *44th Congress of the International Astronautical Federation*. Graz, Austria, 1993.
[43] Conley, B. R. "Utilization of Ambient Gas as a Propellant for Low Earth Orbit Electric Propulsion," *Department of Aeronautics and Astronautics*. Vol. Master of Science, Massachusetts Institute of Technology, 1995.
[44] McGuire, T. J. "Aero-Assisted Orbital Transfer Vehicles Utilizing Atmosphere Ingestion," *Aeronautics and Astronautics*. Massachusetts Institute of Technology, 2001.
[45] Dressler, G. A. "Spacecraft Propulsive Device Using Ambient Upper Atmospheric Constituents for Reaction Mass," *42nd AIAA/ASME/SAE/ASEE Joint Propulsion Conference & Exhibit*. Sacramento, CA, 2006. AIAA 2006-4650.
doi: 10.2514/6.2006-4650
[46] Schamberg, R. "A New Analytic Representation of Surface Interaction for Hyperthermal Free Molecular Flow." Santa Monica, CA, RM-2313, 1959.
[47] Sentman, L. H. "Free Molecule Flow Theory and Its Application to the Determination of Aerodynamic Forces." Lockheed Martin Missile and Space Co.,

LMSC-448514, AD 265-409 (available from National Technical Information Service, Springfield, VA), 1961.

[48] Cook, G. E. "Satellite Drag Coefficients," *Planetary and Space Science* Vol. 13, 1965, pp. 929-946.

[49] Moe, K., Moe, M.M. "Gas-surface interactions and satellite drag coefficients," *Planetary and Space Science* Vol. 53, 2005, pp. 793-801.
doi: 10.1016/j.pss.2005.03.005

[50] King, S. T., Walker, M.L.R., Chianese, S.G. "Atmospheric Electric Propulsion Mission Performance Tool," *Journal of Spacecraft and Rockets* Vol. 51, No. 3, 2014, pp. 931-937.
doi: 10.2514/1.A32235

[51] Nishiyama, K. "Air breathing ion engine concept," *54th International Astronautical Congress of the International Astronautical Federation, the International Academy of Astronautics, and the International Institute of Space Law*. Bremen, Germany, 2003.
doi: 10.2514/6.IAC-03-S.4.02

[52] Clausing, P. "The flow of highly rarefied gases through tubes of arbitrary length.," *Journal of Vacuum Science and Technology* Vol. 8, No. 5, 1971, pp. 636-646.

[53] Tagawa, M., Yokota, K., Nishiyama, K., Kuninaka, H., Yoshizawa, Y., Yamamoto, D., Tsuboi, T. "Experimental Study of Air Breathing Ion Engine Using Laser Detonation Beam Source," *Journal of Propulsion and Power* Vol. 29, No. 3, 2013, pp. 501-506.
doi: 10.2514/1.B34530

[54] Feili, D., Lotz, B., Meyer, B., Loeb, H., Collingwood, C., Leiter, H., Kukies, R., Srminova, M., Khartov, S., Di Cara, D., Bulit, A. "Testing and Comprehensive Modeling of a GIE Utilizing Atmospheric Propellants," *33rd International Electric Propulsion Conference*. Washington, D.C., 2013. IEPC-2013-354.

[55] Di Cara, D., Gonzalez del Amo, J., Santovincenzo, A., Carnicero Dominguez, B., Arcioni, M., Caldwell, A., Roma, I. "RAM Electric Propulsion for Low Earth Orbit Operation: an ESA study.," *30th International Electric Propulsion Conference*. Florence, Italy, 2007. IEPC-2007-162.

[56] Pigeon, T. D., Whitaker, R.B. "Analysis of a Near-Vacuum Hall Thruster," *42nd AIAA Aerospace Sciences Meeting and Exhibit*. Reno, NV, 2004. AIAA 2004-127.
doi: 10.2514/6.2004-127

[57] Bashir, O. S., Sullivan, R.M. "Near-Vacuum Hall Thruster for Drag Compensation." Massachusetts Institute of Technology, 16.622 Final Report, 2004.

[58] Pekker, L., Keidar, M. "Analysis of Airbreathing Hall-Effect Thrusters," *Journal of Propulsion and Power* Vol. 28, No. 6, 2012, pp. 1399-1405.
doi: 10.2514/1.B34441

[59] Diamant, K. D. "A 2-Stage Cylindrical Hall Thruster for Air Breathing Electric Propulsion," *46th AIAA/ASME/SAE/ASEE Joint Propulsion Conference & Exhibit*. Nashville, TN, 2010. AIAA 2010-6522.
doi: 10.2514/6.2010-6522

[60] Charles, C., Boswell, R.W. "Laboratory evidence of a supersonic ion beam generated by a current-free "helicon" double-layer," *Physics of Plasmas* Vol. 11, No. 4, 2004, pp. 1706-1714.
doi: 10.1063/1.1652058

[61] Martinez, R. A., Hoskins, W.A., Peterson, P.Y., Massey, D.R. "Development Status of the Helicon Hall Thruster," *31st International Electric Propulsion Conference*. Ann Arbor, MI, 2009. IEPC-2009-120.

[62] Peterson, P. Y., Massey, D.R., Shabshelowitz, A., Shastry, R., Liang, R. "Performance and Plume Characterization of a Helicon Hall Thruster," *32nd International Electric Propulsion Conference*. Wiesbaden, Germany, 2011. IEPC-2011-269.

[63] Garrigues, L. "Computational Study of Hall-Effect Thruster with Ambient Atmospheric Gas as Propellant," *Journal of Propulsion and Power* Vol. 28, No. 2, 2012, pp. 344-354.
doi: 10.2514/1.B34307

[64] Kirtley, D., Slough, J., Pihl, C., Meier, E., Milroy, R. "Pulsed Plasmoind Propulsion: Air-Breathing Electromagnetic Propulsion," *32nd International Electric Propulsion Conference*. Wiesbaden, Germany, 2011. IEPC-2011-015.

[65] Jones, C., Masse, D., Glass, C., Wilhite, A., Walker, M. "PHARO - Propellant Harvesting of Atmospheric Resources in Orbit," *IEEE Aerospace Conference*. Big Sky, MT, 2010, pp. 1-9.
doi: 10.1109/AERO.2010.5447034

[66] Picone, J. M., Hedin, A.E., Drob, D.P., Aikin, A.C. "NRLMSISE-00 Emprical Model of the Atmosphere: Statistical Comparisons and Scientific Issues," *Journal of Geophysical Research: Space Phsysics (1978-2012)* Vol. 107, No. A12, 2002, pp. SIA 15-1 - 15-16.

[67] Hisamoto, Y., Nishiyama, K., Kuninaka, H. "Design of Air Intake for Air Breathing Ion Engine," *63rd International Astronautical Congress*. Naples, Italy, 2012.

[68] Diamant, K. D., Spektor, R., Beiting, E.J., Young, J.A., Curtiss, T.J. "The Effects of Background Pressure on Hall Thruster Operation," *48th AIAA/ASME/SAE/ASEE Joint Propulsion Conference and Exhibit*. Atlanta, GA, 2012. AIAA 2012-3735.
doi: 10.2514/6.2012-3735

[69] Gilmore, D. G. *Spacecraft Thermal Control Handbook*. El Segundo, CA: The Aerospace Press, 2002.

[70] Hale, G. E., Ellerman, F., Nicholson, S.B., Joy, A.H. "The Magnetic Polarity of Sun-Spots," *Astrophysical Journal* Vol. 49, 1919, pp. 153-178.

[71] Wilhite, A. W., Arrington, J.P., McCandless, R.S. "Performance Aerodynamics of Aero-Assisted Orbital Transfer Vehicles," *AIAA 22nd Aerospace Sciences Meeting*. Reno, NV, 1984. AIAA 84-0406.
doi: 10.2514/6.1984-406

[72] Schultheiss, D. "Gravity Compensation of Deployable Solar Array for Small Spacecraft," *Institut fur Statik und Dynamik*. Universitat Stuttgart, 2003.

[73] Hablanian, M. H. "New concepts in turbomolecular pump design," *Journal of vacuum Science and Technology A* Vol. 11, 1993, pp. 1614-1619.

[74] "Space Solar Panels." Spectrolab Inc., Sylmar, CA, 2010. http://www.spectrolab.com/DataSheets/Panel/panels.pdf.
[75] De Vos, A. "Detailed balance limit of the efficiency of tandem solar cells," *Journal of Physics D: Applied Physics* Vol. 13, 1980, pp. 839-846.
[76] Poston, D. I., Kapernick, R.J., Guffee, R.M., Reid, R.S., Lipinski, R.J., Wright, S.A., Talandis, R.A. "Design of a heatpipe-cooled Mars-surface fission reactor," *Space Technology and Applications International Forum - STAIF 2002*. Vol. 608, American Institute of Physics, 2002, pp. 1096-1106.
[77] Lamarsh, J. R., Baratta, A.J. *Introduction to Nuclear Engineering*. Upper Saddle River, NJ: Prentice Hall, 2001.
[78] Benes, O., Konings, R.J.M. "3.13 - Molten Salt Reactor Fuel and Coolant," *Comprehensive Nuclear Materials*. Vol. 3, Elsevier, Oxford, 2012, pp. 359-389.
[79] Fujita, K. "Air Intake Performance of Air Breathing Ion Engines," *Journal of the Japan Society for Aeronautical and Space Sciences* Vol. 52, No. 610, 2004, pp. 514-521, in Japanese.